Octahedral Deformations and Metal-Insulator Transition in Transition Metal Chalcogenides

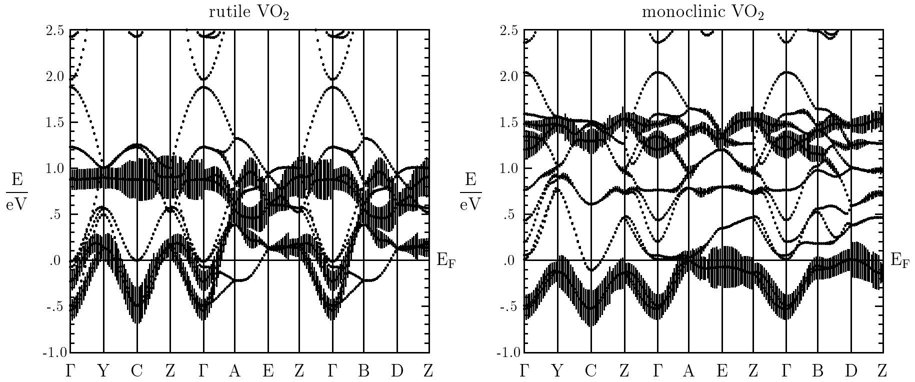

Der Mathematisch-Naturwissenschaftlichen Fakultät
der Universität Augsburg

vorgelegte

Habilitationsschrift

von

Volker Eyert

Juni 1998

Contents

List of Figures

List of Tables

Chapter 1

Introduction

The investigation of phase transitions has a long history in physics. Of course, well known examples include the transformations of matter from the gaseous to the liquid and, finally, to the solid state. In condensed matter further transformations originate from magnetism, superfluidity or superconductivity. In particular the latter transitions have attracted and still do attract a great deal of attention, both experimentally and theoretically. Various approaches to their description have been used and a lot of models were proposed. Yet, white spots of our understanding still remain.

One well known example is the metal-insulator transition. In contrast to the socalled Mott-Anderson transition, which originates from electron localization in disordered materials, the transition in ordered compounds, despite very intense work during the last decades, still awaits a satisfying and all-accepted explanation. Controversies have centered about the ability of various mechanisms to serve as a possible driving force for the transition. In this context, electron-electron correlations as well as electron-lattice interactions have been discussed, sometimes even as opposing and, hence, mutually exclusive mechanisms.

Density functional theory has increasingly become a valuable approach to the description of condensed matter in the past three decades. This is, of course, to a large extent due to the material aspect provided by this method, which allows to calculate many material specific ground state properties to high accuracy, given "only" the atomic numbers of the constituents. Nevertheless, in combination with the local density approximation, the *ab initio* methods have sometimes been regarded as being not well capable in describing systems with larger variations of the electron density, as they occur in many semiconductors and insulators. Nevertheless, since we do not share the opinion that the metal-insulator transition should at any rate be explained from a single source but rather feel that any contribution to identifying the driving force should be welcome, we initiated the first principles studies presented in this work.

It should not be overlooked that electronic structure calculations offer two different ways of using them. First, due to the dependence on the atomic number Z and the consideration of the detailed crystal structure, they may be used for accurate calculations of various material, e.g. electronic, magnetic, or optical, properties. From this point of view density functional theory lays ground for a dedicated tailoring of compounds and thus forms an important toolkit of materials science. Eventually, this has lead to the wide spread use of electronic structure codes, which have even found a commercial market.

Nevertheless, although the forementioned aspect of electronic structure calculations is of invaluable importance, there exists another, more theoretical aspect, which sometimes seems to be somewhat disregarded. Actually, there are only very few cases where density functional based calculations by themselves offer a fundamental insight in the important interactions, which finally lead to material properties. As a consequence, in order to arrive at a deeper understanding we can not leave it with the calculations but instead should use them as a starting point to isolate the important mechanisms and, hence, to develop explanations in terms of models. It is this aspect of electronic structure calculations, which we want to stress in the present work.

The interpretation of results obtained from electronic structure calculations requires some background on the underlying concepts and the methods. For this reason we give in the following second chapter a short and, of course, incomplete outline of the theoretical basis. In the subsequent chapters we will investigate the role played by electron-lattice interactions in several examples, which include the semiconductors FeS_2 and V_2O_5 and metallic MoO_2. Discussion of these compounds also lays ground for our investigation of VO_2, which addresses in particular to the metal-insulator transition.

Chapter 2

Concepts and Methods

2.1 Crystalline Periodicity

The unique characteristic which distinguishes crystals from all other modifications of matter is discrete translational symmetry (see e.g. [15, 138] or any other text-book on solid state physics). Physically speaking it originates from a corresponding symmetry of the Hamiltonian but the basic notions may nevertheless be understood from purely geometric considerations.

From this rather mathematical point of view translational symmetry is equivalent to the existence of a lattice of points

$$\mathbf{R}_\mu = \sum_{i=1}^{d} n_{\mu i} \mathbf{a}_i \tag{2.1.1}$$

which fulfil the condition that the whole crystal looks the same when translated by a lattice vector $\mathbf{R}_\mu$. d is the dimension of space and the vectors $\mathbf{a}_i$ form a set of d linear independent vectors. For each μ the set of integers $n_{\mu i}, i = 1, \ldots, d$ uniquely determines a lattice point.

In three dimensions there exist fourteen different such Bravais lattices among which are for instance the simple cubic (sc), face-centered cubic (fcc), body-centered cubic (bcc) and the hexagonal lattices [15, 138, 52].

The vectors $\mathbf{a}_i$ entering Eq. (2.1.1) are called the primitive translations and the parallelepiped they span is referred to as a primitive unit cell. In general, each volume of space, which, when displaced by all vectors of the Bravais lattice, fills space completely without any overlap, is called a primitive cell. A special choice, which is different from the simple parallelepiped, is the socalled Wigner-Seitz cell. In addition to being a primitive unit cell, it displays the full symmetry of the Bravais lattice. The Wigner-Seitz cell is constructed by selecting a certain lattice point as the origin and drawing planes, which are normal to the lines connecting the origin to the neighbouring points and bisect these lines. Usually a fairly small number of such planes suffices to arrive at a closed surface. The smallest possible cell constructed this way then defines the Wigner-Seitz cell. Below we will show examples for the Wigner-Seitz cells of the most common Bravais lattices.

The definitions of the Bravais lattice and the primitive translations $\mathbf{a}_i$ are complemented with the definition of the reciprocal lattice

$$\mathbf{K}_\nu = \sum_{i=1}^{d} m_{\nu i} \mathbf{b}_i \tag{2.1.2}$$

which likewise is a Bravais lattice. Its primitive translations $\mathbf{b}_i$ are defined by

$$\mathbf{b}_i = 2\pi \frac{\mathbf{a}_j \times \mathbf{a}_k}{\mathbf{a}_i \cdot (\mathbf{a}_j \times \mathbf{a}_k)} \, , \qquad i, j, k \text{ cyclic} \tag{2.1.3}$$

and one may easily check the identity

$$\mathbf{a}_i \cdot \mathbf{b}_j = 2\pi \cdot \delta_{ij} \quad . \tag{2.1.4}$$

According to the definition (2.1.3) the vectors of the reciprocal lattice have the dimension of an inverse length. Although this is related to the name "reciprocal" we note that the reciprocal of the reciprocal lattice again is the original "real space" lattice. Hence the name "reciprocal" lattice is somehow arbitrary.
In passing we write down another important identity which follows from the definitions (2.1.1) and (2.1.2) as well as the identity (2.1.4)

$$\mathbf{R}_\mu \mathbf{K}_\nu = 2\pi \cdot \sum_{i=1}^{d} n_{\mu i} m_{\nu i} \quad . \tag{2.1.5}$$

The sum on the right-hand side results in an integer and, hence, the product of lattice vectors of the "real space" and the reciprocal lattice will always be an integer multiple of 2π.

In the same manner as for the real space lattice there also exist primitive unit cells for the reciprocal lattice. In addition, again a fully symmetric primitive unit cell can be constructed which in reciprocal space is named first Brillouin zone.

We illustrate the previous definitions with the three cubic as well as the hexagonal Bravais lattices. In case of the simple cubic lattice the primitive translations may be chosen along the Cartesian axes and both the Wigner-Seitz cell and the first Brillouin zone simply are cubes. More interesting are the remaining two cubic lattices. Their primitive translations read as

$$\mathbf{a}_1 = \frac{a}{2}(\mathbf{y} + \mathbf{z}), \quad \mathbf{a}_2 = \frac{a}{2}(\mathbf{z} + \mathbf{x}), \quad \mathbf{a}_3 = \frac{a}{2}(\mathbf{x} + \mathbf{y}) \tag{2.1.6}$$

for the fcc lattice and

$$\mathbf{a}_1 = \frac{a}{2}(-\mathbf{x} + \mathbf{y} + \mathbf{z}), \quad \mathbf{a}_2 = \frac{a}{2}(\mathbf{z} - \mathbf{y} + \mathbf{x}), \quad \mathbf{a}_3 = \frac{a}{2}(\mathbf{x} + \mathbf{y} - \mathbf{z}) \tag{2.1.7}$$

for the bcc lattice. Here a denotes the lattice constant and $\mathbf{x}, \mathbf{y}, \mathbf{z}$ are the Cartesian unit vectors. Using Eq. (2.1.3) we calculate the reciprocal space primitive translations as

$$\mathbf{b}_1 = \frac{2\pi}{a}(-\mathbf{x} + \mathbf{y} + \mathbf{z}), \quad \mathbf{b}_2 = \frac{2\pi}{a}(\mathbf{z} - \mathbf{y} + \mathbf{x}), \quad \mathbf{b}_3 = \frac{2\pi}{a}(\mathbf{x} + \mathbf{y} - \mathbf{z}) \tag{2.1.8}$$

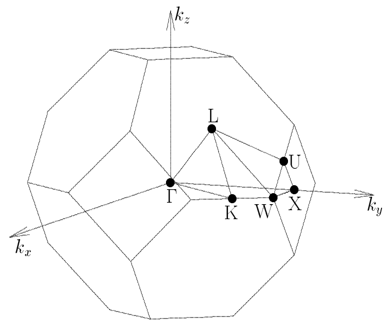

Figure 2.1: First Brillouin zone of the fcc lattice.

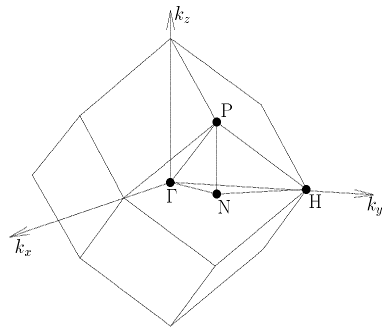

Figure 2.2: First Brillouin zone of the bcc lattice.

for the fcc lattice and

$$\mathbf{b}_1 = \frac{2\pi}{a}(\mathbf{y}+\mathbf{z}), \quad \mathbf{b}_2 = \frac{2\pi}{a}(\mathbf{z}+\mathbf{x}), \quad \mathbf{b}_3 = \frac{2\pi}{a}(\mathbf{x}+\mathbf{y}) \tag{2.1.9}$$

for the bcc lattice. Hence, except for a scale factor the reciprocal of the fcc lattice is just the bcc lattice and vice versa. We thus omit showing the Wigner-Seitz cell and give in Figs. 2.1 and 2.2 the first Brillouin zones of the two lattices. There we have, in addition, highlighted some special $\mathbf{k}$ points which are labelled according to the convention first introduced by Bouckaert et. al. [40] (see also [41]) and which will be discussed in more detail below.

In case of the hexagonal lattice the primitive translations are given by

$$\mathbf{a}_1 = -a\mathbf{y}, \quad \mathbf{a}_2 = a(\frac{\sqrt{3}}{2}\mathbf{x}+\frac{1}{2}\mathbf{y}), \quad \mathbf{a}_3 = c\mathbf{z} \tag{2.1.10}$$

(here we adopted the notation of Bradley and Cracknell [41]). From this the reciprocal space primitive translations are readily written down as

$$\mathbf{b}_1 = \frac{2\pi}{a}(\frac{1}{\sqrt{3}}\mathbf{x}-\mathbf{y}), \quad \mathbf{b}_2 = \frac{2\pi}{a}\frac{2}{\sqrt{3}}\mathbf{x}, \quad \mathbf{b}_3 = \frac{2\pi}{c}\mathbf{z} \quad . \tag{2.1.11}$$

The first Brillouin zone of the hexagonal lattice finally is given in Fig. 2.3.

We turn back to the physics underlying crystal symmetry and discuss its consequences on the electronic states, which finally leads to Bloch's theorem. As already

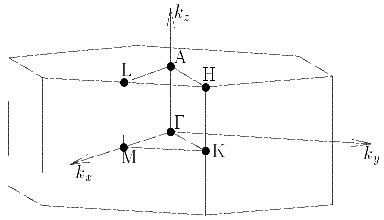

Figure 2.3: First Brillouin zone of the hexagonal lattice.

mentioned at the beginning of this section crystal symmetry results from a corresponding symmetry of the Hamiltonian

$$H(\mathbf{r} + \mathbf{R}_\mu) = H(\mathbf{r}) \quad . \tag{2.1.12}$$

In other words, the Hamiltonian is invariant under a translation by an arbitrary lattice vector and thus it commutes with all the translation operators,

$$\left[H, T_{\mathbf{R}_\mu}\right]_- = 0 \qquad \forall_\mu \quad , \tag{2.1.13}$$

which are defined by the way they act onto a function in space,

$$T_{\mathbf{R}_\mu} f(\mathbf{r}) := f(\mathbf{r} + \mathbf{R}_\mu) \quad . \tag{2.1.14}$$

The basic properties of the translation operators are easily derived. Obviously, successive translations by the lattice vectors $\mathbf{R}_\mu$ and $\mathbf{R}_\nu$ in either order are equivalent to the single translation by $\mathbf{R}_\mu + \mathbf{R}_\nu$, i.e.

$$T_{\mathbf{R}_\mu} T_{\mathbf{R}_\nu} = T_{\mathbf{R}_\nu} T_{\mathbf{R}_\mu} = T_{\mathbf{R}_\mu + \mathbf{R}_\nu} \quad . \tag{2.1.15}$$

Especially for $\mathbf{R}_\nu = -\mathbf{R}_\mu$ we obtain

$$T_{\mathbf{R}_\mu} T_{-\mathbf{R}_\mu} = T_{-\mathbf{R}_\mu} T_{\mathbf{R}_\mu} = T_{\mathbf{0}} = \mathcal{I} \tag{2.1.16}$$

where $\mathcal{I}$ is the unity operator. In particular, Eq. (2.1.16) serves as a definition of the inverse translation operator. We thus arrive at the conclusion that all translation operators form an Abelian group.

Since the translation operators commute with the Hamiltonian both have the same system of eigenfunctions and we are thus able to write

$$T_{\mathbf{R}_\mu} \psi_n(\mathbf{r}) = \lambda_\mu \psi_n(\mathbf{r}) \tag{2.1.17}$$

where the $\psi_n(\mathbf{r})$ are the eigenfunctions of the Hamiltonian,

$$H(\mathbf{r}) \psi_n(\mathbf{r}) = \varepsilon_n \psi_n(\mathbf{r}) \tag{2.1.18}$$

and n labels different eigenfunctions. Still we have to deduce the eigenvalues λ_μ of the translation operators. To this end we use again crystal translational symmetry which implies that the results of any measurement are unaffected by a translation. As a consequence, the square of the norm of the wavefunction must be invariant. In addition, we can tell from Wigner's theorem that the norm itself must be invariant under translations and that the translation operators are either unitary or anti-unitary. Due to the invariance of the norm the eigenvalues λ_μ of the translation operators must be complex and of modulus 1. Hence

$$\lambda_\mu = e^{i\Theta_\mu} \quad . \tag{2.1.19}$$

Combining Eqs. (2.1.15), (2.1.17) and (2.1.19) we obtain the identity

$$e^{i\Theta_\mu} e^{i\Theta_\nu} = e^{i(\Theta_\mu + \Theta_\nu)} \tag{2.1.20}$$

which is fulfilled if

$$\Theta_\mu = \mathbf{k}\mathbf{R}_\mu \tag{2.1.21}$$

with the vector $\mathbf{k}$ as yet unspecified. Combining this with Eqs. (2.1.14), (2.1.17) and (2.1.19) we finally arrive at Bloch's theorem

$$\psi_{n\mathbf{k}}(\mathbf{r} + \mathbf{R}_\mu) = e^{i\mathbf{k}\mathbf{R}_\mu} \psi_{n\mathbf{k}}(\mathbf{r}) \tag{2.1.22}$$

where the function $\psi_{n\mathbf{k}}(\mathbf{r})$ is called a Bloch function [33]. Note that we have used the $\mathbf{k}$ vector as an additional label.

Bloch's theorem sometimes is written in an altenative form which arises from inserting the ansatz

$$\psi_{n\mathbf{k}}(\mathbf{r}) = e^{i\mathbf{k}\mathbf{r}} u_{n\mathbf{k}}(\mathbf{r}) \tag{2.1.23}$$

into Eq. (2.1.22) this resulting in

$$u_{n\mathbf{k}}(\mathbf{r} + \mathbf{R}_\mu) = u_{n\mathbf{k}}(\mathbf{r}) \quad . \tag{2.1.24}$$

Thus, according to Bloch's theorem the wave function can be written as the product of a phase factor and a function $u_{n\mathbf{k}}(\mathbf{r})$ which has the periodicity of the lattice.

Obviously, the vector $\mathbf{k}$ has the dimension of an inverse length and we may thus assign it to reciprocal space. Moreover, it is possible to consider only those $\mathbf{k}$ vectors which belong to the first Brillouin zone. To see this we start from two vectors $\mathbf{k}$ and $\mathbf{k}'$ which are separated by a lattice vector $\mathbf{K}_\nu$, i.e.

$$\mathbf{k}' = \mathbf{k} + \mathbf{K}_\nu \quad . \tag{2.1.25}$$

Due to the identity (2.1.5) wave functions labelled with vectors $\mathbf{k}$ and $\mathbf{k}'$ belong to the same eigenspace, i.e.

$$T_{\mathbf{R}_\mu} \psi_{n\mathbf{k}'}(\mathbf{r}) = e^{i\mathbf{k}\mathbf{R}_\mu} \psi_{n\mathbf{k}'}(\mathbf{r}) \tag{2.1.26}$$

and

$$T_{\mathbf{R}_\mu} \psi_{n\mathbf{k}}(\mathbf{r}) = e^{i\mathbf{k}\mathbf{R}_\mu} \psi_{n\mathbf{k}}(\mathbf{r}) \tag{2.1.27}$$

and thus are identical. The same holds for the eigenvalues and we note the result

$$\psi_{n\mathbf{k}+\mathbf{K}_\nu}(\mathbf{r}) = \psi_{n\mathbf{k}}(\mathbf{r}) \tag{2.1.28}$$

and

$$\varepsilon_{n\mathbf{k}+\mathbf{K}_\nu} = \varepsilon_{n\mathbf{k}} \quad . \tag{2.1.29}$$

Of course, crystals can possess more than translational symmetry and in fact most crystals realized in nature do. The operations connected with the additional symmetries are rotations and reflections and like the translations they form groups. These groups are called point groups since rotations and reflections (which can be viewed as rotations followed by inversion) are all taken about a fixed center. In the same manner as in the case of the translations point group symmetries arise from an underlying symmetry of the Hamiltonian and thus the corresponding operators commute with H.

Finally, the point group operations may be combined with fractional translations which are translations by non-lattice vectors. This gives rise to screw axes and glide planes. Altogether the fourteen Bravais lattices and 32 point groups then lead to the 230 space groups. Each space group is distinguished by the way the atoms are arranged within the primitive cell. Since a more detailed discussion of the subject is beyond the scope of this chapter we refer the interested reader to the literature (see for instance [145, 51, 148, 41, 163]).

Obviously, rotations, reflections and fractional translations lead to planes, lines and points both in real and reciprocal space which are invariant under these operations. In particular, in $\mathbf{k}$ space they moreover define the irreducible wedge of the first Brillouin zone, which, by applying all allowed space group operations, fills the whole first Brillouin zone without overlap. For the evaluation of $\mathbf{k}$ space integrals it is thus sufficient to calculate the wave functions $\psi_{n\mathbf{k}}(\mathbf{r})$ and eigenvalues $\varepsilon_{n\mathbf{k}}$ only in the irreducible wedge. As concerns the representation and interpretations of results it has become customary to plot all the $\varepsilon_{n\mathbf{k}}$ along some of the abovementioned symmetry lines connecting the high-symmetry points (which we have already indicated in Figs. 2.1 to 2.3). This is what we call the band structure.

We illustrate the band structure with the simplest possible example, namely the free electron dispersion curves. They arise from a Hamiltonian containing a constant potential as

$$\varepsilon_{n\mathbf{k}} = |\mathbf{k}|^2 \tag{2.1.30}$$

and are shown for the fcc, bcc, and hexagonal lattice in Figs. 2.4, 2.5, and 2.6, respectively.

In addition, the evaluation of integrals over the first Brillouin zone is illustrated with the calculation of the density of states. Before we do so we must, however, specify appropriate boundary conditions for the wave function which guarantee that the electrons are confined to the macroscopic crystal. Since we are aiming at the description of bulk properties the particular choice of these boundary conditions is not important. Hence, we follow convention and choose Born-von Kármán boundary conditions which require

$$\psi_{n\mathbf{k}}(\mathbf{r} + N_i\mathbf{a}_i) = \psi_{n\mathbf{k}}(\mathbf{r}) \ , \qquad i = 1, 2, 3 \quad . \tag{2.1.31}$$

The $\mathbf{a}_i$ denote the primitive translations and the N_i are integers, where $N = N_1 \cdot N_2 \cdot N_3$ is the total number of primitive cells in the crystal. Applying Bloch's theorem (2.1.22) to the boundary condition (2.1.31) we find that

$$e^{iN_i\mathbf{k}\mathbf{a}_i} = 1 \quad . \tag{2.1.32}$$

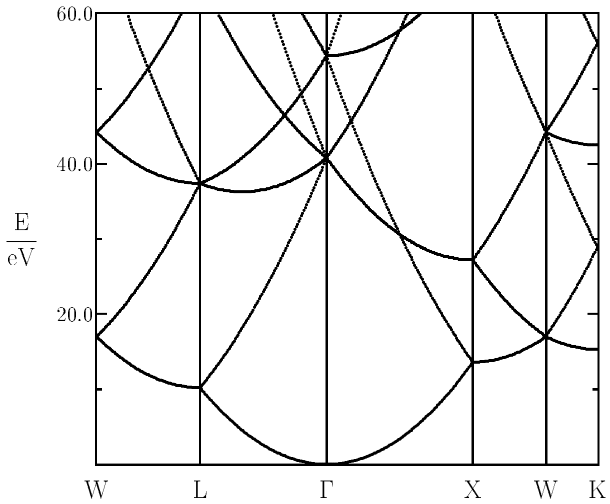

Figure 2.4: Free electron dispersion curves for the fcc lattice along selected symmetry lines of the first Brillouin zone. The points indicated are the same as in Fig. 2.1.

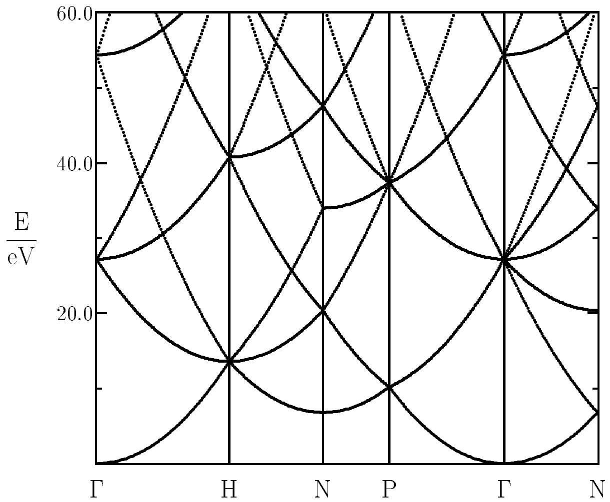

Figure 2.5: Free electron dispersion curves for the bcc lattice along selected symmetry lines of the first Brillouin zone. The points indicated are the same as in Fig. 2.2.

Since any vector $\mathbf{k}$ in reciprocal space can be written as

$$\mathbf{k} = \sum_{i=1}^{d} x_{\mathbf{k}i} \mathbf{b}_i \tag{2.1.33}$$

Eqs. (2.1.4) and (2.1.32) imply

$$x_{\mathbf{k}i} = \frac{m_{\mathbf{k}i}}{N_i} \quad , \tag{2.1.34}$$

where $m_{\mathbf{k}i}$ is an integer, or else

$$\mathbf{k} = \sum_{i=1}^{d} \frac{m_{\mathbf{k}i}}{N_i} \mathbf{b}_i \quad . \tag{2.1.35}$$

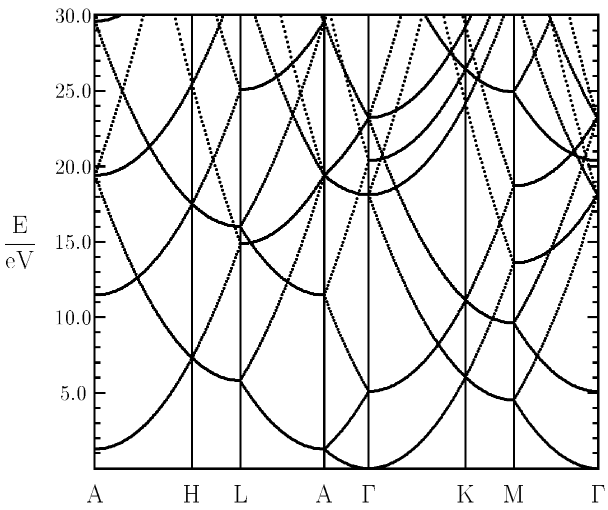

Figure 2.6: Free electron dispersion curves for the hexagonal lattice along selected symmetry lines of the first Brillouin zone. The points indicated are the same as in Fig. 2.3.

As a consequence, all allowed $\mathbf{k}$ vectors lie on an equidistant grid in the reciprocal primitive cell which becomes infinitesimaly fine for $N \to \infty$. It follows from Eq. (2.1.35) that the volume $\Omega_{\mathbf{k}}$ per $\mathbf{k}$ point is just the volume of the reciprocal unit cell

$$\Omega_{BZ} := \mathbf{b}_1 \cdot (\mathbf{b}_2 \times \mathbf{b}_3) = \frac{(2\pi)^3}{\mathbf{a}_1 \cdot (\mathbf{a}_2 \times \mathbf{a}_3)} =: \frac{(2\pi)^3}{\Omega_{UC}} \tag{2.1.36}$$

divided by the number N of micro-parallelepipeds,

$$\Omega_{\mathbf{k}} = \frac{\Omega_{BZ}}{N} = \frac{(2\pi)^3}{N \cdot \Omega_{UC}} \quad . \tag{2.1.37}$$

Due to the grid of $\mathbf{k}$ points given by Eq. (2.1.35) the above mentioned Brillouin zone integrals actually appear to be sums over all allowed $\mathbf{k}$ points, which only in the limit of infinite N can be replaced with an integral

$$\sum_{\mathbf{k}} \to \frac{N \cdot \Omega_{UC}}{(2\pi)^3} \int_{\Omega_{BZ}} d^3\mathbf{k} \quad . \tag{2.1.38}$$

In practice, one is often faced with the calculation of quantities of the form

$$I_A(E) = \frac{1}{N} \sum_{n\mathbf{k}} A_{n\mathbf{k}} \delta(E - \varepsilon_{n\mathbf{k}}) \tag{2.1.39}$$

where the $A_{n\mathbf{k}}$ may be simply viewed as weights associated to each electronic state $\psi_{n\mathbf{k}}(\mathbf{r})$ and $\delta(x)$ is Dirac's δ distribution. Using the prescription (2.1.38) we cast the sum into an integral

$$I_A(E) = \frac{1}{\Omega_{BZ}} \sum_{n} \int_{\Omega_{BZ}} d^3\mathbf{k}\ A_{n\mathbf{k}} \delta(E - \varepsilon_{n\mathbf{k}}) \quad . \tag{2.1.40}$$

Moreover, quite often the quantities $A_{n\mathbf{k}}$ depend on n and $\mathbf{k}$ only via the eigenvalues $\varepsilon_{n\mathbf{k}}$ of the Hamiltonian, i.e.

$$A_{n\mathbf{k}} = \tilde{A}_n(\varepsilon_{n\mathbf{k}}) \quad . \tag{2.1.41}$$

In that case Eq. (2.1.40) reduces to

$$I_A(E) = \frac{1}{\Omega_{BZ}} \sum_n \tilde{A}_n(E) \int_{\Omega_{BZ}} d^3\mathbf{k}\; \delta(E - \varepsilon_{n\mathbf{k}}) \quad . \tag{2.1.42}$$

For $A_{n\mathbf{k}} = 1$, in particular, we arrive at the definition of the density of states for the nth band by

$$\rho_n(E) := \frac{1}{\Omega_{BZ}} \int_{\Omega_{BZ}} d^3\mathbf{k}\; \delta(E - \varepsilon_{n\mathbf{k}}) \tag{2.1.43}$$

which allows to write the integral (2.1.42) as

$$I_A(E) = \sum_n \tilde{A}_n(E) \rho(E) \quad . \tag{2.1.44}$$

The actual calculation of densities of states is not a trivial task and a lot of work has been done in order to develop both accurate and efficient schemes. It includes the selection of socalled special points, which, when used for summations as in Eq. (2.1.39), approximate the Brillouin zone integral very well [20, 58, 186], as well as schemes for the efficient evaluation of integrals from the $A_{n\mathbf{k}}$ calculated at a finite set of points. For electronic structure calculations most often used methods are sampling schemes as well as the linear tetrahedron method (see for example [180, 34] and references therein).

2.2 Adiabatic approximation

When aiming at the calculation of the electronic wave function we are faced with the full problem containing both the ionic and electronic degrees of freedom. Its solution poses a formidable task and for this reason an ansatz for an effective decoupling of the electronic and ionic problems would be desirable. Fortunately such an ansatz exists in form of the Born and Oppenheimer "adiabatic approximation" [38]. From a physical point of view it is based on the fact that the electrons are much lighter than the nuclei. As a consequence, if the ions are not too far from their equilibrium positions the electrons move much faster than the nuclei and, hence, follow the ionic motion adiabatically. In other words, on the timescale of electronic motion the ions appear as being at fixed positions. At the same time the electronic distribution contributes to the potential seen by the nuclei.

A theoretical justification of the adiabatic approximation can be achieved within the framework of perturbation theory where the small expansion parameter is the ratio of electronic and ionic masses. We will not follow this approach here but rather sketch some of the basis ideas while referring the more interested reader to the literature (see e.g. [277, 115, 52, 131]).

We start out from the full Hamiltonian describing the nuclei as well as the electrons,

$$H = H_{ion} + H_{el} + H_{ion-el} \tag{2.2.1}$$

where

$$H_{ion} = \sum_{\mu} \left[-\frac{\hbar^2}{2M_\mu}\nabla_\mu^2 + \frac{1}{2}\sum_{\substack{\nu \\ \nu\neq\mu}} V_{ion-ion}(\mathbf{R}_\mu - \mathbf{R}_\nu) \right] \quad , \tag{2.2.2}$$

$$H_{el} = \sum_{i} \left[-\frac{\hbar^2}{2m}\nabla_i^2 + \frac{1}{2}\sum_{\substack{j \\ j\neq i}} \frac{e^2}{|\mathbf{r}_i - \mathbf{r}_j|} \right] \quad , \tag{2.2.3}$$

$$H_{ion-el} = \sum_{\mu}\sum_{i} V_{ion-el}(\mathbf{r}_i - \mathbf{R}_\mu) \tag{2.2.4}$$

and $V_{ion-ion}$ and V_{ion-el} are the ion-ion and ion-electron interaction, respectively. $\mathbf{R}_\nu$ denotes the position of an ion.

Next, for the time being, we assume that the ions are at fixed positions and solve Schrödinger's equation connected with the electronic problem, i.e.

$$\begin{aligned} H_0\psi_\alpha(\{\mathbf{r}_i,\mathbf{R}_\mu\}) &:= \Big(H_{el} + H_{ion-el}\Big)\psi_\alpha(\{\mathbf{r}_i,\mathbf{R}_\mu\}) \\ &= E_{0\alpha}(\{\mathbf{R}_\mu\})\psi_\alpha(\{\mathbf{r}_i,\mathbf{R}_\mu\}) \end{aligned} \tag{2.2.5}$$

where α labels different solutions, which, being eigenstates of H_0, are orthogonal and assumed to be normalized. Note that the positions of the nuclei still enter the Hamiltonian H_0, the electronic wave functions ψ_α, and the energies $E_{0\alpha}$. However, they are just parameters here.

Since the solutions of Schrödinger's equation (2.2.5) form a complete set we are able to expand the solutions Φ_γ of Schrödinger's equation connected with the full Hamiltonian (2.2.1),

$$H\Phi_\gamma(\{\mathbf{r}_i,\mathbf{R}_\mu\}) = E_\gamma(\{\mathbf{R}_\mu\})\Phi_\gamma(\{\mathbf{r}_i,\mathbf{R}_\mu\}) \tag{2.2.6}$$

in the electronic states ψ_α, i.e.

$$\Phi_\gamma(\{\mathbf{r}_i,\mathbf{R}_\mu\}) = \sum_\alpha \varphi_\alpha(\{\mathbf{R}_\mu\})\psi_\alpha(\{\mathbf{r}_i,\mathbf{R}_\mu\}) \quad . \tag{2.2.7}$$

We insert this expansion into Eq. (2.2.6) and combine it with Schrödinger's equation (2.2.5) for the electronic problem. Using the identity

$$\begin{aligned} & H_{ion}\varphi_\alpha(\{\mathbf{R}_\mu\})\psi_\alpha(\{\mathbf{r}_i,\mathbf{R}_\mu\}) \\ &= \psi_\alpha(\{\mathbf{r}_i,\mathbf{R}_\mu\})H_{ion}\varphi_\alpha(\{\mathbf{R}_\mu\}) \\ &\quad -\sum_\nu \frac{\hbar^2}{2M_\mu}\Big[\Big(\nabla_\mu^2\psi_\alpha(\{\mathbf{r}_i,\mathbf{R}_\mu\})\Big)\varphi_\alpha(\{\mathbf{R}_\mu\}) \\ &\qquad\qquad +2\nabla_\mu\psi_\alpha(\{\mathbf{r}_i,\mathbf{R}_\mu\})\cdot\nabla_\mu\varphi_\alpha(\{\mathbf{R}_\mu\})\Big] \end{aligned} \tag{2.2.8}$$

and integrating out the electronic coordinates we then arrive at

$$\begin{aligned} & \langle\psi_{\alpha'}(\{\mathbf{r}_i,\mathbf{R}_\mu\})|H|\sum_\alpha \varphi_\alpha(\{\mathbf{R}_\mu\})\psi_\alpha(\{\mathbf{r}_i,\mathbf{R}_\mu\})\rangle \\ &= \sum_\alpha \Big[\Big(H_{ion} + E_{0\alpha}(\{\mathbf{R}_\mu\})\Big)\delta_{\alpha'\alpha} + C_{\alpha'\alpha}(\{\mathbf{R}_\mu\})\Big]\varphi_\alpha(\{\mathbf{R}_\mu\}) \\ &= E_\gamma(\{\mathbf{R}_\mu\})\varphi_{\alpha'}(\{\mathbf{R}_\mu\}) \end{aligned} \tag{2.2.9}$$

where the operator $C_{\alpha'\alpha}(\{\mathbf{R}_\mu\})$ is given by

$$
\begin{aligned}
& C_{\alpha'\alpha}(\{\mathbf{R}_\mu\}) \\
&= -\int d^3\{\mathbf{r}_i\}\, \psi_{\alpha'}(\{\mathbf{r}_i, \mathbf{R}_\mu\}) \\
&\qquad \sum_\nu \frac{\hbar^2}{2M_\nu} \Big[\Big(\nabla_\nu^2 \psi_\alpha(\{\mathbf{r}_i, \mathbf{R}_\mu\}) \Big) + 2\nabla_\nu \psi_\alpha(\{\mathbf{r}_i, \mathbf{R}_\mu\}) \nabla_\nu \Big] \quad .
\end{aligned}
\tag{2.2.10}
$$

Obviously, this operator $C_{\alpha'\alpha}(\{\mathbf{R}_\mu\})$ couples different states $\varphi_\alpha(\{\mathbf{R}_\mu\})$ of the ionic lattice and thereby induces transitions between different electronic wave functions. It can be shown (see e.g. [277]) that the contributions to the total energy due to the diagonal terms of this operator are proportional to the ratio of electronic and ionic masses and hence small compared to thermal energies.

In the adiabatic approximation the operator $C_{\alpha'\alpha}(\{\mathbf{R}_\mu\})$ is entirely ignored. Then we are left with only diagonal terms of Eq. (2.2.9) and obtain

$$
\Big(H_{ion} + E_{0\alpha}(\{\mathbf{R}_\mu\}) \Big) \varphi_\alpha(\{\mathbf{R}_\mu\}) = E_\gamma(\{\mathbf{R}_\mu\}) \varphi_\alpha(\{\mathbf{R}_\mu\}) \quad . \tag{2.2.11}
$$

This is just Schrödinger's equation for the ionic states. The Hamiltonian entering Eq. (2.2.11) results from the bare Hamiltonian H_{ion} of the ions as given by Eq. (2.2.2) by adding the "potential" $E_{0\alpha}(\{\mathbf{R}_\mu\})$, which is due to the electrons. The latter depends on the electronic wave functions $\psi_\alpha(\{\mathbf{r}_i, \mathbf{R}_\mu\})$ but still is quite insensitive to the details of the electronic distribution since under normal conductivity conditions rearrangements of the electrons affect only states near the Fermi energy.

It should finally be noted that in Schrödinger's equation (2.2.5) for the electronic states the ions enter in their momentary positions whereas in Eq. (2.2.11) which determines the ionic states the average of the electronic distribution is considered. This reflects the abovementioned presence of different timescales of the ionic and electronic motion.

In summary, thanks to the adiabatic approximation we are able to concentrate on the electronic problem while assuming the ions to stay at fixed positions. Nevertheless, even the Hamiltonian H_0 alone, which determines the electronic wave functions, still constitutes a difficult problem which fact may be traced back to the long-range electron-electron interactions. At this point, we rely on density functional theory (DFT) and the local density approximation (LDA), which, in an albeit approximate manner, cast the full many-body problem connected with the system of interacting electrons into an effective single particle self-consistent field problem and which will be discussed in the following section.

2.3 Density functional theory

2.3.1 General facts

Since its introduction by Hohenberg, Kohn, and Sham in the mid sixties, density functional theory (DFT) in combination with the local density approximation (LDA) has become a standard theory for electronic structure calculations and the single-particle theory [122, 142]. Thus, there exist many review articles about the theory and its various applications, to which the reader is referred [143, 21, 265, 70, 69, 149, 23, 75]. In the present and the following section, we will summarize the basics of DFT and LDA.

We start out writing down the general Hamiltonian for the interacting N-electron system as given within the Born-Oppenheimer adiabatic approximation:

$$\begin{aligned} H_0 &= H_{el} + H_{ion-el} \\ &= T_{el} + H_{ion-el} + U_{el} \end{aligned} \tag{2.3.1}$$

where

$$T_{el} = -\sum_i \frac{\hbar^2}{2m}\nabla_i^2 \quad , \tag{2.3.2}$$

$$H_{ion-el} = \sum_\mu \sum_i V_{ion-el}(\mathbf{r}_i - \mathbf{R}_\mu) = \sum_i v_{ext}(\mathbf{r}_i) \quad , \tag{2.3.3}$$

$$U_{el} = \frac{1}{2}\sum_i \sum_{\substack{j \\ j\neq i}} \frac{e^2}{|\mathbf{r}_i - \mathbf{r}_j|} \tag{2.3.4}$$

and V_{ion-el} is the ion-electron interaction, respectively. Again, $\mathbf{R}_\nu$ denotes the position of an ion. In Eq. (2.3.3), we have added an alternative representation, which emphasizes the role of the potential created by the ions as an external potential seen by the electrons.

Following common practice we will in the remaining part of this section use atomic units and thus measure, for example, lengths in units of Bohr radii, $a_B = \frac{\hbar^2}{me^2} = 0.529177249 \cdot 10^{-10}$m and energies in units of Rydberg, Ryd $= \frac{\mathrm{e}^2}{2\mathrm{a_B}} = \frac{\mathrm{me}^4}{2\hbar^2} =$ 13.6058eV. To arrive at these atomic units one may simply set $\hbar = 1$, $e^2 = 2$, and $m = \frac{1}{2}$ in equations which are formulated in cgs-units [79].

We define the electron-density operator by

$$\hat{n}(\mathbf{r}) = \sum_i \delta(\mathbf{r} - \mathbf{r}_i) \tag{2.3.5}$$

from which we obtain the electron density as

$$n(\mathbf{r}) = \langle \Phi | \hat{n}(\mathbf{r}) | \Phi \rangle \tag{2.3.6}$$

where $|\Phi\rangle$ is a many-body state.

Although numerous techniques exist to deal with the full many-body problem defined by Eqs. (2.3.1) to (2.3.4), no exact solution is known. Density functional theory and the local-density approximation, which cast the full problem posed by the system of interaction electrons into an effective single-particle problem, start out from the work by Hohenberg and Kohn, who established that the electron density is the central variable and formulated the following two theorems:

1. The total ground state energy of any many-electron system is a functional of the particle density $n(\mathbf{r})$:

$$E[n] = F[n] + \int n(\mathbf{r}) v_{ext}(\mathbf{r}) d^3\mathbf{r} \quad , \tag{2.3.7}$$

where $F[n]$ itself is a functional of the density $n(\mathbf{r})$ independent of the external potential.

2. For any many-electron system the functional $E[n]$ for the total energy has a minimum equal to the ground state energy at the ground state density.

This second theorem is of practical importance as it leads to a variational principle.

To prove these theorems we turn to the work of Levy [157, 158], who overcame some of the restrictions of the Hohenberg-Kohn theory concerning, for instance the non-degeneracy of the ground state, by defining a functional

$$O[n] = \inf_{|\Phi\rangle\epsilon M(n)} \langle\Phi|\hat{O}|\Phi\rangle \tag{2.3.8}$$

for a physical observable $\hat{O}$ (we will assume the infimum to exist, which is quite reasonable for the functionals of interest). The set $M(n)$ contains all those many-body wave functions which yield the density n. It might be further limited by certain conditions, e.g., that this set picks out only wave functions giving the ground state to an external potential or corresponding to an N-particle state. These situations normally are referred to as v-representability or N-representability, respectively. It should be noted that the Levy construction not only is a natural generalization of the Hohenberg-Kohn ansatz of a v-representable density but, in addition, allows to handle spin-polarized systems or relativistic calculations [21, 22].

Using the Levy functional to set up the functionals of the operators H_0, H_{ion-el}, and $F = T_{el} + U_{el}$ for an N-representable density, the validity of the first theorem can be seen directly (one uses Eqs. (2.3.5) and (2.3.6) to obtain the second term on the right-hand side of eq. (2.3.7) as the functional of H_{ion-el}). The proof of the second theorem is carried out in the following way: We denote by $|\Phi_0\rangle$, n_0 and E_0 the ground state (or any ground state in case of degeneracy), its density and its energy, respectively. $|\Phi_n\rangle$ may be any state yielding the density $n(\mathbf{r})$ and minimizing the functional $F[n]$ and thus $E[n]$. We have to show that in this case E_n, n and E_0, n_0 are the same.

Since E_0 was defined as the ground state energy, we have

$$E[n] \geq E_0 \tag{2.3.9}$$

for any density $n(\mathbf{r})$. On the other hand, if we calculate $F[n]$ with the ground state according to Eq. (2.3.8) we obtain

$$F[n_0] = \inf_{|\Phi\rangle} \langle\Phi|T_{el} + U_{el}|\Phi\rangle \leq \langle\Phi_0|T_{el} + U_{el}|\Phi_0\rangle \quad . \tag{2.3.10}$$

Thus, by adding the functional of the external potential we arrive at

$$E[n_0] \leq E_0 \quad . \tag{2.3.11}$$

The expressions (2.3.9) and (2.3.11) can be fulfilled simultaneously only if $n = n_0$ and thus $E[n] = E[n_0]$. From this it follows immediately that

$$E[n_0] = E_0 \quad . \tag{2.3.12}$$

Although the basic facts of density functional theory are stated now, we still need a key to its applications. Such a key was given by Kohn and Sham, who used the variational principle implied by the minimal properties of the energy functional to derive single-particle Schrödinger-like equations [142].

Following Kohn and Sham we first split the functional $F[n]$ into three parts

$$F[n] = T[n] + \int\int n(\mathbf{r}) v_{el-el}(\mathbf{r}-\mathbf{r}') n(\mathbf{r}') d^3\mathbf{r}' d^3\mathbf{r} + E_{xc}[n] \quad . \tag{2.3.13}$$

The terms on the right hand side of Eq. (2.3.13) denote the kinetic, Hartree and exchange-correlation energy, respectively. In contrast to the Hartree integral the explicit form of the other functionals, T and E_{xc}, is not known in general. We will ignore this problem for now and proceed in writing down the Euler-Lagrange equation following from the variational principle:

$$\frac{\delta E[n]}{\delta n(\mathbf{r})} - \mu \frac{\delta(N - \int n(\mathbf{r}) d^3\mathbf{r})}{\delta n(\mathbf{r})} = 0 \quad , \tag{2.3.14}$$

where μ is a Lagrange-parameter taking care of particle conservation. Inserting Eq. (2.3.13) into the Euler-Lagrange equation we get:

$$\frac{\delta T[n]}{\delta n(\mathbf{r})} + v_{ext}(\mathbf{r}) + 2\int v_{el-el}(\mathbf{r}-\mathbf{r}') n(\mathbf{r}') d^3\mathbf{r}' + \frac{\delta E_{xc}[n]}{\delta n(\mathbf{r})} - \mu = 0 \quad . \tag{2.3.15}$$

The functional $E_{xc}[n]$ is still not known, but concerning the kinetic energy, Kohn and Sham realized that the above equation can be interpreted as the Euler-Lagrange equation of non-interacting particles moving in an external, effective potential, given by

$$v_{eff}(\mathbf{r}) = v_{ext}(\mathbf{r}) + 2\int v_{el-el}(\mathbf{r}-\mathbf{r}') n(\mathbf{r}') d^3\mathbf{r}' + v_{xc}(\mathbf{r}) \tag{2.3.16}$$

where the exchange-correlation potential

$$v_{xc}(\mathbf{r}) = \frac{\delta E_{xc}[n]}{\delta n(\mathbf{r})} \tag{2.3.17}$$

contains all the many-body effects. So they took advantage of the fact that the case of non-interacting electrons allows an exact computation of the single-particle density and the kinetic energy

$$n(\mathbf{r}) = \sum_i |\psi_i(\mathbf{r})|^2 \Theta(E_F - E_i) \tag{2.3.18}$$

$$T_0[n] = -\sum_i \int \psi_i^*(\mathbf{r}) \nabla^2 \psi_i(\mathbf{r}) d^3\mathbf{r} \Theta(E_F - E_i) \quad , \tag{2.3.19}$$

where $\Theta(E_F - E_i)$ is the Heaviside step function restricting the sums to only the occupied states. Fermi statistics was thus implicitly introduced by filling the single-particle states ψ_i in Eq. (2.3.18) up to the Fermi-energy E_F. In addition, we assumed the states to be normalized. Furthermore, we used the new symbol T_0 to designate the kinetic energy of noninteracting electrons, thus part of the kinetic energy is contained in the exchange-correlation energy E_{xc}, for which we use the same symbol as in Eq. (2.3.13), for simplicity in writing.

We next derive the single-particle equations. We start with Eq. (2.3.18) and write down again the Euler-Lagrange equation, this time in terms of the single-particle wave functions:

$$\sum_i \left[\frac{\delta E[n]}{\delta \psi_i^*(\mathbf{r})} - \epsilon_i \frac{\delta(N - \int n(\mathbf{r}) d^3\mathbf{r})}{\delta \psi_i^*(\mathbf{r})} \right] \delta \psi_i^* = 0 \quad , \tag{2.3.20}$$

where we introduced Lagrange multipliers for every ψ_i. Since the wave functions are independent of each other, the expression in brackets must vanish for each ψ_i. Now using Eqs. (2.3.16) to (2.3.19), we obtain

$$\begin{aligned} & \frac{\delta T_0[n]}{\delta \psi_i^*(\mathbf{r})} + v_{eff}(\mathbf{r}) \frac{\delta n(\mathbf{r})}{\delta \psi_i^*(\mathbf{r})} - \epsilon_i \frac{\delta(N - \int n(\mathbf{r}) d^3\mathbf{r})}{\delta \psi_i^*(\mathbf{r})} \\ = & \ \left[-\Delta + v_{eff}(\mathbf{r}) - \epsilon_i \right] \psi_i(\mathbf{r}) = 0 \quad . \end{aligned} \tag{2.3.21}$$

This effective single-particle equation is often called the Kohn-Sham equation. It is a single-particle Schrödinger equation with the external potential exchanged by the effective potential (2.3.16), which depends on the density. According to Eq. (2.3.18) the density itself depends on the single-particle states ψ_i. The Kohn-Sham equation thus constitutes a self-consistent field problem.

The Kohn-Sham equation furthermore allows us to derive an alternative expression for the total energy. It follows from Eq. (2.3.21) by multiplying with ψ_i^*, summing over all i and integrating over all space

$$T_0[n] + \int v_{eff}(\mathbf{r}) n(\mathbf{r}) d^3\mathbf{r} - \sum_i \epsilon_i \Theta(E_F - E_i) = 0 \quad . \tag{2.3.22}$$

Combining this with Eqs. (2.3.7), (2.3.13) and (2.3.16) we obtain the result

$$\begin{aligned} E[n] &= T_0[n] + \int \int n(\mathbf{r}) v_{el-el}(\mathbf{r} - \mathbf{r}') n(\mathbf{r}') d^3\mathbf{r}' d^3\mathbf{r} \\ &\quad + E_{xc}[n] + \int n(\mathbf{r}) v_{ext}(\mathbf{r}) d^3\mathbf{r} \\ &= \sum_i \epsilon_i \Theta(E_F - E_i) - \int \int n(\mathbf{r}) v_{el-el}(\mathbf{r} - \mathbf{r}') n(\mathbf{r}') d^3\mathbf{r}' d^3\mathbf{r} \\ &\quad - \int n(\mathbf{r}) v_{xc}(\mathbf{r}) d^3\mathbf{r} + E_{xc}[n] \quad . \end{aligned} \tag{2.3.23}$$

The total energy thus consists of the sum of the eigenvalues and the so called two-electron or "double-counting" terms.

Density functional theory as outlined above provides an efficient scheme to reduce the entire many-body problem to a Schrödinger-like effective single-particle equation, which has proven to give very good agreement of experimental and theoretical results in numerous cases. Nevertheless, taking a closer look we raise the question as to which material properties are accessible at all by electronic structure calculations which use this formalism. Of course, from the foundations of DFT we expect ground state properties to be well described of which we just mention quantities like the ionic positions, the electronic density or magnetic moments, which can be directly compared to experimental results e.g. from X-ray or neutron diffraction measurements.

As far as excitation processes are concerned the situation is somewhat more complicated. Within the concept of DFT/LDA the single particle energies resulting from the Kohn-Sham equation (2.3.21) from a very formal point of view are not eigenvalues but Lagrange multipliers. They entered the formalism just to ensure charge conservation. Hence these eigenvalues a priori have no physical meaning although in many cases they can indeed be successfully interpreted as single particle energies (see e.g. the discussion in [150] and references therein).

In view of the aforementioned theoretical foundation of DFT/LDA based electronic structure calculations we understand that relating calculated and measured results requires some care as well as knowledge about the limitations of both theoretical approaches and experimental techniques. As the most striking example in this context we refer to the wellknown problem arising from the straightforward comparison of measured energy gaps of semiconductors and insulators to the energy difference between the highest occupied and lowest unoccupied single particle state. Related difficulties might show up in the theoretical description of photoemission experiments where actually the energy difference between the ground state and an excited state of the correlated electronic many body system, hence, the energy of a quasiparticle is measured.

Still, our cautional remarks are somewhat contrasted by the fact that in many cases a remarkably good agreement between photoemission results and calculated single particle bands has been found. Of course, many investigations have centered about this seeming contradiction. Without going into too much detail we here refer to an argument given by von Barth [21, 22]. Considering, in particular, the homogeneous, interacting electron gas he related the exact quasiparticle excitation energy $\tilde{\varepsilon}_{\mathbf{k}}$ to the single particle eigenvalues $\varepsilon_{\mathbf{k}}$ of a ground state theory. In the former case formal solution of the Dyson equation yields

$$\tilde{\varepsilon}_{\mathbf{k}} = |\mathbf{k}|^2 + \Sigma(\mathbf{k}, \tilde{\varepsilon}_{\mathbf{k}}) \tag{2.3.24}$$

where $\Sigma(\mathbf{k}, \tilde{\varepsilon}_{\mathbf{k}})$ is the momentum- and energy-dependent self-energy operator. Density functional theory in contrast employs a $\mathbf{k}$-independent, translationally invariant potential and the single particle energies thus follow the free electron dispersion curve, equation (2.1.30), shifted by a constant. Since, as has been already shown by Kohn and Sham [142], DFT correctly describes the Fermi energy E_F, we may write the ground state eigenvalues as

$$\varepsilon_{\mathbf{k}} = |\mathbf{k}|^2 + \Sigma(\mathbf{k}_F, \varepsilon_{\mathbf{k}_F}) \quad . \tag{2.3.25}$$

As a comparison of these two previous expressions clearly reveals, the difference between the quasiparticle energies $\tilde{\varepsilon}_{\mathbf{k}}$ and the single particle energies $\varepsilon_{\mathbf{k}}$ raises from zero as we move away from the Fermi energy. However, $\tilde{\varepsilon}_{\mathbf{k}}$ and $\varepsilon_{\mathbf{k}}$ differ only to the extent that the self energy varies with $\mathbf{k}$ and $\tilde{\varepsilon}_{\mathbf{k}}$. If these variations are rather small we can expect the single particle energies resulting from density functional theory to provide an accurate description of the photoemission process not only in the vicinity of the Fermi energy.

Summarizing the previous discussion we can say that we have a good chance of being not too far off the mark when interpreting the calculated eigenvalues as excitation energies. Nevertheless, caution is necessary. Strictly speaking, this statement applies not only to density functional theory but also to a greater extent to the local density approximation, an approximation required in order to obtain a practical computational scheme. However, before turning to its discussion, we will extend density functional theory to magnetic systems.

2.3.2 The magnetic instability

Apparently, von Barth and Hedin as well as Rajagopal and Callaway were the first to generalize density functional theory to include effects of spin polarization [24, 212]. They used a matrix formalism to represent the density and the external potential instead of single variables. We omit the basic proofs here, since they are very similar to those given in the previous subsection, and concentrate on facts that are typical for spin density functional theory.

In the simplest version of a theory for magnetic materials we attach the bispinors χ_+ and χ_- to the wave function which so far depended only on the position vector. Such a two component spinor function consequently requires a 2×2 matrix for the Hamiltonian which may again be written in three parts representing the kinetic energy, the external potential and the Coulomb interaction of the electrons. The elements of these latter matrices are given by

$$T_{el,\alpha\beta} = -\delta_{\alpha\beta} \sum_i \frac{\hbar^2}{2m} \nabla_i^2 \quad , \tag{2.3.26}$$

$$H_{ion-el,\alpha\beta} = \sum_\mu \sum_i V_{ion-el,\alpha\beta}(\mathbf{r}_i - \mathbf{R}_\mu) = \sum_i v_{ext,\alpha\beta}(\mathbf{r}_i) \quad , \tag{2.3.27}$$

$$U_{el,\alpha\beta} = \frac{1}{2} \delta_{\alpha\beta} \sum_i \sum_{\substack{j \\ j \neq i}} \frac{e^2}{|\mathbf{r}_i - \mathbf{r}_j|} \tag{2.3.28}$$

where α and β are spin indices. Again we will use for the rest of this section atomic units and, hence, set $\hbar = 1$, $e^2 = 2$, and $m = \frac{1}{2}$. Comparing this with the corresponding equations of the preceding subsection we see that it is only external potential that needs special attention. Furthermore, if we generalize the definition of the electron density operator Eq. (2.3.5) by

$$\hat{n}_{\alpha\beta}(\mathbf{r}) = \delta_{\alpha\beta} \sum_i \delta(\mathbf{r} - \mathbf{r}_i) \tag{2.3.29}$$

then the electron density is obtained as in Eq. (2.3.6) where the many-body state is now assumed to be given by a spinor function. But we would like to go a little further and include also those cases where the spin state cannot be desccibed by a single, global quantization axis. According to the laws of quantum mechanics such a mixed state is described by the density operator $\rho_{\alpha\beta}$, which takes the place of the spinor function. The electron density is then given by

$$n(\mathbf{r}) = Tr\langle \rho \, \hat{n}(\mathbf{r}) \rangle \tag{2.3.30}$$

where the trace is the sum of the diagonal elements. However, for a complete description of the magnetic state we need the spin density in addition to the electron density. To this end we define the 2×2 matrix

$$\tilde{n}(\mathbf{r}) = \langle \rho\ \hat{n}(\mathbf{r}) \rangle \tag{2.3.31}$$

which is frequently called the density matrix, but should not to be confused with the term density operator for ρ. In general, the quantity $\tilde{n}(\mathbf{r})$ will not be diagonal, but it can be locally diagonalized in which case the difference of the eigenvalues results in the spin density [248, 249, 234].

It should now be clear that the generalized Levy functional depends on the full density matrix, too. Thus the definition

$$O[\tilde{n}] = \inf_{\rho \epsilon M(\tilde{n})} Tr\langle \rho \hat{O} \rangle \tag{2.3.32}$$

is a straightforward extension of the functional given in Eq. (2.3.8), the only difference being that the constrained search for the infimum this time includes all density operators ρ which yield the required density matrix $\tilde{n}$.

We can now set up the functional of the total energy and subsequently derive the single-particle equation. Thus we proceed by replacing Eq. (2.3.7) by

$$E[\tilde{n}] = F[\tilde{n}] + V[\tilde{n}] \quad , \tag{2.3.33}$$

with

$$\begin{aligned}
V[\tilde{n}] &= \inf_{\rho \epsilon M(\tilde{n})} Tr\langle \rho \hat{V} \rangle \\
&= \inf_{\rho \epsilon M(\tilde{n})} Tr \sum_{\beta} \int \sum_{i=1}^{N} v_{ext,\alpha\beta}(\mathbf{r}_i) \rho_{\beta\alpha}(\mathbf{r}_i \ldots \mathbf{r}_N) d^3\mathbf{r}_i \ldots d^3\mathbf{r}_N \\
&= \inf_{\rho \epsilon M(\tilde{n})} Tr \sum_{\beta} \int \sum_{i=1}^{N} v_{ext,\alpha\beta}(\mathbf{r}) \delta(\mathbf{r} - \mathbf{r}_i) \rho_{\beta\alpha}(\mathbf{r}_i \ldots \mathbf{r}_N) d^3\mathbf{r}_i \ldots d^3\mathbf{r}_N, d^3\mathbf{r} \\
&= \sum_{\alpha\beta} \int v_{ext,\alpha\beta}(\mathbf{r}) \tilde{n}_{\beta\alpha}(\mathbf{r}) d^3\mathbf{r} \quad .
\end{aligned} \tag{2.3.34}$$

As we have already mentioned we may now benefit from the universality of the proofs of the Hohenberg-Kohn theorems in the preceding subsection and directly turn to the derivation of the single-particle equations. However, we point out that the variational properties of the total energy this time apply to all four components of the density matrix. Therefore when defining the functional $F[\tilde{n}]$ by

$$F[\tilde{n}] = T_0[\tilde{n}] + \int\int n(\mathbf{r}) v_{el-el}(\mathbf{r} - \mathbf{r}') n(\mathbf{r}') d^3\mathbf{r}' d^3\mathbf{r} + E_{xc}[\tilde{n}] \tag{2.3.35}$$

we obtain a matrix form for the effective potential according to

$$\begin{aligned}
v_{eff,\alpha\beta}(\mathbf{r}) &= \frac{\delta(E[\tilde{n}] - T_0[\tilde{n}])}{\delta \tilde{n}_{\beta\alpha}(\mathbf{r})} \\
&= v_{ext,\alpha\beta}(\mathbf{r}) + 2\delta_{\alpha\beta} \int v_{el-el}(\mathbf{r} - \mathbf{r}') n(\mathbf{r}') d^3\mathbf{r}' + v_{xc,\alpha\beta}(\mathbf{r})
\end{aligned} \tag{2.3.36}$$

where

$$v_{xc,\alpha\beta}(\mathbf{r}) = \frac{\delta E_{xc}[\tilde{n}]}{\delta \tilde{n}_{\beta\alpha}(\mathbf{r})} \tag{2.3.37}$$

is the exchange-correlation potential.

The Kohn-Sham idea of assuming independent particles moving in an effective potential leads to the following extensions for the density matrix and the kinetic energy

$$\begin{aligned}
\tilde{n}_{\beta\alpha}(\mathbf{r}) &= \sum_i \psi_{i\beta}(\mathbf{r})\psi^*_{i\alpha}(\mathbf{r})\Theta(E_F - E_{i\alpha})\Theta(E_F - E_{i\beta}) && (2.3.38)\\
T_0[\tilde{n}] &= -\sum_{\alpha\beta}\delta_{\alpha\beta}\sum_i \int \psi^*_{i\alpha}(\mathbf{r})\nabla^2\psi_{i\beta}(\mathbf{r})d^3\mathbf{r}\Theta(E_F - E_{i\alpha})\Theta(E_F - E_{i\beta}) \quad , && (2.3.39)
\end{aligned}$$

where the Fermi energy is determined according to

$$n(\mathbf{r}) = \sum_\alpha \sum_i |\psi_{i\alpha}(\mathbf{r})|^2 \Theta(E_F - E_{i\alpha}) \tag{2.3.40}$$

Finally, the generalized Euler-Lagrange equation is

$$\sum_i \sum_\beta \left[\frac{\delta E[\tilde{n}]}{\delta \psi^*_{i\beta}(\mathbf{r})} - \epsilon_{i\beta}\frac{\delta(N - \int n(\mathbf{r})d^3\mathbf{r})}{\delta\psi^*_{i\beta}(\mathbf{r})}\right]\delta\psi^*_{i\beta}(\mathbf{r}) = 0 \quad , \tag{2.3.41}$$

where the $\epsilon_{i\beta}$ once again secure particle conservation. Since the single-particle orbitals $\psi_{i\beta}$ are independent of each other we obtain

$$\sum_\beta \left[-\delta_{\alpha\beta}\nabla^2 + v_{eff,\alpha\beta}(\mathbf{r}) - \delta_{\alpha\beta}\epsilon_{i\beta}\right]\psi_{i\beta}(\mathbf{r}) = 0 \quad , \qquad \alpha = 1, 2 \quad . \tag{2.3.42}$$

As a consequence of the mixed state, we arrive at a set of two coupled equations instead of separate equations for the spin-up and spin-down components of the spinor function. However, in many systems a global spin quantization axis does exist in which case the density matrix becomes diagonal.

We close this subsection by writing down the expression for the total energy functional similar to Eq. (2.3.23)

$$\begin{aligned}
E[\tilde{n}] &= \sum_\alpha \sum_i \epsilon_{i\alpha}\Theta(E_F - E_{i\alpha}) - \int\int n(\mathbf{r})v_{el-el}(\mathbf{r}-\mathbf{r}')n(\mathbf{r}')d^3\mathbf{r}'d^3\mathbf{r}\\
&\quad - \sum_{\alpha\beta}\int v_{xc,\alpha\beta}(\mathbf{r})\tilde{n}_{\beta\alpha}(\mathbf{r})d^3\mathbf{r} + E_{xc}[\tilde{n}] && (2.3.43)
\end{aligned}$$

which finishes our excourse to spinpolarized systems.

2.4 Local density approximation

Our discussion in the preceding section was of completely theoretical nature without regard to practical applications. We now turn to an approximation scheme to deal with the exchange-correlation functional which has not yet been specified. This is the local-density approximation (LDA) where the homogeneous, interacting electron gas serves to model the exchange-correlation energy in the form

$$E_{xc}[n] = \int n(\mathbf{r})\epsilon_{xc}(n(\mathbf{r}))d^3\mathbf{r} \quad . \tag{2.4.44}$$

$\epsilon_{xc}(n)$ is a function of the density instead of a functional and Eq. (2.4.44) may be viewed as dividing the inhomogeneous electron system into small "boxes", each containing an interacting but homogeneous electron gas with a density $n(\mathbf{r})$ appropriate for the "box" at $\mathbf{r}$.

From Eqs. (2.3.17) and (2.4.44) we derive for the exchange-correlation potential

$$v_{xc}(\mathbf{r}) = \left[\frac{\partial}{\partial n}\left\{n\epsilon_{xc}(n)\right\}\right]_{n=n(\mathbf{r})} \quad . \tag{2.4.45}$$

The local-density approximation may be readily generalized to the spin polarized case. Even in the general situation described in subsection 2.3.2, where a global spin quantization axis is missing, the eigenvalues $n_\uparrow$ and $n_\downarrow$ of the density matrix (2.3.31), which represent the spin-up and spin-down density, are locally well defined. The exchange-correlation energy is then written as [24]

$$E_{xc}[\tilde{n}] = \int n(\mathbf{r})\epsilon_{xc}(n_\uparrow(\mathbf{r}), n_\downarrow(\mathbf{r}))d^3\mathbf{r} \quad . \tag{2.4.46}$$

This results in the following form of the exchange-correlation potential

$$v_{xc,\alpha}(\mathbf{r}) = \left[\frac{\partial}{\partial n_\alpha}\left\{n\epsilon_{xc}(n_\uparrow, n_\downarrow)\right\}\right]_{n_\uparrow=n_\uparrow(\mathbf{r})n_\downarrow=n_\downarrow(\mathbf{r})} \tag{2.4.47}$$

where $\alpha = \uparrow, \downarrow$.

To obtain an explicit expression for the exchange-correlation energy, $\epsilon_{xc}(n_\uparrow, n_\downarrow)$, we initally neglect correlation and and begin with the Hartree-Fock approximation for a spin polarized gas of electrons. Using atomic units we write [24]

$$\epsilon_{xc}(n_\uparrow, n_\downarrow) \approx \epsilon_x(n_\uparrow, n_\downarrow) = -6(\frac{3}{4\pi})^{\frac{1}{3}}\frac{1}{n}(n_\uparrow^{\frac{4}{3}} + n_\downarrow^{\frac{4}{3}}) \tag{2.4.48}$$

where the density is $n = n_\uparrow + n_\downarrow$.

This is merely the exchange energy density, thus correlation gives rise to another term $\epsilon_c(n_\uparrow, n_\downarrow)$ that must be added to the exchange term to give

$$\epsilon_{xc}(n_\uparrow, n_\downarrow) = \epsilon_x(n_\uparrow, n_\downarrow) + \epsilon_c(n_\uparrow, n_\downarrow) \quad . \tag{2.4.49}$$

The correlation energy density of a homogeneous but interacting electron gas, although known only approximately, has been determined numerically to a very high accuracy. The numerical results gave rise to different parametrizations. Much used schemes were proposed by Hedin and Lundquist as well as by von Barth and Hedin for the non-spinpolarized and spinpolarized case, respectively [117, 24]. Another well known parametrization goes back to Vosko *et al.* who used Monte Carlo calculations by Ceperley and Alder [255, 57]. Finally, extensions for relativistic calculations have been given by Rajagopal, by McDonald and Vosko as well as by Ramana and Rajagopal [211, 167, 213].

Before we proceed with the implementation of the LDA we mention common practice to express the energies in terms of the density parameter r_S which is connected to the density by the definition

$$\frac{4\pi}{3} r_S^3 a_0^3 = \frac{1}{n} \tag{2.4.50}$$

where a_0 is the Bohr radius. With the help of this abbreviation the exchange and the correlation energy density as given by von Barth and Hedin write as

$$\begin{aligned} \epsilon_x(n_\uparrow, n_\downarrow) &= \epsilon_x^P(r_S) + (\epsilon_x^F(r_S) - \epsilon_x^P(r_S)) f(n_\uparrow, n_\downarrow) && (2.4.51) \\ \epsilon_c(n_\uparrow, n_\downarrow) &= \epsilon_c^P(r_S) + (\epsilon_c^F(r_S) - \epsilon_c^P(r_S)) f(n_\uparrow, n_\downarrow) \quad . && (2.4.52) \end{aligned}$$

where the function f is given by

$$f(n_\uparrow, n_\downarrow) = \frac{1}{2^{\frac{4}{3}} - 2} \left[(\frac{2n_\uparrow}{n})^{\frac{4}{3}} + (\frac{2n_\downarrow}{n})^{\frac{4}{3}} - 2 \right] \tag{2.4.53}$$

and vanishes for equal spin-up and spin-down densities [24]. The other functions incorporated in Eqs. (2.4.51) and (2.4.52) are

$$\begin{aligned} \epsilon_x^P(r_S) &= -\frac{\epsilon_x^0}{r_S} \qquad , \epsilon_x^0 = \frac{3}{2\pi} (\frac{9\pi}{4})^{\frac{1}{3}} = 0.91633\text{Ryd} && (2.4.54) \\ \epsilon_x^F(r_S) &= 2^{\frac{1}{3}} \epsilon_x^P(r_S) && (2.4.55) \end{aligned}$$

which reproduce the Hartree-Fock results and

$$\begin{aligned} \epsilon_c^P(r_S) &= -c_P F(\frac{r_S}{r_P}) && (2.4.56) \\ \epsilon_c^F(r_S) &= -c_F F(\frac{r_S}{r_F}) && (2.4.57) \end{aligned}$$

where we have defined one more function which has the form

$$F(z) = (1 + z^3) \ln(1 + \frac{1}{z}) + \frac{z}{2} - z^2 - \frac{1}{3} \tag{2.4.58}$$

The correlation energy is further modeled by the set of parameters

$$\begin{aligned} c_P &= 0.0504, & r_P &= 30 \\ c_F &= 0.0254, & r_F &= 75 \end{aligned} \tag{2.4.59}$$

as given by von Barth and Hedin [24] or

$$\begin{aligned} c_P &= 0.045, & r_P &= 21 \\ c_F &= \frac{c_P}{2} = 0.025, & r_F &= 2^{\frac{4}{3}} r_P = 52.91668 \end{aligned} \tag{2.4.60}$$

as given by Moruzzi *et al.* [188]. The connection between c_F and c_P as well as r_F and r_P refers to the RPA scaling.

From the above equations the exchange-correlation potential can be calculated by means of Eq. (2.4.47)

$$\begin{aligned} v_{xc,\alpha}(n_\uparrow, n_\downarrow) &= \left[\frac{4}{3}\epsilon_x^P(r_S) + \gamma\left(\epsilon_c^F(r_S) - \epsilon_c^P(r_S)\right)\right]\left(\frac{2n_\alpha}{n}\right)^{\frac{1}{3}} \\ &\quad +\mu_c^P(r_S) - \gamma\left(\epsilon_c^F(r_S) - \epsilon_c^P(r_S)\right) \\ &\quad + \left[\mu_c^F(r_S) - \mu_c^P(r_S) - \frac{4}{3}\left(\epsilon_c^F(r_S) - \epsilon_c^P(r_S)\right)\right] f(n_\uparrow, n_\downarrow) \end{aligned} \tag{2.4.61}$$

with

$$\mu_c^P(r_S) = -c_P \ln(1 + \frac{r_P}{r_S}) \tag{2.4.62}$$

$$\mu_c^F(r_S) = -c_F \ln(1 + \frac{r_F}{r_S}) \tag{2.4.63}$$

and

$$\gamma = \frac{4}{3}\frac{1}{2^{\frac{1}{3}} - 1} \quad . \tag{2.4.64}$$

This completes the specification of the effective potential. The local density approximation is exact in the limit of a constant density or density matrix, respectively. In addition, we would expect it to be quite good for slowly varying densities but not for systems as atoms or molecules where the density depends strongly on position. Even for solids the deviation from a homogeneous density is substantial and thus cannot be neglected. Surprisingly, experience shows that the local density approximation works well in a large number of cases.

Despite its success, there have been attempts to improve the local density approximation. The earliest came from Kohn and Sham themselves. Like the von Weizsäcker correction to the Thomas-Fermi theory they proposed to add a gradient correction term to the exchange-correlation energy. However, attempts along these lines were not successful and in many cases the good agreement that is obtained by using the simple approximation above was spoiled. In recent years, this gave rise to the development of more general schemes as e.g. the generalized gradient approximation (GGA) which has proven very successful for the calculation of structural properties [26, 27, 201, 227].

2.5 Methods for electronic structure calculations

Besides representing the determination of the ground state of an interacting electron system as an effective single particle problem density functional theory also offers an ansatz for the solution of the latter. By this we mean the variational principle arising from the second of the ground state theorems formulated by Hohenberg and

Kohn. It implies to expand the wave function entering Eq. (2.2.5) in a suitable set of basis functions,

$$\psi_{\mathbf{k}}(\mathbf{r}) = \sum_i c_i(\mathbf{k}) \chi_{\mathbf{k}i}(\mathbf{r}) \tag{2.5.1}$$

and to minimize the total energy with respect to the coefficients $c_i(\mathbf{k})$. For simplicity in writing we here have included the band index, which labels different solutions at a particular $\mathbf{k}$ point, into the $\mathbf{k}$ index. The variation of the total energy with respect to the coefficients is easily written down as

$$\sum_{\mathbf{k}i} \left[\frac{\delta E[n]}{\delta c_i^*(\mathbf{k})} + \varepsilon_{\mathbf{k}i} \frac{\delta(N - \int n(\mathbf{r}) d^3\mathbf{r})}{\delta c_i^*(\mathbf{k})} \right] \delta c_i^*(\mathbf{k}) = 0 \tag{2.5.2}$$

where $E[n]$ is the total energy as provided by density functional theory, Eq. (2.3.23).

Since all the coefficients $c_i(\mathbf{k})$ are independent of each other the expression in square brackets in Eq. (2.5.2) must vanish for each $c_i(\mathbf{k})$. Using the standard expressions for the electron density, the kinetic energy and the exchange-correlation potential as supplied by density functional theory,

$$n(\mathbf{r}) = \sum_{\mathbf{k}} |\psi_{\mathbf{k}}(\mathbf{r})|^2 \Theta(E_F - E_{\mathbf{k}}) \quad , \tag{2.5.3}$$

$$T_0[n] = \sum_{\mathbf{k}} \langle \psi_{\mathbf{k}}(\mathbf{r})| - \nabla^2 |\psi_{\mathbf{k}}(\mathbf{r})\rangle \Theta(E_F - E_{\mathbf{k}}) \tag{2.5.4}$$

and

$$v_{xc}(\mathbf{r}) = \frac{\delta E_{xc}[n]}{\delta n(\mathbf{r})} \quad , \tag{2.5.5}$$

where again the Heaviside step function $\Theta(E_F - E_{\mathbf{k}})$ restricts the sums to only the occupied states, we arrive at the secular equation

$$\sum_j \left[\langle \chi_{\mathbf{k}i}(\mathbf{r}) | \tilde{H}_0 | \chi_{\mathbf{k}j}(\mathbf{r}) \rangle - \varepsilon_{\mathbf{k}i} \langle \chi_{\mathbf{k}i}(\mathbf{r}) | \chi_{\mathbf{k}j}(\mathbf{r}) \rangle \right] c_j(\mathbf{k}) = 0 \quad . \tag{2.5.6}$$

The Hamiltonian entering Eq. (2.5.6) is the density functional theory counterpart to the Hamiltonian H_0 entering Eqs. (2.2.5) which besides the kinetic energy operator contains the effective single particle potential. In order that the linear equation system has non-trivial solutions the determinant of the secular matrix, i.e. of the matrix in square brackets in Eq. (2.5.6) must vanish the single particle energies hence arising as its roots.

Being clear in concept the ansatz (2.5.1) in practice still leaves some freedom for different choices of basis functions. Of course, the set $\{\chi_{\mathbf{k}i}(\mathbf{r})\}$ is finite and we cannot expect it to be complete. In addition, the basis functions are not necessarily orthogonal. As a consequence, the actual shape of the basis functions is an important factor governing the size of the basis set, the Hilbert space sampled by the variational procedure and, finally, the effort to solve the secular Eq. (2.5.6). Obviously, a good choice thus consists of basis functions $\chi_{\mathbf{k}i}(\mathbf{r})$ which resemble the final wave function $\psi_{\mathbf{k}}(\mathbf{r})$ quite much. In this case, the latter would have a large portion within the Hilbert space spanned by the basis function for only a small set $\{\chi_{\mathbf{k}i}(\mathbf{r})\}$ this fact reducing the size of the secular matrix.

At a first glance, for crystals the canonical set of basis functions seems to be a plane wave basis,

$$\chi_{\mathbf{k}\nu}(\mathbf{r}) = e^{i(\mathbf{k}+\mathbf{K}_\nu)\mathbf{r}} \tag{2.5.7}$$

which offers the additional advantage of being orthogonal. However, plane waves are not really a good choice for the following physical reasons. Since the crystal potential arises from a superposition of atomic potentials the valence electrons are feeling a strong potential in the vicinity of the nuclei, which behaves like $-\frac{Ze^2}{r}$, whereas far away from the nuclei the potential changes to $-\frac{Z_v e^2}{r}$, where Z_v is the valence charge. This is due to the electrostatic screening by the core electrons. Finally, in the region between the atoms the potential becomes rather flat because of crystalline periodicity. Thus the wave function shows large oscillations near the nuclei and is rather smooth in the region outside the atomic cores. As a consequence, in order to describe such a wave function by a plane wave basis we would need a huge number of functions. Indeed, as Heine has demonstrated this could well lead to a secular matrix having a rank of the order 10^6 [118].

Obviously, the basis functions have to be adapted in order to better account for the details of the crystal potential. There exist mainly two approaches to do so one being the pseudopotential (PP) concept, which traces back to Herring's orthogonalized plane wave (OPW) method [119] (see also [51, 52]). In the latter scheme one starts out from plane waves as basis functions but orthogonalizes them to the core states from the very beginning. We write

$$\chi_{\mathbf{k}\nu}(\mathbf{r}) = |\mathbf{k}+\mathbf{K}_\nu\rangle - \sum |\varphi_c\rangle\langle\varphi_c|\mathbf{k}+\mathbf{K}_\nu\rangle \tag{2.5.8}$$

where $|\mathbf{K}_\nu\rangle$ and $|\varphi_c\rangle$ denote a plane wave and the Bloch sum of the core states, respectively. Each orthogonalized plane wave consists of a long range term and a part which shows strong oscillations in the core regions. Hence, it has the appropriate shape near the nuclei built in and already a moderate number of OPW's is sufficient for a good description of the wave function. Starting out from Herring's scheme, Phillips and Kleinman as well as Antoncik lateron reformulated the orthogonalization ansatz in terms of an additional potential seen by the valence electrons and thereby laid ground for pseudopotential theory [203, 204, 14]. In the following years the latter was refined by the introduction of socalled norm-conserving pseudopotentials (see e.g. [112, 17, 113]). Recently, Vanderbilt developed socalled ultra-soft pseudopotentials, which even allowed to treat transition metal atoms [244]. A full description of all this clearly is beyond the scope of this chapter and we thus refer the reader to the literature (see e.g. [63, 118, 16, 62] as well as references therein).

The second approach mentioned above is based on Slater's muffin-tin approximation (MTA) [229] (see also [230]). In this approximation the crystal potential is restricted to an idealized shape and assumed to be spherical symmetric within (non-overlapping) muffin-tin spheres and constant in the remaining region, the socalled interstitial. The wave function in the latter region is well described by plane waves and inside the muffin-tin spheres the radial Schrödinger equation can be solved numerically with the actual potential. Matching the radial functions continuously to the plane waves at the sphere boundary we arrive at a single basis function, which, due to the way it was constructed, is called an augmented plane wave (APW). A detailed description of the APW method has been given by Loucks [162].

Note that, despite its simplicity, the MTA does not really mean a restriction to the method. In particular, when one employs the MTA for the construction of the basis functions but uses the full potential for the calculation of matrix elements of the secular matrix one arrives at a scheme of very high accuracy which allows for instance for the evaluation of elastic properties. This is due to the fact that the muffin-tin potential constitutes already a good approximation to the full unrestricted potential — a fact which only allowed for Slater's important step — and thus the basis functions resemble the wave function quite much. Methods using the unrestricted potential together with basis functions grown out of the muffin-tin potential are called full potential methods and nowadays for almost every method based on the MTA there exists a counterpart employing the full potential.

When we view the crystal as a collection of single atoms we may ask wether there exist alternatives to using plane waves as the interstitial part of the basis functions which are even better adapted to the problem at hand. As well known, the alternative consists of spherical waves which are products of spherical harmonics and spherical Hankel, Neumann or Bessel functions. Like plane waves they solve Schrödinger's equation with a constant potential. Augmenting the spherical waves with numerical solutions of the radial equation inside the muffin-tin spheres just in the same manner as in the APW method we arrive at the Korringa-Kohn-Rostoker (KKR) method, even if this has been developed originally in a much different way [144, 141] (see also [264, 267, 224]). Compared to methods based on plane waves, spherical waves offer the particular advantage of leading to a smaller secular matix, usually an order of magnitude less. Moreover, from their very nature spherical waves are much better adapted to the notions known from atomic physics or from chemistry.

The radial solutions of Schrödinger's equations inside the muffin-tin spheres appearing in both the APW and the KKR method are energy dependent functions and so are the basis functions. Although making calculations of very high accuracy feasible this means a great computational effort since with energy dependent basis functions the solutions of the secular Eq. (2.5.6) can be accessed only via time consuming root tracing. In contrast, were it not for the energy dependence, Eq. (2.5.6) would reduce to a generalized eigenproblem which can be solved much faster numerically.

It was therefore a great success when Andersen observed that the energy dependence within the APW and the KKR method actually is rather weak in the energy region of interest for the valence electrons [7, 8]. Using this as a starting point, Andersen modelled the weak energy dependence by a Taylor series expansion where only the first two terms are kept. In doing so, he arrived at the socalled linear methods. In particular, Andersen devised the linear augmented plane waves (LAPW) and the linear muffin-tin orbitals (LMTO) methods as linearized counterparts of the APW and the KKR method (see e.g. Refs. [9, 10, 11, 12, 228, 227]). Combining Andersens idea to linearize the energy dependence of the wave function with the renormalized-atom description of solids as invented by Watson, Ehrenreich, Hodges, and Gelatt [257, 120, 93], Williams, Kübler and Gelatt lateron developed the augmented spherical wave (ASW) method [266] (see also [76, 150, 80] for more recent descriptions). Altogether, besides being much faster than the classical schemes, the linear methods enabled for the first time calculations on much more realistic and complex systems. This way, Andersen opened the door to a so far unexpected understanding of physical as well as the chemical properties of condensed matter.

Another approach to circumvent the problem of energy dependent basis functions is provided by the linear combination of atomic orbitals (LCAO) methods which use products of spherical harmonics and analytically know radial functions. Several schemes along this line have been proposed of which we just mention the work of Wang and Callaway or of Eschrig [256, 74].

Despite the great success of density functional theory based electronic structure calculations it was not until the mid eighties that a simultaneous minimization of the electronic and ionic energies could be performed. Indeed, any band calculation scheme, if accurate enough, in principle allows to determine the forces acting onto the atoms,

$$\mathbf{F}_\mu = -\nabla_{\mathbf{R}_\mu} E(\{\psi_{\mathbf{k}}, \mathbf{R}_\mu\}) \quad , \tag{2.5.9}$$

which could be used to optimize the atomic positions. However, such an approach is not very efficient since it requires in each step a renewed self-consistent calculation of the electronic structure before the atoms can be moved.

A substantial improvement was made by Car and Parrinello who introduced a new approach to do first principles molecular dynamics [53]. Their essential step was to treat the electronic wave functions as dynamical variables. In order to do so Car and Parrinello started out from the Lagrangian

$$\begin{aligned} L \;=\; & \bar{\mu} \sum_{\mathbf{k}} \int d^3\mathbf{r} |\dot{\psi}_{\mathbf{k}}(\mathbf{r},t)|^2 + \frac{1}{2} \sum_{\mu} M_\mu \left[\dot{\mathbf{R}}_\mu\right]^2 \\ & - E(\{\psi_{\mathbf{k}}, \mathbf{R}_\mu\}) + \sum_{\mathbf{k}\mathbf{k}'} \left\{ \int d^3\mathbf{r} \psi^*_{\mathbf{k}}(\mathbf{r},t) \psi_{\mathbf{k}'}(\mathbf{r},t) - \delta_{\mathbf{k}\mathbf{k}'} \right\} \lambda_{\mathbf{k}\mathbf{k}'} \end{aligned} \tag{2.5.10}$$

where a dot as usual denotes $\frac{d}{dt}$ and M_μ and $\mathbf{R}_\mu$ are the ionic masses and positions, respectively. Moreover, $\bar{\mu}$ is a fictitious mass associated with the electronic wave functions which are assumed to follow an artificial classical dynamics. Note that the total energy in this context plays the role of a potential term. The last term on the right hand side of Eq. (2.5.10) finally ensures orthonormality of the electronic wave functions and is coupled via a Langrange multiplier. Finally, we remind the reader of our convention to include the band index in the $\mathbf{k}$ index.

Following the laws of classical mechanics we easily derive from the Lagrangian (2.5.10) the equations of motions for the electronic wave functions

$$\bar{\mu} \ddot{\psi}_{\mathbf{k}}(\mathbf{r},t) = -\tilde{H}_0 \psi_{\mathbf{k}}(\mathbf{r},t) + \sum_{\mathbf{k}'} \lambda_{\mathbf{k}\mathbf{k}'} \psi_{\mathbf{k}'}(\mathbf{r},t) \quad , \tag{2.5.11}$$

where $\tilde{H}_0$ is the Kohn-Sham Hamiltonian, and for the ionic motion

$$M_\mu \ddot{\mathbf{R}}_\mu = -\nabla_{\mathbf{R}_\mu} E(\{\psi_{\mathbf{k}}, \mathbf{R}_\mu\}) \quad . \tag{2.5.12}$$

Note that in the stationary state the left hand side of Eq. (2.5.11) vanishes while the right hand side reduces to the usual Kohn-Sham equation except for a possible unitary transformation.

The last decade has witnessed numerous work to implement and improve different first principles molecular dynamics schemes the discussion of which again would be far beyond the scope of this chapter (recent references are for instance [200, 240]). Nevertheless, the idea of Car and Parrinello in addition to leading to first principles molecular dynamics had a large influence also on the electronic problem by itself since it opened a way to determining the electronic wave function by direct minimization instead of solving the secular equation. This likewise marked a starting point for new developments [200].

2.6 Computational aspects of the ASW method

The calculations to be presented in the remaining chapters of this work are all based on the framework outlined in the preceding sections, i.e. that provided by the adiabatic approximation, density functional theory and the local density approximation. As a calculational scheme we employ the augmented spherical wave (ASW) method [266] in its scalar-relativistic implementation [140, 105] which has been already used in our previous studies on stoichiometric and Ir-substituted CrO_2 [171, 176]. Since there exist various recent comprehensive treatments of the ASW method [76, 150, 80] we omit a more refined discussion in the present context. Nevertheless, some aspects, which are important for the understanding of the subsequent chapters and which are not covered by previous work, will be discussed.

2.6.1 Sphere geometry optimization

The ASW method uses the atomic sphere approximation (ASA) [8], which is a variant of the muffin-tin approximation (MTA). As already mentioned in section 2.5, the latter models the full crystal potential by spherically symmetric potential wells and a constant potential in the remaining interstitial region [79]. It thus allows for a very simple, transparent, and problem adapted way of constructing basis functions for a subsequent variational solution of Schrödinger's equation.

The atomic sphere approximation (ASA), in addition to being based on the MTA, requires the spheres to fill all space this leading to the formal elimination of the interstitial region. The ASA was introduced by Andersen in the course of inventing the linearized schemes mentioned in section 2.5, since it allowed to restrict the Taylor series expansion of the energy dependent wave function to only its first term in the formally non-existing interstitial region, which thus serves only the purpose of yielding boundary conditions for the intrasphere contributions to the basis functions.

For open crystal structures both the MTA and the ASA might be faced with problems arising from possibly large overlaps of only atom-centered spheres. For this reason, both approaches are usually extended by the introduction of socalled empty spheres inside of which the interstitial potential is replaced with a spherically symmetric one [134]. These empty spheres may be regarded as pseudo atoms without a nucleus which are used to model the correct shape of the crystal potential in large voids [12]. The collection of all, physical and empty spheres, then again leads to an artificially close packed structure. Since the potential resulting from all spherical wells should represent the full crystal potential as closely as possible it remains a challenge to find, first, optimal empty sphere positions and, second, optimal radii for all spheres.

To achieve an efficient solution of the aforementioned problem, we have recently developed the sphere geometry optimization (SGO) algorithm which solves the forementioned problem automatically [78, 81]. Although allowing for complicated crystal structures the algorithm has proven to be very fast. The SGO method is based on the observation that the full crystal potential is well approximated by the overlapping free atom potential of the constituent atoms [177] and thus could be used for the selection of empty sphere positions and sphere radii *before* the self-consistent calculation is actually started [130].

In a first step, the SGO algorithm locates optimal empty sphere positions: Since the empty spheres enter as spherical potential wells, searching for their optimal positions is equivalent to tracing the (local) maxima of the overlapping free atom potential. As an alternative, we implemented a search for the centers of the largest spherical voids. Experience showed that both approaches yield identical results. At the same time, the second method turned out to be much faster than the first one. This way we were able to reduce the problem of locating the empty sphere positions to the standard problem of optimizing a rather simple objective function. Nevertheless, since we are dealing with a highly non-linear function in a multidimensional space, this optimization process still is a quite complicated problem. Having tested different optimization techniqes we finally opted for using genetic algorithms which have found widespread use in recent years [104].

Next, the radii of all spheres have to be determined: Within the ASA, we thus have to search for that set of radii, which keeps the overlaps of the spheres small, while it gives rise to atomic potentials, which superposition still resembles the full potential. We have found that the best solution consists of maximizing the volume filled by all spheres while enforcing certain overlap limits. Hence, we have again transformed the problem to a multidimensional optimization procedure which is accessible to the same means as that mentioned before.

In summary, by developing the SGO algorithm we have arrived at an efficient method, which supplies an optimal set of empty sphere positions and sphere radii for a subsequent all-electron self-consistent field calculation given only the atomic coordinates.

2.6.2 Crystal orbital overlap population

In addition to the band structures and (partial) densities of states we will in the following sections use the crystal orbital overlap population (COOP) as a tool for analyzing the electronic and chemical properties of materials. The concept of the COOP has been introduced by Hoffmann in order to allow for a detailed discussion of chemical bonding [121]. Roughly speaking, the COOP is based on the expectation values of operators which consist of the non-diagonal elements of the overlap population matrix,

$$c_{ni}^*(\mathbf{k}) S_{ij} c_{nj}(\mathbf{k}) = c_{ni}^*(\mathbf{k}) \langle \chi_{\mathbf{k}i}(\mathbf{r}) | \chi_{\mathbf{k}j}(\mathbf{r}) \rangle c_{nj}(\mathbf{k}) \tag{2.6.1}$$

where S_{ij} represents an element of the overlap matrix of the basis functions and the $c_{nj}(\mathbf{k})$ are the expansion coefficients entering the wave function of the nth band, equation (2.5.1) (in order to make things clear we have written the band index explicitly in the present context). Inserting these operators into equation (2.1.40) we are able to define the socalled partial COOP by

$$C_{ij}(E) = C_{ji}(E) = \frac{1}{\Omega_{BZ}} \sum_n \int_{\Omega_{BZ}} d^3\mathbf{k} \; Re\left(c^*_{ni}(\mathbf{k}) S_{ij} c_{nj}(\mathbf{k})\right) \delta(E - \varepsilon_{n\mathbf{k}}) \quad , \tag{2.6.2}$$

which in a somewhat lax notation is often designated as the overlap population weighted density of states. From equation (2.6.2) the total COOP can be readily evaluated as the sum over all non-diagonal elements, i.e.

$$C(E) = \sum_{\substack{ij \\ i \neq j}} C_{ij}(E) \quad . \tag{2.6.3}$$

Connection to the chemistry stems from the fact that positive contributions to the COOP indicate a bonding of the respective orbitals whereas negative terms in equation (2.6.2) point to antibonding states. The evaluation of the COOP has been recently implemented in the ASW method [86] and already successfully applied to the interpretation of bonding properties of various intermetallic actinide compounds [172, 173, 174, 175].

In order to obtain an impression of the chemical stability we calculate, in addition to the COOP as given by equation (2.6.3), the integrated COOP, which is defined by

$$\bar{C}(E') = \int_{-\infty}^{E'} dE \; C(E) \quad . \tag{2.6.4}$$

In particular, the integrated partial COOP, $\bar{C}_{ij}(E_F)$, which result from integrating the partial COOP to the Fermi energy, provide a measure for the total stability of certain bonds.

2.6.3 Miscellaneous

In the course of the calculations to be presented in the subsequent chapters the Brillouin zones are sampled with an increasing number of $\mathbf{k}$ points within the irreducible wedge. This way we are able to ensure convergence of our results with respect to the fineness of the $\mathbf{k}$ space grid. Usually, the calculations start with a mesh of $6 \times 6 \times 6$ points and end up with $16 \times 16 \times 16$ and $30 \times 30 \times 30$ points for semiconductors and metals, respectively. However, the actual number of points in the irreducible wedge will be given in the respective context.

Finally, self-consistency is achieved by employing an efficient algorithm for convergence acceleration [77]. As convergence criteria we require that the deviations of the atomic charges and the total energy of subsequent iterations are less than 10^{-8} electrons and 10^{-8} Ryd, respectively.

Chapter 3

Electron-lattice interaction in FeS_2

3.1 Motivation

The pyrite-type transition metal disulfides MS_2 with M = Fe, Co, Ni, Cu, Zn, Ru have long been attracting scientific and technological interest because of a broad range of electronic, magnetic and optical properties (see e.g. Refs. [193, 31, 128, 270, 269, 196, 137] just to mention a few). Among these compounds are semiconductors like the van Vleck paramagnet FeS_2 and the wide-bandgap diamagnet ZnS_2. In contrast, CoS_2 is a ferromagnetic metal ($T_C \approx 130K$) while CuS_2 becomes superconducting [31, 184, 2, 195]. Much interest has also been focused on the antiferromagnetic insulator NiS_2 which undergoes two magnetic phase transitions at $T_{N_1} \approx 54K$ and $T_{N_2} \approx 31K$ [31, 2, 195, 114, 183] and has been interpreted in terms of the Mott-Hubbard type picture for highly correlated electron systems [196, 195]. In general, the changing influence of electron correlations across the series, which is related to the successive filling of the e_g manifold of the crystal field split d bands, remains a central issue. A systematic study is favoured by the fact that the pyrites from FeS_2 to CuS_2 and the selenides of Co and Ni form solid solutions [195, 271]. As a consequence, the occupation of the e_g band can be continuously varied thus allowing for the construction of comprehensive phase diagrams [195].

A lot of both experimental and theoretical work has been performed on the pyrite-type transition metal disulfides. Whereas photoelectron spectroscopy (XPS, UPS, X-ray Absorption Spectroscopy (XAS), Bremsstrahlung Isochromate Spectroscopy (BIS)) addressed to determine the occupied and unoccupied electronic states [263, 159, 198, 237, 245, 236, 235, 91] optical measurements were used to evaluate the bandgaps [235, 220, 147]. As a matter of fact, many different numbers for the optical bandgap of FeS_2 were published ranging from 0.7 eV to 2.62 eV (see e.g. Refs. [48, 88, 73] for an overview). As Ferrer *et al.* as well as Ennaoui *et al.* pointed out this diversity traces back mainly to differences of samples, experimental techniques and treatment of the experimental data [88, 73]. Most reliable results are obtained from photoconductivity measurements, which yield 0.9 to 0.95 eV and agree with optical and conductivity experiments [220, 73]. Raman and IR-experiments were guided by the peculiarities of the pyrite structure with its interplay of metal-sulfur and relatively short S-S bonds [164, 251, 165, 232] and accompanied by force constant calculations [166]. Susceptibility, magnetization, neutron diffraction, Mößbauer and

PAC measurements finally aimed at the low-spin/high-spin question, the formation of local moments and the resolution of the magnetic structure especially of the Ni member of the series [184, 2, 114, 183, 271, 90, 233, 192].

As concerns the theoretical description of the MS_2 compounds, qualitative one-electron band schemes and phase diagrams were supplied already by the end of the sixties [31, 270, 268, 107, 109]. They were complemented by more accurate band calculations mainly on FeS_2 ranging from non-self-consistent tight-binding [136, 48] and semiempirical calculations [156] to self-consistent state-of-the-art studies [91, 238, 276] which, except for the work by Khan, show a remarkably good agreement. However, there are still distinct discrepancies concerning the exact shape of the bands. In particular, the upper valence and lower conduction bands of FeS_2 and, hence, the location of the valence band maximum and conduction band minimum are not yet fully resolved. These complications might be traced back to the fact that even the latest calculations involved limiting approximations as e.g. an uncomplete basis set [91] or use of the rigid core approximation [276]. In view of the high standard band theory has reached the situation is unsatisfactory and calls for a renewed calculation in order to reactivate materials research on these compounds.

Much interest has focused on iron pyrite FeS_2 for its promising capabilities as a material for photovoltaics applications [73]. This is, of course, related to the high quantum efficiency ($> 90\%$) and the high absorption coefficient ($\geq 10^5 \mathrm{cm}^{-1}$ for $h\nu >$ 1.3 eV) but also benefits from the nontoxity of the constituents [72, 30]. Yet, the rather small value of the optical bandgap prohibits optimal use of the solar spectrum. For this reason, many investigations aimed at increasing the bandgap e.g. by alloying with other materials. Recently, we found a considerable increase of the optical bandgap by about 0.07 eV on the implantation of only a very small amount ($< 5 \times 10^{20} \mathrm{cm}^{-3}$) of Zn into FeS_2 [46]. From the absence of any indications of additional phases and the fact that Zn and Fe are frequently associated in minerals we conclude that the Zn atoms homogeneously substitute for Fe atoms. The forementioned concentration then corresponds to a Zn content of $\approx 2\%$ and an average Zn-Zn distance of about 15 Å. In view of this small concentration as well as the fact that ZnS_2 is a wide-gap semiconductor with $3d$ states located well below the valence band maximum an explanation of this gap widening exclusively in terms of the electronic states seemed unlikely. Since Zn has a larger atomic radius as compared to iron we propose instead a mechanism based on crystal structure distortions caused by the incorporation of Zn impurities into iron pyrite and a considerable electron-lattice interaction [46]. The latter would transform the structural deviations into the observed changes of the electronic structure.

In order to get more support for these ideas and to resolve in general the above-mentioned uncertainties of the electronic structure we initiated the present first principles study. In doing so, we decided to concentrate for the time being on pure FeS_2 and to leave a systematic investigation of the mixed system $Fe_{1-x}Zn_xS_2$ for later work. Hence, we study in a first step the effects of symmetry conserving deviations from the measured crystal structure without actually taking the Zn impurities into account. In addition, we address the chemical bonding by using the concept of crystal orbital overlap population (COOP) [121] which was recently implemented into the ASW method by one of us [86].

The chapter is organized as follows: Starting out with a short summary of the crystal structure data in Sec. 3.2 we sketch computational aspects of the calculations in Sec. 3.3. Turning to the results we present in Sec. 3.4.1 the calculations using the experimentally reported crystal structure whereas in Sec. 3.4.2 we look in more detail at the influence of deviations from the "real" crystal structure on the electronic structure. Sec. 3.5 finally summarizes the most important results. This work has been published recently [83].

3.2 Crystal structure

At room temperature FeS_2 crystallizes in the pyrite structure which is based on a simple cubic (sc) lattice with space group $Pa\bar{3}$ (T_h^6) [90, 233, 30] and lattice constant $a = 5.4160$ Å [233]. We display the crystal structure in Fig. 3.1. The positions of the

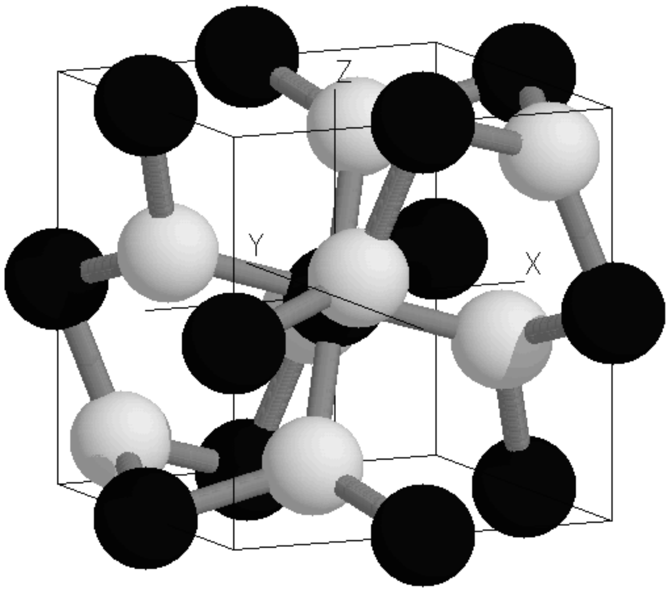

Figure 3.1: Crystal structure of FeS_2. Iron and sulfur atoms are printed in black and light gray, respectively.

atoms and the crystal structure parameter are listed in Table 3.1 where the Wyckoff positions (4a) and (8c) are special cases of the general position (24d): $\pm(x, y, z)$, $\pm(\frac{1}{2}-x, -y, \frac{1}{2}+z)$, $\pm(-x, \frac{1}{2}+y, \frac{1}{2}-z)$, $\pm(\frac{1}{2}+x, \frac{1}{2}-y, -z)$, (and cyclic permutations of x, y, and z).

The pyrite crystal structure is best described in terms of the NaCl structure with the sublattices occupied by iron atoms and the centers of gravity of sulfur atom pairs, respectively. These sulfur dumb-bells are oriented along the $\langle 111 \rangle$ axes. Being 2.161 Å their bond length is still shorter than the Fe-S distance of 2.265 Å. Whereas the sulfur atoms are tetrahedrally coordinated by one sulfur and three

Atom	Wyckoff positions	parameter
		x
Fe	(4a)	
S	(8c)	0.38484

Table 3.1: Crystal structure parameters of pyrite FeS_2 (from Ref. [233]).

iron atoms the six nearest neighbour sulfur atoms at each iron site form slightly distorted octahedra. Due to the deformations of the octahedra the local symmetry at these sites is reduced from cubic (O_h) to trigonal (C_{3i}). The distorted FeS_6 octahedra are interlinked by common corners and, due to the formation of the $\langle 111 \rangle$ sulfur pairs, have rotated away from the cartesian axes by about 23°. For a two-dimensional crystal the situation is sketched in Fig. 3.2. Obviously, the formation

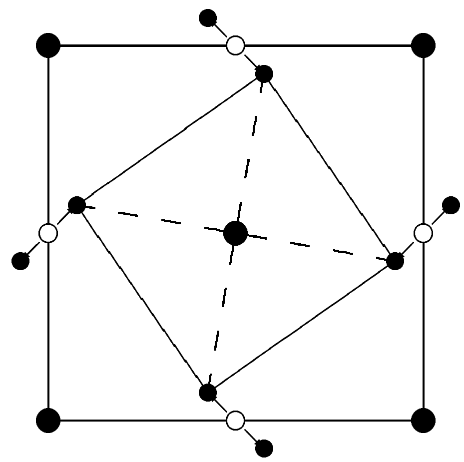

Figure 3.2: Two-dimensional analogue of the pyrite structure. Big and small filled circles designate iron and sulfur atoms, respectively. Small open circles mark the ideal positions of the rocksalt structure.

of the $\langle 111 \rangle$ sulfur pairs does not destroy the square planar coordination of the iron atoms. Instead, the squares built by the sulfur atoms just shrink and rotate. Since the orientation of the dumb-bells conforms with the cubic point group the underlying Bravais lattice is no longer face-centered but simple cubic and the unit cell comprises four formula units. Yet, as we will see below, some features of the electronic structure may still be understood in terms of the face-centered cubic (fcc) lattice.

According to Bradley and Cracknell the space group $Pa\bar{3}$ (T_h^6) is exceptional among the 230 space groups as it is the only one which is neither an invariant subgroup of any larger space group based on the simple cubic Bravais lattice nor a member of a pair of isomorphic space groups [41]. For this reason, the irreducible wedge of the first Brillouin zone as given in Fig. 3.3 is twice as big as that of the more familiar monoatomic case and we have to distinguish the high symmetry points

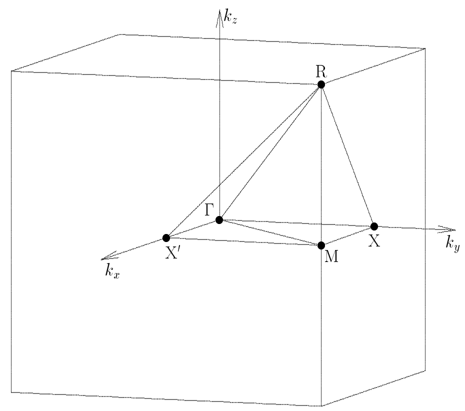

Figure 3.3: First Brillouin zone of the simple cubic lattice.

X $= (0, \frac{1}{2}, 0)$ and X′ $= (\frac{1}{2}, 0, 0)$.

3.3 Computational aspects

As already announced in section 2.6, the open structure of FeS_2 calls for inclusion of empty spheres to model the full crystal potential in an appropriate manner. We used the sphere geometry optimazation algorithm described in Sec. 2.6.1 in order to find optimal empty sphere positions as well as radii of all spheres. As a result, by inserting 32 empty spheres into the simple cubic unit cell of FeS_2, we were able to keep the linear overlap of any two physical spheres below 10% and the overlap of any pair of physical and empty spheres below 18%. The positions of the empty spheres are listed in Table 3.2. In addition to the empty sphere positions the algorithm

Atom	Wyckoff positions	parameters		
		x	y	z
E_1	(8c)	0.1935		
E_2	(24d)	0.4446	0.1373	0.1980

Table 3.2: Empty sphere positions for pyrite FeS_2.

proposed the following sphere radii: Fe: 2.243 a_B, S: 2.223 a_B, E_1: 1.630 a_B and E_2: 1.543 a_B.

Our automatically generated result differs considerably from the choice taken by Folkerts *et al.* who, likewise using the ASW method and thus relying on the ASA, faced the same problem of selecting good empty sphere positions and atomic sphere radii [91]. These authors discussed two possible solutions, one using no empty sphere at all and the other with one type of empty sphere. Checking their numbers we found that the first choice leads to a linear overlap of up to 34% whereas with the second choice one can reduce the maximum linear overlap to 30% between physical spheres and 34% between a physical and an empty sphere. Folkerts *et al.* reported on substantial discrepancies of the electronic structure calculated with these two sphere geometries. At the same time, their second choice resulted in a better agreement of the calculated electronic properties with the experimental data from XPS-, BIS- and optical experiments [91]. Nevertheless, as we will demonstrate below, there are still substantial improvements of the electronic structure when we use the above listed empty sphere positions and sphere radii from our own algorithm. As a recalculation of the work of Folkerts *et al.* with their second choice of sphere radii, however, revealed, the shortcomings of their bandstructure result only to a lesser degree from the sphere geometry alone but are rather due to the fact that, with their choice of sphere radii, the selected basis set for the variational procedure was not fully complete.

The basis set used for the present calculations comprises Fe $4s$, $4p$, and $3d$ orbitals, S $3s$, $3p$, and $3d$ orbitals and $1s$, $2p$ orbitals of the empty spheres. In addition, $4f$ states of Fe and S as well as empty sphere $3d$ states were included as tails of the forementioned orbitals (see Refs. [266, 76, 150, 80] for more details on the ASW method).

Finally, as already outlined in section 2.6.3, the Brillouin zone sampling was done using an increasing number of $\mathbf{k}$ points, which range from 11, 24, 76 to 176 points within the irreducible wedge.

3.4 Results and Discussion

3.4.1 Calculations using the experimental crystal structure

To the first approximation, the electronic structure of FeS_2 may be discussed in terms of a molecular orbital picture where the formation of $(S_2)^{2-}$ pairs leads to five occupied sulfur states per pair. The remaining antibonding $p\sigma^*$ band, in contrast, will be located above the insulating gap. Accordingly, iron turns out to be in a $3d^6$ configuration and has a low-spin $(t_{2g})^6(e_g)^0$ state in octahedral coordination. Since the distortion of the FeS_6 octahedra lowers the symmetry of the crystal field at the iron site from cubic (O_h) to trigonal (C_{3i}) the t_{2g} levels are further split into a low lying twofold degenerate e_g^π level and a higher a_{1g} singlet [107, 109]. For clarity the original e_g level is then designated as the e_g^σ state. Nevertheless, since the deviations from octahedral symmetry are rather small we still expect that the crystal field splitting is dominated by its cubic part.

To start with the presentation of our own *ab initio* results we show in Fig. 3.4 the band structure of FeS_2 along selected high symmetry lines within the first Brillouin zone of the simple cubic lattice, Fig. 3.3. The corresponding density of states (DOS) is given in Fig. 3.5 where we have added the dominant partial densities of states.

In Figs. 3.4 and 3.5 we clearly identify five groups of bands. In the energy range between 17 and 10 eV below the valence band maximum we observe two groups each comprising four single bands. Bands are most easily counted along the line M-R where they are fourfold degenerate. According to the partial densities of states these bands almost exclusively trace back to the S $3s$ states which form a bonding and antibonding subset of about 2.5 and 1.8 eV width, respectively. Whereas the large splitting between these two groups of ≈ 3 eV is due to the short S-S distance

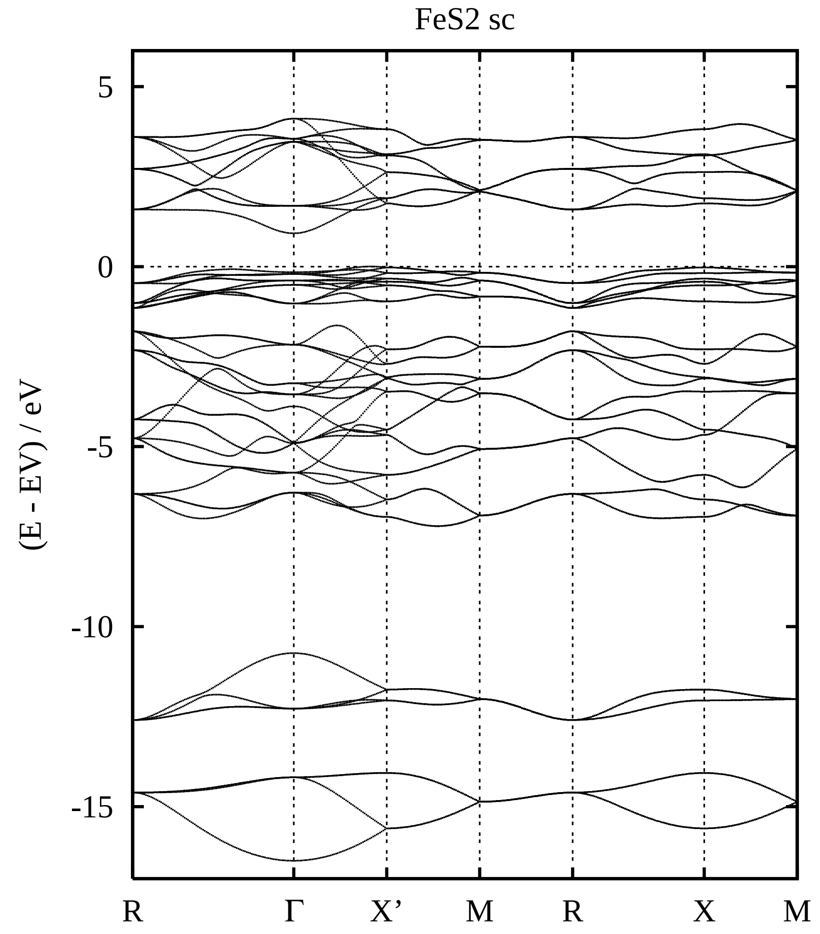

Figure 3.4: Electronic bands of FeS_2 along selected symmetry lines within the first Brillouin zone of the simple cubic lattice, Fig. 3.3. Here and in the following Figures energies are given relative to the valence band maximum E_V.

the intrinsic band widths of both groups mainly result from the dispersion across the face-centered cubic (fcc) lattice formed by the sulfur pairs. This we conclude from the level sequence at the Γ point into a lower nondegenerate and an upper threefold degenerate state the latter of which results from folding the fcc bands into the simple cubic Brillouin zone (for the antibonding group of bands the sequence of levels is reversed). Further support comes from the striking similarity of the density of states in particular of the bonding bands to that of a band calculated within the tight-binding approximation for an fcc lattice [129]. These two groups of bands and especially the asymmetric shape of their densities of states compare nicely to the results of the previous band calculations as well as to the XPS core level spectra of van der Heide *et al.* [245] who find the corresponding peaks at -16.4 and -13.3 eV, respectively. The downshift of the experimental peaks by ≈ 1 eV relative to the calculated ones may be explained by the screening of the remaining core hole.

In the energy range from -7.3 eV to -1.5 eV we find a group of 20 bands which derive from hybridized Fe $3d$ and S $3p$ orbitals with larger contributions from the latter. Just below the valence band maximum a fourth group of 12 bands appears

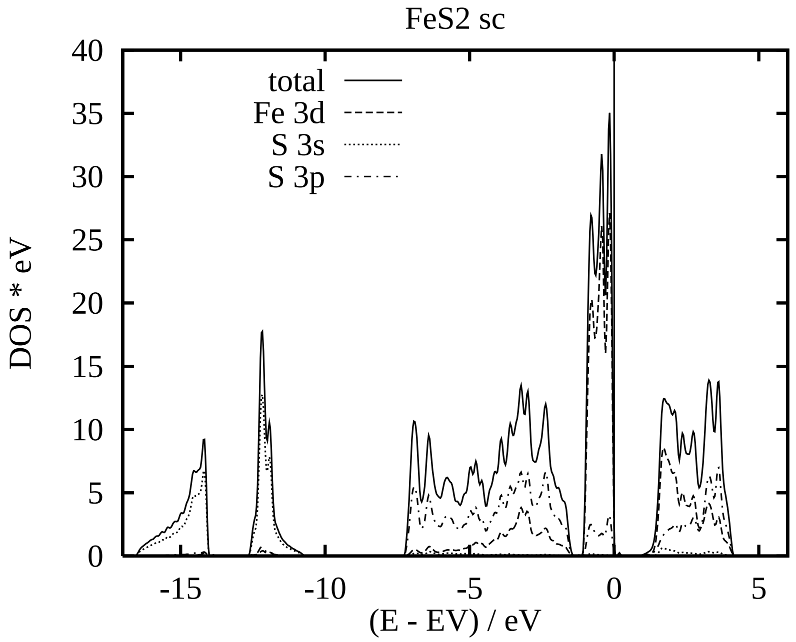

Figure 3.5: Total and partial densities of states (DOS) of FeS_2.

which mainly originates from iron $3d$ states with a small admixture from sulfur $3p$ states. In the following discussion we will designate these two groups of bands as the lower and upper valence bands, respectively. The conduction band finally comprises likewise 12 bands. They are of Fe $3d$ and S $3p$ character with the relative contributions gradually changing as the energy increases. In particular, the S $3p$ states show up in the pronounced double peak at $\approx$ 3.5 eV. All other states of Fe and S which are not included in Fig. 3.5 play only a negligible role in the given energy interval. Finally, the optical bandgap separating occupied and unoccupied states amounts to $\approx$ 0.95 eV. This is in very good agreement with the experimental values ranging from 0.9 to 0.95 eV as deduced from optical and conductivity measurements [220, 73].

As already mentioned, from the fact that the iron atoms are located at the centers of rotated and slightly distorted FeS_6 octahedra we expect a considerable crystal field splitting of the Fe $3d$ levels into a lower t_{2g} and upper e_g manifold. This is well demonstrated by the partial Fe $3d$ DOS given in Fig. 3.6 where we have included only one single iron atom. Note that due to the tilting of the FeS_6 octahedra by 23° we had to rotate the frame of reference before performing the projection on the partial $3d$ states. Fig. 3.6 clearly reveals the almost perfect energetical separation of the $3d$ t_{2g} and e_g groups of bands by the crystal field splitting. The former states appear mainly in the upper valence band without any substantial bonding-antibonding splitting. This is different for the e_g levels which, forming σ bonds hence having a much larger overlap with the sulfur $3p$ orbitals, experience a considerable splitting into bonding and antibonding states with the main peaks at $\approx$ -3.5 and 2 eV, respectively.

Next we turn to the S $3p$ states. The corresponding partial densities of states of those two sulfur atoms which are near the center of the cubic unit cell are shown

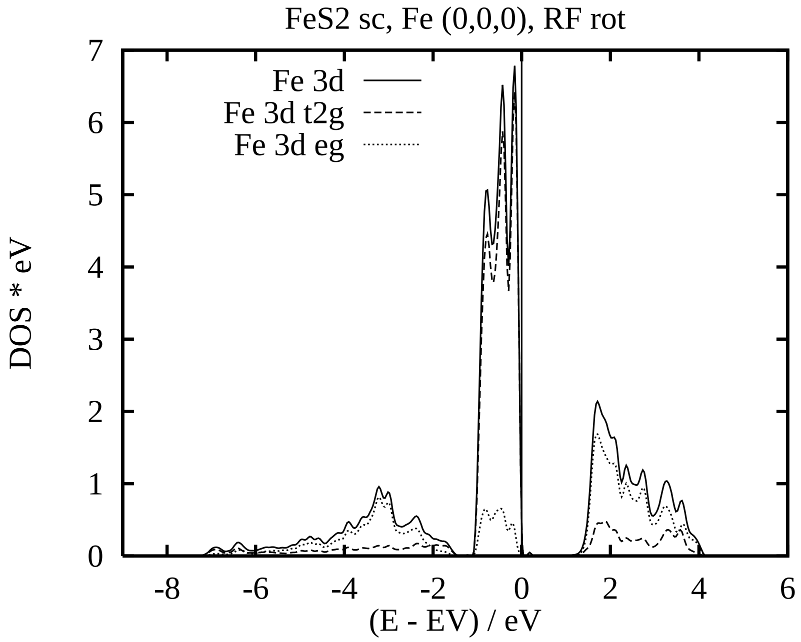

Figure 3.6: Partial Fe $3d$ densities of states (DOS) of FeS_2. The selection of orbitals is relative to a rotated reference frame (see text).

in Fig. 3.7 where we have now rotated the frame of reference such that the local

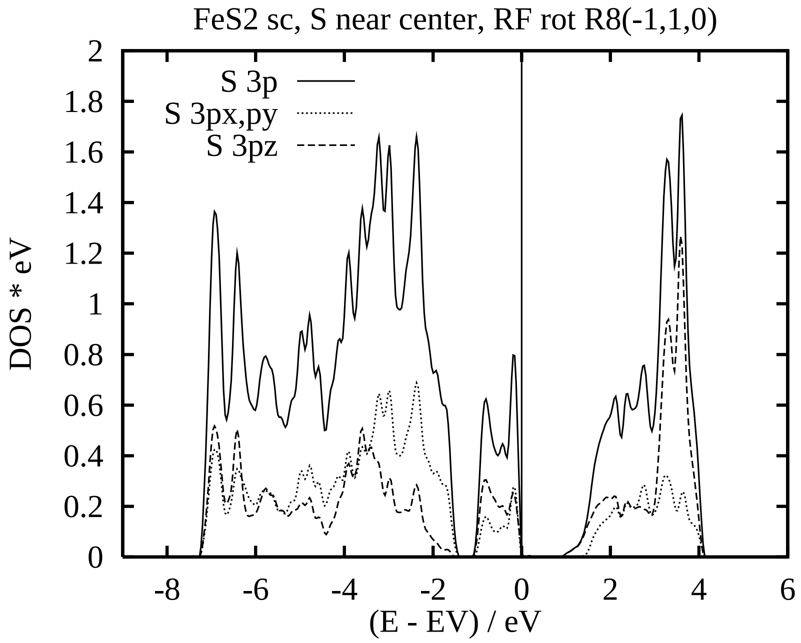

Figure 3.7: Partial S $3p$ densities of states (DOS) of FeS_2. The selection of orbitals is relative to a rotated reference frame (see text).

z-axis lies parallel to the $\langle 111 \rangle$ line connecting both sulfur atoms. As Fig. 3.7 clearly reveals, the $3p_x$ and $3p_y$ partial DOS are still identical while the $3p_z$ curve shows distinct deviations. In particular, the latter dominates the unoccupied hence antibonding S $3p$ states. This becomes rather obvious from the characteristic double peak of the $3p_z$ DOS at about 3.5 eV. The bonding counterpart is found at -6.75 eV whereas the $3p_x$ and $3p_y$ curves dominate in the energy range between ≈ -4 and $\approx$ -1.5 eV. Hence, among the three sulfur $3p$ bands, the p_z states show the largest bonding-antibonding splitting. This is not suprising since the $3p_z$ states form σ bonds between the two sulfur atoms of a pair whereas the $3p_x$ and $3p_y$ orbitals experience a much smaller overlap via π bonds.

Besides discussing the main peaks of the Fe $3d$ and S $3p$ DOS we focus the readers attention in particular on the peak of the $3p_z$ DOS at $\approx$ -3.9 eV as well as on the lowest edge of the conduction band which is exclusively due to the $3p_z$ orbitals without any contributions from the other two $3p$ or the Fe $3d$ e_g orbitals. The latter fact is clearly demonstrated in Figs. 3.8 and 3.9 where we display the

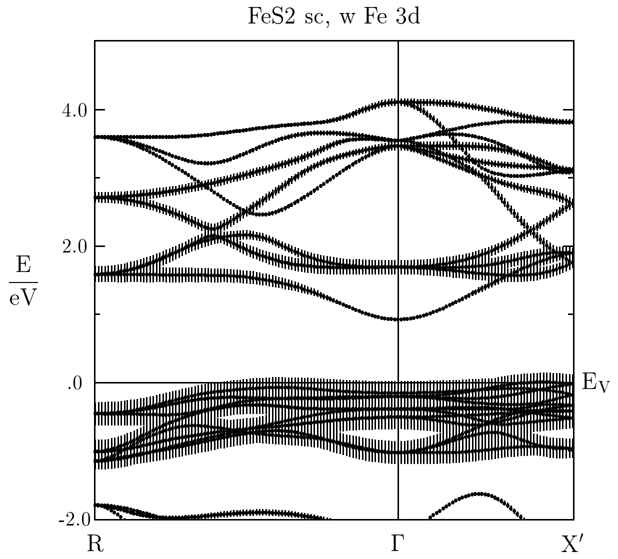

Figure 3.8: Weighted electronic bands of FeS_2. The width of the bars given for each band indicates the contribution due to the Fe $3d$ orbitals.

near-gap electronic bands in a special representation. In both Figures, each band at each $\mathbf{k}$ point is given a bar which length is a measure for the contribution from a specified orbital. In particular, we derive the dominating influence of the Fe $3d$ states to the upper valence band from the long bars in Fig. 3.8. According to Fig. 3.9 these bands have no bars indicative of S $3p$ states. For the conduction bands we observe strong Fe $3d$ contributions in the energy window from $\approx$ 1.5 to 3.0 eV, whereas for energies above this range and especially at the lowest edge of the conduction bands S $3p$ dominate. The change of band character from Fe $3d$ to S $3p$ can be clearly observed in the lowest conduction band along the line R-Γ. As can be seen in Fig. 3.9, at the Γ point this band is exclusively due to S $3p$ states but, due to hybridization with the Fe $3d$ states, looses this dominance as one goes to the R point. In contrast, in the middle between both points the band at 2.5 eV takes over the S $3p$ character and keeps it until the R point is reached at about 3.7 eV. From a different point of view we interprete the band starting at Γ at $\approx$ 1.0 eV and dispersing almost linearly to 3.7 eV at the R point as the S $3p$ band which hybridizes with the dispersionless e_g bands in the energy region between 1.5 and 2.5 eV half way between Γ and R. The situation is thus not unlike that in elementary

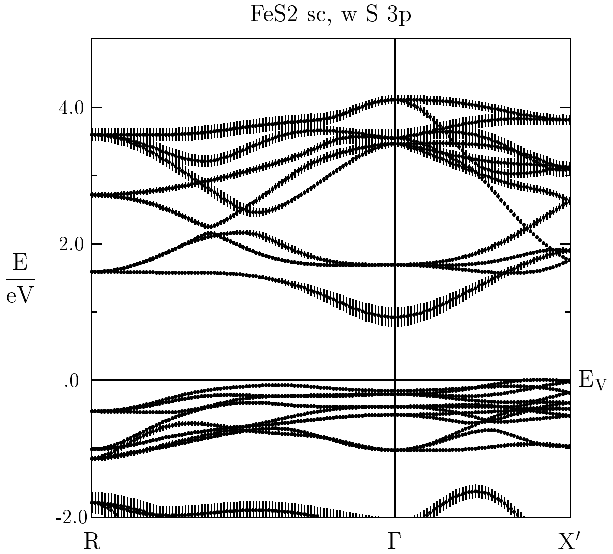

Figure 3.9: Weighted electronic bands of FeS_2. The width of the bars given for each band indicates the contribution due to the S $3p$ orbitals.

Cu where the lowest s like hybridizes with the $3d$ states just below the Fermi energy but again assumes the original $4s$ character above E_F [79].

As for the S $3s$ bands the states at -3.9 eV and at the conduction band minimum originate from a dispersion of the sulfur $3p$ bands accross the underlying fcc lattice. Hence, the formation of the sulfur dominated bands evolves mainly in two steps. First, due to the close coupling of the sulfur pairs, the S $3p$ states are strongly split into bonding and antibonding states which, in case of the $3p_z$ orbitals, leads to the rather sharp double peaks at -6.75 and 3.5 eV. Once these effective sulfur pair states have been formed they disperse across the fcc lattice but are folded back to the smaller Brillouin zone of the simple cubic lattice. As a consequence, both the bonding and antibonding subband have a considerable band width. Finally, we arrive at the rather surprising conclusion that the optical bandgap separates Fe $3d$ t_{2g} and S $3p_z$ orbitals and hence, although being strongly influenced by the crystal field splitting, cannot be described exclusively in terms of it. In contrast, the different orbital composition of the valence band maximum and the conduction band minimum provides a natural explanation of the high optical absorption.

We complement the previous discussion by addressing the chemical bonding of FeS_2 via the crystal orbital overlap population as shown in Fig. 3.10. The COOP curves display the rather "canonical" behaviour being positive (bonding) and negative (antibonding) in the low and high energy regions of a band. In case of the sulfur-sulfur overlap this is nicely visible for both the valence and the conduction bands separately the absolute values being higher in the latter. Below -4.5 eV we find bonding S-S σ and π bands. The corresponding antibonding states, in contrast, are separated in energy. S-S π^* states lead to the negative COOP in the interval from -4.5 to -1.5 eV whereas S-S σ^* dominate in the upper half of the conduction band. Sulfur states in the upper valence band and the lower half of the conduction band finally are rather nonbonding. As a consequence of the complete filling of the sulfur π and π^* bonds the net contribution of the occupied sulfur-sulfur bonds to

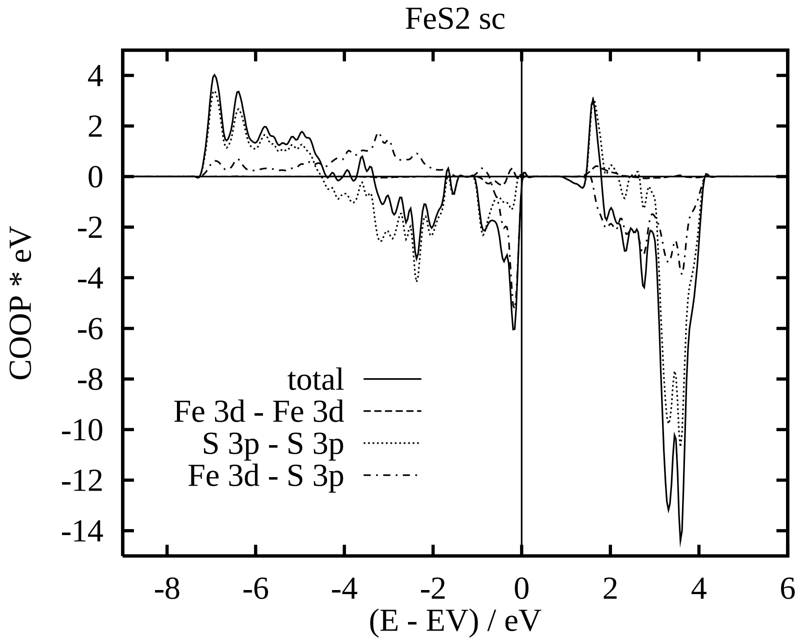

Figure 3.10: Total and partial crystal orbital overlap populations (COOP) of FeS_2.

the chemical stability is rather small. The same holds for the metal-metal bonding the effect of which is almost negligible due to the large Fe-Fe separation. The dominating contribution to the chemical stability results from the overlap of Fe $3d$ and S $3p$ orbitals. They lead to a COOP curve which is positive throughout the lower valence band and negative only in the t_{2g} derived and in the conduction band. Bonding Fe $3d$ - S $3p$ contributions result from σ bonds of the e_g and S $3p$ states as well as π bonds formed by overlap of the t_{2g} and the $3p$ states. The corresponding antibonding π^* and σ^* orbitals, in contrast, show up in the upper valence and the lower half of the conduction band, respectively. Since a large portion of these antibonding states is shifted to the bands above the insulating gap the iron-sulfur bonding can be identified as the decisive factor for the stability of FeS_2.

There is an overall good agreement of the calculated electronic structure with experimental data. This holds especially for the photoemission measurements which find the upper valence band of 0.8 to 1.3 eV width at 0.8-0.9 eV below the valence band maximum [159, 198, 245, 91] whereas the calculation locates this band at about -0.6 eV. According to Li *et al.* the S $3p$ dominated bands extend from -8.6 to -1.8 eV [159]. XPS spectra by Ohsawa *et al.* clearly reveal a main peak at -4 eV and a pronounced shoulder at about -7 eV. From our calculation we get the S $3p$ contribution in the interval from -7.3 to -1.5 eV with dominant peaks at about -3.2 eV and -7 eV. Again attributing the relative shift of the lower edge to screening effects we observe almost quantitative agreement. From Kβ emission and K absorption spectra Sugiura *et al.* extract values of 2.7 and 5.9 eV for the position of the upper valence and the conduction band, respectively relative to the main peak of the occupied S $3p$ bands [237, 236] which compare very good with the calculated numbers of 2.6 and $\approx$ 6.5 eV, respectively. Finally, the calculated position of the unoccupied S $3p$ states conform very well with the value of 3.3 eV as derived from

BIS-measurements by Folkerts *et al.* [91]. Still, it would be interesting to compare our results to angle resolved photoemission data which, however, do not seem to be published so far. In passing we mention that our results confirm the magnetic measurements by giving a low-spin state for the Fe $3d$ orbitals [184].

Comparing our results to the previous band calculations we likewise arrive at satisfactory agreement as concerns the band positions and edges. This is true in particular for the calculations by Bullett, by Folkerts *et al.*, and by Temmerman *et al.* their densities of states being almost identical to ours. Visible deviations shows the calculation of Zhao *et al.* which place the S $3s$ and occupied $3p$ derived bands considerably lower [276] this fact being in conflict with the values given by Sugiura *et al.* for the relative band positions [237].

Although all electronic structure calculations including our own agree in finding an indirect bandgap there exist some deviations concerning the extremal band positions. Obviously, they trace back to the differences showing up for the near-gap electronic states which we already mentioned in the introduction. Concentrating on only the latest state-of-the-art work we witness, however, some agreement coming up. Folkerts *et al.* reported on a valence band maximum (VBM) lying not on a high symmetry line but somewhere within the first Brillouin zone and found the conduction band minimum (CBM) at $\approx 0.7(\frac{1}{2}, \frac{1}{2}, \frac{1}{2})$ (in units of $\frac{2\pi}{a}$) [91]. From their band structure it seems likely that the VBM is located near the X-point. The latter fact would compare well with the findings of Zhao *et al.* who locate the VBM at the X-point and the CBM at the center of the first Brillouin zone [276]. With respect to the VBM we conclude from the band structure as well as from a scan through the first Brillouin zone on a mesh of $30 \times 30 \times 30$ points that the valence band maximum is located at the point $(0.0, 0.0, 0.4136)$, which indeed is in the vicinity of the X-point and thus compares well with the result of Zhao *et al.* [276].

At a first glance, agreement for the CBM seems to be less satisfactory. Yet, besides clearly locating the CBM at the Γ point and thus confirming the results of Zhao *et al.* we were able to assign the deviating result of Folkerts *et al.* to their use of an incomplete basis set. This was clearly revealed by a recalculation of their work. To be specific, with the sphere geometry and basis set reported by these authors we get an occupation of the Fe $4f$ states of 0.45 electrons which is not accounted for by an inclusion of these states into the secular matrix (see e.g. Refs. [266, 150, 76] for details on the ASW and related methods). We are thus able to note agreement of the remaining band studies and to summarize the results to the effect, that the VBM and CBM reside near the X-point at $(0.0, 0.0, 0.4136)$ and at the Γ point, respectively.

3.4.2 Role of pressure and crystalline distortions

Still, we did not yet pay much attention to the factors which might influence the optical bandgap. Indeed, it would be desirable to identify mechanisms which change the size or the indirect nature of the gap or modify the composition of the near-gap states. More insight into such mechanisms would finally allow to address the question of why incorporation of small amounts of Zn into FeS_2 leads to the experimentally observed widening of the optical bandgap [46].

Since it is unlikely that the changes of the electronic structure of FeS_2 on the substitution of Zn for Fe can be explained from the differences in the electronic configurations alone we propose a rather strong influence of the accompanying distortions of the crystal structure due to the larger atomic radius of Zn in addition to a considerable electron-lattice interaction. Nevertheless, we decided to stay for the time being with pure FeS_2 and to study from a more general point of view the sensitivity of the electronic structure to symmetry conserving deviations from the measured crystal structure. Obviously, such an investigation not only serves as a necessary prerequisite to a solution of the forementioned problem but is an interesting topic in itself.

To start with, we simulated in a first step the application of external pressure and performed a fully self-consistent calculation for FeS_2 with the lattice constant reduced by 5%. As a result, there are mainly two effects. As expected, hydrostatic pressure leads to a broadening of all bands without noticeable reorderings of the electronic states. At the same time, there is a corresponding reduction of the total and partial DOS. Second, the main peaks of the lower valence and the conduction band experience rather large shifts to lower and higher energies, respectively. For the lowest and highest peaks the shifts are even as large as about 1 eV. In particular, the pronounced S $3p_z$ dominated double peaks at about -6.75 and 3.5 eV move to ≈ -7.5 and ≈ 4.4 eV, respectively. To a lesser degree the same happens to the peaks between -4 and -2 eV as well as at 2 eV. These large shifts of all electronic states away from the valence band maximum add to the effect of the forementioned band broadening and, as a consequence, the size of the optical bandgap remains essentially unchanged.

This result conforms quite well with pressure experiments mentioned by Schlegel and Wachter [220]. These authors report on a hydrostatic pressure study by Batlogg who finds a slight blue shift of $2 \times 10^{-6}\,\mathrm{eV\,bar^{-1}}$ of the optical absorption edge. According to Schlegel and Wachter this can be explained by the increased crystal field splitting between the iron $3d$ t_{2g} and e_g levels on the application of pressure [220]. Although fully correct, in view of the information gained in the previous subsection this interpretation appears to be incomplete. In particular, it cannot explain the largest shifts appearing for the S $3p_z$ bands which, however, were not accessible by the measurements of Schlegel and Wachter.

Guided by the discussion of subsection 3.4.1 we describe the gross features of the electronic structure in terms of three different energies, namely the crystal field splitting, Δ_{CEF}, the bonding-antibonding splitting due to the overlap of Fe $3d$ e_g and S $3p$ orbitals, $\Delta_{e_g p}$, and finally the strong bonding-antibonding splitting due to the S-S $3p_z$ overlap, Δ_{p_z}. In this rather crude scheme we have not included splittings due to the $3d$ t_{2g} – $3p$ π-type overlap as well as the π bonds within the sulfur pairs both of which are much smaller than the previous three energies. On the application of isotropic pressure, all three of the forementioned energies are likewise increased this resulting in an overall spreading of the band structure. As a consequence, we witness not only a band broadening but at the same time the bands shift apart to a similar degree. Since the crossover from bonding to antibonding states as well as the separation of the $3d$ t_{2g} and the main part of the e_g states appears near or at the valence band maximum the optical bandgap finally is not affected.

The situation becomes more complicated in the second part of our simulation. Here we concentrate on the variation of the internal x parameter which determines the sulfur position. To be specific, we again performed fully self-consistent calculations for FeS_2 but now changed the internal sulfur parameter to $x = 0.38084$ and $x = 0.38884$, respectively which are just below and above the experimental value of $x = 0.38484$ listed in Table 3.1. The resulting band structures are shown in Figs. 3.11 and 3.12.

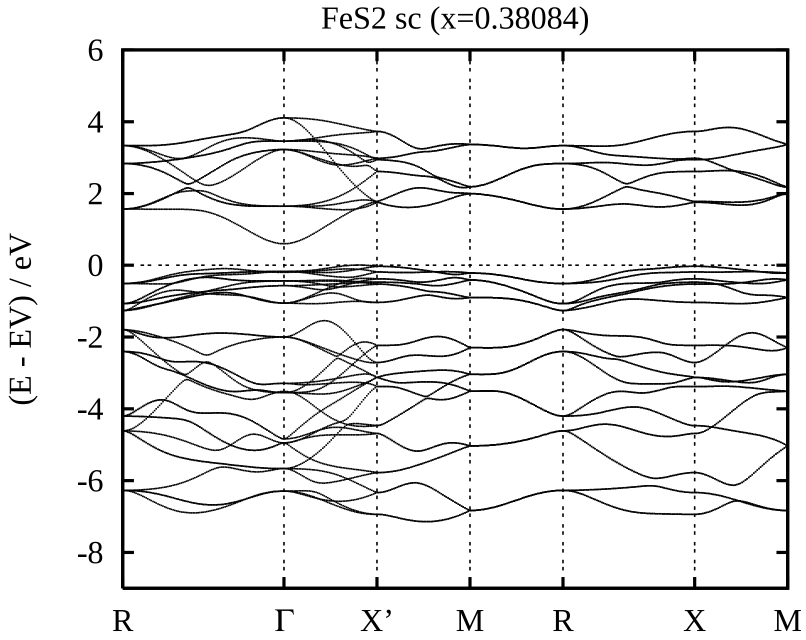

Figure 3.11: Electronic bands of distorted FeS_2.

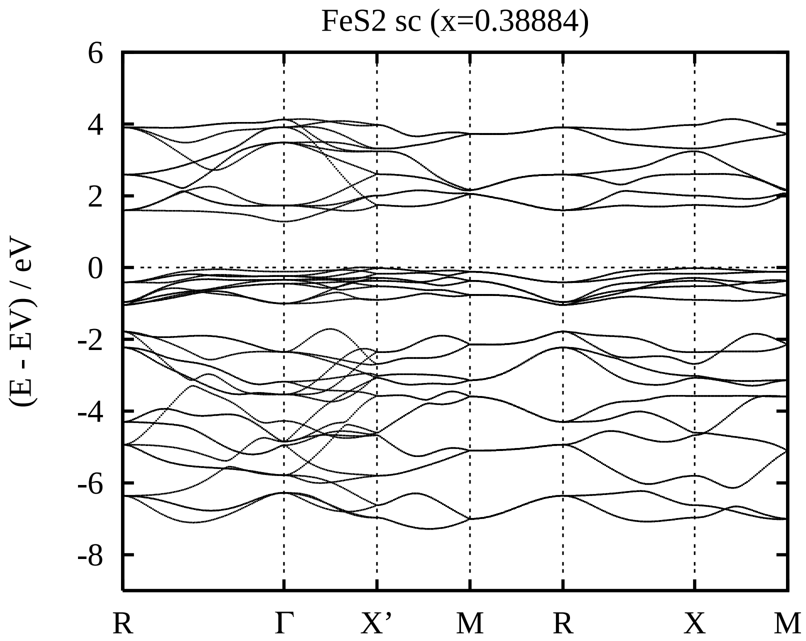

Figure 3.12: Electronic bands of distorted FeS_2.

Again, the results are rather surprising. First of all, we observe a large shift of the optical bandgap of about 0.67 eV when going from $x = 0.38084$ to $x = 0.38884$ hence moving the sulfur atoms by less than 1% of the lattice constant. Obviously, this change of the bandgap is due to the equivalent shift of the conduction band minimum relative to the centers of gravity of both the valence and conduction band which stay essentially inert. From the large shift of the CBM we might even expect that for larger values of the x parameter FeS_2 turns over to a direct gap semiconductor which, of course, would have great implications for the optical properties. Indeed, this trend was confirmed by an additional calculation for $x = 0.39084$. A shift of similar size as that of the CBM is observed only for the single band which in Fig. 3.4 can be found at -3.9 eV at the Γ point and moves to -3.6 and -4.3 eV in Figs. 3.11 and 3.12. Furthermore, there is a noticeable shift of the sulfur $3p_z$ dominated double peak at about 3.5 eV which moves by approximately 0.5 eV. As a consequence, the total width of the conduction band is reduced.

We thus conclude that variation of the x parameter affects almost entirely the S $3p$, especially the $3p_z$ states. Their response to the changes of the crystal structure is essentially twofold. First, increase of the sulfur x parameter leads to a closer coupling of the sulfur pairs and hence to a larger bonding-antibonding splitting. This is revealed by the shifts of the $3p_z$ double peaks. Second, the increase of the x parameter, while shortening the sulfur-sulfur bonds, at the same time reduces the hopping across the lattice. For this reason the dispersion of the $3p_z$ bonding and antibonding bands decreases this leading to the observed downshift of the $3p_z$ state at -3.9 eV at the Γ point as well as to the corresponding upshift of the CBM. From these results we conclude that the sulfur sublattice of FeS_2 should be rather discussed in terms of a molecular S_2 crystal. Furthermore, we identify the reduced dispersion across the lattice as the main responsible for the rise of the CBM and the accompanying widening of the optical bandgap. This effect is supported by the shift of the antibonding double peak at 3.5 eV which pulls the CBM even further to higher energies.

Of course, the latter effect can not be obtained by the application of pressure which, while likewise increasing the bonding-antibonding splitting, supports hopping between the S_2 molecules by reducing the lattice constant and thus leads to an increase of the $3p_z$ band width. As a result, the CBM would move down (relative to the antibonding double peak) which is indeed observed.

Still, we may ask why the Fe $3d$ dominated bands and, in particular the crystal field splitting Δ_{CEF} as well as the bonding-antibonding splitting due to the overlap of Fe $3d$ e_g and S $3p$ orbitals, $\Delta_{e_g p}$, are almost unaffected by the changes of the sulfur x parameter. From the increase of x we would rather expect a reduced crystal field splitting hence a lowering of the e_g states in the lower part of the conduction band. At the same time, the $e_g - p$ overlap, i.e. $\Delta_{e_g p}$ should decrease and again the lower half of the conduction band should move downwards. However, we observe none of these two effects. This may be explained in a rather simple manner from the projection of the pyrite structure, Fig. 3.2. Obviously, any change of the x parameter affects first of all the length of the sulfur-sulfur bond. Its implications on the geometry of the FeS_6 octahedron, in contrast, are much smaller since the movement of the sulfur atoms relative to the central iron atoms has a substantial tangential component which leads to a much reduced effect on the size of the octahedron and, even more important, preserves the square planar coordination.

We thus arrive at the conclusion that the crystal field splitting plays only a minor role for the optical properties of FeS_2. In contrast, it is rather the bond length of the S_2 molecules which turns out to be the key parameter to a dedicated and strong influence on the S $3p$, in particular $3p_z$ states this fact revealing a substantial electron-lattice interaction. The latter in turn tunes the energetical position of the conduction band minimum and thereby the optical bandgap.

In this context it is interesting to recall the results of Raman measurements which demonstrated that the sulfur-sulfur bond in FeS_2 is rather soft as compared to that of other pyrite type transition metal chalcogenides [232]. As a consequence, one expects that on the application of external isotropic pressure the interatomic distances are reduced to a different degree and, in particular, that the sulfur-sulfur bond compression is larger than that of the Fe-S bonds. Hence, the resulting band structure should include both the effects of scaling of the lattice constant and increase of x: On the application of pressure we would expect the band structure to resemble that of Fig. 3.12 with an additional broadening of all bands. This finally yields a conclusive understanding of the blue shift of the optical bandgap as observed by Batlogg [220].

We are finally able to sketch a possible scenario for the substitution of Zn atoms for Fe. From the larger atomic radius of Zn as compared to Fe we can easily imagine that each Zn impurity will push apart its six nearest neighbour sulfur atoms. This might have two different consequences for the corresponding S_2 molecules. They will be either rigidly pushed away or else compressed with the distances to the neighbouring Fe atoms being essentially unchanged. Of course, any combination of both effects might be also possible. From the previous discussion, however, we expect the second alternative to be the more likely one. In case that the sulfur pairs are compressed we expect the CBM to raise because of the mechanisms outlined before. If, however, the bond length of the S_2 molecules would be preserved they would shift away from the ideal positions of the rocksalt structure this leading to a structural disorder. Again, the dispersion of S $3p_z$ states across the lattice were affected and we would obtain an upshift of the CBM. Hence, in both cases introduction of Zn impurities will push the CBM to higher energies and, most important, while addressing to the band dispersion of the $3p_z$ orbitals across the lattice, in both cases the effect is of rather long range. Hence we expect it to show up already for a small amount of Zn impurities which indeed is observed in experiment.

3.5 Conclusion

In the present chapter first-principles ASW calculations were used to describe the electronic properties of iron pyrite. Chemical stability as investigated by the crystal orbital overlap population (COOP) results from overlap of crystal field splitted Fe $3d$ t_{2g} and e_g orbitals with the sulfur ligand $3p$ states. Hybridization of the latter with the e_g orbitals leads to the lower valence and the conduction band whereas the relatively narrow upper valence band stems mainly from t_{2g} states.

Formation of strong σ bonds within the sulfur pairs leads to large bonding-antibonding splitting of the S $3p_z$ states. Dispersion of these states across the lattice causes a considerable bandwidth and places the antibonding states at the conduction band minimum which is thus rather sensitive to the σ bonds. The difference in band characters at the valence band maximum and the conduction band minimum, finally, gives a natural explanation of the high optical absorption.

The influence of electron-lattice interaction has been probed by simulating both external pressure and changes of the sulfur-sulfur distance. The former leads to the expected band broadening which is accompanied by a spread of all band centers due to increased crystal field as well as bonding-antibonding splittings and hence does not change the optical bandgap. Change of the sulfur x parameter, in contrast, causes drastic changes which can be partially traced back to an increase of the bonding-antibonding splitting of the S $3p_z$ bands on shortening the S_2 bond length. However, the main effect originates from disturbance of the dispersion across the lattice resulting in a reduced band width of the $3p_z$ antibonding band and an upshift of the conduction band minimim. Being a long range effect it is sensitive to only small disturbances of the crystal structure.

Hence, FeS_2, despite being a transition metal chalcogenide with an unfilled d shell, is extraordinary insofar as its electronic structure as well as its response to crystal structure distortions are almost entirely determined by the sulfur ligand $3p$ states.

Chapter 4

Octahedral deformations in V_2O_5

4.1 Motivation

The transition metal oxides attract a lot of attention due to their interesting physical and chemical properties, which arise from the narrow d states and their hybridization with the ligand p orbitals. Among this large class of materials the vanadium-oxygen system arouses special interest. Although made up of only two constituents, the vanadium-oxygen phase diagram contains several stoichiometric compounds and a broad spectrum of physical phenomena could be studied [45].

Some of the vanadium oxides undergo reversible metal-insulator transitions as a function of temperature, pressure, or doping, which come along with magnetic transitions and/or structural changes. Prominent examples are VO_2 and V_2O_3 where the change in resistivity extends over several orders of magnitude [187]. In both compounds, the first order phase transition is accompanied by structural changes affecting the geometry of the characteristic VO_6 octahedra [45]. In addition, V_2O_3 exhibits long-range antiferromagnetic order below the transition temperature [187]. The origin of the metal-insulator transition, however, is still a matter of controversy. Several models have been proposed ranging from models stressing the importance of electron-phonon coupling to such favouring strong electron-electron correlations as the driving force. As a consequence, a complete and accepted picture of the physics of the vanadium oxides has not yet evolved.

In an attempt to split the forementioned problem of identifying the predominant physical mechanisms into subproblems, which might be easier to attack, it is worthwhile to study related compounds where, for instance, electron-electron correlations are regarded as playing a minor role. One such system is vanadium pentoxide which is a semiconductor at all temperatures without exhibiting a phase transition [45, 39]. At the same time, the crystal structure of V_2O_5 shows distinct deformations of the VO_6 octahedra some of which are equivalent to those present in VO_2 and V_2O_3. Hence, by investigating V_2O_5, we might be able to shed some light onto the influence of these structural peculiarites on the electronic structure without being blinded by electron-electron correlations.

For some time, V_2O_5 has been the subject of intense work because of its small and highly anisotropic n-type electrical conductivity [45, 39, 6]. The anisotropy was related to the peculiarities of the crystal structure: the atoms form double chains within planes which are separated by a van der Waals gap [50, 18, 19, 71]. From Hall effect, thermopower and EPR measurements, Ioffe and Patrina concluded that the reduced conductivity, in contrast, can be attributed to the formation of small polarons [126]. According to optical absorption measurements the fundamental absorption edges amount to 2.15, 2.17 and 2.22 eV for E||a, E||b and E||c, respectively [135]. From optical reflectance measurements, Mokerov *et al.* concluded that the optical properties for energies between 2.2 and 8-9 eV are dominated by transitions from oxygen $2p$ to vanadium $3d$ states, whereas above 8-9 eV the transitions are to the vanadium $4s$ states [185]. These authors reported that the fundamental absorption is due to a band of only 0.4 eV width, located at about 2.5 eV above the highest occupied states. In addition, they found a second absorption edge at an energy above 2.6 eV [185]. Their finding of a low energy split-off conduction band provided a different clue to the understanding of the low carrier mobility.

These findings were confirmed by photoemission experiments using UPS, XPS, XAS, and Auger electron spectroscopy [89, 61, 226, 275, 99, 100, 101]. According to Zhang and Henrich, the valence band of about 5.5 eV width divides mainly into three peaks [275]. The two lower peaks are due to the V – O bonding, whereas the highest peak corresponds to non-bonding O $2p$ orbitals. In addition, these authors found considerable changes of UPS spectra taken before and after XPS measurements on the (001) surface, which, in particular, affected the two high-binding valence band peaks and which they attributed to the tendency of V_2O_5 to form defects and to undergo transitions to other oxides [275].

In the past years, V_2O_5 has attracted renewed interest as a starting material for the intercalation of alkaline atoms into the van der Waals gap. Attention focused, in particular, on the stoichiometric sodium intercalation system α'-NaV_2O_5 where the sodium atoms form ordered chains within the van der Waals gap [54] and which exhibits a Spin-Peierls transition at $T_{SP} = 33.5K$ [127, 92, 197, 258, 246, 274, 160].

Theoretical work on V_2O_5 comprises semi-empirical tight-binding calculations, a non-self-consistent first principles approach as well as self-consistent calculations for clusters near the (001) surface [153, 154, 47, 155, 181]. However, a state-of-the-art first principles study of the bulk material is still missing. In order to fill this gap we initiated the present study. In doing so, we aim in particular at a comprehensive analysis of the electronic structure in terms of few relevant orbitals. Nevertheless, for a detailed investigation of the mechanisms which cause the characteristic octahedral deformations it is not sufficient to stay with only the experimentally determined crystal structure. For this reason, we extended our study to calculations for V_2O_5 with hypothetical crystal structures in which ideal octahedral geometry was gradually restored. The resulting changes of the electronic structure allow to deduce detailed information concerning the stability of the actual crystal structure. Finally, we complement the electronic properties with a discussion of the chemical bonding by evaluating the crystal orbital overlap population (COOP) [121] which was recently implemented into the augmented spherical wave (ASW) method [86].

A brief account of the present results has been given recently [79, 221, 222, 81] whereas a detailed comparison with angle resolved photoemission data will be published in the near future [223]. The chapter is organized as follows: Starting with a short summary of the crystal structure data in Sec. 4.2, we outline the calculational method in Sec. 4.3. The results are presented in Sec. 4.4. The conclusion, Sec. 4.5, sums up the most important findings.

4.2 Crystal structure

V_2O_5 crystallizes in a simple orthorhombic (so) lattice with space group *Pmmn* (D_{2h}^{13}) and lattice constants $a = 11.512$Å, $b = 3.564$Å, and $c = 4.368$Å [71]. The primitive cell comprises two formula units. We display the crystal structure in Fig. 4.1 where

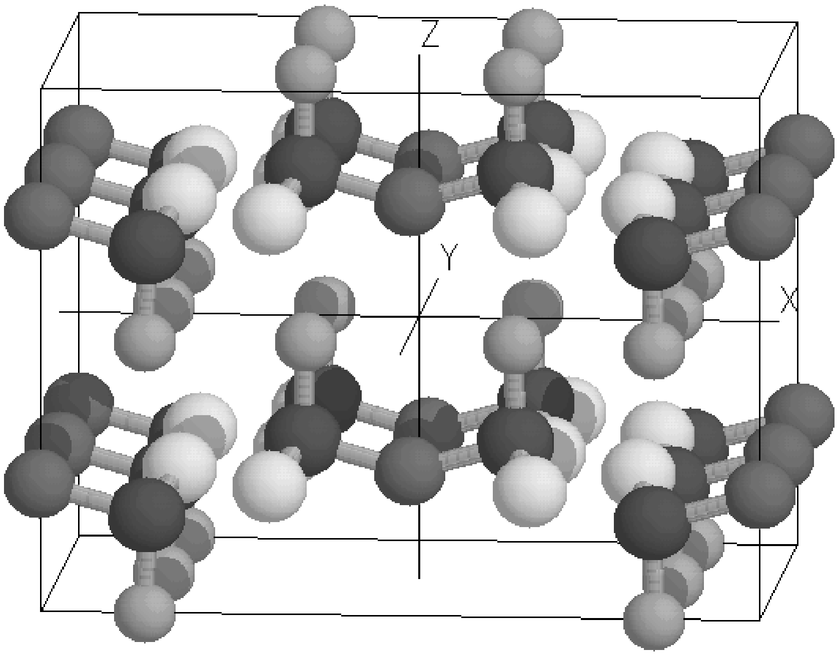

Figure 4.1: Crystal structure of V_2O_5. Lines parallel to the x, y, and z axes mark the a, (double) b and (double) c orthorhombic axes. Vanadium atoms are printed in black. Vanadyl, chain and bridge oxygens are shaded medium, light and dark gray, respectively.

we also indicate the three different types of oxygens. They are usually designated as vanadyl (O_v), chain (O_c) and bridge (O_b) oxygens. The positions of the atoms and the crystal structure parameters are listed in Table 4.1 where the Wyckoff positions (2a) and (4f) are special cases of the general position (8g): $\pm(x, y, z)$, $\pm(x, \frac{1}{2} - y, z)$, $\pm(\frac{1}{2} - x, y, z)$, $\pm(\frac{1}{2} - x, \frac{1}{2} - y, z)$.

The crystal structure consists of alternating (horizontal) layers which contain either vanadium, chain and bridge oxygen atoms or, alternatively, vanadyl oxygen

Atom	Wyckoff positions	parameters		
		x	y	z
V	(4f)	0.10118	0.25	-0.1083
O_v	(4f)	0.1043	0.25	-0.469
O_c	(4f)	-0.0689	0.25	0.003
O_b	(2a)	0.25	0.25	0.001

Table 4.1: Crystal structure parameters of V_2O_5.

atoms. Within the first type of layers, vanadium and chain oxygen atoms form double zigzag chains along the ⟨010⟩ direction which, within the planes, are connected via the bridge oxygen atoms. The vanadyl oxygen atoms, finally, are located just below and above the vanadium atoms: thus the vanadium atoms reside near the centers of VO_6 octahedra formed by one bridge, two vanadyl, and three chain oxygen atoms. These octahedra share edges via the chain oxygens and corners via the bridge oxygens.

Still, the vanadium atoms experience distinct displacements away from the centers of the octahedra. First, the vanadium and the vanadyl oxygen atoms move vertically towards each other. One short (1.577Å) and one long (2.791Å) V – O_v distance evolves, and the interaction along the latter reduces to rather weak van der Waals forces this fact explaining the observed easy cleavage of V_2O_5 crystals parallel to the (ab) layers [45]. Second, the vanadium and the chain oxygen atoms experience shifts parallel to the x axis towards the bridge oxygen atoms. This leads to the zigzag shape of the ⟨010⟩ double chains. The resulting in-plane distances within the octahedra amount to 1.779Å for the V – O_b bond and 1.878Å and 2.017Å for the V – O_c bonds parallel to the y and x axis, respectively. Due to these displacements the remaining basic units finally become VO_5 pyramids rather than regular octahedra.

4.3 Calculational details

As for iron pyrite, the open crystal structure of V_2O_5 requires to fill the unit cell with empty spheres. Applying the sphere geometry optimization algorithm described in section 2.6.1 we were able, by inserting 24 empty spheres into the simple orthorhombic unit cell, to keep the linear overlap of any pair of physical spheres below 18% and the overlap of any pair of physical and empty spheres below 24%. The positions of the empty spheres are listed in Table 4.2. In addition to the empty sphere positions the algorithm proposed atomic sphere radii for all spheres, which are listed in Table 4.3. Table 4.3 moreover supplies the orbitals used as the basis set for the present calculations. Again, states given in parentheses were included as tails of the other orbitals. Finally, the Brillouin zone sampling was done using an increasing number of **k** points, which range from 27, 64, 216 to 512 points within the irreducible wedge.

Atom	Wyckoff positions	parameters		
		x	y	z
E_1	(4f)	-0.38	0.25	0.5
E_2	(2b)	-0.25	0.25	0.1389
E_3	(2a)	0.25	0.25	0.4208
E_4	(8g)	0.0217	0.0595	0.2533
E_5	(8g)	0.1561	0.0238	0.1672

Table 4.2: Empty sphere positions for V_2O_5.

Atom	Radius/a_B	Orbitals				
V	1.965	$4s$	$4p$	$3d$	$(4f)$	
O_v	1.521	$2s$	$2p$	$(3d)$		
O_c	2.079	$2s$	$2p$	$(3d)$		
O_b	1.680	$2s$	$2p$	$(3d)$		
E_1	2.598	$1s$	$2p$	$3d$	$4f$	$(5g)$
E_2	2.583	$1s$	$2p$	$3d$	$(4f)$	
E_3	2.516	$1s$	$2p$	$3d$	$4f$	$(5g)$
E_4	1.532	$1s$	$(2p)$			
E_5	1.613	$1s$	$(2p)$			

Table 4.3: Atomic sphere radii and basis set orbitals for V_2O_5.

4.4 Results and Discussion

4.4.1 Electronic structure and density of states

To the first approximation, the semiconducting groundstate of V_2O_5 may be understood within an ionic picture where the O $2p$ orbitals are completely filled (O^{2-}), whereas the V $3d$ states are unoccupied (V^{5+}, $3d^0$). From the nearly octahedral surrounding of the vanadium ions, we would furthermore expect that crystal field splitting leads to t_{2g} states at the lower edge of the conduction band, while the e_g bands are located at higher energies. Due to strong deviations from octahedral coordination, however, all orbitals will finally split into singlets. Nevertheless, in the present context these rather schematic considerations just serve as a framework for further discussions.

We display in Fig. 4.2 the electronic states along selected high symmetry lines within the first Brillouin zone of the simple orthorhombic lattice, Fig. 4.3. The corresponding density of states (DOS) is given in Fig. 4.4 where we have added the dominant partial densities of states. Not shown are low lying oxygen $2s$ states.

In general, the bands shown in Fig. 4.2 reflect the anisotropies of the crystal

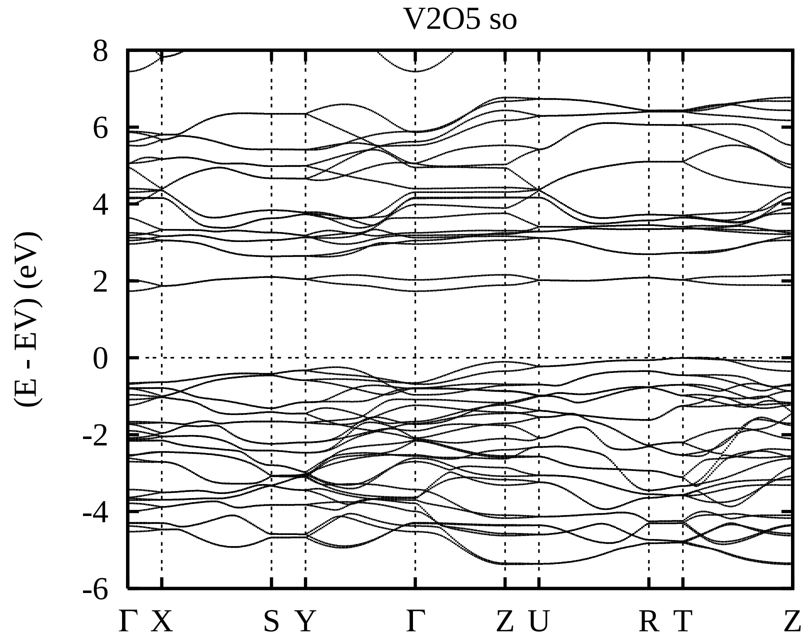

Figure 4.2: Electronic bands of V_2O_5 along selected symmetry lines within the first Brillouin zone of the simple orthorhombic lattice, Fig. 4.3. Energies are given relative to the valence band maximum E_V.

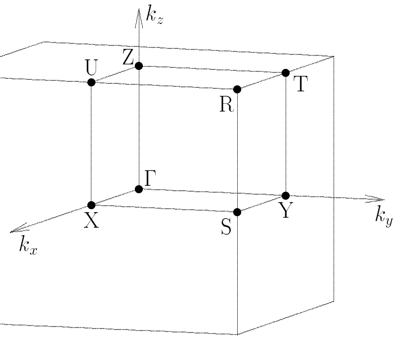

Figure 4.3: First Brillouin zone of the simple orthorhombic lattice.

structure. Obviously, there exists only a small dispersion along the direction Γ-X which is the in-plane direction perpendicular to the V-O_c chains. In contrast, we observe larger dispersions along Γ-Y, i.e. parallel to the double chains. For the direction Γ-Z the dispersion arises distinctly for different bands. Whereas the conduction bands below 4.5 eV display hardly any dispersion, the valence bands as well as the higher conduction bands have a dispersion similar to that along Γ-Y.

In Figs. 4.2 and 4.4 we identify three groups of bands. The valence band starts at ≈ -5.5 eV below the valence band maximum and consists of 30 bands which trace back mainly to O 2*p* states but have a non-negligible contribution due to the V 3*d* states. Bands are most easily counted along the line X-S where they are twofold degenerate.

Above the band gap we find, in good agreement with the experimental data of Mokerov *et al.* [185], a narrow conduction band of only 0.45 eV width which is separated from the broad higher conduction band by an additional gap of ≈ 0.35 eV.

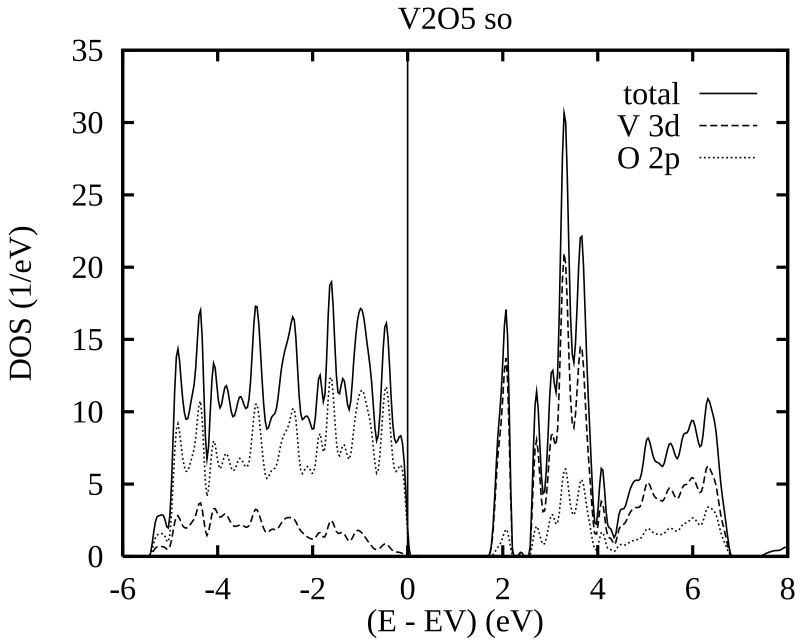

Figure 4.4: Total and partial densities of states (DOS) of V_2O_5. Here and in the following figures, partial DOS include all atoms of a species.

Whereas this so-called split-off band comprises two single bands, the high energy region consists of 18 bands. Both groups originate mainly from the vanadium $3d$ orbitals, but again we observe in Fig. 4.4 a substantial $p-d$ hybridization especially for the upper conduction band. The vanadium $4s$ derived bands are visible at the top of Fig. 4.2. All other states which are not included in Fig. 4.4 play only a negligible role in the given energy interval.

The valence and conduction band are separated by an indirect optical band gap with the band extrema located near the T and Γ point, respectively. The calculated size of the gap of ≈ 1.74 eV is smaller than the experimental value of ≈ 2.2 eV.

4.4.2 Partial DOS

Despite the strong distortions of the oxygen octahedra centered around the vanadium atoms, the dominant splitting of the V $3d$ states results from the cubic part of the crystal field. This is demonstrated in Fig. 4.5 where we display the partial V $3d$ density of states together with the contributions from the t_{2g} and e_g orbitals. In the conduction band we observe an almost complete separation of these two groups. The t_{2g} states appear almost exclusively in the energy range from ≈ 1.74 to ≈ 4.5 eV whereas the e_g states dominate at higher energies. The small but finite t_{2g} – e_g configuration mixing is a measure of the octahedral distortion which reduces the local symmetry at the V sites to monoclinic (C_{1h}). The forementioned reduced dispersion of the conduction bands below 4.5 eV is reflected by the higher density of states of the t_{2g} states. It is a consequence of the smaller overlap with the ligand $2p$ states via π bonds. The e_g states, in contrast, form σ bonds with the oxygen $2p$ states, and thus exhibit a larger overlap and hence a stronger dispersion of the bands as well as a larger bonding-antibonding splitting. The latter becomes obvious

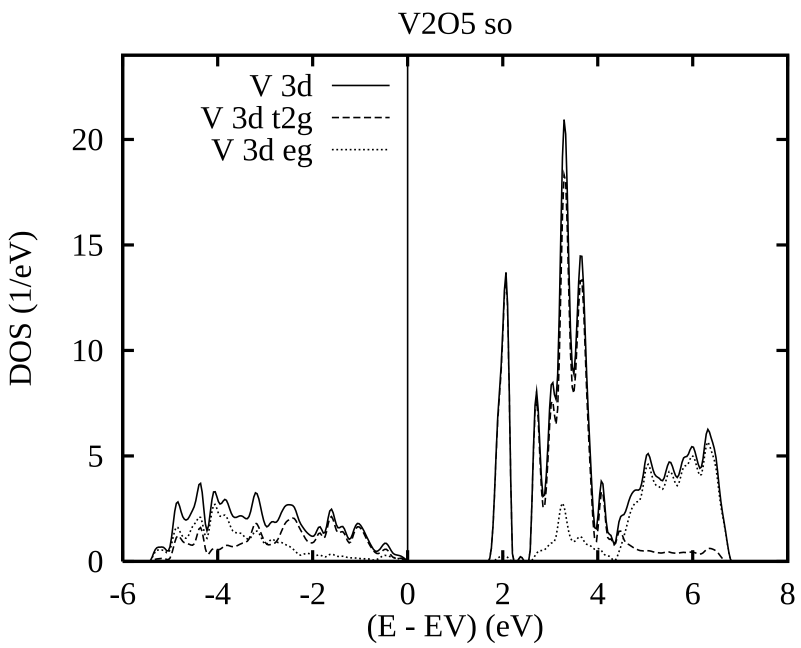

Figure 4.5: Partial V $3d$ densities of states (DOS) of V_2O_5.

from the vanadium contributions to the density of states of the valence band, where the e_g states lie below the t_{2g} states. Although the energetical separation of the t_{2g} and e_g manifolds is not as complete as for the conduction bands, we clearly identify a change of the dominating V $3d$ character at $\approx$ -3 eV.

We display in Fig. 4.6 the partial DOS of the V $3d$ t_{2g} and e_g states resolved into their symmetry components. We concentrate especially on the conduction bands. Due to the substantial hybridization of the V $3d$ with the O $2p$ states the distinct structure of the partial DOS visible in Fig. 4.6 should be reflected by the partial oxygen densities of states. This is indeed observed in Fig. 4.7 where we display the contributions from each type of oxygen separately. We have resolved the partial DOS into their three p contributions. In order to facilitate the discussion we complement the figures with Table 4.4 where we combine those particular V $3d$ and O $2p$ orbitals

	O_v	O_c	O_b
V $3d_{xy}$		$2p_y, 2p_x$	$2p_y$
V $3d_{xz}$	$2p_x$	$2p_z$	$2p_z$
V $3d_{yz}$	$2p_y$	$2p_z$	
V $3d_{x^2-y^2}$		$2p_x, 2p_y$	$2p_x$
V $3d_{3z^2-r^2}$	$2p_z$		

Table 4.4: V $3d$ – O $2p$ orbital overlaps.

which, within a molecular orbital picture, are expected to overlap.

Turning to the e_g derived bands first we mention the double peak structure of the V $3d_{x^2-y^2}$ partial DOS with peaks at 5 and $\approx$ 6.3 eV as well as the appearance

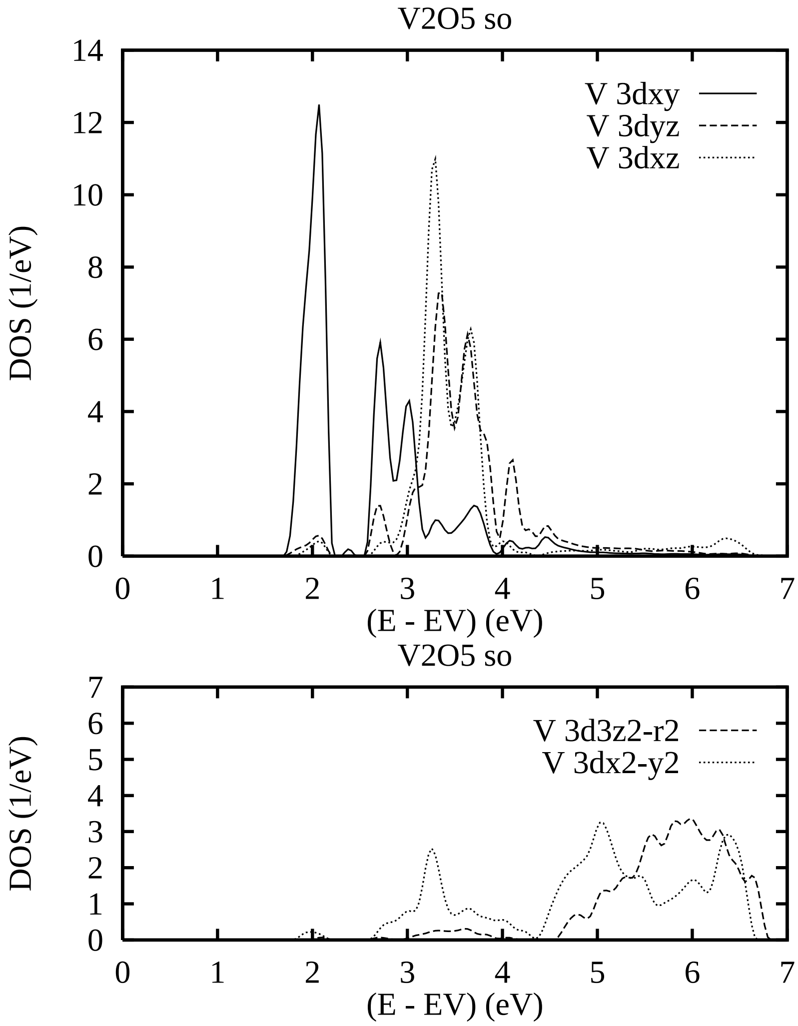

Figure 4.6: Partial V $3d$ t_{2g} and e_g densities of states (DOS) of V_2O_5.

of the dominant V $3d_{3z^2-r^2}$ contribution in the energy region above $\approx$ 5.5 eV. The shape of the V $3d_{x^2-y^2}$ peak around 5 eV resembles that of the O_c $2p_x$ and $2p_y$ DOS and thus indicates the $p-d$ hybridization. The peak at $\approx$ 6.3 eV, in contrast, is derived mainly from overlap with the O_b $2p_x$ states and, to a much lesser degree, with the $2p_x$ and $2p_y$ states of the chain oxygen atoms. Still, overlap with the O_c $2p_y$ orbitals is larger than with the $2p_x$ states. The high energy $3d_{3z^2-r^2}$ contribution, finally, originates from strong hybridization with the O_v $2p_z$ states.

For the t_{2g} states, which are responsible for the weaker π type overlap with the oxygen $2p$ states, we observe mainly three features in Fig. 4.6: (i) the striking double peak in the interval between 3 and 4 eV of both the V $3d_{xz}$ and $3d_{yz}$ partial DOS clearly indicates overlap with the O_v $2p_x$ and $2p_y$ orbitals. (ii) the double peak in the energy range from 2.5 to 3.5 eV in the V $3d_{xy}$ partial DOS results from hybridization with the O_b $2p_y$ orbitals. (iii) the peak of the split-off conduction band is due to the V $3d_{xy}$ – O_c $2p_x/2p_y$ hybridization.

Of the remaining peaks we point out the $d_{x^2-y^2}$ DOS at about 3 eV. It results from the vertical shifts of the vanadium atoms towards the vanadyl oxygen atoms,

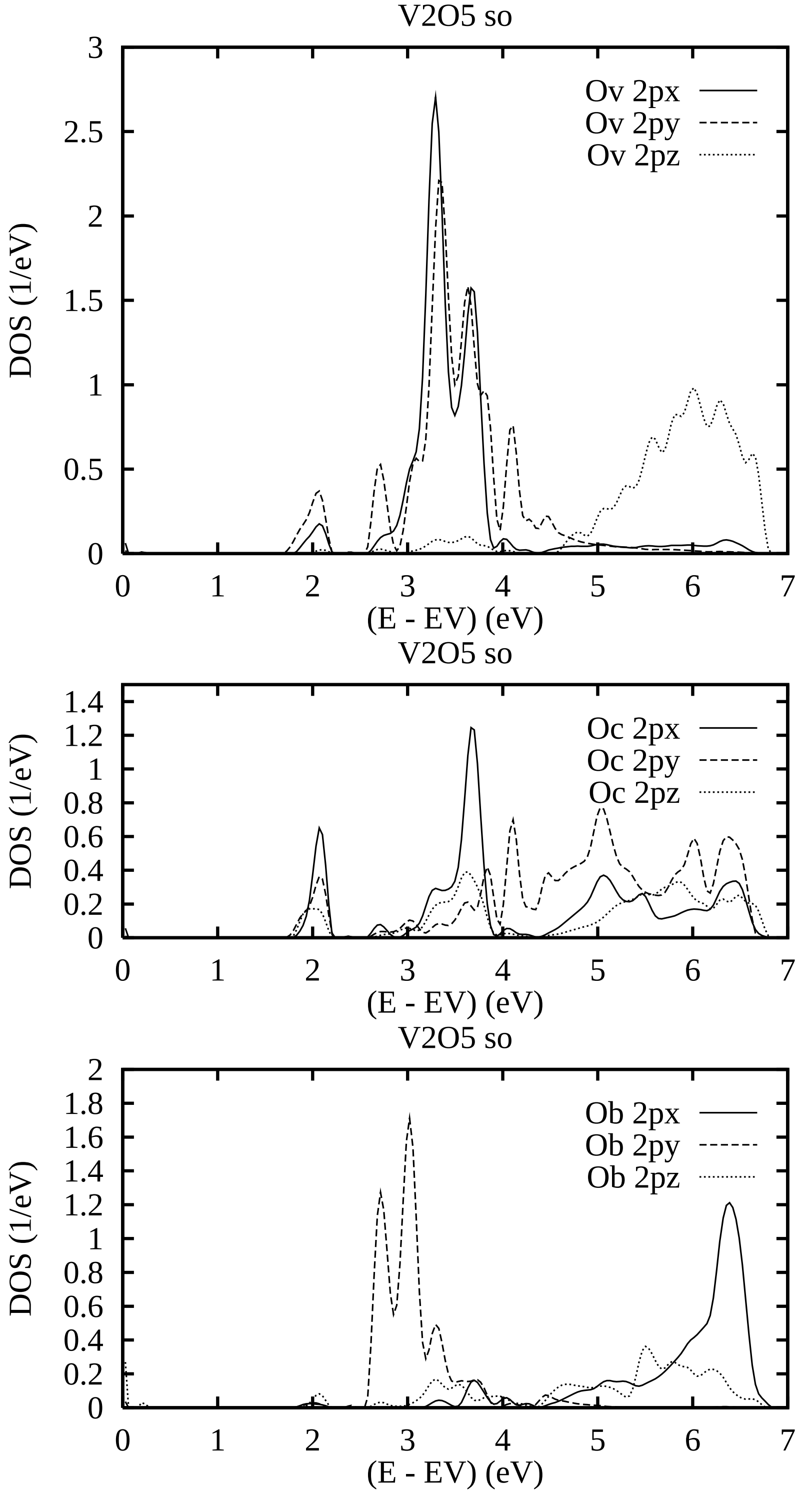

Figure 4.7: Partial O $2p$ densities of states (DOS) of V_2O_5.

which induces a partial π like overlap of this orbital with the O_v $2p_x$ and $2p_y$ orbitals.

Both the vanadium and oxygen partial DOS thus reflect the peculiarities of the crystal structure. The short V-O_b and, in particular, V-O_v bonds cause an increased bonding-antibonding splitting of the resulting orbitals, hence an upshift of the corresponding antibonding states relative to the valence band maximum. In reversed order, a similar shift of partial DOS is found in the occupied bonding vanadium-oxygen states where bands with predominantly V $3d_{3z^2-r^2}$ – O_v $2p_z$ and V $3d_{x^2-y^2}$ – O_b $2p_x$ character appear in the lower half of the valence band. Bands with dominant contributions from the chain oxygen atoms, in contrast, experience a smaller bonding-antibonding splitting due to the larger V – O_c bond length and hence their antibonding bands stay at lower energies. In particular, the relative weakly bound V $3d_{xy}$ – O_c $2p_x/2p_y$ derived bands separate from the main part of the unoccupied states and form the split-off conduction band. Our results thus confirm the work of Lambrecht *et al.* who, by using an effective tight-binding Hamiltonian and symmetry considerations, likewise attributed the split-off band to those V $3d$ and O $2p$ orbitals which have the smallest π-type overlap, hence, the smallest bonding-antibonding splitting [155].

4.4.3 Chemical bonding

We complement the previous discussion by addressing the chemical bonding of V_2O_5 via the crystal orbital overlap population, as shown in Fig. 4.8. The COOP curves

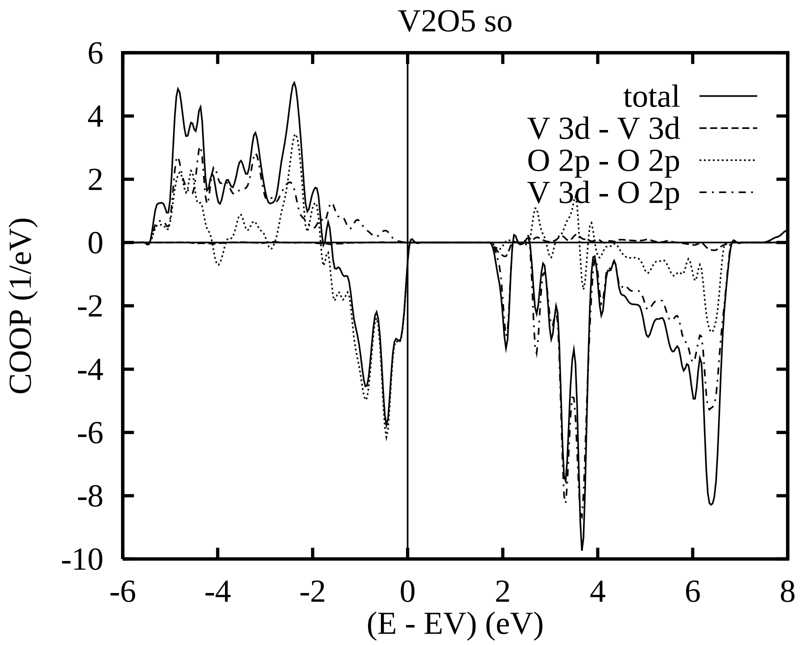

Figure 4.8: Total and partial crystal orbital overlap populations (COOP) of V_2O_5.

display the rather “canonical” behaviour, being positive (bonding) and negative (antibonding) in the low and high energy regions of a band, respectively. Whereas the V – V bonding is almost negligible, this canonical trend is visible for the oxygen-oxygen overlap for both the valence and the conduction bands separately. The COOP curve resulting from V $3d$ – O $2p$ bonding, in contrast, extends from the bottom of the valence band to the top of the conduction band, and changes sign at the valence band maximum. As a consequence, there are only bonding V $3d$ – O $2p$

contributions in the occupied part of the spectrum, whereas antibonding states are shifted to above the band gap. The vanadium-oxygen bonding is thus the decisive factor for the stability of V_2O_5. Note, however, that the low binding part of the valence band appears to be almost V – O non-bonding. This is in accordance with the results of Zhang and Henrich [275].

4.4.4 Comparison to experiment

We display in Figs. 4.9, 4.10 and 4.11 the total and partial V 3*d* and O 2*p* densities

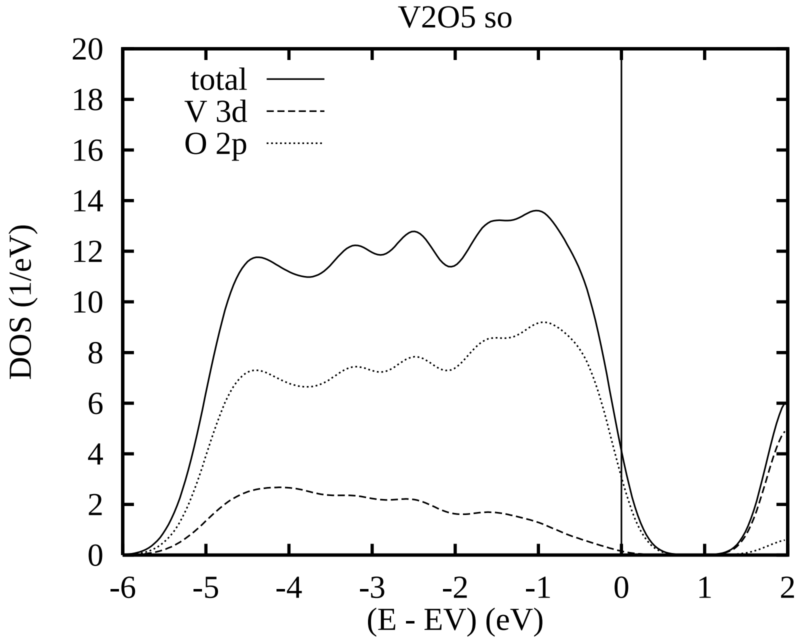

Figure 4.9: Total and partial densities of states (DOS) of V_2O_5 folded with a 0.5 eV wide Gaussian.

of states folded with a Gaussian of 0.5 eV width for the occupied and unoccupied part of the spectrum, respectively. The total DOS in Fig. 4.9 compares very well with the XPS spectra by Fiermans *et al.* [89] and the UPS spectra by Shin *et al.* as well as by Zhang and Henrich [226, 275] which show an approximately 5.5 eV wide valence band. In the curves given by Zhang and Henrich, the valence band falls into three peaks at about 1.0, 2.5, and 4.5 eV below the valence band maximum, the relative weights of which, however, are quite sensitive to photon energy [275]. This is in agreement with the spectra displayed by Shin et al., which have two peaks at 0.8 and 2.5 eV, but only a shoulder at 4.3 eV binding energy [226]. The three peak structure is less marked in the XPS curves. In contrast, these spectra resemble more the form of the V 3*d* partial DOS which is consistent with the fact that the latter states have a larger cross section in XPS [226, 272, 125].

For the unoccupied states the calculated band positions and widths are in close agreement with those deduced from the optical reflectance data by Mokerov *et al.* [185]. In Figs. 4.10 and 4.11 we have added soft-X-ray absorption spectra as measured by Goering *et al.* [101]. In order to probe the angular dependence, in these experiments the polarization vector **E** was oriented either nearly parallel ($\phi = 85°$)

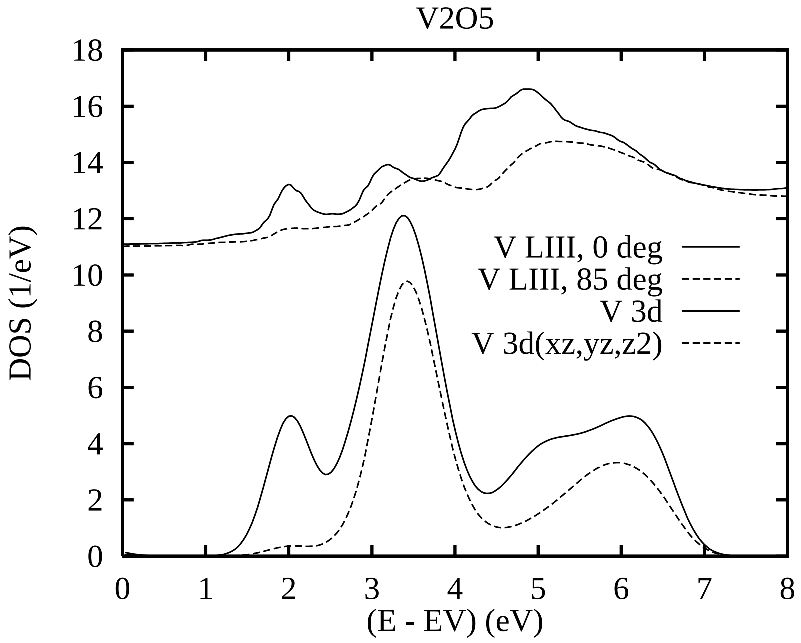

Figure 4.10: Partial V $3d$ densities of states (DOS) of V_2O_5 folded with a 0.5 eV wide Gaussian (lower set of curves) and XAS V L_{III} edge spectra (upper set of curves; from Ref. [101]).

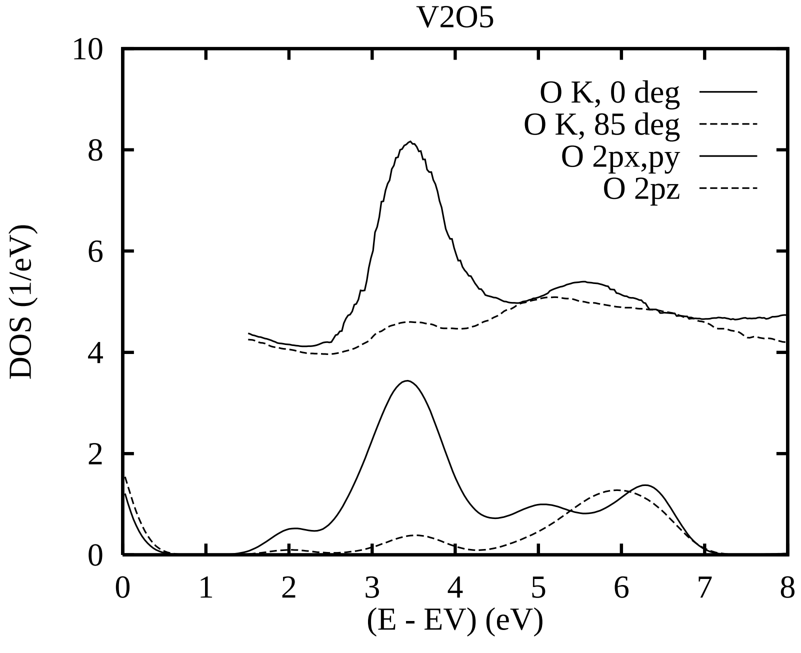

Figure 4.11: Partial O $2p$ densities of states (DOS) of V_2O_5 folded with a 0.5 eV wide Gaussian (lower set of curves) and XAS O K edge spectra (upper set of curves; from Ref. [101]).

or else perpendicular ($\phi = 0°$) to the crystals c axis which is perpendicular to the (ab) planes. In the former case, dipole selection rules allow for transitions from V $2p$ to the V $3d_{xz}$, $3d_{yz}$, $3d_{3z^2-r^2}$ states and from O $1s$ to the O $2p_z$ state. In contrast, for **E** perpendicular to the c axis transitions to all five V $3d$ as well as to the O $2p_x$

and $2p_y$ states may occur. We have added the partial DOS of the corresponding final states in Figs. 4.10 and 4.11. The agreement between experiment and theory is striking. This holds not only for the positions of the peaks but also for their angular dependence. We point especially to the suppression, on increase of the angle ϕ, of the peak due to the split-off conduction band in Fig. 4.10 as well as of the O $2p$ peak at 3.4 eV in Fig. 4.11 which is a consequence of the V $3d_{xy}$ – O $2p_x/2p_y$ character of this band. Even smaller details as, for instance, the double peak structure in the V $3d$ and O $2p_x/2p_y$ DOS above ≈ 4 eV ($\phi = 0°$ spectra) and its reduction to a single peak in the spectra for $\phi = 85°$ are described correctly.

4.4.5 Role of crystalline distortions

In this section we address the question of why vanadium pentoxide reveals the peculiar quasi-twodimensional crystal structure as compared to the neighbouring $3d^0$ compound, TiO_2, which is a semiconductor with an optical band gap of 3.05 eV and crystallizes in the more regular rutile structure with only one type of oxygen atoms and two different Ti – O bond lengths [79]. For this reason we investigate various hypothetical crystal structures for V_2O_5 resulting from an increase of the local symmetry.

From the discussion of the crystal structure given in Sec. 4.2 one might conclude that in the fictitious reference structure both the vertical movements of the vanadium and vanadyl oxygen atoms as well as the lateral displacement of the vanadium and chain oxygen atoms parallel to the x axis should be eliminated. The atoms would then form perfect (ab) planes with their z values being either zero or 0.5. Within the planes, the zigzag of the double chains were eliminated and the x components of the vanadium, vanadyl and chain oxygen atoms would take the values $x(O_b) \pm 1/6$. The crystal structure parameters for the resulting idealized positions of the atoms are listed in Table 4.5. However, the so constructed idealized crystal structure is

Atom	Wyckoff positions	parameters		
		x	y	z
V	(4f)	0.08333	0.25	0.0
O_v	(4f)	0.08333	0.25	0.5
O_c	(4f)	-0.08333	0.25	0.0
O_b	(2a)	0.25	0.25	0.0

Table 4.5: Crystal structure parameters of hypothetically idealized V_2O_5.

based on a simultaneous reduction of both types of displacements and hence does not allow to unambiguously attribute changes of the electronic structure to one of the two modes. For this reason, we proceed in two steps where we either eliminate the vertical or the lateral displacement. Still, in both cases the resulting crystal structures are artificial. The calculations are performed in complete analogy to those for the "real" structure as described in Sec. 4.3. The only difference is that, due to the changes in the atomic positions, different empty sphere positions and sphere radii for all atomic spheres have to be used [82].

Out-of-plane displacements

First, we turn to the vertical shifts and set the z components of all atoms either to zero or 0.5. Note, that this actually changes the lattice from simple to base-centered orthorhombic. However, in order to facilitate the subsequent discussion we will stay with the notions of the simple orthorhombic lattice.

As is seen in Fig. 4.12, the artificial idealization of the z components leads to

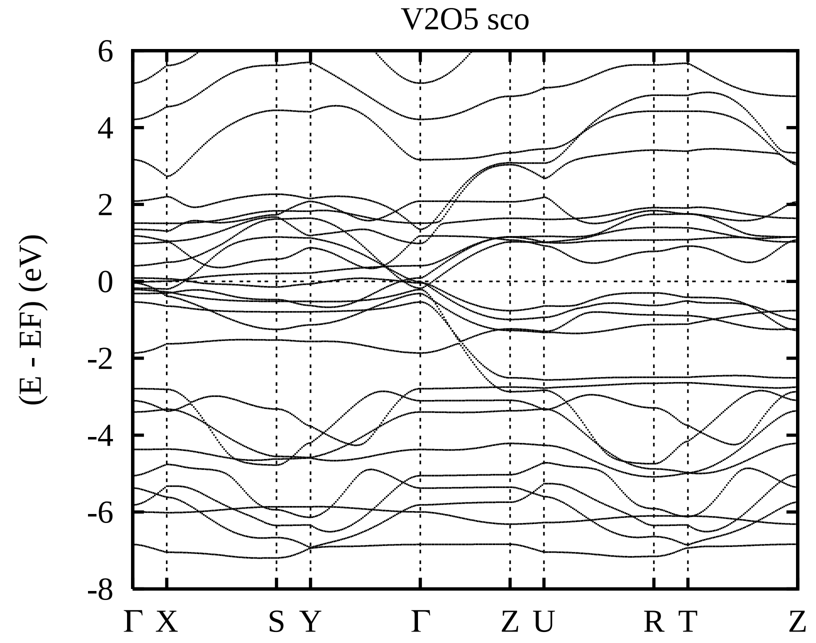

Figure 4.12: Electronic bands of hypothetical V_2O_5 with idealized z components along selected symmetry lines.

a metallic band structure. However, as analysis of the band characters reveals, we are actually dealing with a semimetal where the former valence and conduction bands just share a common energy range of about 0.3 eV width without experiencing additional hybridizations. The partial DOS as shown in Figs. 4.13 and 4.14 can be understood in the light of the discussion of Sec. 4.4.2. We observe the strong V d_{xz}/d_{yz} dominated peaks at $\approx$ 1 and 1.5 eV as well as the V d_{xy} contributions at $\approx$ 0.7 and 1.7 eV. The accompanying oxygen $2p$ partial DOS follow the schematics of the orbital overlaps listed in Table 4.4.

As compared to the partial DOS of "real" V_2O_5 shown in Figs. 4.6 and 4.7 we observe a striking broadening of the V d_{xz}, d_{yz} and $d_{3z^2-r^2}$ derived bands. This causes the enhanced dispersion along the line Γ-Z in the energy range from -3 to 3.5 eV and results from the assumption of equal V – O_v bond lengths. The considerable downshift of these states results from the increase of the shorter of the V – O_v distances. This reduces the overlap between the V d_{xz}/d_{yz} and the O_v $2p_x/2p_y$ orbitals and, hence, the bonding-antibonding splitting. Both the broadening and the downshift cause the finite density of states at E_F. Substantial shifts are also

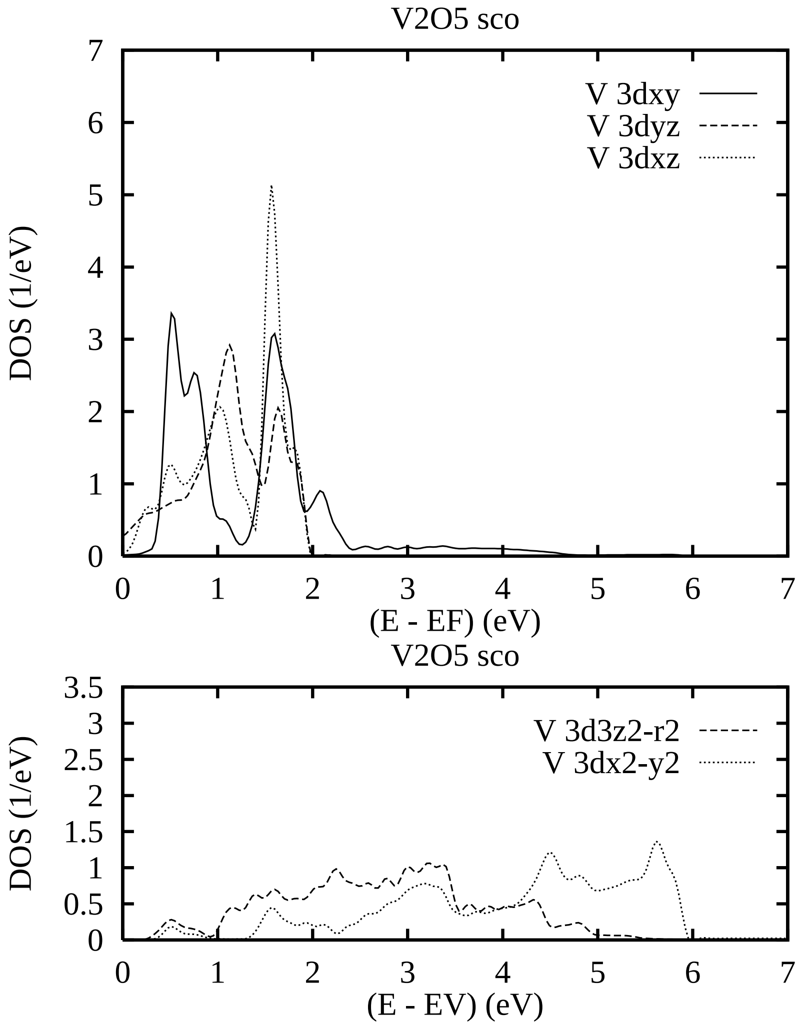

Figure 4.13: Partial V $3d$ t_{2g} and e_g densities of states (DOS) of hypothetical V_2O_5 with idealized z components.

observed below the Fermi energy where the O_v $2p$ states are destabilized and the corresponding occupied bandwith is reduced from 5.5 to 3 eV. Finally, the downshift of the unoccupied V d_{xy} states can be attributed to the decreasing overlap of the V $3d$ states with the O_v $2p_x/2p_y$ orbitals which contribute to the split-off conduction band in Fig. 4.7.

In-plane displacements

The situation is different when we adjust the in-plane projections of the atomic positions while keeping the observed z components. According to the band structure displayed in Fig. 4.15, this hypothetical V_2O_5 is at the borderline between a semiconductor and a semimetal. However, the increase in dispersion now is along the lines Γ-X and Γ-Y. According to the partial DOS shown in Figs. 4.16 and 4.17 the most striking changes are due to the V d_{xy} states. The distance between the peaks at 2 and 3 eV in Fig. 4.7 has shrunk due to the lateral shifts of the atoms which make the V – O_c and V – O_b more alike and thereby lead to a comparable

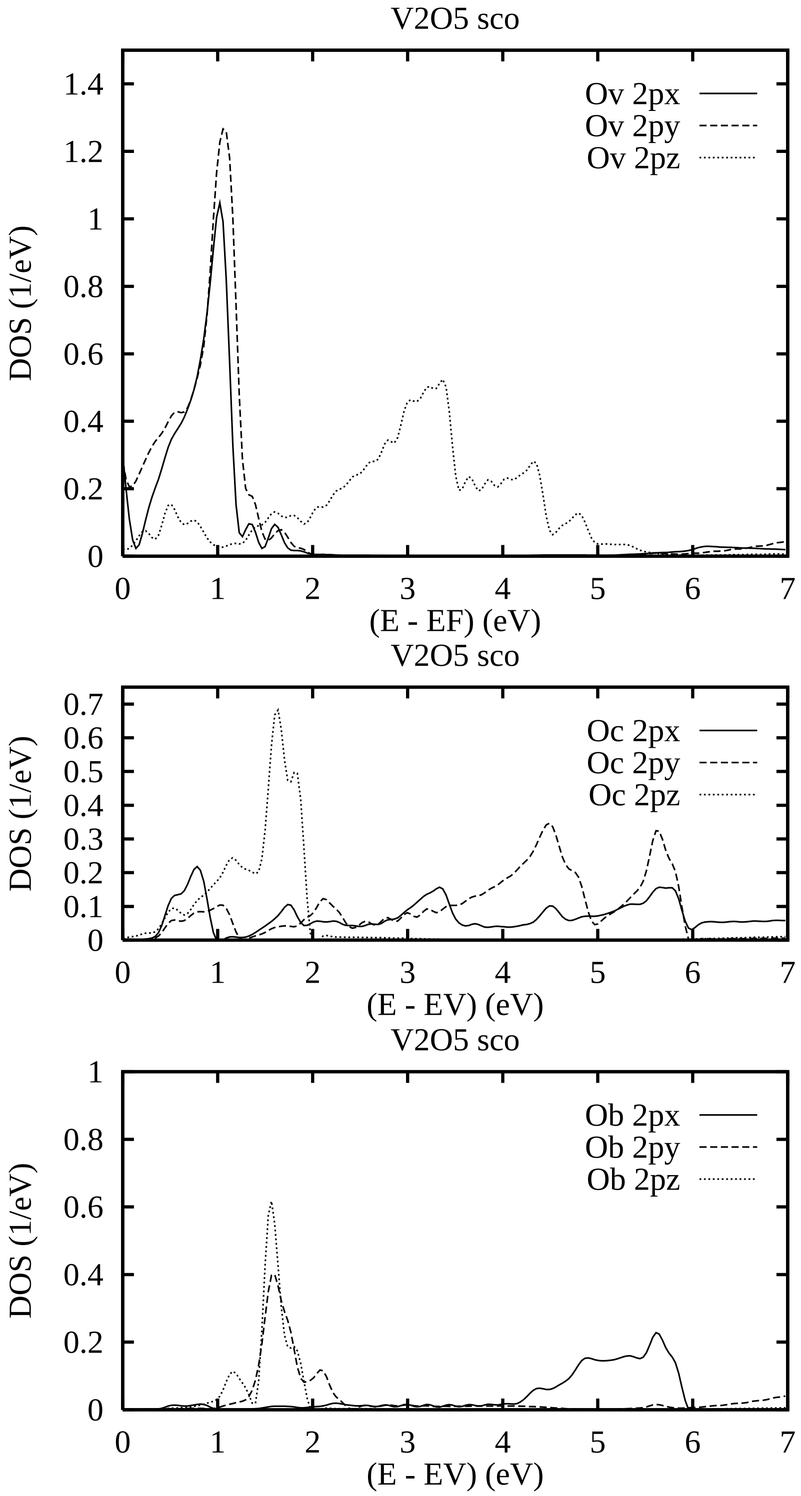

Figure 4.14: Partial O $2p$ densities of states (DOS) of hypothetical V_2O_5 with idealized z components.

bonding-antibonding splitting. At the same time, due to the alignment of the V – O_c double chains, the in-plane dispersion increases substantially. Although the split-off conduction band has a larger width, it is still separated from the higher

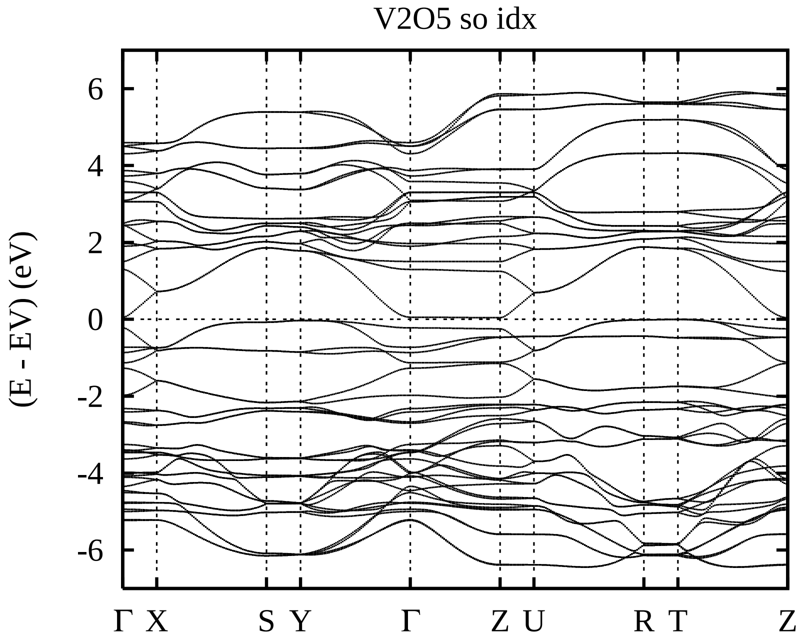

Figure 4.15: Electronic bands of hypothetical V_2O_5 with idealized x components along selected symmetry lines.

bands.

Summarizing, the crystal structure of V_2O_5 can be described in terms of two different atomic displacements which cause distinct changes of the electronic structure. (i) starting from the idealized reference crystal structure given in Table 4.5, the vertical displacement of the vanadium and vanadyl oxygen atoms increases the overlap between the V d_{xz}/d_{yz} and O_v $2p_x/2p_y$ orbitals and, hence, the corresponding bonding-antibonding splitting. As a consequence, the antibonding V d_{xz}/d_{yz} derived states move up in energy and increase the optical band gap. The bonding O_v $2p_x/2p_y$ dominated states, in contrast, are stabilized, thus lowering the total energy. The latter effect could be explained by the strong V $3d$ – O $2p$ hybridization which has been reported for several vanadium oxides [101, 191, 278]. (ii) the distortions resulting from the lateral displacement of the vanadium and chain oxygen atoms lead to a drastic decrease of the width of the V $3d_{xy}$ derived split-off conduction band and contribute to the separation of occupied and unoccupied states.

Taken together, both the vertical and lateral displacements, while causing substantial deformations of the octahedra, contribute to the optical band gap and thus lead to the semiconducting ground state of V_2O_5. This is different for TiO_2 where the energy separation of the atomic Ti $3d$ and O $2p$ states is larger from the outset and, hence, leaves enough room for a complete separation between the resulting bonding and antibonding states without the need for additional stabilizing mechanisms.

4.5 Conclusion

In the present chapter first-principles ASW calculations were used to describe the electronic properties of vanadium pentoxide. Strong $p-d$ hybridization leads to the

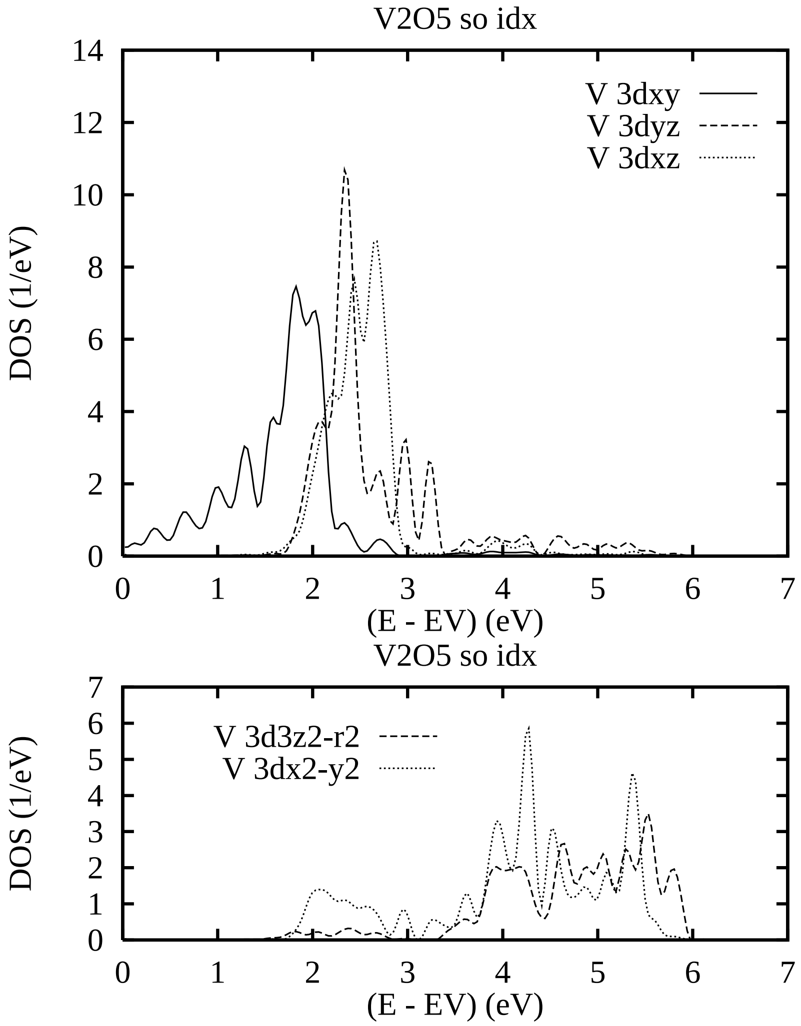

Figure 4.16: Partial V $3d$ t_{2g} and e_g densities of states (DOS) of hypothetical V_2O_5 with idealized x components.

formation of a O $2p$ dominated bonding valence band whereas the conduction band comprises the antibonding states which mainly derive from crystal field split V $3d$ t_{2g} and, at higher energies, e_g orbitals.

The deviations of the VO_6 octahedra from cubic symmetry cause additional splittings and result in the appearence of a narrow split-off conduction band right above the optical band gap. This originates from weakly bound V $3d_{xy}$ and O_c $2p_x$ orbitals and is responsible for the observed low carrier mobility.

In order to access the role of the striking deformations of the VO_6 octahedra additional calculations were performed where either the vertical or the lateral displacements of the vanadium atoms were removed. From these simulations we find that the vertical mode predominantly increases the bonding-antibonding splitting of the V $3d_{xz}/3d_{yz}$ derived bands which stabilizes the compound and increases the optical gap. The lateral mode, in contrast, suppresses the dispersion of the split-off V $3d_{xy}$ conduction band and thus also leads to an increase of the gap. The combination of both modes, finally, enhances the chemical stability and ensures the semiconducting ground state.

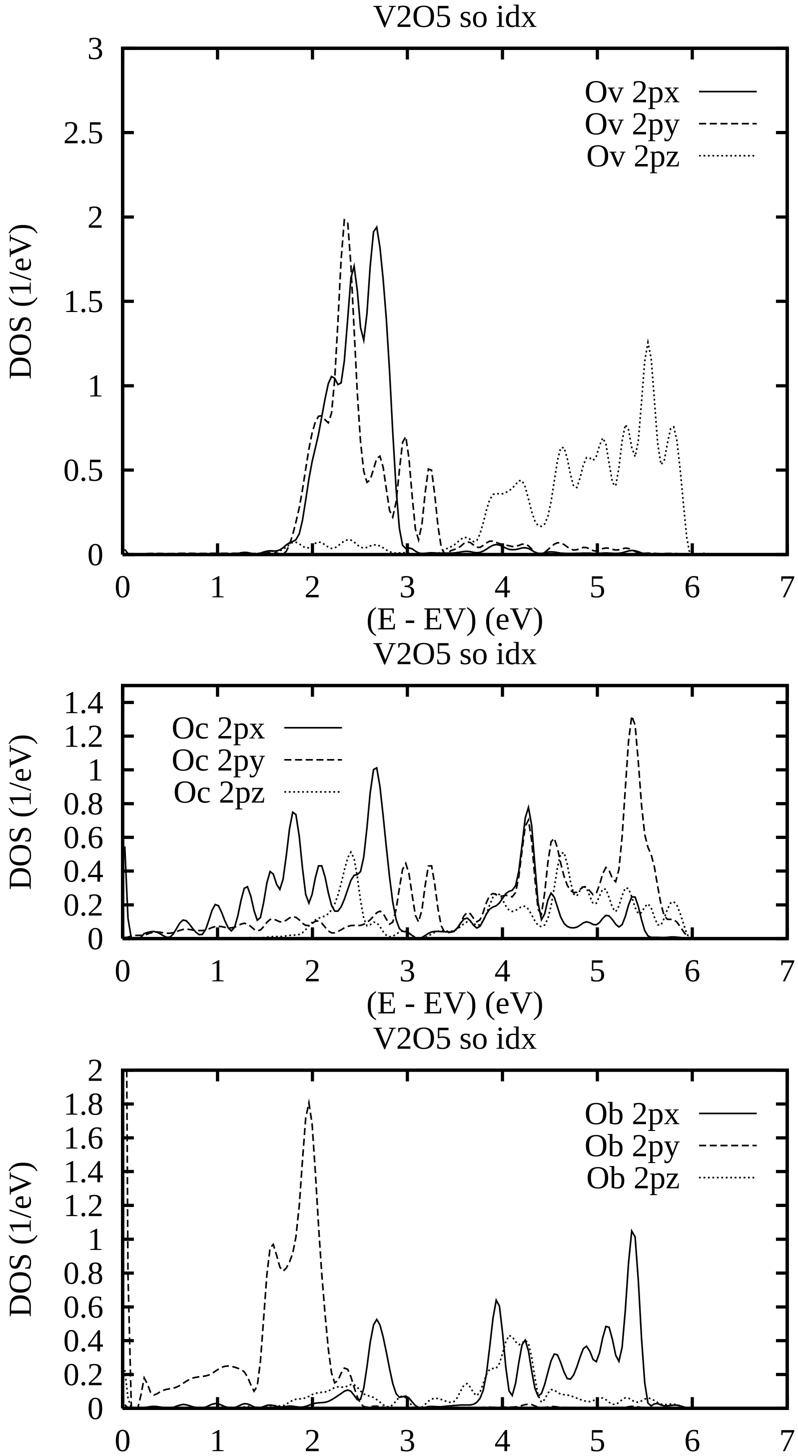

Figure 4.17: Partial O $2p$ densities of states (DOS) of hypothetical V_2O_5 with idealized x components.

Chapter 5

MoO_2: I. The rutile reference

5.1 Motivation

The rutile-related transition metal dioxides attract a lot of attention due to a large variety of physical phenomena arising from the hybridization of the narrow d states with the ligand p orbitals [216]. This diversity shows up mainly in the $3d$ series which comprises e.g. the large-gap semiconductor TiO_2, the half-metallic ferromagnet CrO_2, and the antiferromagnetic semiconductor MnO_2 [178, 79] whereas most of the $4d$ and $5d$ compounds are neither semiconducting nor magnetic. However, there exist several members in each group which display small but characteristic deviations from the rutile structure [216, 178, 35].

Among the transition metal dioxides the d^1 members VO_2 and NbO_2 are exceptional since they both undergo a metal-insulator transition which is accompanied by a structural transition from the high-temperature rutile phase to a low-temperature low-symmetry phase. The change in resistivity especially for vanadium dioxide extends over several orders of magnitude and, occuring at 340K, led to expect a broad range of applications [187]. Nevertheless, the origin of the metal-insulator transition is still a matter of controversy. Several models have been proposed emphasizing either electron-phonon coupling or strong electron-electron correlations as the driving force. As a consequence, a complete and accepted picture of the physics of the rutile-related transition metal oxides has not yet evolved.

As a matter of fact, the deviations from the rutile structure, if present, are of the same kind for all the early transition metal dioxides. To be specific, MoO_2, WO_2, TcO_2, α-ReO_2, and low-temperature VO_2 crystallize in a structure with monoclinic space group and exhibiting the same characteristics as compared to the rutile structure, namely, a pairing of the metal atoms parallel to the rutile c axis and a lateral displacement [216]. In contrast, insulating NbO_2, while displaying the same local shifts of the metal atoms, crystallizes in a body-centered lattice with 32 formula units per cell [170, 225, 210, 60]. Thus, to get an idea about the general tendency of the rutile-type transition metal dioxides to crystallize in a low-symmetry structure as well as about the impact of the structural properties on the metal-insulator transition it is worthwhile to look at compounds neighbouring VO_2 which display the same distortion but no such transition. A possible candidate is MoO_2 which is metallic and shows neither a metal-insulator nor a structural phase transition [216].

The electronic structure of MoO_2 has been probed by optical and photoemission experiments as well as by de Haas-van Alphen measurements. According to the optical reflectivity measurements the lowest unfilled Mo $4d$ levels lie about 2.5 eV above the top of the O $2p$ bands [59, 68]. UPS and XPS experiments revealed an ≈ 9 eV wide occupied band falling into the low binding, 3 eV wide Mo $4d$ bands and a 6 eV wide group of O $2p$ bands at higher binding energies [25, 261, 98]. The Mo $4d$ bands further split into a doublet with peaks at ≈ 1.5 and 0.5 eV below the Fermi energy [25, 98]. The unoccupied O $2p$ states, in contrast, as measured by XAS experiments, fall into three peaks at ≈ 1.4, 3.1, and 4.6 eV above the Fermi energy [190]. Finally, de Haas-van Alphen and Shubnikov-de Haas measurements revealed marked anisotropies of the Fermi surface [253, 254, 252, 239, 139].

Theoretical investigations so far comprise phenomenological molecular-orbital schemes as well as tight-binding and cluster calculations [216, 108, 152, 218, 219, 273, 49] whereas state-of-the-art band calculations for crystalline MoO_2 are still missing. In order to fill this gap we initiated the present study. We aim, in particular, at a comprehensive analysis of the electronic structure in terms of few relevant orbitals. Nevertheless, for an investigation of the mechanisms forcing some of the dioxides into distorted variants of the rutile structure it is not sufficient to stay with only the experimentally determined monoclinic structure. For this reason we extended our study to the calculation of the electronic structure of MoO_2 in an assumed rutile crystal structure. This serves two purposes: (i) The results for hypothetical rutile MoO_2 establish a reference to which the electronic structure of "real" MoO_2 could be compared. From the differences between both calculations important information concerning the stability of the monoclinic structure can be deduced. (ii) The investigation of the rutile system in itself may allow to identify those mechanisms which would destabilize the rutile phase and make MoO_2 monoclinic. To this end, we also discuss the Fermi surface as calculated with the hypothetical rutile structure. Finally, we relate the electronic properties to the chemical bonding by evaluating the crystal orbital overlap population (COOP).

Leaving the investigation of the "real" monoclinic phase to the following chapter we turn in the present chapter to the rutile reference system. The chapter is organized as follows: Starting with a short description of the rutile crystal structure and its relation to the monoclinic structure in Sec. 5.2, we outline the calculational method in Sec. 5.3. The results are presented in Sec. 5.4. The conclusion, Sec. 5.5, sums up the most important findings. Previous discussions of the work on MoO_2 include the Refs. [123, 124] while a more detailed description will be given soon [84, 85].

5.2 The rutile structure

The rutile structure as displayed in Fig. 5.1 is based on a simple tetragonal (st) lattice with space group $P4_2/mnm$ (D_{4h}^{14}). The metal atoms are located at the Wyckoff positions (2a): $(0,0,0)$, $(\frac{1}{2},\frac{1}{2},\frac{1}{2})$ and the oxygen atoms occupy the positions (4f): $\pm(u,u,0), \pm(\frac{1}{2}+u,\frac{1}{2}-u,\frac{1}{2})$.

The structure is best described in terms of a regular body-centered tetragonal

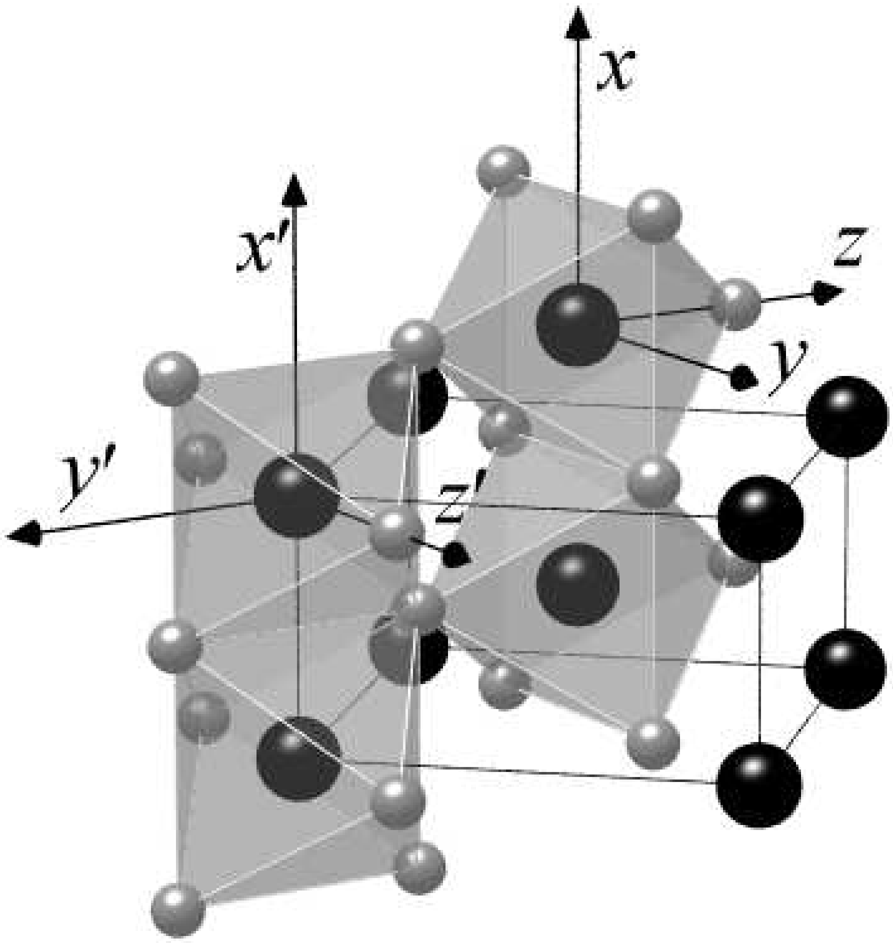

Figure 5.1: The rutile structure. Metal and ligand atoms are shaded black and gray, respectively.

(bct) lattice formed by the metal atoms where each metal is surrounded by an oxygen octahedron. However, octahedra centered at the corners and the center of the cell are rotated by 90° about the tetragonal c axis relative to each other. As a consequence, the lattice translational symmetry reduces to simple tetragonal and a unit cell with two formula units results. Octahedra which are neighboured along the rutile c axis share edges whereas the resulting octahedral chains are interlinked via corners. Each octahedron has orthorhombic symmetry although the deviations from tetragonal geometry for most compounds are relatively small and still allow for a discussion in terms of the latter. There exist two different metal-oxygen distances, namely, the apical distance which is between metal and oxygen atoms having the same z value and the equatorial distance between the metal atom and the four neighbouring ligand atoms with $z = z_{\mathrm{metal}} \pm 1/2$ [178, 79, 231].

It is useful to discuss the electronic structure of rutile-type compounds in terms of local coordinate systems centered at each metal site as indicated in Fig. 5.1. In each coordinate system the local z axis is parallel to the apical metal-ligand bond and points alternately along the [110] and [$1\bar{1}0$] direction. The local x axis is chosen to be parallel to the rutile c axis and, hence, is identical for all octahedra. In contrast, the local y axes again lie completely in the rutile basal plane and point alternately to the $[1\bar{1}0]$ and $[110]$ direction. Our choice of the local coordinate system deviates from that used by other authors by a rotation of 45° about the local z axis [231]. However, the present choice allows for a more simple analysis of the electronic structure.

With the previous choice of local coordinate systems the e_g states resulting from the cubic part of the crystal field splitting of the metal d orbitals comprise the d_{xy} and $d_{3z^2-r^2}$ orbitals whereas the t_{2g} states contain the $d_{x^2-y^2}$, d_{xz}, and d_{yz} orbitals. We display the angular parts of the d orbitals relative to the local rotated reference frame in Fig. 5.2. The $d_{x^2-y^2}$ orbitals point along the rutile c and the local y axes,

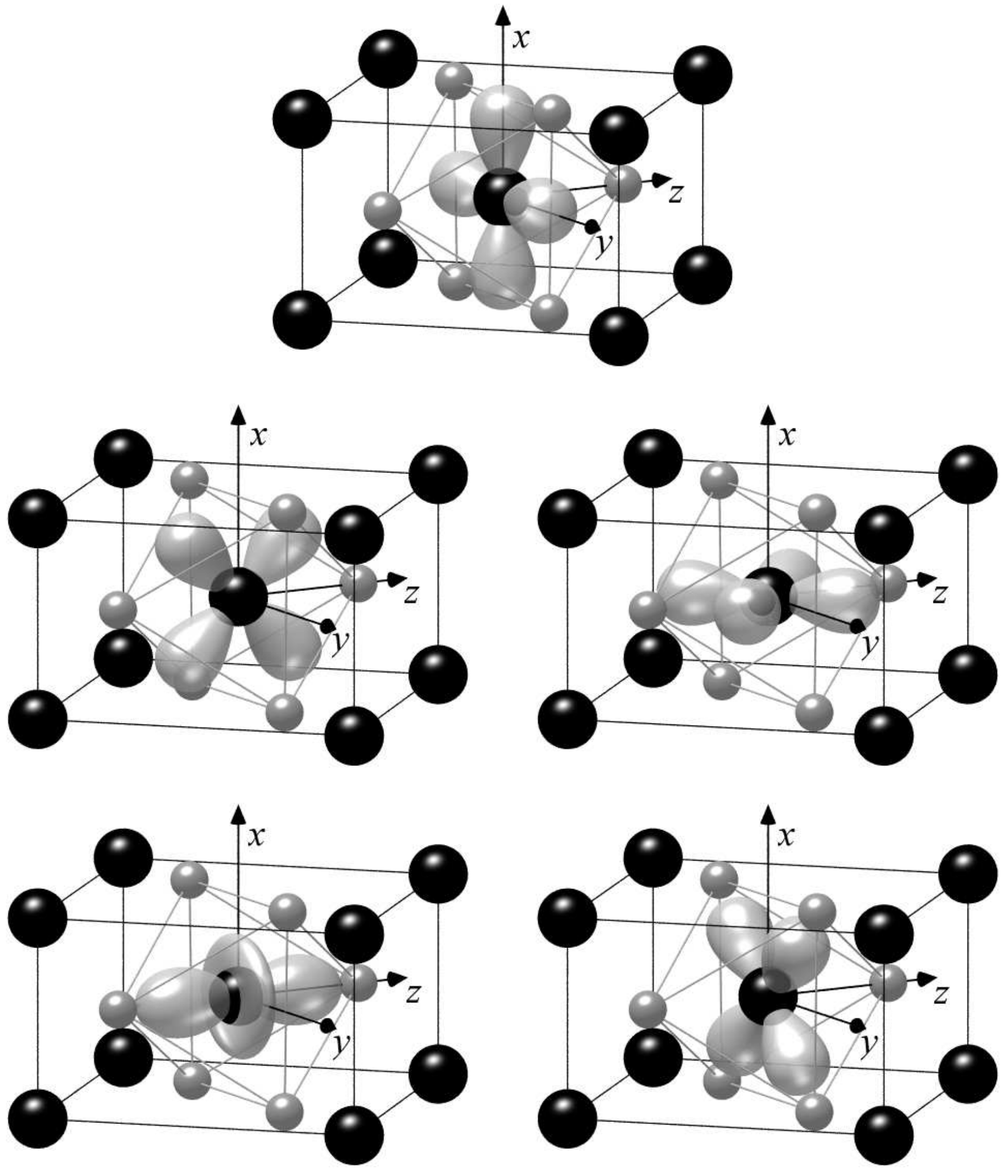

Figure 5.2: Angular parts of the d orbitals. Upper line: $d_{x^2-y^2}$, middle line: d_{xz} and d_{yz}, lower line: $d_{3z^2-r^2}$ and d_{xy}.

i.e. towards the edges of the basal plane of the octahedron. In contrast, the d_{xz} and

d_{yz} orbitals are directed towards the faces. In particular, the latter point along the $\langle 100 \rangle$ directions. As a consequence, the $d_{x^2-y^2}$ and d_{xz} orbitals mediate σ- and π-type overlap, respectively, between metal sites within the vertical octahedron chains whereas the d_{yz} orbitals at one metal site have smaller σ-type overlap with their counterparts at metal sites translated by the vectors $(a, 0, 0)$ and $(0, a, 0)$. While the overlap of both the $d_{x^2-y^2}$ and d_{yz} orbitals with orbitals of the same kind at neighbouring atoms connects atoms, which are separated by lattice vectors of the simple tetragonal lattice, coupling between metal atoms, which are located at the corner and the center of the cell, is mediated by the d_{xz} orbitals. These orbitals point to the voids between the metal atoms of the neighbouring octahedral chains where they overlap with the $d_{x^2-y^2}$ orbitals of these chains.

As mentioned before, MoO_2 actually crystallizes in a structure having a simple monoclinic lattice and space group $P2_1/c$ (C_{2h}^5) [168, 42]. Although there have been indications for the possible onset of a monoclinic-to-rutile transition at temperatures above 1100°C for $Mo_{0.975}Ti_{0.025}O_2$ [96, 250] no structural phase transition has been reported for the stoichiometric compound.

Nevertheless, since the monoclinic structure is closely related to the rutile structure we may construct a hypothetical rutile cell by properly symmetrizing the atomic positions. As a result, we arrive at lattice constants $a = 4.8562$Å and $c = 2.80545$Å which are identical to the monoclinic lattice constants b_M and $a_M/2$, respectively [42]. The rather small c/a ratio of 0.5777 is a consequence of the metal-metal bonding along the rutile c axis and is characteristic of the $4d$ and $5d$ d^2 and d^3 compounds [216]. Finally, the internal u parameter of the rutile structure, which determines the oxygen position, assumes the value 0.2847. Note that while symmetrizing the monoclinic structure we have ignored the strain inherent in this lattice. For this reason, the lattice constants and the internal u parameter of the symmetrized rutile cell still contain a small uncertainty.

5.3 Calculational details

In the same manner as the crystal structures considered in the previous chapters the rutile structure requires insertion of empty spheres. Again we employ the sphere geometry optimization (SGO) alpgorithm for fixing optimal empty sphere positions as well as radii for all spheres. By inserting 8 empty spheres into the hypothetical rutile unit cell of MoO_2 we kept the linear overlap of any pair of physical spheres below 22% and the overlap of any pair of physical and empty spheres below 25%. The positions of the empty spheres are listed in Table 5.1. In addition to the empty

Atom	Wyckoff positions	parameter
		x
E_1	(4c)	
E_2	(4g)	0.3497

Table 5.1: Empty sphere positions for hypothetical rutile MoO_2.

sphere positions the SGO algorithm proposed atomic sphere radii for all spheres, which we list in Table 5.2 together with the orbitals, which are used as the basis

Atom	Radius/a_B	Orbitals			
Mo	2.330	$5s$	$5p$	$4d$	$(4f)$
O	2.138	$2s$	$2p$	$(3d)$	
E_1	1.741	$1s$	$2p$	$(3d)$	
E_2	1.740	$1s$	$2p$	$(3d)$	

Table 5.2: Atomic sphere radii and basis set orbitals for hypothetical rutile MoO_2.

set for the present calculations. Finally, the Brillouin zone sampling was done using an increasing number of **k** points, which range from 18, 40, 126, 288, 550 to 1800 points within the irreducible wedge.

5.4 Results and Discussion

5.4.1 Electronic structure and partial DOS

Within a molecular-orbital picture we expect the oxygen $2p$ levels to be completely filled whereas the Mo $4d$ levels comprise two electrons. Due to the orthorhombic rather than cubic symmetry of the octahedra surrounding the metal sites the low lying t_{2g} and the high lying e_g manifold are further split into singlets. Yet, since the deviations from local tetragonal symmetry are small we still expect the crystal field splitting to be dominated by its tetragonal part.

We display in Fig. 5.3 the electronic states along selected high symmetry lines within the first Brillouin zone of the simple tetragonal lattice, Fig. 5.4. The corresponding density of states (DOS) is given in Fig. 5.5 where we have added the dominant partial densities of states. The total density of states at the Fermi energy, $N(E_F)$, amounts to 1.3 states/f.u./eV. Not shown are low lying oxygen $2s$ states.

In Figs. 5.3 and 5.5 we identify three groups of bands. In the energy range from -9.2 to -3.6 eV we observe 12 bands which trace back mainly to O $2p$ states but have a non-negligible contribution due to the Mo $4d$ states. Bands are most easily counted along the direction X-R where they are twofold degenerate. The upper two groups which extend from -2 to 2.7 and from 3.1 to 6.8 eV contain six and four bands, respectively and originate mainly from Mo $4d$ states. Yet, $p-d$ hybridization causes additional O $2p$ contributions in this energy range.

Crystal field splitting expected from the fact that the metal atoms are located at the centers of distorted MoO_6 octahedra is observed in the partial Mo $4d$ DOS shown in Fig. 5.6. There we have included only the single molybdenum atom at $(0, 0, 0)$ and used the local rotated reference frame. Fig. 5.6 clearly reveals the almost perfect energetical separation of the $4d$ t_{2g} and e_g groups of bands. The former states appear almost exclusively in the energy range from -2 to 2.7 eV whereas the e_g

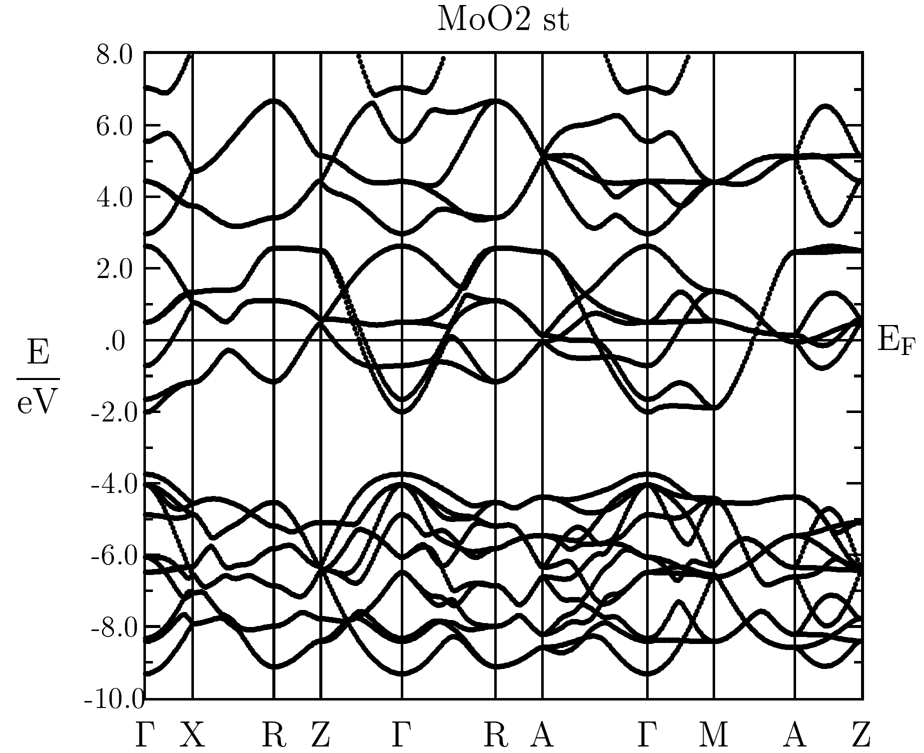

Figure 5.3: Electronic bands of rutile MoO_2 along selected symmetry lines within the first Brillouin zone of the simple tetragonal lattice, Fig. 5.4.

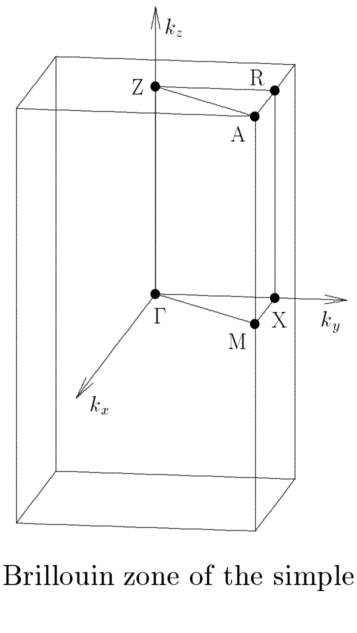

Figure 5.4: First Brillouin zone of the simple tetragonal lattice.

states dominate the bands between 3.1 and 6.8 eV. The small but finite t_{2g} – e_g configuration mixing is a measure of octahedral distortions. Contributions of the Mo 4d states to the oxygen bands below -3.6 eV are slightly larger for the e_g states which, forming σ bonds, experience a larger overlap with the O 2p states. For the same reason, the bonding-antibonding splitting is larger for the e_g states as compared to the t_{2g} states, which give rise to π bonds.

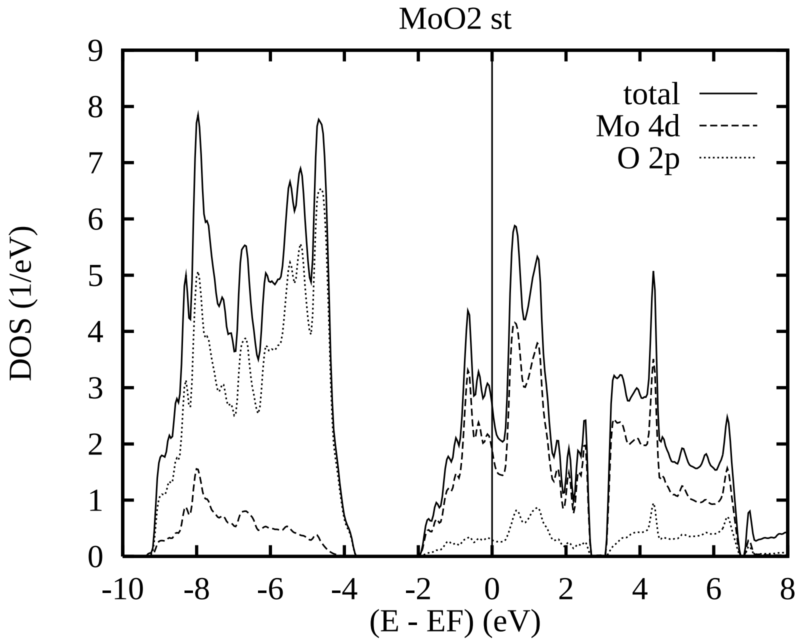

Figure 5.5: Total and partial densities of states (DOS) of rutile MoO_2 per unit cell.

In Fig. 5.6 the differences between the single symmetry components of the t_{2g} and e_g orbitals, respectively, reflect the orthorhombic site symmetry. Yet, especially the d_{xz} and d_{yz} partial DOS still bear a certain similarity this being a measure of the remaining tetragonal component of the crystal field. As the most striking feature we mention the different behaviour of the $d_{x^2-y^2}$ partial DOS which exhibits strong tendency towards splitting into two peaks at -1 eV and above 2 eV. In contrast, the depletion in between contributes substantially to the DOS minimum just above the Fermi energy visible in Fig. 5.5.

Although our results grew out of calculations for the hypothetical rutile structure the gross features already compare quite well to the molecular-orbital pictures sketched by Rogers *et al.* as well as by Goodenough [216, 108]. In these phenomenological schemes the socalled $d_{\|}$ band, which is identical to our $d_{x^2-y^2}$-derived band, experiences a strong bonding-antibonding splitting due to metal-metal pairing along the tetragonal c axis. Since the pairing is suppressed in the high-symmetry rutile structure we observe only a reduced bonding-antibonding splitting of this band. In contrast, the d_{xz} and d_{yz} bands, which Goodenough designates as the π^* bands, are found between the two $d_{\|}$ peaks without any further splittings.

5.4.2 Chemical bonding

We address chemical bonding via the crystal orbital overlap population as shown in Fig. 5.7. The COOP curves display the rather "canonical" behaviour being positive (bonding) and negative (antibonding) in the low and high energy regions of a band. In case of the oxygen-oxygen overlap this is nicely visible for both the oxygen and molybdenum dominated bands separately the absolute values being higher in the former. Below $\approx$ -6.5 eV we find bonding O-O bands whereas the antibonding

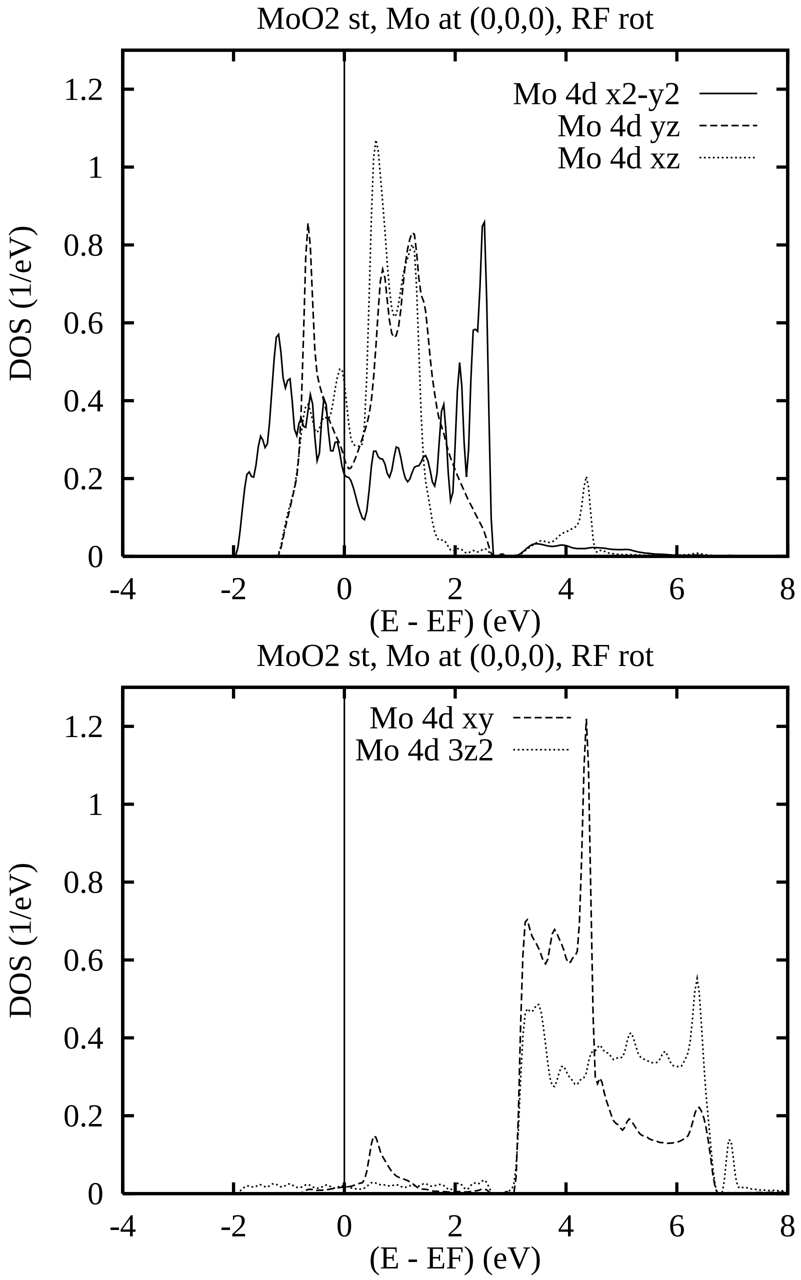

Figure 5.6: Partial Mo $4d$ t_{2g} and e_g densities of states (DOS) of rutile MoO_2. Selection of orbitals is relative to the local rotated reference frame.

bands appear in the energy range between ≈ -6.5 and -3.5 eV. As a consequence, the net contribution of the occupied oxygen-oxygen bonds to the chemical stability is rather small. The same holds for the almost negligible metal-metal bonding. The dominating contribution to the chemical stability results from the overlap of Mo $4d$ and O $2p$ orbitals. The corresponding COOP curve is positive below -3.5 eV and negative only in the Mo $4d$ derived bands. Hence, the metal-ligand bonding is the main responsible for the chemical stability of MoO_2.

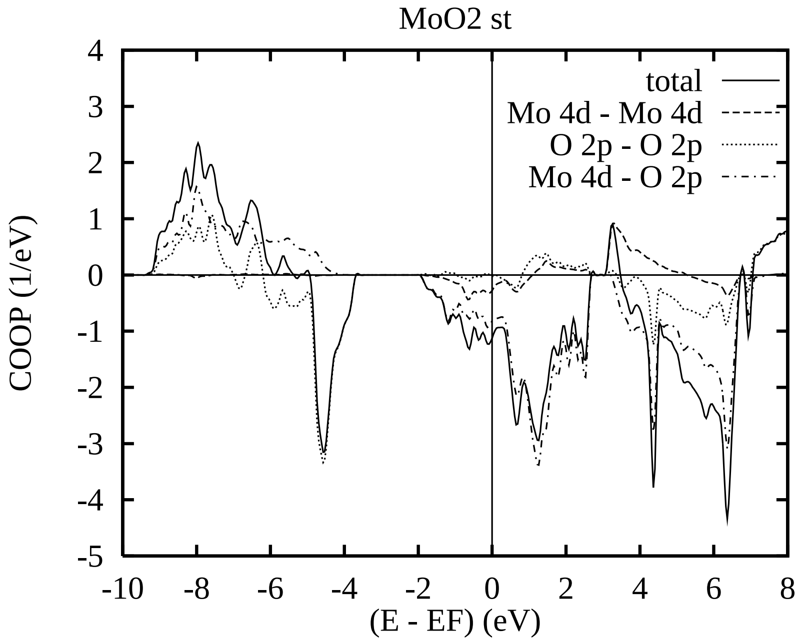

Figure 5.7: Total and partial crystal orbital overlap populations (COOP) of rutile MoO_2.

5.4.3 Fermi surface

Still, more conclusive arguments for the destabilization of the rutile structure are needed. Of course, the partial DOS of the Mo $4d_{x^2-y^2}$ bands with its double peak structure and the depletion in between gives a first hint to the observed Mo-Mo pairing in the monoclinic structure and the complete bonding-antibonding splitting of this band as sketched by Rogers *et al.* and Goodenough [216, 108]. Hence, we would expect that in a calculation for the "real" structure the bonding-antibonding splitting is further increased and the DOS in between, at best, vanishes completely. Nevertheless, we still seek for an explanation of the mechanism driving this scenario.

To this end we investigate the Fermi surface calculated within the hypothetical rutile structure. Cuts through the Fermi surface parallel to the $\{100\}$ and $\{110\}$ planes are shown in Figs. 5.8, 5.9, and 5.10. They contain the Γ-X-Z-R, Γ-M-Z-A, and X-M-R-A plane, respectively which are the vertical borders of the irreducible wedge of the first Brillouin zone, Fig. 5.4. The interpretation of these figures is greatly facilitated by combining them with the band structure shown in Fig. 5.3. From this, we recognize electron- and hole-like regions near the Γ and Z point, respectively. Along the line Z-A as given in Fig. 5.9 several electron-like pockets interpenetrate. Of course, the most striking feature are the two flat Fermi surface sheets in Fig. 5.9 half way between the lines Γ-M and Z-A which hardly depend on the lateral position of the **k** vector. These flat sheets show up likewise in Figs. 5.8 and 5.10 where, however, they extend only over part of the respective horizontal line. Taking the information from Figs. 5.8 to 5.10 together we conclude that the Fermi surface forms two almost perfect $\{001\}$ planes at height $\frac{\pi}{2c}$ which have rather small interruptions above the X points. These planes give rise to Fermi surface nesting with the z component of the wave vector being $q_z = \frac{\pi}{c}$.

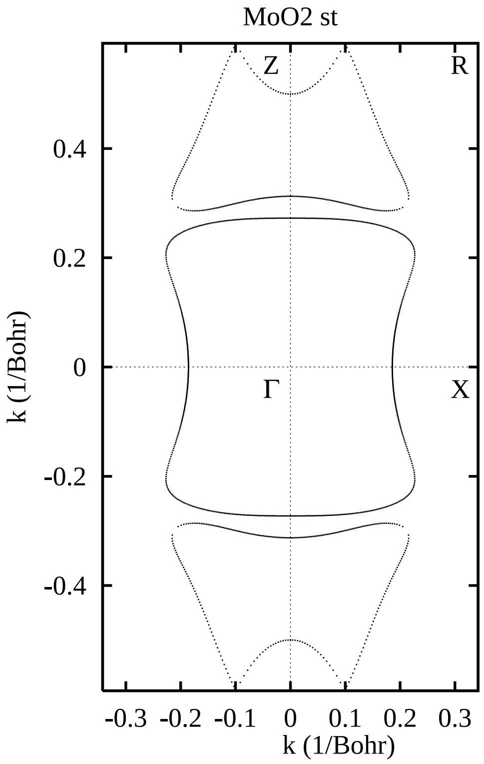

Figure 5.8:{100} cut through the Fermi surface of rutile MoO_2.

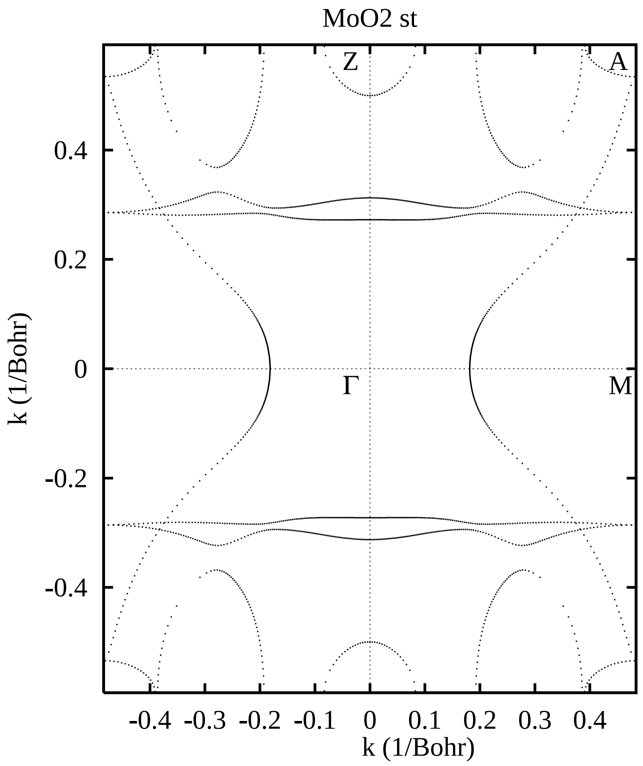

Figure 5.9:{110} cut through the Fermi surface of rutile MoO_2.

Still, the lateral components of the **q** vector are unspecified: Any wave vector

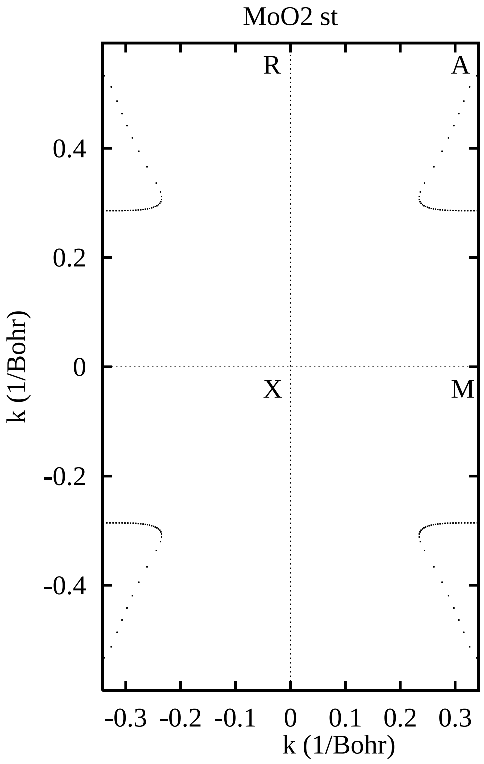

Figure 5.10:{100} cut through the Fermi surface of rutile MoO$_2$.

with $q_z = \frac{\pi}{c}$ transforms the flat sheets to themselves irrespective of the other two components. In order to fully specify the wave vector we thus have to take the remaining portions of the Fermi surface into consideration. In doing so, we may deduce further nesting from the nearly rectangular sheet centered about the Γ point in Fig. 5.8 which has a small lace in the basal plane of the Brillouin zone. This part of the Fermi surface favours wave vectors with the x or y component equal to $\frac{\pi}{a}$. Nevertheless, the Fermi surface area visible in Fig. 5.8 is much smaller than the previously discussed twofold flat {001} sheet and thus the lateral components of the wave vector may be more sensitive to the details of the entire Fermi surface than q_z. To summarize, we are as yet not able to arrive at a complete determination of the $\mathbf{q}$ vector.

5.4.4 Structural instability

Having identified the dominant contribution to the Fermi surface nesting vector which might destabilize the hypothetical rutile structure of MoO$_2$ we next aim at deducing information about the corresponding atomic displacements. This can be achieved by a more detailed discussion of the band structure using Figs. 5.11, 5.12, and 5.13. There we display the electronic bands in the narrow energy range from -2.5 to 3.5 eV about the Fermi energy in a special representation. In all three Figures, each band at each $\mathbf{k}$ point is given a bar, the length of which is a measure for the contribution from a specified orbital. Note, however, that again we refer to the local frame of reference. Hence, Figs. 5.11 to 5.13 correspond to the partial Mo $4d$ t_{2g}

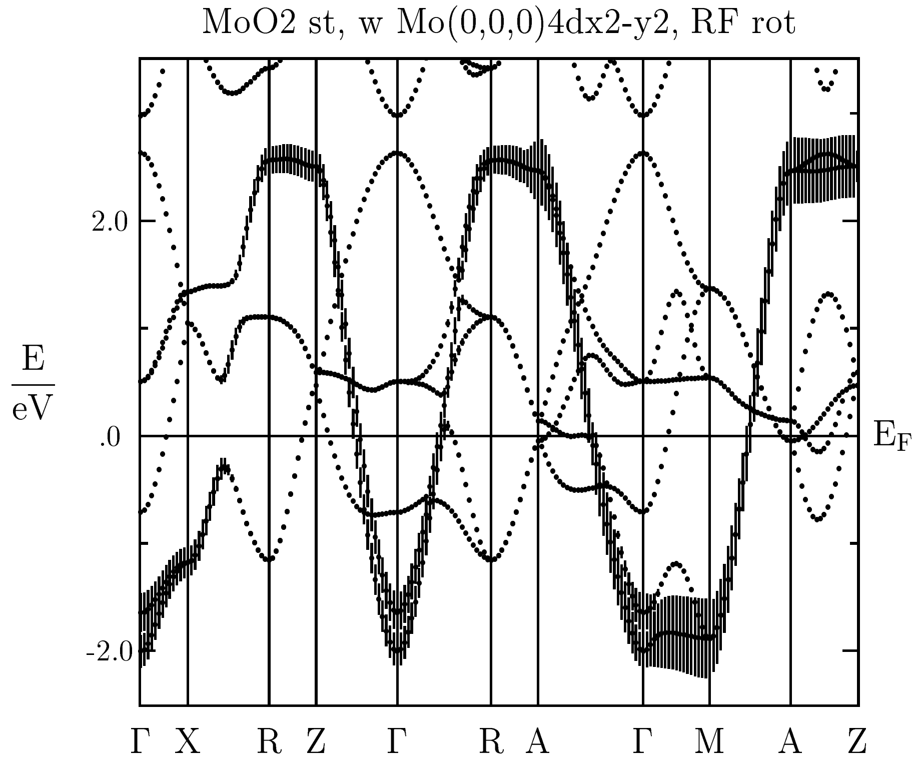

Figure 5.11: Weighted electronic bands of rutile MoO_2. The width of the bars given for each band indicates the contribution due to the $4d_{x^2-y^2}$ orbital of the Mo atom at (0,0,0) relative to the local rotated reference frame.

DOS shown in Fig. 5.6 which likewise made use of the local reference frame. In Fig. 5.11 we observe a strong dispersion of the Mo $4d_{x^2-y^2}$ derived bands along all lines parallel to Γ-Z whereas the dispersion perpendicular to this line is almost vanishing. Recalling the fact that the local x axes point along the rutile c axis we attach the strong dispersion in this direction to the overlap of the $d_{x^2-y^2}$ orbitals at metal sites neighbouring in z direction. The large bandwidth thus reflects the small metal-metal distance in this direction. The splitting of these bands along the lines Γ-M and A-Z and, albeit to a much smaller degree, along the lines where the strong dispersion is observed, is caused by the overlap of these states across the neighbouring octahedral chains i.e. the inter-chain interaction.

The situation is similar for the Mo $4d_{yz}$ derived bands which are highlighted in Fig. 5.13. They show a large dispersion in all directions the bandwidth being somewhat reduced as compared to that of the $d_{x^2-y^2}$ derived bands. Worth mentioning is the rather large splitting at the Γ point. It is a consequence of the underlying body-centered tetragonal (bct) lattice formed by the metal atoms and results from backfolding the bands from the Brillouin zone of the bct lattice to the smaller one of the simple tetragonal lattice. This effect is visible especially in the bands along the lines connecting the Γ point to the X, M, A, and Z point, respectively. Since the formation of the d_{yz} bands results from σ-type overlap of these orbitals across the body-centered tetragonal lattice and the a lattice constants are larger than the c lattice constant the overlap is reduced as compared to the $d_{x^2-y^2}$ orbitals and so is

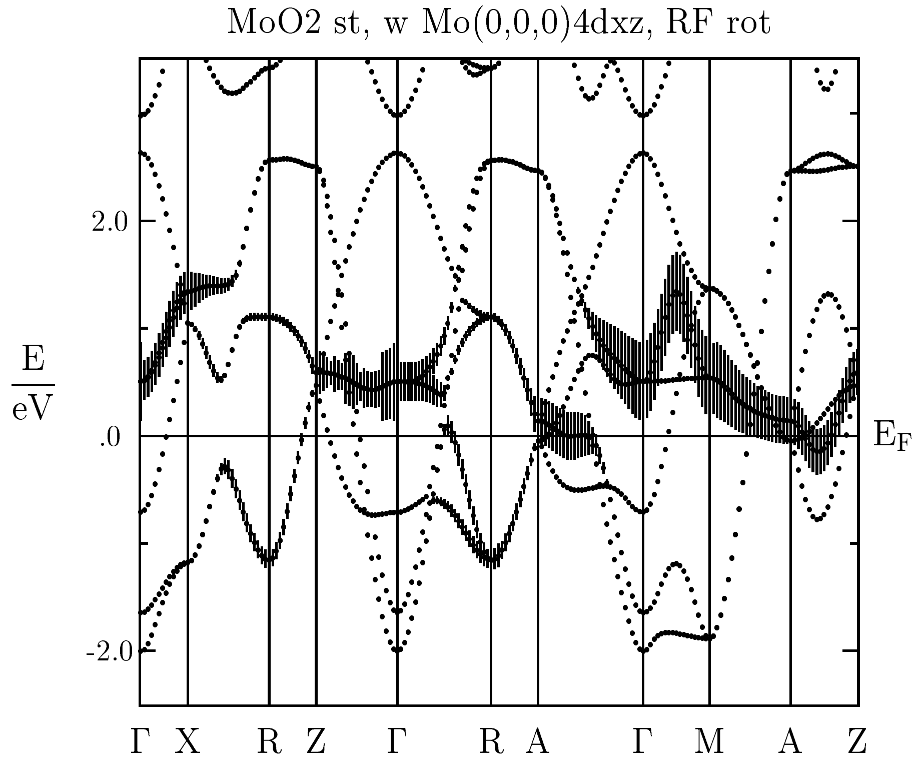

Figure 5.12: Weighted electronic bands of rutile MoO_2. The width of the bars given for each band indicates the contribution due to the $4d_{xz}$ orbital of the Mo atom at (0,0,0) relative to the local rotated reference frame.

the dispersion. The Mo $4d_{xz}$ derived bands, finally, display the smallest dispersion. This is a consequence of the fact that these orbitals induce no substantial σ-type overlap with neighbouring metal atoms but take part in the albeit small coupling between the octahedral chains.

The most striking result of the previous band structure analysis, however, consists of the fact that all three bands disperse without any considerable hybridization among each other. The only substantial exception stems from the strong hybridization of the $d_{x^2-y^2}$ bands with the d_{yz}- and d_{xz}-derived bands in the middle of the symmetry line X-R. Otherwise there are only some degeneracies of the d_{yz} and d_{xz} bands e.g. along the lines Γ-R and R-A which, however, do not induce large shifts of the bands near the Fermi energy. Hence, the three t_{2g}-derived bands behave almost completely independent.

This fact has important implications for the interpretation of the Fermi surface nesting and the resulting Peierls-type instability since it allows to assign each section of the Fermi surface to one of the t_{2g} bands. First, we attribute the almost perfect twofold flat Fermi surface in Figs. 5.8 to 5.10 exclusively to the $d_{x^2-y^2}$ bands. The abovementioned interruptions of this sheet above the X points can be clearly connected to the hybridization of the $d_{x^2-y^2}$ bands with the d_{yz}- and d_{xz}-derived bands along the symmetry line X-R. It pushes the bands away from the Fermi energy and thereby suppresses the Fermi surface portions in this **k** space region. Nevertheless, the size of these interruptions is rather limited and hence does not diminish the

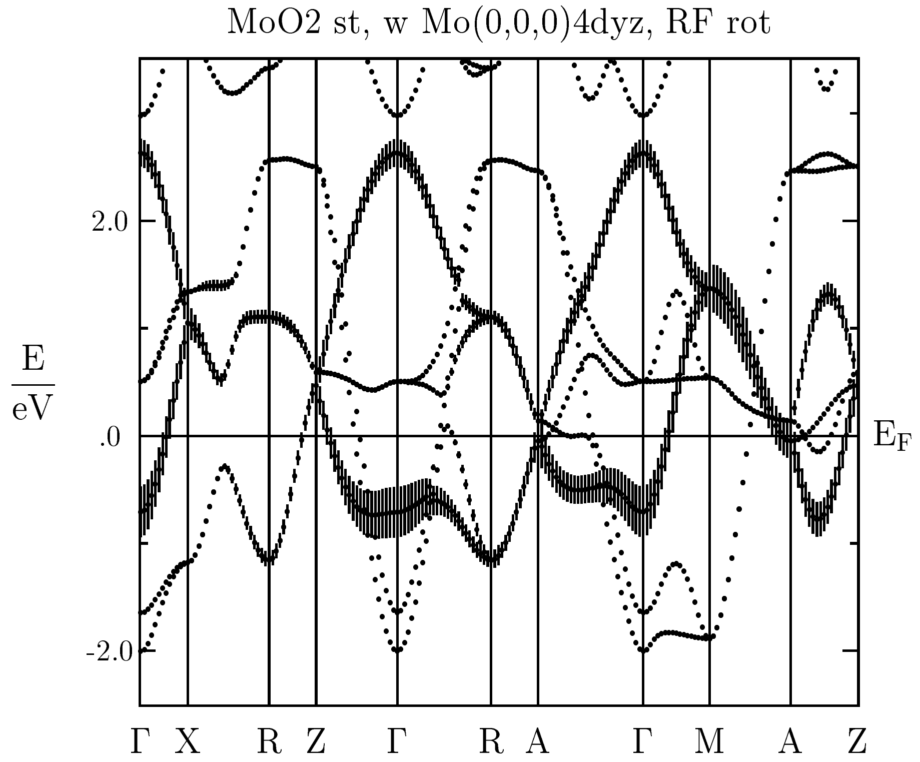

Figure 5.13: Weighted electronic bands of rutile MoO_2. The width of the bars given for each band indicates the contribution due to the $4d_{yz}$ orbital of the Mo atom at (0,0,0) relative to the local rotated reference frame.

predominant influence of the z component $q_z = \frac{\pi}{c}$ of the nesting vector. Finally, the d_{yz} bands, which cut the Fermi energy along the lines Γ-X and Γ-M, are responsible for those parts of the Fermi surface which are perpendicular to the basal plane. In particular, the vertical edges of the rectangle centered about the Γ point as seen in Fig. 5.8 can be attributed to these bands.

In real space, the Fermi surface nesting resulting from the twofold flat sheets may give rise to a Peierls-type instability which is accompanied by a modulation of the metal atom positions along the rutile c axis with a wave vector component $q_z = (0, 0, \frac{\pi}{c})$, i.e. a doubling of the c axis and a metal-metal pairing along this axis. Since the $d_{x^2-y^2}$ bands display hardly any dispersion perpendicular to the rutile c axis information about the in-plane components of the $\mathbf{q}$ vector, hence, about the remaining two primitive translation vectors of the new lattice, can be gained, if at all, only from the d_{yz}- and d_{xz}-derived bands. Yet, as has been outlined above, we were not able to determine the in-plane components of $\mathbf{q}$ from Fermi surface considerations. This fact leaves room for two different conclusions: Either, the nesting of the Fermi surface portions other than the twofold flat sheet is more complicated than to be detected by our present means or the d_{yz} and d_{xz} bands do not give rise to Fermi surface nesting at all. The latter situation would, for example, occur if these bands experience mainly rigid shifts on going from the hypothetical rutile to the monoclinic structure. Then it would be impossible to deduce information about the remaining two components of the $\mathbf{q}$ vector from Fermi surface considerations alone. This, however, seems to be the case here.

Still, we may look for other indicators, which might explain or at least give a plausible explanation for an instability towards the observed monoclinic crystal structure. In doing so, we start out from the just sketched situation where the $d_{x^2-y^2}$ bands are split due to a Peierls-type instability while the other two bands retain their metallic nature. We ask for the possible and most probable response of the latter two bands to the changes of the $d_{x^2-y^2}$ states. Of course, the simplest perturbation of the π^* bands consists of a rigid shift of both bands as a whole. On the other hand, such a shift will be nessessary to account for the removal of the $d_{x^2-y^2}$ states from the Fermi surface. A band shift of this kind arises from lateral displacements of the molybdenum atoms parallel to the local z axes, which increases the π-type overlap of the d_{yz} and d_{xz} orbitals with the p_x and p_y states of the apical oxygen atoms of the respective octahedron, and thus pushes the corresponding antibonding t_{2g} – p-derived states to higher energies. This mechanism has been clearly demonstrated in the previous chapter on V_2O_5 where the vertical displacements of the vanadium atoms away from the centers of local VO_6 octahedra couple to those (antibonding) t_{2g}-derived states which stick out of the basal plane and shift them to higher energies [81]. In MoO_2, the lateral displacements of the metal atoms along the local z axes can be most easily realized within a lattice which arises from an instability of the rutile structure against modulation with the vector $\mathbf{q} = (\frac{\pi}{a}, 0, \frac{\pi}{c})$, i.e. from an instability at the tetragonal R point. In contrast, an instability at the Z or A point would not allow for these modes. Of course, more complicated structures with larger unit cells or even an incommensurate structure cannot be ruled out.

The R point instability finally leads to a simple monoclinic lattice with primitive translations

$$\mathbf{a}_1 = \begin{pmatrix} 0 \\ 0 \\ -2c \end{pmatrix}, \quad \mathbf{a}_2 = \begin{pmatrix} -a \\ 0 \\ 0 \end{pmatrix}, \quad \mathbf{a}_3 = \begin{pmatrix} 0 \\ a \\ c \end{pmatrix}. \tag{5.4.1}$$

Here, we have already adopted the usual notation for the representation of the monoclinic transition metal dioxides. As a consequence of the tetragonal symmetry of the rutile structure there will be, in addition, a twinning of the monoclinic cell. The situation is sketched in Fig. 5.14 where we have omitted the oxygen atoms for simplicity. The previous discussion is in full accordance with the observed crystal structure of MoO_2 [42]. For this reason, we expect that the electronic structure of monoclinic molybdenum dioxide indeed reveals a Peierls-type instability. Investigation of the monoclinic cell, however, is subject of the following chapter.

5.5 Conclusion

In the present chapter first-principles ASW calculations were used to describe the electronic properties of MoO_2 evaluated in a hypothetical rutile structure. It grew out of the "real" monoclinic structure by symmetrizing the atomic positions. The investigation of the hypothetical structure served two purposes: First, we were able to study the gross characteristics of the electronic structure of MoO_2 in a much simpler crystal structure. The electronic properties are dominated by strong hybridization

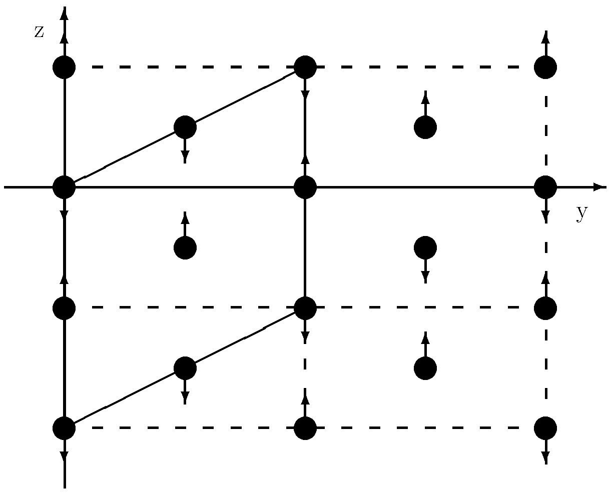

Figure 5.14: Modulation of metal atom displacements, side view. Dashed and solid lines mark the boundaries of the rutile and the monoclinic cell, respectively.

of O $2p$ and crystal field split Mo $4d$ states. Overlap of these orbitals leads to chemical stability while the details of the electronic structure near the Fermi energy are due almost exclusively to the Mo $4d$ t_{2g} orbitals. The results for the rutile structure serve as a reference for the subsequent investigation of the monoclinic structure.

Second, study of the rutile structure allowed to discuss mechanisms leading to the observed monoclinic structure: Investigation of the Fermi surface calculated within the rutile structure revealed nesting on characteristic twofold Fermi surface sheets perpendicular to the rutile c axis which originate from the local Mo $4d_{x^2-y^2}$ orbitals. No nesting could be observed for the other two t_{2g} bands. The results indicate a Peierls-type instability with doubling of the unit cell along the rutile c axis. In addition, discussion of possible in-plane shifts of the molybdenum atoms and the resulting response of the electronic states allowed to give a natural explanation for the observed monoclinic structure and the zigzag-like displacements of the metal atoms. Finally, our findings should be reflected by the electronic properties of monoclinic MoO_2.

Chapter 6

MoO_2: II. The monoclinic phase

6.1 Motivation

The continuing interest in the early transition metal dioxides originates from a broad range of electronic and magnetic properties which comprises metallic and semiconducting, non-magnetic, ferro- and antiferromagnetic ground states [216, 178, 79]. At the same time, crystal structures of these compounds are very similar and either identical or closely related to the rutile structure [216, 178, 35]. The deviations from the rutile structure, if present, are of the same kind for all compounds except for NbO_2 and lead to a monoclinic lattice which allows for a characteristic pairing of the metal atoms along the rutile c axis as well as lateral displacements. Macroscopically, the metal-metal bonding is reflected by the smallest rutile c/a ratios among the whole class of compounds [216].

The strong coupling of these structural characteristics to the electronic degrees of freedom is most clearly demonstrated by the phase transitions experienced by the d^1 members VO_2 and NbO_2 [187]. In both materials the metal-insulator transition is accompanied by a structural transition from the high-temperature rutile structure to a low-temperature low-symmetry phase. Still, it remains a matter of controversy whether the metal-insulator transition is driven predominantly by electron-phonon coupling or rather by electron-electron correlations.

In order to probe the influence of the structural details on the electronic properties we initiated a band theoretical study of metallic MoO_2 which likewise crystallizes in the monoclinic structure but does not exhibit any phase transition. Effective masses similar to the free electron mass have been reported for this material [253, 254, 139] which is regarded as an uncorrelated metal [64]. Thus, by investigating molybdenum dioxide we might be able to determine factors which govern the stability of the monoclinic phase without being faced with the effects of electon-electron correlations.

In the preceding chapter (hereafter denoted as I) we reported on calculations for MoO_2 in a hypothetical rutile structure which arises from a proper symmetrization of the observed monoclinic structure. These calculations served the purpose of (i) establishing a reference to which the electronic structure of "real" monoclinic MoO_2 could be compared and (ii) identifying mechanisms which destabilize the rutile phase. As a result, we observed a dominant influence of the Mo $4d$ t_{2g} states near the

Fermi energy whereas O $2p$- and Mo $4d$ e_g-derived bands are located, respectively, well below and above these states. Of the three almost independently dispersing t_{2g} bands the local $d_{x^2-y^2}$ states, which mediate overlap between metal atoms neighbouring along the rutile c axis, show strong tendency towards bonding-antibonding splitting. In addition, the $d_{x^2-y^2}$ bands give rise to Fermi surface nesting on characteristic twofold flat sheets perpendicular to the c axis this fact being indicative of a Peierls-type instability against unit cell doubling and metal-metal pairing. The results led us to expect that in a calculation for the "real" crystal structure the pairing of the metal atoms causes an increase of the bonding-antibonding splitting of the local $d_{x^2-y^2}$ states and removes the Fermi surface due to these bands.

In the present chapter we continue by investigating MoO_2 in the "real" monoclinic structure and comparing the results to those of I. From the differences between both calculations we will be able to separate those features of the electronic structure which are artefacts of the rutile structure from those which are unique to the monoclinic structure and thus are important for the stability of the latter. In particular, we will analyze the electronic structure with respect to the aforementioned expectations.

The chapter is organized as follows: Referring to the discussion of the rutile structure as given in the preceding chapter we describe the main characteristics of the monoclinic crystal structure in Sec. 6.2. After shortly summarizing in Sec. 6.3 methodological details which are unique to the present calculations we present the results in Sec. 6.4. The conclusion, Sec. 6.5, sums up the most important findings.

6.2 Crystal structure

MoO_2 crystallizes in a simple monoclinic (sm) lattice with space group $P2_1/c$ (C_{2h}^5) [168, 42]. The lattice constants and the monoclinic angle amount to $a_M = 5.6109$Å, $b_M = 4.8562$Å, $c_M = 5.6285$Å, and $\beta = 120.95°$, respectively [42]. The crystal structure is displayed in Fig. 6.1. The unit cell comprises four formula units and the metal atoms as well as the two different types of oxygen atoms occupy the general Wyckoff position (4e): $\pm(x, y, z)$, $\pm(x, \frac{1}{2} - y, \frac{1}{2} + z)$ with the parameters listed in Table 6.1. Here we have adopted the usual notation

Atom	Wyckoff positions	parameters		
		x	y	z
Mo	(4e)	0.2316	-0.0084	0.0164
O_1	(4e)	0.1123	0.2171	0.2335
O_2	(4e)	0.3908	-0.3031	0.2987

Table 6.1: Crystal structure parameters of monoclinic MoO_2 (from Ref. [42]).

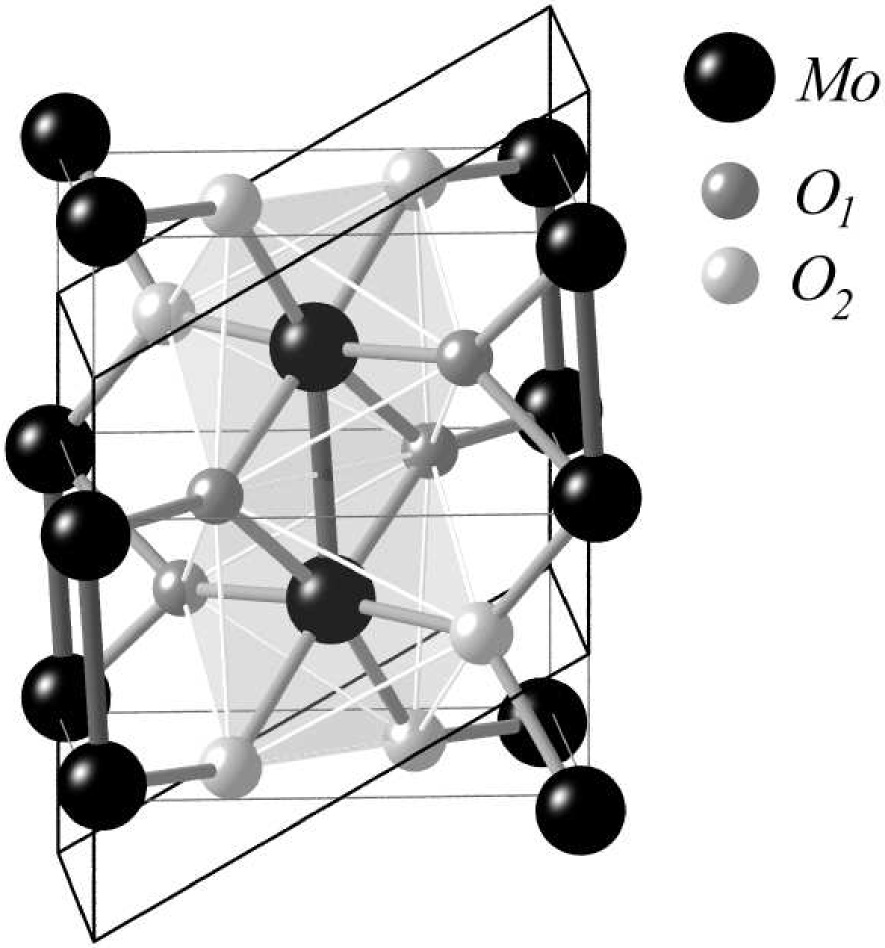

Figure 6.1: Crystal structure of MoO_2. Molybdenum atoms are printed in black whereas oxygen atoms O_1 and O_2 are shaded medium and light gray, respectively.

$$\mathbf{a}_{M1} = \begin{pmatrix} 0 \\ 0 \\ -a_M \end{pmatrix} , \quad \mathbf{a}_{M2} = \begin{pmatrix} -b_M \\ 0 \\ 0 \end{pmatrix} ,$$

$$\mathbf{a}_{M3} = \begin{pmatrix} 0 \\ c_M \sin\beta \\ -c_M \cos\beta \end{pmatrix} \tag{6.2.1}$$

for the primitive translations.

The close relationship of the monoclinic crystal structure to the rutile structure, which only laid ground for the use of hypothetical rutile MoO_2 as a reference system, becomes visible from a comparison of Fig. 6.1 to Fig. 1 of I. However, there exist distinct differences: (i) We observe in Fig. 6.1 the metal-metal pairing along the tetragonal c axis. Due to the alternation of the vertical metal atom displacements in the directions of the y axis the lattice is simple monoclinic rather than simple tetragonal with a double c axis (see also Fig. 13 of I). (ii) Slightly less marked are the in-plane displacements of the Mo atoms which make an angle of 18° with the local z axes (see I for a description of the local coordinate systems). These shifts likewise alternate along both the tetragonal a and c axis thus causing a zigzag like shape of the vertical metal chains. The oxygen atoms follow the lateral displacements of the metal atoms to a large degree whereas the deviations of the z components from the ideal rutile values are much smaller. (iii) There is a lattice strain which causes deviations of the ratios

$$\frac{c_M \sin\beta}{b_M} = 0.9940 \; , \qquad \frac{-2c_M \cos\beta}{a_M} = 1.0318$$

from unity and prohibits representation of the primitive translations (6.2.1) in the form given by equation (4) of I.

6.3 Calculational details

By applying of the sphere geometry optimization (SGO) algorithm to the open crystal structure of simple monoclinic MoO_2 we were able, by inserting 12 empty spheres, to keep the linear overlap of any pair of physical spheres below 20%, and the overlap of any pair of physical and empty spheres below 22%. The positions of the empty spheres are listed in Table 6.2. The atomic sphere radii for all spheres as

Atom	Wyckoff positions	parameters		
		x	y	z
E_1	(2d)	0.5	0.5	0.0
E_2	(2c)	0.0	0.0	0.5
E_3	(4e)	0.3458	0.3754	0.1805
E_4	(4e)	0.1544	-0.1070	0.3110

Table 6.2: Empty sphere positions for monoclinic MoO_2.

proposed by the SGO algorithm as well as the basis set orbitals are listed in Table 6.3. Finally, the Brillouin zone sampling was done using an increasing number of **k** points, which range from 54, 128, 432, 1024, 2000 to 6750 points within the irreducible wedge.

6.4 Results and Discussion

6.4.1 Electronic structure and partial DOS

We display in Fig. 6.2 the electronic states along selected high symmetry lines within the simple monoclinic Brillouin zone, Fig. 6.3. The corresponding density of states (DOS) is given in Fig. 6.4 where we have added the dominant partial densities of

Atom	Radius/a_B	Orbitals				
Mo	2.600	$5s$	$5p$	$4d$	$4f$	$(5g)$
O_1	1.650	$2s$	$2p$	$(3d)$		
O_2	1.843	$2s$	$2p$	$(3d)$		
E_1	2.197	$1s$	$2p$	$3d$	$(4f)$	
E_2	2.372	$1s$	$2p$	$3d$	$(4f)$	
E_3	1.908	$1s$	$2p$	$3d$	$(4f)$	
E_4	1.788	$1s$	$2p$	$(3d)$		

Table 6.3: Atomic sphere radii and basis set orbitals for monoclinic MoO_2.

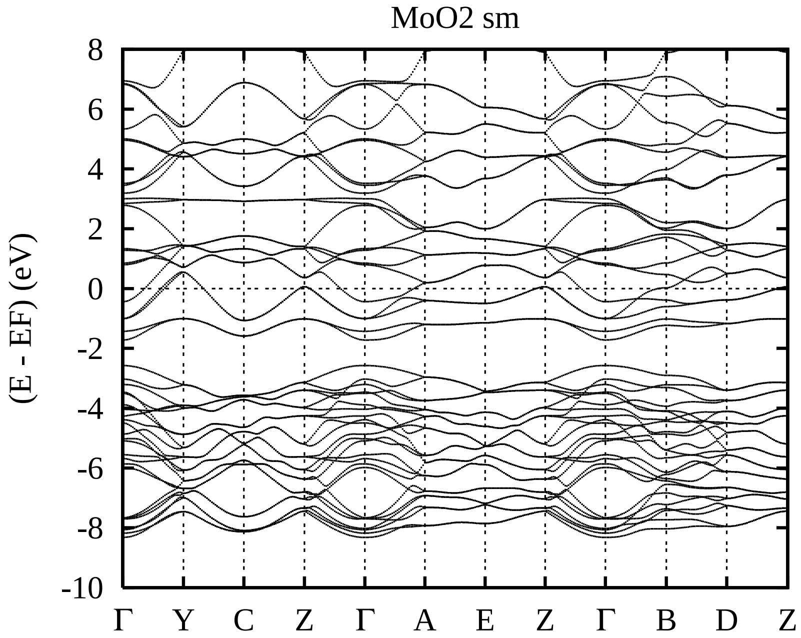

Figure 6.2: Electronic bands of MoO_2 along selected symmetry lines within the simple monoclinic Brillouin zone, Fig. 6.3.

states. In both representations we concentrate on the same energy interval as in I and do not include e.g. low lying oxygen $2s$ states. The total density of states at the Fermi energy, $N(E_F)$ amounts to 0.58 states/f.u./eV.

The similarities of the results for "real" monoclinic and hypothetical rutile MoO_2 are easily stated. Again, we identify in Figs. 6.2 and 6.4 three groups of bands. Well below the Fermi energy we find 24 oxygen $2p$ dominated bands. Bands are most easily counted along the lines A-E-Z where they are twofold degenerate. The remaining groups, which range from -1.8 to 3 eV and from 3 to 7 eV, originate mainly from Mo $4d$ states and comprise 12 and eight single bands, respectively. As in I we observe considerable $p-d$ hybridization of the order of about 10%.

In Fig. 6.5 we show the partial Mo $4d$ DOS separated into its symmetry components. In doing so we again include only the single molybdenum atom at $(0, 0, 0)$ and

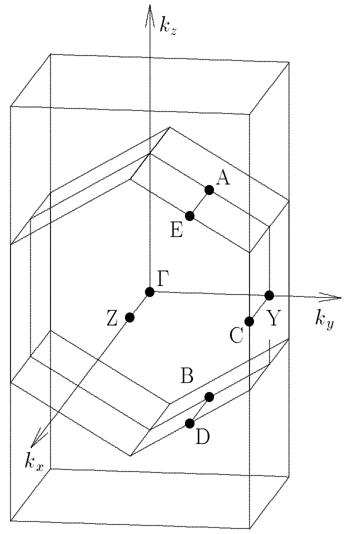

Figure 6.3: First Brillouin zone of the simple monoclinic lattice. The outer box marks the first Brillouin zone of the simple tetragonal lattice, see Fig. 5.4.

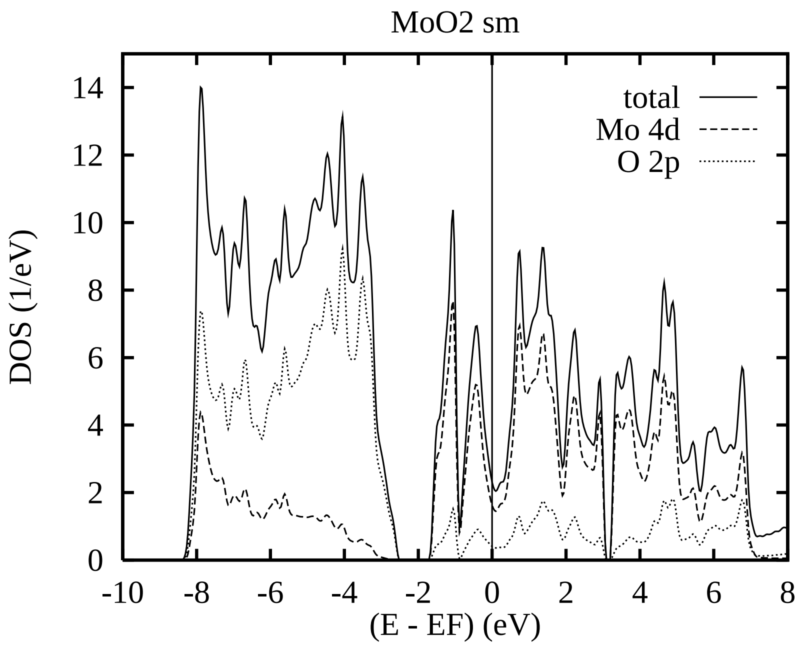

Figure 6.4: Total and partial densities of states (DOS) of MoO_2 per unit cell.

use the local, rotated reference frame as defined in I for the rutile structure. Again, we recognize the almost perfect energetical separation of the $4d$ t_{2g} and e_g groups of bands resulting from the octahedral crystal field splitting. Due to tetragonal rather than cubic symmetry of the MoO_6 octahedra the d_{xz} and d_{yz} partial DOS are still similar whereas the $d_{x^2-y^2}$ DOS deviates significantly.

The differences arising from replacing the hypothetical rutile structure by the "real" monoclinic one are twofold: (i) On comparing Fig. 4 of I with Fig. 6.4 of the present chapter, we observe an upshift of the O $2p$ dominated group of bands

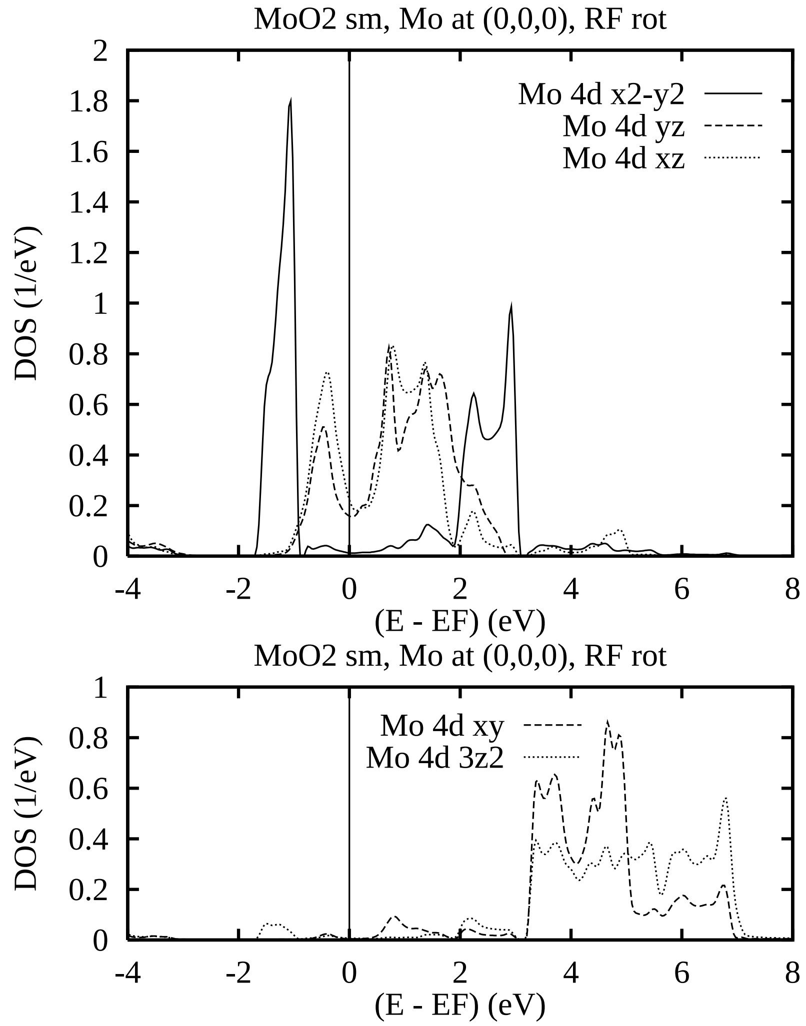

Figure 6.5: Partial Mo $4d$ t_{2g} and e_g densities of states (DOS) of MoO_2. Selection of orbitals is relative to the local rotated reference frame.

by $\approx$ 1 eV relative to the Fermi energy. It can be attributed to the increase of the bond lengths between the molybdenum atoms and the oxygen ligands in the monoclinic structure by about 1% which reduces the bonding-antibonding splitting of the σ-bonded Mo $4d$ and O $2p$ states. (ii) As has been already suspected in the preceding chapter and as is obvious from a comparison of Fig. 5 of I to Fig. 6.5 of the present chapter the splitting of the Mo $4d_{x^2-y^2}$ partial DOS into two peaks has increased by about 0.5 eV. Whereas in the calculation for hypothetical rutile MoO_2 the two main peaks are still connected by a finite DOS in between the separation of the peaks is complete in the monoclinic structure. This becomes even more obvious from a comparison of the band structures. To this end we display in Fig. 6.6 the band structure of hypothetical rutile MoO_2 which results from backfolding the bands calculated within the rutile structure to the first Brillouin zone of the simple monoclinic lattice, Fig. 6.3. In the rutile calculation, those two bands which, at the Γ point, give rise to the lowest states within the t_{2g}-derived group of bands bend upwards along the line Γ-A and cross the higher lying bands. In contrast, in the "real" monoclinic structure these two bands are well separated from the other

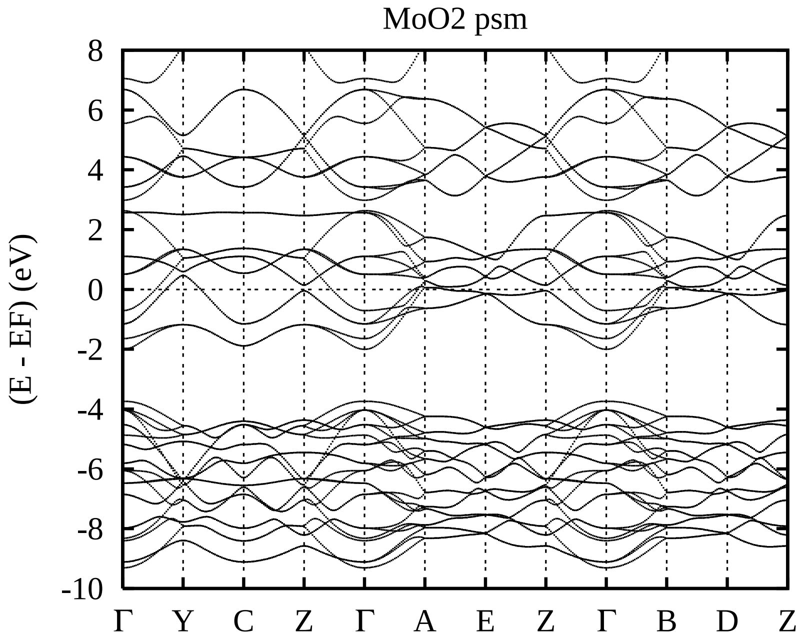

Figure 6.6: Electronic bands of hypothetical rutile MoO_2 along selected symmetry lines within the simple monoclinic Brillouin zone, Fig. 6.3.

states and form a split-off doublet. From the discussion in the preceding chapter we attribute these changes to the increased bonding-antibonding splitting within the $d_{x^2-y^2}$ dominated bands coming with the metal-metal pairing along the rutile c axis. Our results are thus in very good agreement with the simple band schemes presented by Rogers et al. as well as by Goodenough [216, 108] where the $d_{x^2-y^2}$ band, designated as the $d_{||}$ band, experiences a strong bonding-antibonding splitting due to the metal-metal pairing while the π^* bands (d_{xz} and d_{yz} in our notation) stay in between the two $d_{||}$ peaks without any further splittings.

6.4.2 Chemical bonding

The previous findings on the band structure and the partial densities of states are well reflected by the chemical bonding. We have calculated the crystal orbital overlap population (COOP). The results for monoclinic MoO_2 are shwon in Fig. 6.7. We have omitted the partial COOP curves for O $2p$ – O $2p$ as well as Mo $4d$ – O $2p$ bonding which, like the total COOP, agree closely with the curves calculated for the hypothetical rutile structure, see Fig. 6 of I. Differences arise mainly from the bonding and antibonding Mo $4d_{x^2-y^2}$ peaks which lead to a distinct positive contribution to the Mo-Mo curve between -2 and -1 eV and to an additional negative peak at the upper edge of the t_{2g} bands between 2 and 3 eV. These two peaks signal the increased metal-metal bonding coming along with the pairing of the atoms in the monoclinic structure. Finally, the formation of bonding and antibonding Mo $4d_{x^2-y^2}$ states below and above the Fermi energy, respectively increases the value of the total integrated COOP at the Fermi level (see Ref. [79] for details) and thus contributes significantly to the overall chemical stability of the compound.

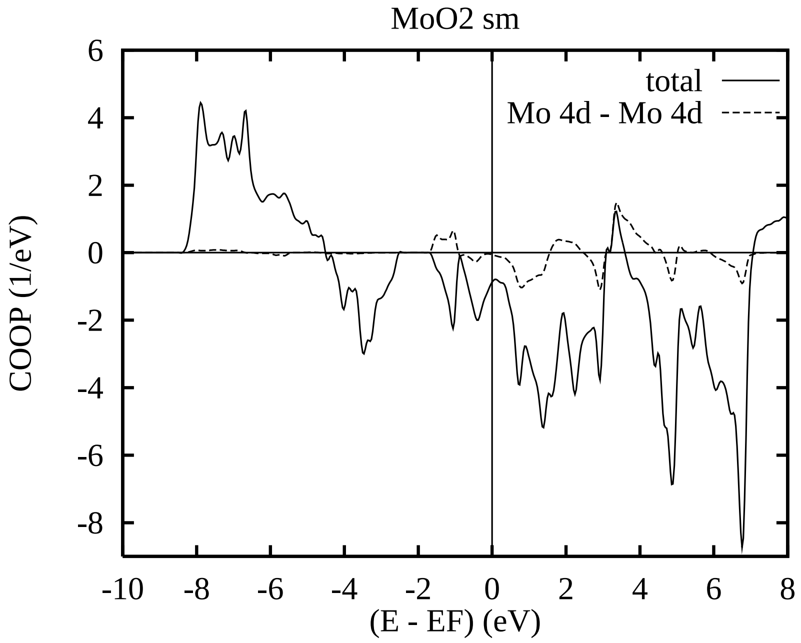

Figure 6.7: Total and partial crystal orbital overlap populations (COOP) of MoO_2.

6.4.3 Comparison to experiment

We display in Figs. 6.8 and 6.9 total and partial Mo $4d$ and O $2p$ densities of states

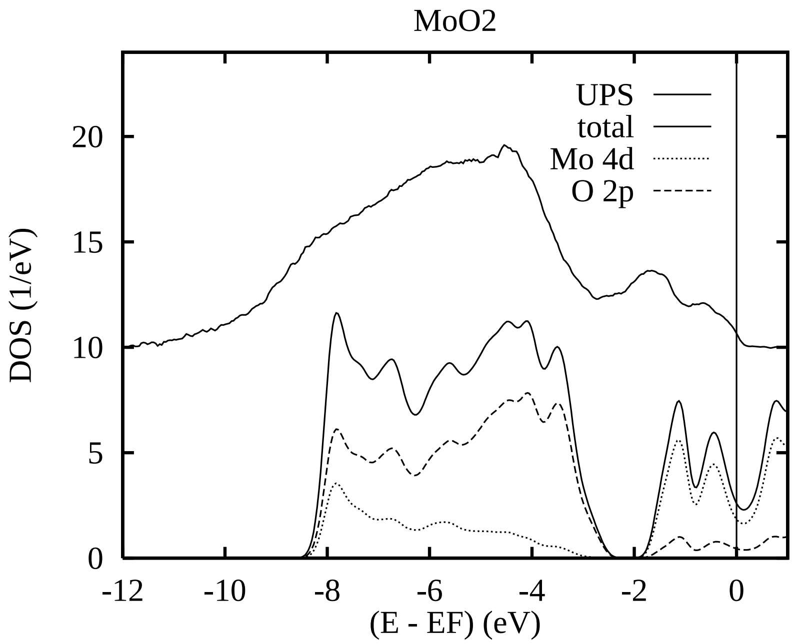

Figure 6.8: Total and partial densities of states (DOS) of MoO_2 folded with a 0.25 eV wide Gaussian (lower set of curves) and UPS spectra (upper curve; from Ref. [98]).

folded with a Gaussian of 0.25 and 0.5 eV width, respectively for the occupied and unoccupied part of the spectrum. In Fig. 6.8 we have added UPS spectra as measured

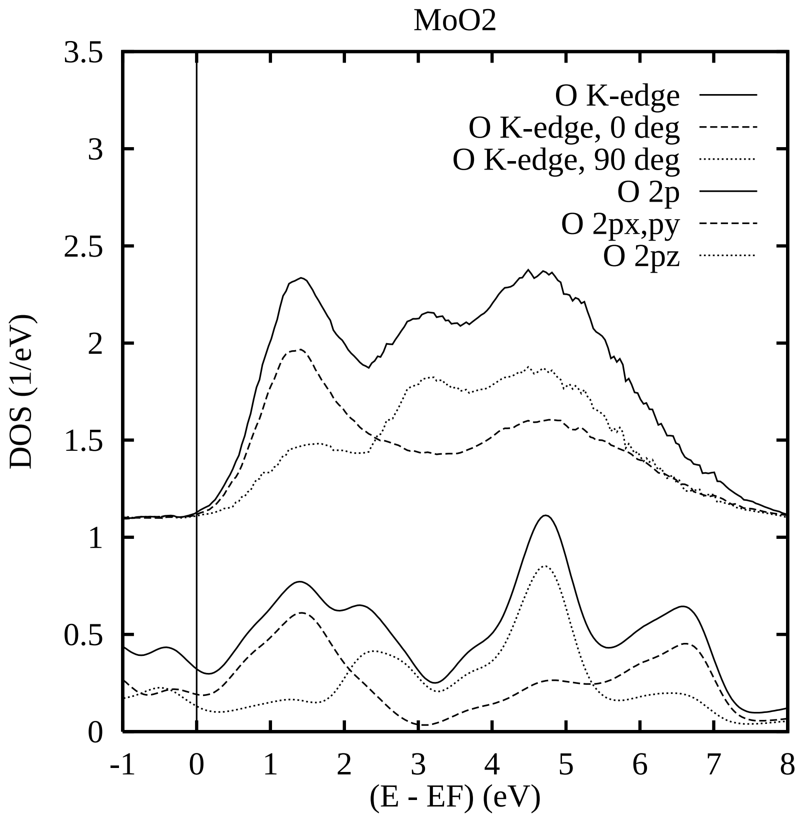

Figure 6.9: Partial O $2p$ densities of states (DOS) of MoO_2 folded with a 0.5 eV wide Gaussian (lower set of curves) and XAS O K edge spectra (upper set of curves; from Ref. [190]).

by Goering [98]. Good agreement of the calculated and measured curves is found. In addition, the calculated total DOS compares very well with the XPS spectra by Beatham and Orchard as well as by Werfel and Minni [25, 261]. The occupied bandwidth of $\approx$ 8.8 eV deduced from the experiments is close to the calculated 8.5 eV. According to Beatham and Orchard the valence band is split into a low and high binding part of about 3 and 6 eV width, respectively [25]. As their UPS measurements furthermore reveal the low binding region falls into two main peaks at $\approx$ -1.5 and -0.5 eV. In the UPS spectra shown in Fig. 6.8 we find the corresponding peaks at -1.7 and -0.6 eV whereas in the calculations they show up at -1.15 and -0.45 eV. Hence, we state almost perfect agreement for the Mo $4d_{xz}$ and $4d_{yz}$ states but an energetical upshift of the bonding Mo $4d_{x^2-y^2}$ bands of $\approx$ 0.45 eV relative to experiment. In passing we note that the position of the calculated O $2p$-derived bands compares very well with the optical reflectance data by Chase as well as by Dissanayake and Chase who find these states 2.5 eV below the Fermi energy [59, 68].

In Fig. 6.9 we have complemented the theoretical results by soft-x-ray absorption spectra as measured by Müller [190]. In order to probe the angular dependence, in these experiments the polarization vector **E** was oriented either parallel ($\phi = 90°$) or else perpendicular ($\phi = 0°$) to the rutile c axis. In the former case, dipole selection rules allow for transitions from O $1s$ to the O $2p_z$ state. In contrast, for **E** perpendicular to the c axis transitions to the O $2p_x$ and $2p_y$ states may occur. We have added the partial DOS of the corresponding final states in Fig. 6.9. Note, however, that the curve marked O $2p_x, p_y$ comprises only the mean average of these orbitals since the component perpendicular to **E** is not seen in experiment. For the same reason, the curve marked O $2p$ actually contains the contribution from $\frac{1}{2}(p_x + p_y) + p_z$. Again, there is an overall good agreement between experiment and theory. This holds not only for the positions of most peaks but also for their relative intensity as well as their angular dependence. We point especially to the suppression, on increase of the angle ϕ, of the peak due to the Mo $4d_{xz}$ and $4d_{yz}$ bands at 1.2 eV. Still, this good agreement is contrasted with two distinct deviations: First, the broad maximum at 6.6 eV in the calculated DOS, which results from the O $2p_x$ and $2p_y$ states, is not seen by experiment. According to the molybdenum partial DOS shown in Fig. 6.5 this maximum originates mainly from the Mo $4d_{3z^2-r^2}$ orbitals. Second, the maximum in the O $2p_z$ partial DOS at ≈ 2.4 eV is located at ≈ 3.1 eV in the XAS spectra. From a comparison to the partial Mo $4d$ DOS, Fig. 6.5, we attribute this maximum to the antibonding $d_{x^2-y^2}$ orbitals. Their energetical downshift relative to experiment adds to the forementioned deviation of about 0.45 eV of the corresponding bonding states. It thus seems that the calculations underestimate the bonding-antibonding splitting of the Mo $4d_{x^2-y^2}$ states by approximately 1 eV.

6.4.4 Peierls-like scenario

Still, it remains to be shown that the increase in bonding-antibonding splitting of the Mo $4d_{x^2-y^2}$ bands on going from the hypothetical rutile to the "real" monoclinic structure, which we proposed in I and which indeed was found in the preceding subsections, can be attributed to a Peierls-type instability. We start the discussion by displaying in Fig. 6.10 the electronic structure of hypothetical rutile MoO_2 in the narrow energy range from -2.5 to 3.5 eV about the Fermi energy again referring to the high symmetry lines within the first Brillouin zone of the simple monoclinic lattice. We use the same special representation as in Figs. 10 to 12 of I and attach to each band at each **k** point a bar the length of which is a measure for the contribution from a specified orbital. In doing so, we concentrate especially on the Mo $4d_{x^2-y^2}$ orbitals, again relative to the local frame of reference. Note that Fig. 6.10 could be constructed from Fig. 10 of I by folding the bands back from the simple tetragonal to the simple monoclinic Brillouin zone. We thus recognize the strong dispersion along the lines Γ-A, E-Z, Γ-B, and D-Z which have components perpendicular to the rutile basal plane and correspond to half of the lines Γ-R and X-A of the tetragonal Brillouin zone. In contrast, the dispersion parallel to the rutile basal plane is almost completely suppressed with the bands staying at energies either well below or above the Fermi energy. An exception are the lines A-E and B-D where the Mo $4d_{x^2-y^2}$ states, while showing an almost vanishing dispersion, are found at E_F. This is connected to the fact that these lines extend *within* the planes at height $\frac{\pi}{2c}$. As has been discussed in I these planes contain the characteristic twofold flat Fermi surface sections coming with the rutile structure. Hence, the lines A-E and B-D just extend through the dominating part of the rutile Fermi surface.

The situation changes completely when we turn to monoclinic MoO_2 for which we show the analogous band structure in Fig. 6.11. Again, the bars given to the

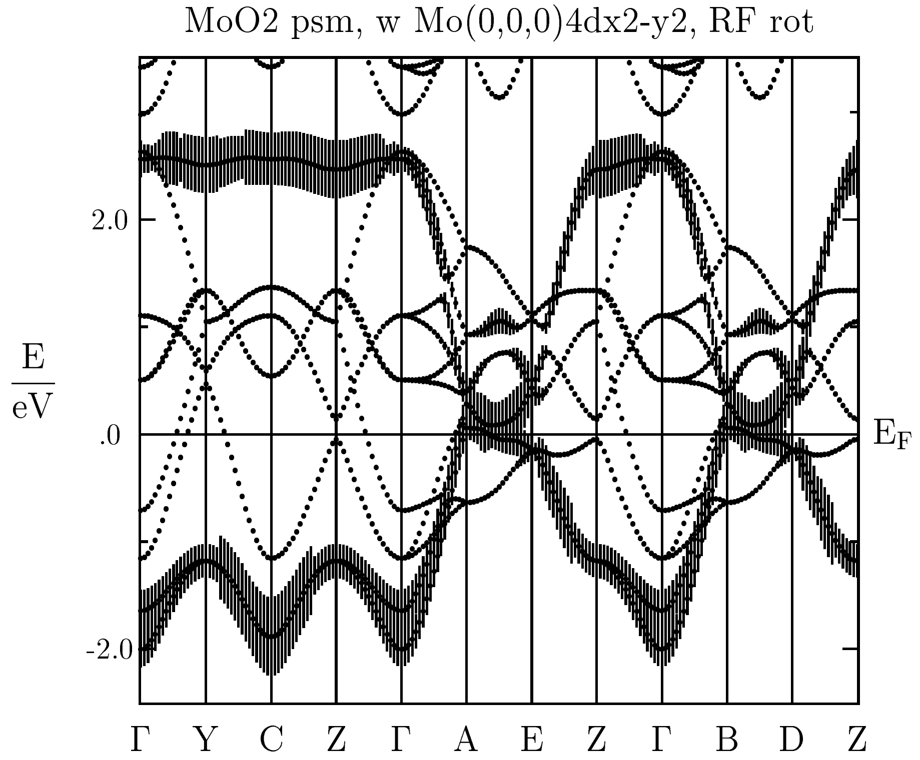

Figure 6.10: Weighted electronic bands of hypothetical rutile MoO_2. The width of the bars given for each band indicates the contribution due to the $4d_{x^2-y^2}$ orbital of the Mo atom at (0,0,0) relative to the local rotated reference frame.

bands are a measure of the contribution from the local Mo $4d_{x^2-y^2}$ states. The striking difference between both Figures clearly reveals the validity of the Peierls-type mechanism proposed in I which, in the $d_{x^2-y^2}$ partial DOS, Fig. 6.5, led to the complete separation of the bonding and antibonding peaks. In Fig. 6.11 the occupied and unoccupied Mo $4d_{x^2-y^2}$-dominated bands along the lines Γ-A-E-Z and Γ-B-D-Z have moved by as much as $\approx$ 2 eV downward and upward, respectively relative to their position in hypothetical rutile MoO_2. This leads, in particular, to the formation of the split-off double band at the lower edge of the t_{2g} group. As a consequence of these drastic bandshifts, the Fermi surface due to the $d_{x^2-y^2}$ states has vanished completely. In contrast, all other bands in the energy range from -2 to 2.5 eV, which according to the analysis given in I are mainly of Mo $4d_{xz}$ and $4d_{yz}$ character, experienced only minor changes and maintain the (anisotropic) metallic conductivity. Finally, the downshift of the $d_{x^2-y^2}$ states along the lines Γ-A-E-Z and Γ-B-D-Z causes a considerable lowering of the total energy and, hence, a stabilization of the monoclinic structure.

6.5 Conclusion

In the present chapter first-principles ASW calculations were used to describe the electronic properties of monoclinic MoO_2. As in the previous study, which used the

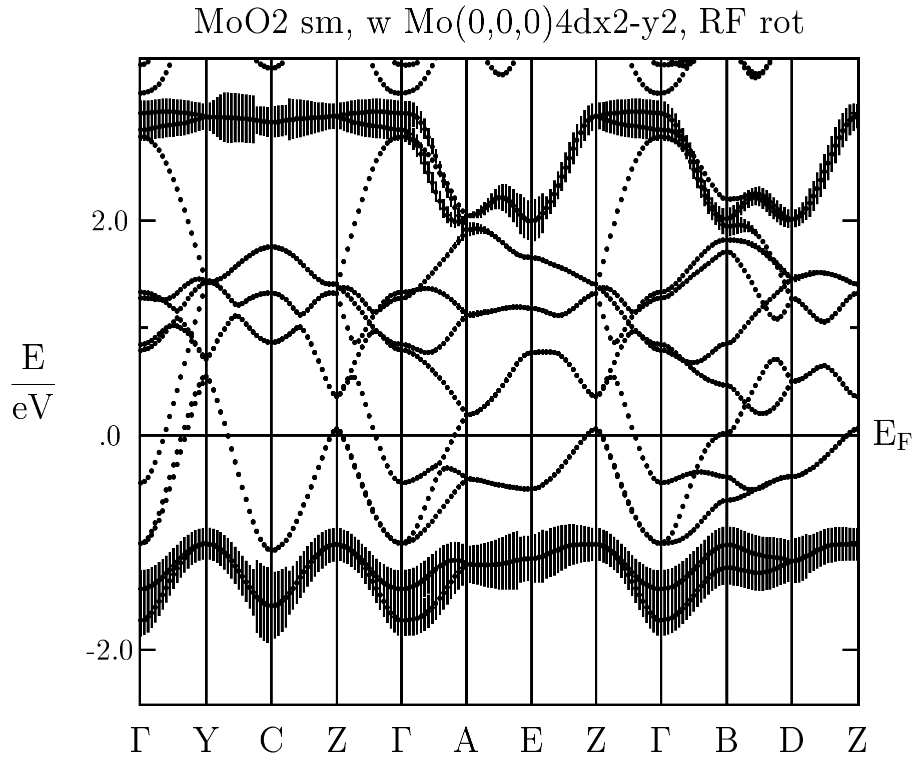

Figure 6.11: Weighted electronic bands of monoclinic MoO_2. The width of the bars given for each band indicates the contribution due to the $4d_{x^2-y^2}$ orbital of the Mo atom at (0,0,0) relative to the local rotated reference frame.

hypothetical rutile structure, molybdenum $4d$ t_{2g} states resulting from octahedral crystal field splitting are found near the Fermi energy while strongly hybridized O $2p$ and Mo $4d$ e_g states are located well below and above, respectively.

Distinct deviations between both calculations arise from metal-metal pairing along the rutile c axis which causes strong increase of the bonding-antibonding splitting of the $d_{x^2-y^2}$ bands. As a consequence, the Fermi surface portions due these states, which showed considerable nesting in the hypothetical rutile structure, are completely removed. In contrast, the d_{xz} and d_{yz} orbitals experience only minor changes and, in particular, maintain the anisotropic metallic conductivity. These results confirm the general picture sketched in the previous chapter which proposed a Peierls-like scenario for the $d_{x^2-y^2}$ bands but only minor changes for the remaining t_{2g}-derived states. The rather small adjustments of the latter states may be interpreted as a response to the splitting of the $d_{x^2-y^2}$ bands. Finally, the downshift of the occupied $d_{x^2-y^2}$ bands by as much as 2 eV coming with the Peierls-type instability leads to substantial lowering of the total energy as well as an increase of the chemical bonding and stabilizes the monoclinic structure.

Chapter 7

VO_2: I. The rutile phase

7.1 Motivation

At 340 K, VO_2 undergoes a metal-insulator transition which is accompanied by a structural transition from the high-temperature rutile phase to a low-temperature monoclinic phase [187, 45]. Since its discovery fourty years ago this transition has attracted a lot of interest for reasons of both fundamental questions and applications [45]. The latter results from the sharp change in resistivity, which extends over several orders of magnitude, as well as from the fact that the transition occurs near room temperature [187, 45]. Despite this strong motivation, understanding of the origin of the phase transition is still far from complete. Several models have been proposed ranging from Peierls- [106, 3, 4, 107, 108, 259] and spin-Peierls- [3, 207, 205, 199] to Mott-Hubbard-type [189, 279, 215] scenarios which stress, to a different degree, the role of lattice instabilities, electron-phonon interaction and electron-electron correlations as the driving force for the transition. Yet, neither of these pictures has so far been successful in explaining a broader range of physical phenomena occuring in vanadium dioxide which fact hindered a complete and accepted picture of the physics of this material in particular and a more comprehensive understanding of the rutile-related transition metal oxides in general.

Interestingly, the distortions of the rutile structure occuring at the phase transition of VO_2 are very similar for all the early transition metal dioxides, which display such deviations, i.e. for VO_2, NbO_2, MoO_2, WO_2, TcO_2, and α-ReO_2 [216]. There exist two different characteristics, namely a pairing of the metal atoms parallel to the tetragonal c axis and a lateral zigzag-like displacement [13, 216, 161, 169]. As a consequence, unit cells of all these compounds double with a simple monoclinic lattice the only exception being NbO_2, which assumes a body centered tetragonal lattice comprising 16 rutile cells [108]. The structural similarities are contrasted with striking differences in the electronic properties: While the d^1 compounds VO_2 and NbO_2 undergo a metal-insulator transition their four neighbours remain metallic. The different trends of structural and electronic properties over the whole class of the early transition metal dioxides led Goodenough to rule out a Jahn-Teller effect as a major source for the crystal structure characteristics [106].

The important role of the lattice degrees of freedom for the stabilization of the different phases of VO_2 has been further deduced from several experiments, which revealed striking differences between the metallic and insulating state. Together with the symmetry change at the metal-insulator transition these findings were taken as evidence for strong electron-phonon coupling and a lattice softening at the transition [179]: X-ray measurements revealed large thermal displacements in the rutile phase of both stoichiometric and Cr-doped VO_2, which exceed the values measured in the respective low-temperature phases as well as in the neighbouring rutile compounds TiO_2 and CrO_2 considerably [169, 179]. Rao *et al.* observed a large thermal anisotropy of the thermal expansion in the rutile phase ($\alpha_{\|} \approx 5 - 6 \times \alpha_{\perp}$) [214, 151], which causes a strong temperature dependence of the electric field gradient at the vanadium site [205]. In addition, an anisotropic change of the lattice constants at the phase transition was reported [182, 151]: While the rutile c axis increases by $\approx 1\%$ the a axis decreases by $\approx 0.6\%$. At the same time, the volume changes discontinuously by -0.044% and the thermal expansion coefficient drops by a factor of three [133, 151]. X-ray diffuse scattering measurements performed just above the metal-insulator transition by Terauchi and Cohen [241] point to a lattice instability at the tetragonal R point with wave vector parallel to Γ-R and a polarization vector parallel to the c axis. This result confirmed the symmetry analysis by Brews, who had shown that the rutile-to-monoclinic transition would be compatible with a phonon instability at the R point [43]. Finally, an oxygen isotope effect was observed for the transition temperature [242].

The electronic structure of metallic VO_2 has been probed by optical and photoemission experiments. According to optical measurements by Verleur *et al.* the lowest unfilled V $3d$ levels lie about 2.5 eV above the top of the O $2p$ bands [247]. This result was supported by photoemission measurements by Powell *et al.* [208]. UPS and XPS experiments revealed an ≈ 8.5 eV wide occupied band falling into the low binding, approximately 1.5 eV wide V $3d$ band and an ≈ 6 eV wide group of O $2p$ bands at higher binding energies [226, 29, 98, 102, 103]. In contrast, the unoccupied states, as measured by O K-edge XAS experiments, mainly fall into two peaks at ≈ 0.9 and 3.5 eV above the Fermi energy [1, 191]. The nearly isotropic electrical conductivity, which is only twice as large parallel to the rutile c axis as compared to its in-plane value [36, 146], has been attributed to the existence of at least two different bands near the Fermi energy and a rather complex Fermi surface [28]. The same conclusion was drawn from optical, Seebeck coefficient and magnetization measurements [247, 28, 44]. For the insulating phase photoemission studies revealed a sharpening and downshift of the occupied V $3d$ bands [32, 226, 29, 102, 103] while the XAS measurements revealed a splitting of the lowest unoccupied $3d$ state [1, 191].

Theoretical approaches to the insulating ground state as well as to the metal-insulator transition range from phenomenological models to first principles studies. In a survey over oxides with octahedral coordinated transition metals Goodenough pointed out the important role of direct cation-cation interactions, which add to and often supersede the cation-anion-cation interactions [106]. If strong enough, the cation-cation interactions may give rise to a covalent-type bonding at low temperatures going along with a displacement of the metal atom away from the center of symmetry of the anion interstice as well as with a spin pairing of the bonding electrons. In the case of VO_2, the latter would explain the observed Curie-Weiss behaviour above T_c and the small temperature-independent van Vleck susceptibility below [146]. Since those d electrons, which are responsible for the metal-metal bonding, do not contribute to metallic conductivity, the phase transition may be from metallic to semiconducting. Subsequently, Kawakubo proposed that the metal-insulator transition might be due to electronic excitations from the bonding to the antibonding state, which originate from the covalent-type bonding [132]. The relationship between the size of the energy gap and the number of excited carriers was explicitly formulated by Adler and Brooks who, in addition, attributed the insulating ground state to a doubling of the high-temperature phase unit cell due to either antiferromagnetic order or a crystalline distortion [3, 4].

Lateron, Goodenough presented a schematic energy band diagram for both the metallic and the insulating phase [107, 108]. Using electrostatic considerations for the effective ionic charges he placed the oxygen $2p$ levels well below the vanadium $3d$ states, which in turn are subject to octahedral crystal splitting into lower t_{2g} and higher e_g levels. Furthermore, the t_{2g} orbitals were split into a $d_{\|}$ orbital, which is directed along the rutile c axis, and the remaining π^* orbitals. In the monoclinic phase metal-metal pairing along the rutile c axis causes splitting of the $d_{\|}$ band into bonding and antibonding states while the π^* bands are shifted to higher energies due to the antiferroelectric-type zigzag displacement of the vanadium atoms. As a result, a band gap opens between the bonding $d_{\|}$ band and the other t_{2g} bands. Nevertheless, in proposing this scheme Goodenough questioned the covalent-type bonding arising from metal-metal pairing as the major source of the phase transition and put more emphasis on the antiferroelectric-type distortion of the VO_6 octahedra [107, 108]. Using this general band scheme Hearn performed numerical calculations for one-dimensional vanadium chains and demonstrated the validity of the scenario sketched by Goodenough [116].

First principles studies for rutile VO_2 range from calculations using semiempirical or overlapping free atom potentials [55, 111] to self-consistent state-of-the-art investigations [194, 5, 259]. Work on the insulating and monoclinic (M_1) phase includes a semiempirical calculation [56] as well as a recent molecular dynamics study [259]. Most of these calculations confirmed the general molecular-orbital scheme sketched by Goodenough in that they found the same order of bands for the metallic phase and related the change in electronic structure occuring at the phase transition to the simultaneous symmetry-lowering distortions of the crystal structure.

Nevertheless, the situation was complicated by the discovery of a second low-temperature phase of VO_2, which appeared on application of uniaxial stress or on doping with acceptor-like ions as e.g. Cr, Fe, or Al [169, 207]. For this monoclinic socalled M_2 phase, x-ray and NMR measurements revealed two types of vanadium chains, which display either metal-metal pairing or the zigzag-like in-plane displacement [169, 97, 207]. These experiments allowed to view the M_1 phase as a superposition of two M_2-type displacements [207, 199]. Susceptibility measurements on the M_2 phase were interpreted to the effect that the zigzag-type chains behave like linear antiferromagnetic spin-$\frac{1}{2}$ Heisenberg chains [207]. These findings were difficult to reconcile with all those theoretical approaches, which had explained the insulating ground state as originating from crystal structure distortions with a predominant influence of either the pairing or the zigzag-type displacement. Furthermore, from the presence of localized $3d$ electrons on the zigzag chains and the antiferromagnetic ordering of the moments forming non-interacting linear Heisenberg chains many authors concluded that band theory were unable to correctly describe the physics of the M_2 and, hence, also M_1 phase. Instead, electronic correlations were regarded as essential and localized models called for [207, 279, 215].

Although, as Rice *et al.* have pointed out again only recently [215], discussion of the monoclinic M_2 phase of VO_2 thus is essential for a comprehensive understanding of the physics underlying the metal-insulator transition, state-of-the-art first principles calculations for this phase do not seem to exist. In order to close this gap we initiated the present first principles study, which addresses to the rutile as well as the monoclinic M_1 and M_2 phases on the same footing. Since the low-temperature M_1 and M_2 phases involve characteristic but still relative small deviations from the rutile phase we follow the lines of the previous chapters on MoO_2 and start out investigating the rutile structure. The results will then serve as a reference for the subsequent investigation of the low-temperature phases. From the differences important information concerning the stability of the latter structures can be deduced. Furthermore, investigation of the rutile system in itself may allow to identify those mechanisms, which might destabilize the rutile phase and drive the phase transition.

Leaving investigation of the low-temperature phases to the following chapters we turn in the present chapter to the rutile structure. The chapter is organized as follows: Starting with a short description of the rutile crystal structure in Sec. 7.2, we outline the calculational method in Sec. 7.3. The results are presented in Sec. 7.4. The conclusion, Sec. 7.5, sums up the most important findings.

7.2 The rutile structure

In the metallic phase VO_2 crystallizes in the rutile structure, which is based on a simple tetragonal lattice with space group $P4_2/mnm$ (D_{4h}^{14}) [262, 179]. The metal atoms are located at the Wyckoff positions (2a): $(0, 0, 0)$, $(\frac{1}{2}, \frac{1}{2}, \frac{1}{2})$ and the oxygen atoms occupy the positions (4f): $\pm(u, u, 0), \pm(\frac{1}{2}+u, \frac{1}{2}-u, \frac{1}{2})$. The crystal structure is displayed in Fig. 7.1. According to McWhan *et al.* the lattice constants and the internal oxygen parameter amount to $a_R = 4.5546$Å, $c_R = 2.8514$Å and $u = 0.3001$ [179]. These numbers will be used in the calculations. The ratio of the crystal axes assumes the value $c_R/a_R = 0.626048$, which is intermediate among the rutile related transition dioxides [216]. Nevertheless, as McWhan *et al.* pointed out, the value for c_R, hence, the shortest metal-metal distance, is anomalously small as compared to the neighbouring compounds TiO_2 and CrO_2 [179]. While Westman reported slightly different lattice parameters for metallic VO_2 [262], the numbers by McWhan *et al.* are in very close agreement with the values given by Marezio *et al.* for $V_{0.976}Cr_{0.024}O_2$ ($u = 0.3004$) as well as with those by Ghedira *et al.* for VO_2 doped with 1.5% of Al ($a_R = 4.5546$Å, $c_R = 2.8528$Å and $u = 0.3001$) [169, 97].

A more detailed description of the rutile structure and the local coordinate systems used for the discussion of the electronic bands and partial densities of states has been already given in section 5.2. Since we use the same notations in the present as well as the following chapters we refer to reader to the above section for details.

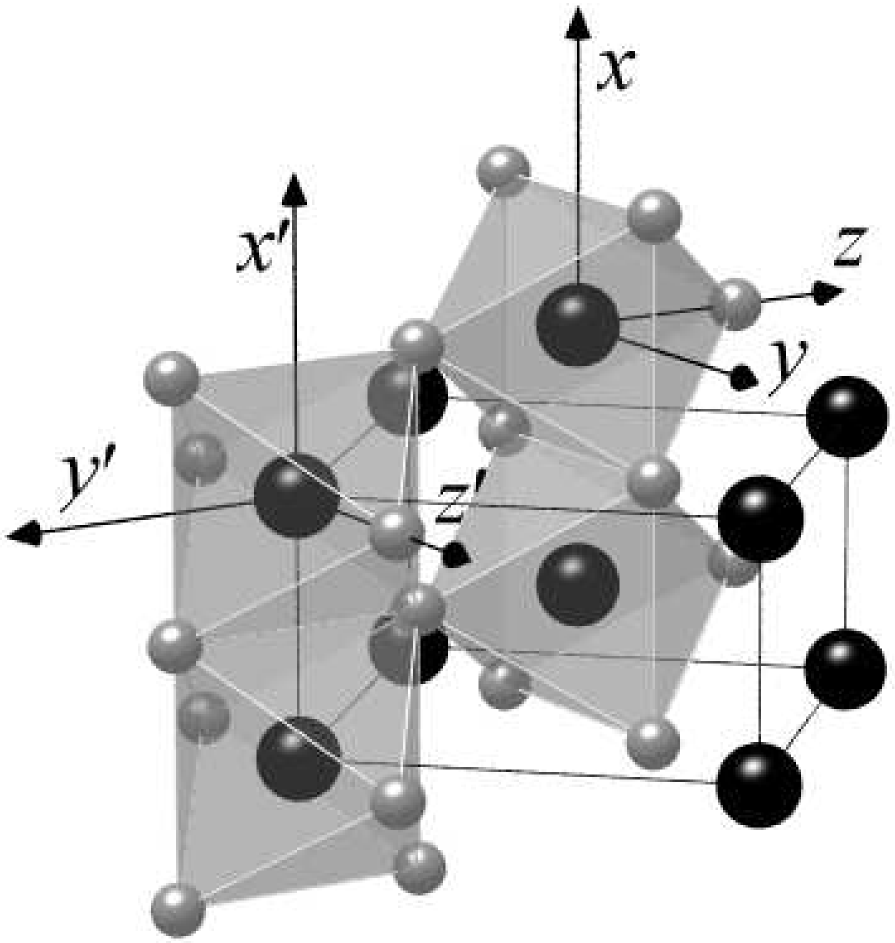

Figure 7.1: Crystal structure of rutile VO_2. Metal and ligand atoms are shaded black and light gray, respectively.

7.3 Method of calculation

We use the sphere geometry optimization algorithm for fixing the necessary empty sphere positions as well as the radii of all spheres automatically. By inserting 16 empty spheres into the rutile unit cell of VO_2, we kept the linear overlap of any pair of physical spheres below 15%, and the overlap of any pair of physical and empty spheres below 20%. The positions of the empty spheres are listed in Table 7.1. There the Wyckoff position (8i) corresponds to the atomic coordinates $\pm(x, y, 0), \pm(y, x, 0), \pm(\frac{1}{2}+x, \frac{1}{2}-y, \frac{1}{2}), \pm(\frac{1}{2}+y, \frac{1}{2}-x, \frac{1}{2})$. In addition to the empty sphere positions the SGO algorithm proposed atomic sphere radii for all spheres, which are listed in Table 7.2. Table 7.2 moreover supplies the orbitals used as the basis set for the present calculations where states given in parentheses were included as tails of the other orbitals. The Brillouin zone sampling was done using an increasing number of **k** points, which range from 18, 40, 126, 288, 550 to 1800 points within the irreducible wedge.

Atom	Wyckoff positions	parameters	
		x	y
E_1	(4d)		
E_2	(4g)	0.3237	
E_3	(8i)	-0.0674	0.3123

Table 7.1: Empty sphere positions.

Atom	Radius/a_B	Orbitals			
V	2.077	$4s$	$4p$	$3d$	$(4f)$
O	2.058	$2s$	$2p$	$(3d)$	
E_1	1.506	$1s$	$(2p)$		
E_2	1.545	$1s$	$2p$	$(3d)$	
E_3	1.207	$1s$	$(2p)$		

Table 7.2: Atomic sphere radii and basis set orbitals.

7.4 Results and Discussion

7.4.1 Electronic structure and partial DOS

From the phenomenological band scheme sketched by Goodenough as well as from our results for hypothetical rutile MoO_2 we expect the oxygen $2p$ levels to be completely filled whereas the V $3d$ levels, which comprise one electron, will be found at and above the Fermi energy [106, 108]. Octahedral crystal field splitting shifts the $3d$ e_g levels to higher energies while the $3d$ t_{2g} derived bands are located at the Fermi energy. Yet, further splitting of the $3d$ levels will arise from the fact that the local octahedral symmetry actually is orthorhombic.

We display in Fig. 7.2 the electronic states along selected high symmetry lines within the first Brillouin zone of the simple tetragonal lattice, Fig. 7.3. The corresponding density of states (DOS) is given in Fig. 7.4 where we have added the dominant partial densities of states. The total density of states at the Fermi energy, $N(E_F)$, amounts to 3.36 states/f.u./eV. Not shown are low lying oxygen $2s$ states.

In Figs. 7.2 and 7.4 we identify four groups of bands. In the energy range from -8.0 to -2.4 eV we observe 12 bands which trace back mainly to O $2p$ states but have a non-negligible contribution due to the V $3d$ states. Bands are most easily counted along the direction X-R where they are twofold degenerate. The next two groups, which extend from -0.6 to 2.0 eV and from 2.0 to 5.3 eV, contain six and four bands, respectively and originate mainly from V $3d$ states. Yet, $p-d$ hybridization, which has shown to be substantial in recent photoemission experiments [278], causes additional O $2p$ contributions in this energy range. Finally, we observe V $4s$ states starting at 8.0 eV.

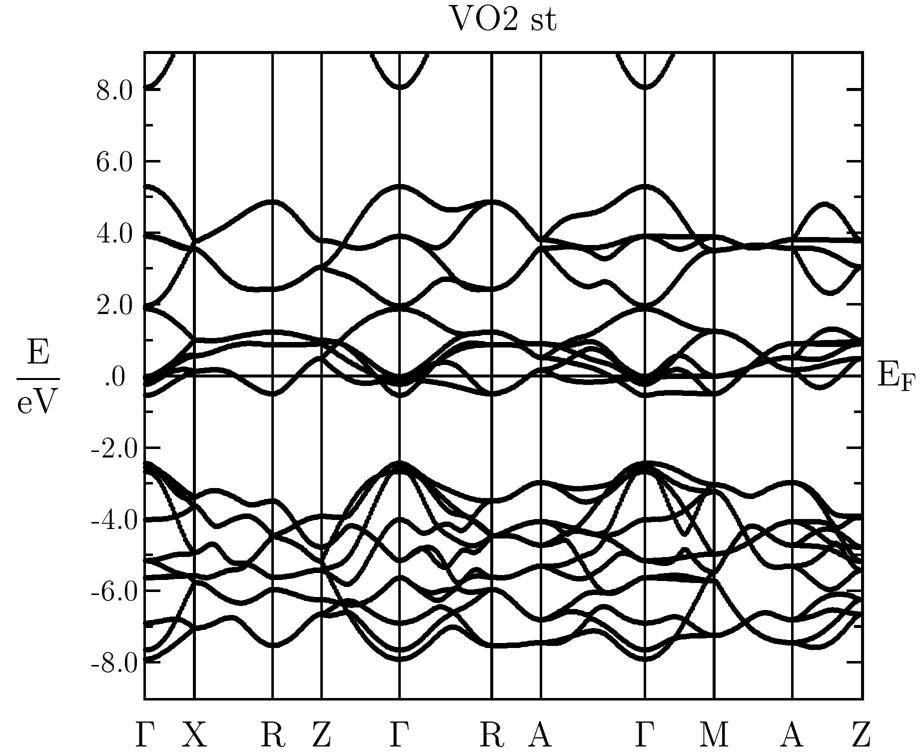

Figure 7.2: Electronic bands of rutile VO_2 along selected symmetry lines within the first Brillouin zone of the simple tetragonal lattice, Fig. 7.3.

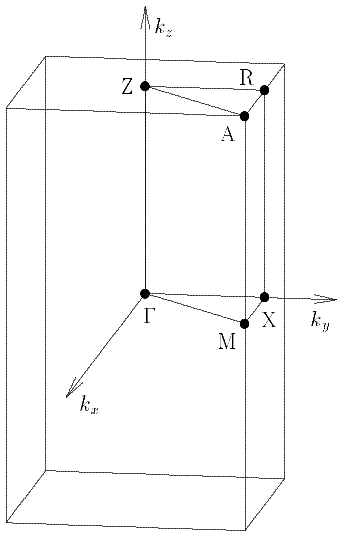

Figure 7.3: First Brillouin zone of the simple tetragonal lattice.

Crystal field splitting expected from the fact that the metal atoms are located at the centers of distorted VO_6 octahedra is observed in the partial V $3d$ DOS shown in Fig. 7.5. There we have included only the single vanadium atom at $(0, 0, 0)$ and used the local rotated reference frame. Fig. 7.5 clearly reveals the almost perfect energetical separation of the $3d$ t_{2g} and e_g groups of bands. The former states appear almost exclusively in the energy range from -0.6 to 2.0 eV whereas the e_g states dominate the bands between 2.0 and 5.3 eV. The small but finite t_{2g} – e_g

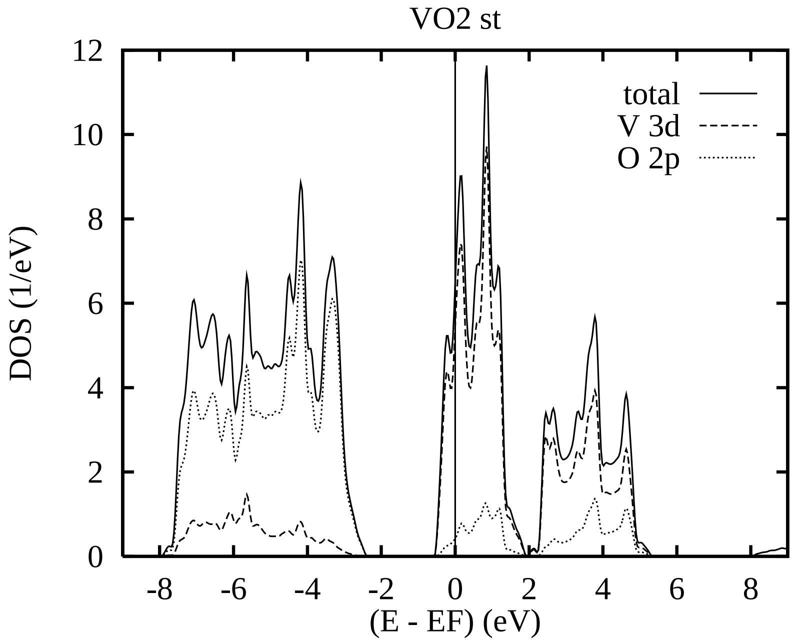

Figure 7.4: Total and partial densities of states (DOS) of rutile VO_2 per unit cell.

configuration mixing is a measure of octahedral distortions. Contributions of the V $3d$ states to the oxygen bands are slightly larger for the e_g states which, forming σ bonds, experience a larger overlap with the O $2p$ states. For the same reason, the bonding-antibonding splitting is larger for the e_g states as compared to the t_{2g} states, which give rise to π bonds.

So far, our results fully agree with those for hypothetical rutile MoO_2. However, deviations show up in a more detailed analysis of the single symmetry components of the t_{2g} and e_g orbitals as given in Fig. 7.5, which reflect the orthorhombic site symmetry. In MoO_2 the Mo $4d_{x^2-y^2}$ band shows a strong tendency towards bonding-antibonding splitting while the remaining t_{2g} bands give rise to very similar densities of states. In contrast, in VO_2 bonding-antibonding splitting of the V $3d_{x^2-y^2}$ band is mainly suppressed. In addition, the $3d_{xz}$ and $3d_{yz}$ partial DOS show distinct deviations. In particular, the latter reveals some splitting into two peaks at about -0.3 and 1.1 eV. These features may be traced back to the much larger c axis of VO_2 (2.8514Å vs. 2.805Å in MoO_2) which leads to a larger separation of the metal atoms along this axis. In contrast, the rutile a axis is reduced (4.5546Å vs. 4.856Å in MoO_2) this causing a larger overlap of metal d orbitals within the planes and, hence, a visible bonding-antibonding splitting of the local d_{yz} orbitals.

From a molecular-orbital point of view we interprete the bands between -8.0 and -2.4 eV as O $2p$-dominated lower σ and higher π states while the respective π^* and σ^* states are found in the energy intervals from -0.6 to 2.0 eV and 2.0 to 5.3 eV. These latter bands trace back mainly to V $3d$ t_{2g} and e_g states. In this context, classification as bonding and antibonding refers to the overlap of O $2p$ and V $3d$ orbitals, which has to be distinguished from the metal-metal bonding. As mentioned before, the latter applies mainly to the V $3d_{x^2-y^2}$ and $3d_{yz}$ states due to their overlap along the rutile c and a axes. However, in the low-temperature monoclinic phases only the

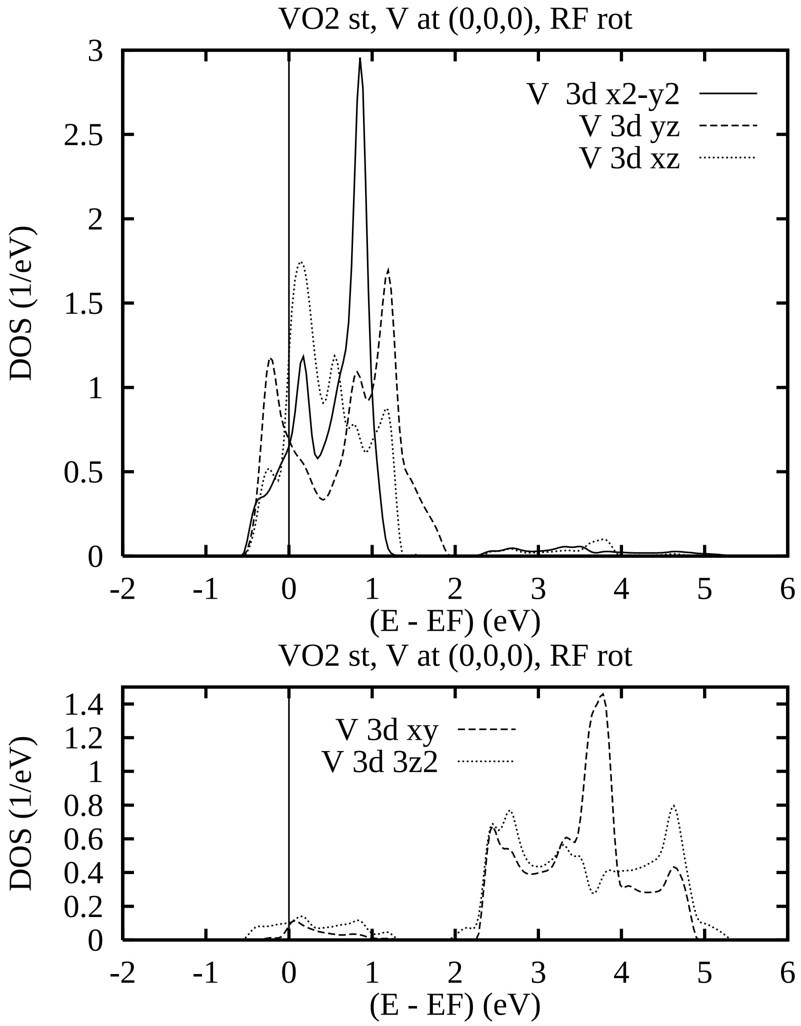

Figure 7.5: Partial V $3d$ t_{2g} and e_g densities of states (DOS) of rutile VO_2. Selection of orbitals is relative to the local rotated reference frame.

$d_{x^2-y^2}$ orbitals reveal major changes in that they experience increased metal-metal pairing and, hence, bonding-antibonding splitting. For that reason the $d_{x^2-y^2}$ orbital has been distinguished from the d_{xz} and d_{yz} states and, following Goodenough, the notations $d_{\|}$ and π^* for these states have become customary [107, 108]. As expected from the previous discussion all our results agree well with the molecular-orbital scheme put forward by Goodenough [107, 108]. However, in contrast to Goodenough's scheme our $d_{x^2-y^2}$ band displays a considerable width of ≈ 1.5 eV and, hence, cannot be regarded as narrow.

While our calculations are in qualitative agreement with the calculations by Caruthers *et al.* as well as by Gupta *et al.* [55, 111], a more detailed analysis reveals small but distinct deviations concerning the exact band positions and, consequently, the Fermi surface. We attribute these differences to the approximations inherent to the old calculations. Good agreement, however, is found in a comparison with the existing state-of-the-art calculations by Wentzcovitch *et al.* [259]. Minor differences in the band structures may result from the use of the crystal structure data of Ref. [262] or from Brillouin zone samplings with different numbers of **k** points. Finally, we observe distinct deviations in the recent calculations by Nikolaev *et al.* with respect to the band positions [194]. While our calculations give an occupied V 3*d* bandwidth of 0.6 eV, in close agreement with Wentzcovitch *et al.*, Nikolaev *et al.* report a value of 0.77 eV. At the same time, the latter authors locate the upper edge of the O 2*p* bands 1.39 eV below the Fermi level whereas in our calculation the band maximum is found at -2.4 eV in almost perfect agreement with both the optical measurements by Verleur *et al.* and the photoemission data by Powell *et al.*, Shin *et al.*, Bermudez *et al.* as well as Goering *et al.* who find these states 2.4-2.5 eV below the Fermi energy [247, 208, 226, 29, 98, 103]. The total width of the O 2*p* band of 5.37 eV reported by Nikolaev *et al.*, finally, is again in agreement with our value of $\approx$ 5.6 eV.

In passing we point to the almost equal densities of states of all three t_{2g} orbitals, which confirm the reported isotropic conductivity [36, 146].

7.4.2 Chemical bonding

We address chemical bonding via the crystal orbital overlap population as shown in Fig. 7.6. The COOP curves display the rather "canonical" behaviour being positive

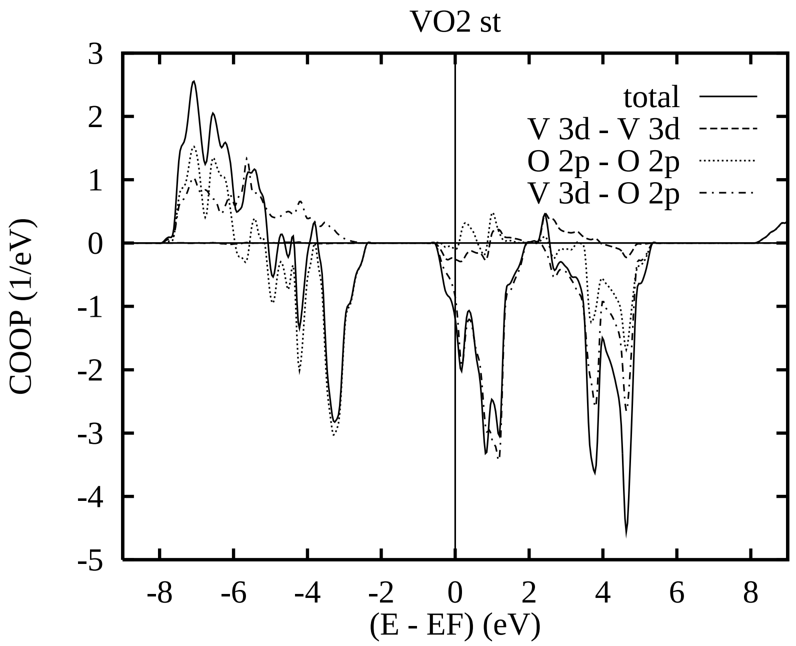

Figure 7.6: Total and partial crystal orbital overlap populations (COOP) of rutile VO_2.

(bonding) and negative (antibonding) in the low and high energy regions of a band. In case of the oxygen-oxygen overlap this is visible for both the oxygen and vanadium dominated bands separately the absolute values being higher in the former. Below $\approx$ -6.0 eV we find bonding O-O bands whereas antibonding bands appear in the energy range between $\approx$ -5.0 and -2.4 eV. As a consequence, the net contribution of the occupied oxygen-oxygen bonds to the chemical stability is rather small. The same holds for the almost negligible metal-metal bonding. The dominating contribution to the chemical stability, finally, results from the overlap of V 3*d* and O 2*p* orbitals. The corresponding COOP curve is positive below -2.4 eV and negative only in the V 3*d* derived bands. The metal-ligand bonding is thus the main responsible for the chemical stability of rutile VO_2.

7.4.3 Comparison to experiment

We display in Figs. 7.7 and 7.8 total and partial V 3*d* and O 2*p* densities of states

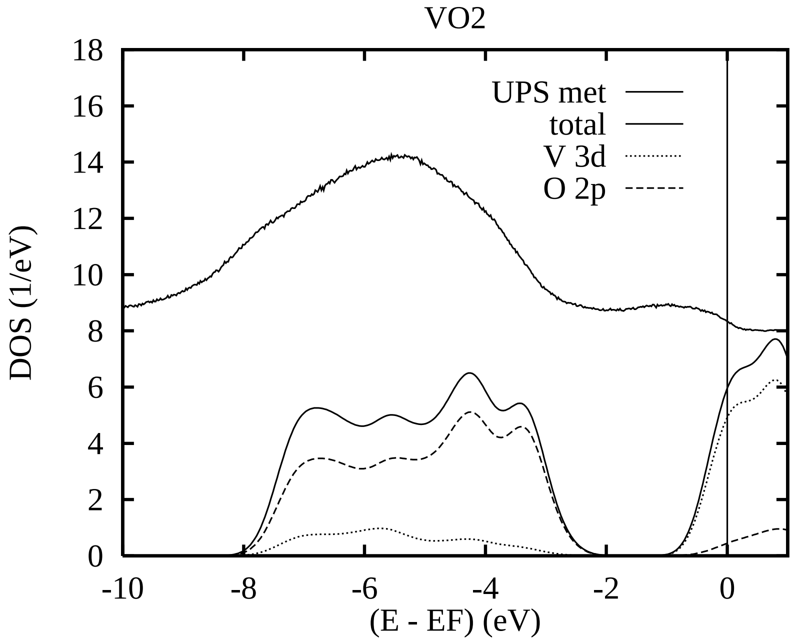

Figure 7.7: Total and partial densities of states (DOS) of VO_2 folded with a 0.25 eV wide Gaussian (lower set of curves) and UPS spectra (upper curve; from Ref. [98, 103]).

folded with a Gaussian of 0.25 and 0.5 eV width, respectively, for the occupied and unoccupied part of the spectrum. In Fig. 7.7 we have added UPS spectra as measured by Goering *et al.* [98, 103]. Good agreement of the calculated and measured curves is found. In addition, the calculated total DOS compares very well with the XPS and UPS spectra by Blaauw *et al.*, Shin *et al.* and Bermudez *et al.* [32, 226, 29]. The occupied bandwidth of $\approx$ 8.5 eV deduced from the experiments is close to the calculated 8.0 eV. According to the XPS and UPS spectra the valence band is split into a low and high binding part of about 1.5 and 6 eV width, respectively [32, 226, 103]. Whereas the low binding region results from a single peak centered at $\approx$ -1.0 eV, which is attributed to the V 3*d* states, the high binding region, resulting mainly from the O 2*p* states, is dominated by a large peak at $\approx$ -5.5 eV and shows two slight shoulders at -4.0 and -7.5 eV [98, 103]. In contrast, as compared to the UPS data, the XPS spectra display a considerably higher intensity at energies below -5.5 eV and a strong decrease in intensity around the top of the O 2*p* band [32, 226]. Since the V 3*d* states have a larger cross section in XPS [272, 125] this shift of intensity reveals a considerable V 3*d* contribution especially to the bands

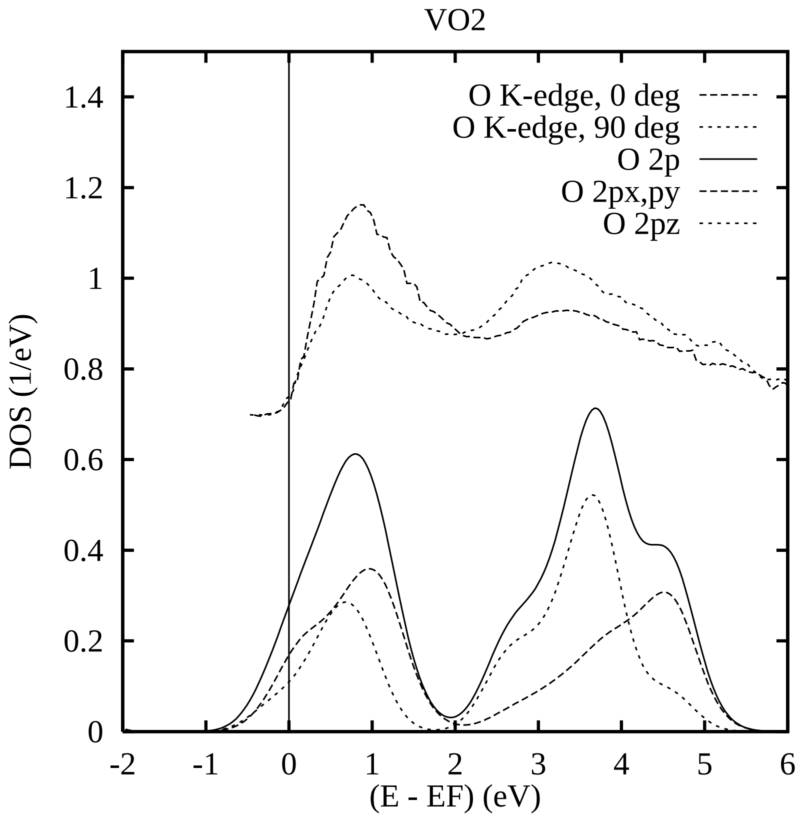

Figure 7.8: Partial O $2p$ densities of states (DOS) of VO_2 folded with a 0.5 eV wide Gaussian (lower set of curves) and XAS O K edge spectra (upper set of curves; from Ref. [190, 191]; data shifted by 529.5 eV).

below -5.5 eV and, hence, a strong $p-d$ hybridization in this energy region. This is well reflected by the calculations.

In Fig. 7.8 we have complemented the theoretical results by soft-x-ray absorption spectra as measured by Müller *et al.* [190, 191]. The experimental data are shifted by 529.5 eV. In order to probe the angular dependence, in these experiments the polarization vector $\mathbf{E}$ was oriented either parallel ($\phi = 90°$) or else perpendicular ($\phi = 0°$) to the rutile c axis. In the former case, dipole selection rules allow for transitions from O $1s$ to the O $2p_z$ state. In contrast, for $\mathbf{E}$ perpendicular to the c axis transitions to the O $2p_x$ and $2p_y$ states may occur. The curves given by Müller conform with the spectra by Abbate *et al.* who found, for metallic VO_2, two peaks at 529.9 and 532.5 eV photon energy for $\mathbf{E} \parallel \mathbf{c}$ [1]. In the spectra given by Müller *et al.* these peaks are located at 530.3 and 532.7 eV, respectively [191]. However, as Müller has pointed out previously, the curves actually can be fitted to four peaks at 530.1, 530.7, 532.7, and 534.7 eV [190]. In the energy-shifted spectra of Fig. 7.8 these peaks are located at 0.6, 1.2, 3.2, and 5.2 eV.

In Fig. 7.8, the partial DOS correspond to the final states, which are occupied in the XAS experiments. Note that the curve marked O $2p_x, p_y$ comprises only the mean average of these orbitals since the component perpendicular to $\mathbf{E}$ is not seen in experiment. For the same reason, the curve marked O $2p$ actually contains the contribution from $\frac{1}{2}(p_x + p_y) + p_z$. As for the occupied part of the spectrum we observe overall good agreement between experiment and theory. This holds for the positions of the peaks, their relative intensity and their angular dependence. Still, agreement seems to be less satisfactory in the high energy region between 4 and 5 eV. However, the discrepancy is resolved by the forementioned four peak analysis of the experimental spectra. Differences with respect to intensities may finally be attributed to matrix element and core-hole effects, which might be important but are not accounted for in our present analysis [65, 1].

7.4.4 Fermi surface

Despite the good agreement of our results with previous experimental and calculated data we are still seeking for more conclusive arguments for the destabilization of the rutile structure of VO_2 at low temperatures. Since the metal-insulator transition is accompanied by a structural transformation one might be tempted to deduce more information about the origin of the transition from an investigation of the Fermi surface. This has been already done by Gupta *et al.* in the course of their non-selfconsistent calculations [111]. Furthermore, investigation of the Fermi surface of hypothetical rutile MoO_2 in chapter 5 revealed strong nesting on flat portions at height $q_z = \pm\frac{\pi}{2c}$, which pointed to a splitting of the $d_{x^2-y^2}$ band. The latter was indeed observed in monoclinic MoO_2.

Cuts through the Fermi surface parallel to the {100} and {110} planes as resulting from the present calculations are shown in Figs. 7.9, 7.10, and 7.11. They contain

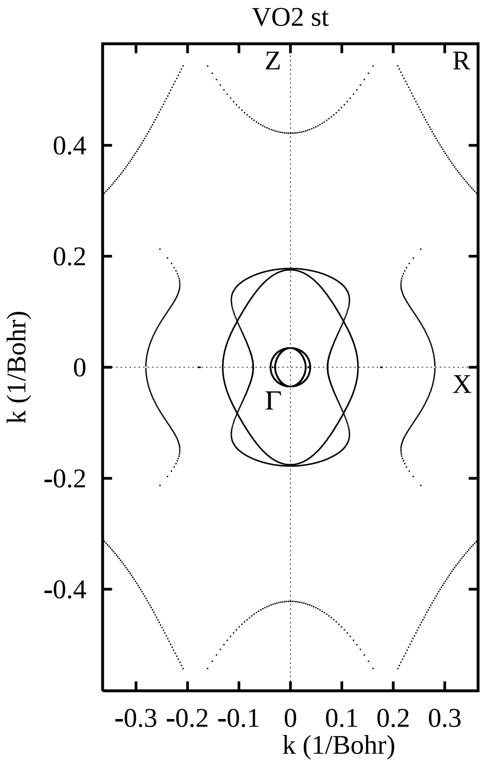

Figure 7.9:{100} cut through the Fermi surface of rutile VO_2.

the Γ-X-Z-R, Γ-M-Z-A, and X-M-R-A planes, which are the vertical borders of the

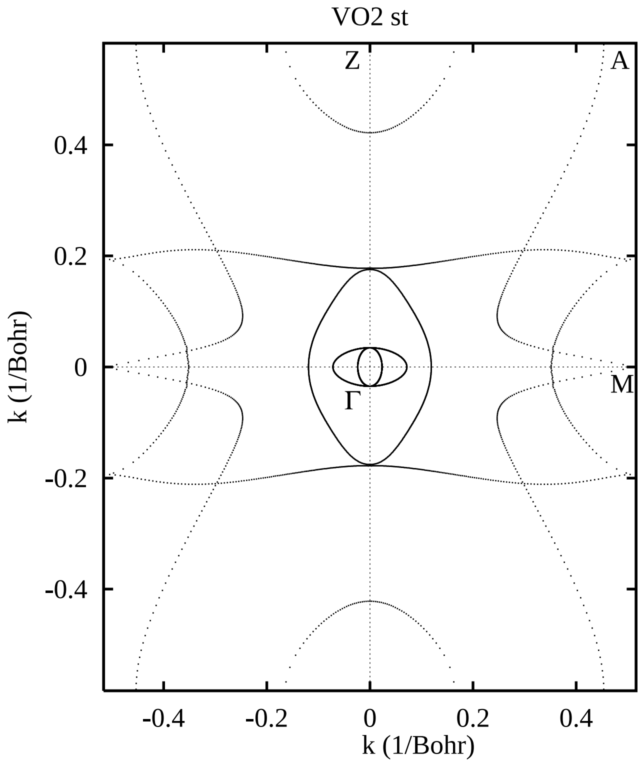

Figure 7.10:{110} cut through the Fermi surface of rutile VO_2.

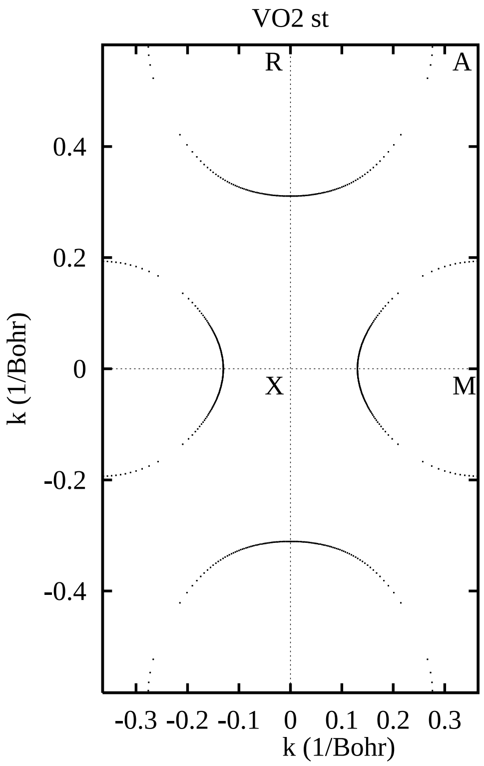

Figure 7.11:{100} cut through the Fermi surface of rutile VO_2.

irreducible wedge of the first Brillouin zone, Fig. 7.3. As before, interpretation of the figures is greatly facilitated by combining them with the band structure shown in Fig. 7.2. We recognize electron- and hole-like regions near the Γ and Z point, respectively. Nevertheless, in contrast to the non-selfconsistent calculations by Gupta *et al.*, our calculations do not allow to identify any Fermi surface nesting in Figs. 7.9 to 7.11, which might be indicative of a destabilization of the rutile structure. This is in sharp contrast to our findings for hypothetical rutile MoO_2. However, since there is one d electron less in VO_2, the differences between both compounds actually are not too suprising. We thus conclude, that investigation of the Fermi surface does not allow for an explanation of the low-temperature instability of the rutile structure. In so far, our result resembles the above mentioned argument of Goodenough against a Jahn-Teller-type distortion as the major source for the crystal structure distortions.

7.4.5 Lattice instability

Still, we expect that the existence of the monoclinic phases in both molybdenum and vanadium dioxide should have a common origin even if a Fermi surface instability seems to be spoiled by the missing d electron in the latter compound. For this reason, it is worthwhile to proceed along the same lines as in our work on MoO_2 and to draw as many conclusions as possible from a comparison of both compounds. To this end, we start the following discussion with a more detailed analysis of the electronic structure shown in Fig. 7.2. The result is presented in Figs. 7.12, 7.13, and 7.14 where we display the electronic bands in the narrow energy range from -1.0 to 2.5 eV about the Fermi energy in the same special representation as in chapter 5 on MoO_2: In all three Figures, each band at each **k** point is given a bar which length is a measure for the contribution from a specified orbital. Since we again refer to the local frame of reference, Figs. 7.12 to 7.14 correspond to the partial V $3d$ t_{2g} DOS shown in Fig. 7.5, which likewise made use of the local coordinate system.

As in MoO_2, we observe a strong dispersion of the V $3d_{x^2-y^2}$ derived bands along all lines parallel to Γ-Z in Fig. 7.12, whereas the dispersion perpendicular to this line is almost vanishing. Again, we attribute this dispersion to the overlap of $d_{x^2-y^2}$ orbitals at metal sites neighbouring in z direction. As compared to MoO_2 the width of these bands is reduced this fact reflecting the increased value of the rutile c axis and, hence, the larger metal-metal distance in this direction. In contrast, the smaller value of the a axis in VO_2 causes a larger interchain interaction thus leading to an increased splitting of the $d_{x^2-y^2}$ bands along the lines Γ-M and A-Z as well as along the lines where the strong dispersion is observed.

The V $3d_{yz}$ derived bands are highlighted in Fig. 7.14. They show a large dispersion in all directions and, as in MoO_2, a large splitting at the Γ point, which is a consequence of the underlying body-centered tetragonal (bct) lattice formed by the metal atoms and results from backfolding the bands from the Brillouin zone of the bct lattice to the smaller one of the simple tetragonal lattice. This effect can be read off from the bands along the lines connecting the Γ point to the X, M, A, and Z point, respectively. Finally, the V $3d_{xz}$ derived bands display the smallest dispersion due to the fact that these orbitals induce no substantial σ-type overlap with neighbouring metal atoms but instead mediate the small coupling between the

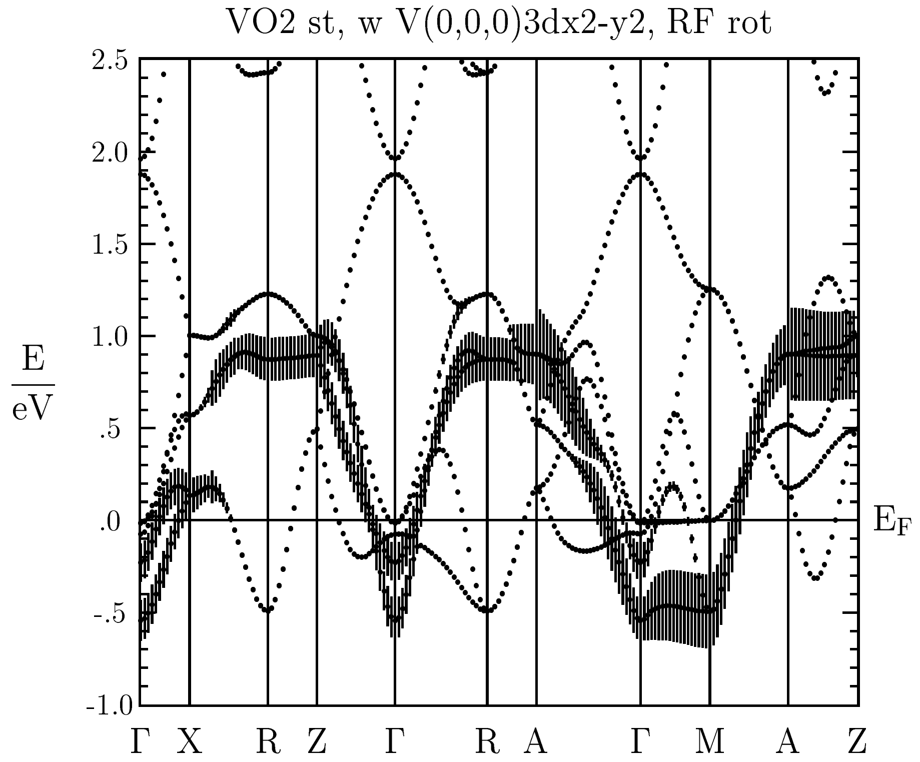

Figure 7.12: Weighted electronic bands of rutile VO_2. The width of the bars given for each band indicates the contribution due to the $3d_{x^2-y^2}$ orbital of the V atom at (0,0,0) relative to the local rotated reference frame.

octahedral chains. Still, the larger width of these bands as compared to MoO_2 results from the increased interchain coupling coming with the smaller value of the a lattice constant.

Of course, the previous analysis of the t_{2g} bands with its nearly unique assignment of a single character to each band and the subsequent interpretation in terms of the geometric coordination of the atoms and their orbitals benefitted from the very small mixing among these states. Exceptions are the hybridization of the $d_{x^2-y^2}$ bands with the d_{yz}- and d_{xz}-derived bands along the symmetry line X-R and, to a smaller degree, along the line Γ-A. Nevertheless, we summarize that the three t_{2g} bands disperse almost completely independent. Eventually, this fact has a strong impact on our further understanding since it lays ground for an interpretation of changes of the electronic properties in terms of structural changes and vice versa. In particular, it allows to address the question as to which changes of the crystal structure might shift a particular band in a certain direction and thus might lower the total energy. This way, we may find a route to the low-temperature monoclinic structure.

Using the molecular orbital picture outlined in Sec. 7.4.1 and concentrating on the early transition metal oxides we discuss mechanisms which could lower the total energy and thus drive the phase transition. As already pointed out by Goodenough, two different mechanisms are effective, namely metal-oxygen and metal-metal bonding [106]: Strengthening of the metal-oxygen bonds will increase the bonding-antibonding splitting of both the π and σ bands and, since the respective

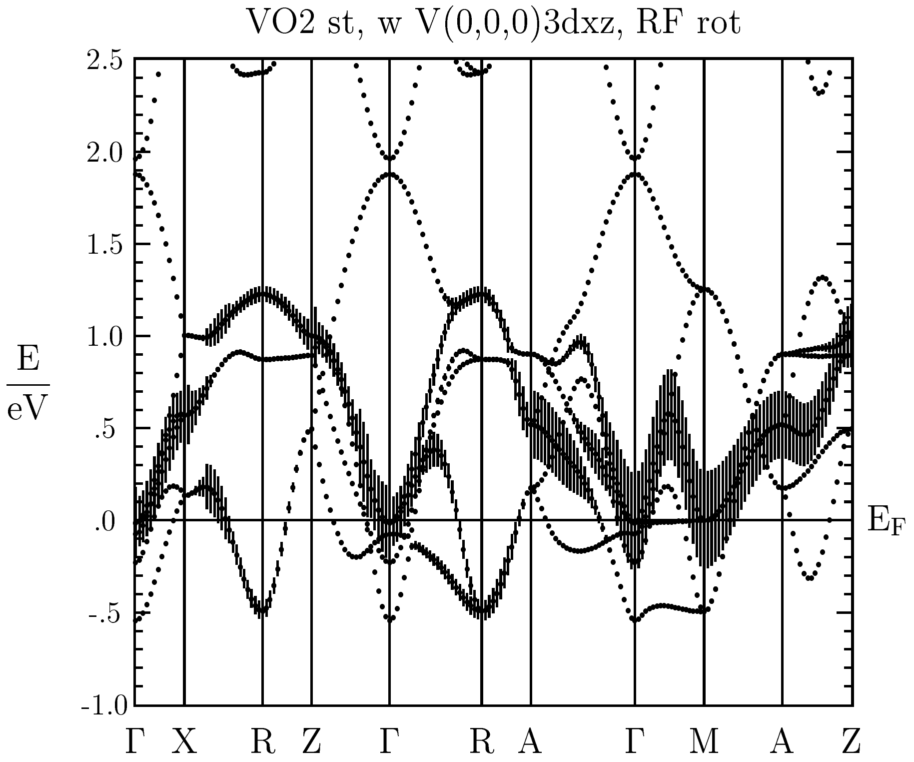

Figure 7.13: Weighted electronic bands of rutile VO_2. The width of the bars given for each band indicates the contribution due to the $3d_{xz}$ orbital of the V atom at (0,0,0) relative to the local rotated reference frame.

antibonding states are only partially occupied, furthen chemical stability and lower the total energy. Hence, even without any prior knowledge of the low-temperature monoclinic structure of VO_2 we would expect an increase of metal-oxygen bonding at lower temperatures. The situation has been studied in chapter 4 on semiconducting V_2O_5, where the vanadium atoms are vertically shifted away from the center of the surrounding oxygen octahedra in a ferroelectric-like mode. As a consequence, the V $3d_{xz}$ and $3d_{yz}$ orbitals experience increased overlap with the $2p_x$ and $2p_y$ orbitals of the apical oxgen atoms thus causing an increased bonding-antibonding splitting of the V $3d$ t_{2g}/O $2p$-derived π bands and, hence, an upshift of the π^* states. However, the third t_{2g}-derived band, which is the V $3d_{xy}$ band in the case of V_2O_5, is not affected by the vertical vanadium shifts.

In contrast, metal-metal bonding allows to split a specific t_{2g} band into a bonding and antibonding subband. Depending on the position of the original band this situation may lead to an increase and decrease of the respective band occupations and, hence, likewise enhance chemical stability. The ability of such a mechanism has been demonstrated in the previous chapters on MoO_2, where metal-metal pairing along the rutile c axis leads to substantial splitting of the $d_{x^2-y^2}$ band into occupied bonding and empty antibonding bands, which are separated by more than 3.5 eV. Since, in addition, all those portions of the Fermi surface calculated for hypothetical rutile MoO_2, which originated from the $d_{x^2-y^2}$ band, are removed the dimerization suggested an interpretation in terms of a Peierls-like instability towards the "real"

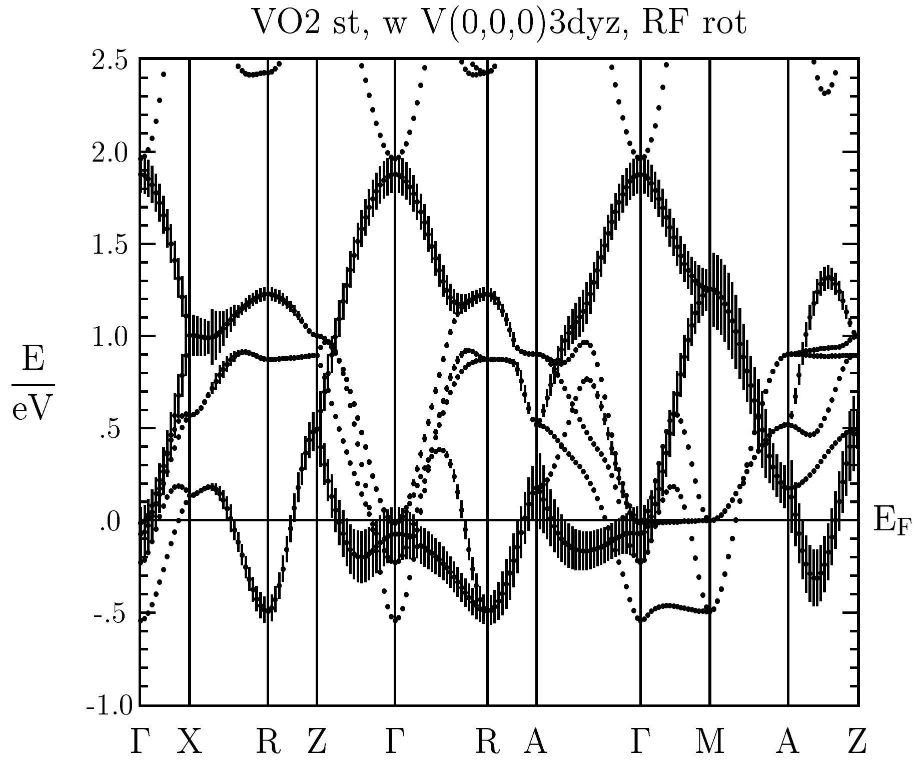

Figure 7.14: Weighted electronic bands of rutile VO_2. The width of the bars given for each band indicates the contribution due to the $3d_{yz}$ orbital of the V atom at (0,0,0) relative to the local rotated reference frame.

monoclinic structure.

These rather general ideas are most easily stated in terms of the concept of bond order. The bond order as given e.g. by Pettifor [202] provides a measure for the strength of a particular bond and is closely related to the integrated COOP [121]. From the "canonical" sinusoidal-like behaviour of the latter as mentioned in Sec. 7.4.2 we deduce a cosine- or triangular-like shape for the bond order, which, except for a factor of two, is given by the difference between the occupations of the bonding and antibonding states. To be more pictorial, on filling a band, bonding states are occupied first until the band is half filled. In this energy range the bond order increases from zero to its maximum value of unity. At higher energies the antibonding states are successively occupied and the bond order decreases, finally reaching zero again. Obviously, chemical stability is highest when the bonding and antibonding states are occupied and empty, respectively, hence, when the bond order assumes its maximum. As a consequence, a compound can be efficiently stabilized by increasing the order of as many bonds as possible. We call this scenario bond order optimization and we will demonstrate in the following that our "bond order optimization model" (BOOM) provides an explanation for many aspects of the transition metal oxides.

Applying the bond order optimization model to VO_2 and considering metal-metal bonding first, we recall the tendency towards pairing along the rutile a axis, which we deduced from the splitting of the d_{yz} partial DOS in Fig. 7.5. Actually, σ-type overlap between the vanadium orbitals may be mediated both by the $d_{x^2-y^2}$ and the d_{yz} orbitals along the c and a axis, respectively. For this reason, two corresponding types of pairing must be taken into account. However, according to the weighted band structure for the d_{yz} band as shown in Fig. 7.14, simple dimerization along one of the in-plane tetragonal axes does not lead to a complete separation of the resulting bonding and antibonding states, which might thus be only accessible by more complicated distortion patterns. In contrast, as the results for MoO_2 have clearly demonstrated, due to the rather one-dimensional dispersion of the $d_{x^2-y^2}$ bands, pairing along the c axis enables a complete splitting and thus an efficient lowering of the total energy. Hence, we expect c axis pairing also in VO_2.

From these considerations it becomes clear that metal-oxygen bonding is most efficient for the d_{xz} and d_{yz} bands. In contrast, for the bonding-antibonding split $d_{x^2-y^2}$ band it could cause depopulation of the bonding band and, hence, reduction of the bond order. Transferring the situation of V_2O_5 to VO_2 we realize that the d_{xz} and d_{yz} bands are most easily shifted by a displacement of the vanadium atoms along the local z axis.

In summary, we arrive at the conclusion that the total energy of the rutile structure of VO_2 could still be lowered by metal-metal pairing along the tetragonal c axis and a ferroelectric or antiferroelectric mode which shifts the vanadium atoms along the local z axis. Whereas the pairing causes bonding-antibonding splitting of the local $d_{x^2-y^2}$ bands and thus stabilizes the metal-metal bonds, the (anti)ferroelectric distortion increases the bonding-antibonding splitting coming with metal-ligand hybridization. Obviously, the energy gain due to these atomic shifts would be greatest if the bonding $d_{x^2-y^2}$ states were fully occupied (thus comprising two electrons per unit cell) and all other states, which are antibonding with respect to either metal-metal or metal-ligand bonding, would end up above. With the number of electrons given for VO_2 this situation could be realized. Nevertheless, we point out that the bond order optimization is the primary source of the structural changes, which are identical for all rutile-related transtion metal dioxides at least with respect to their local components. In contrast, the metal-insulator transition seems to be a secondary effect, which results from the particular electron count of the d^1 compounds.

Still, three points should be noticed: i) As was mentioned by Pouget *et al.* as well as by Paquet and Leroux-Hugon the two displacement components of the metal atoms in the monoclinic structure are *not* independent [207, 199, 215]. This is due to symmetry arguments which may be also understood from electrostatics. According to these considerations the pairing on one chain is intimately connected with the zigzag-type displacement on the neighbouring chains: If the vanadium atoms pair on one chain, the atoms on the neighbouring chains, which from the outset are vertically displaced by half the rutile c axis, move off the chain axis towards the apical oxygen atom whose V neighbours of the first sublattice have pulled apart. For this reason, the zigzag-like displacement may be viewed as being induced by the metal-metal pairing along the rutile c axis. These arguments contrast a previous discussion by Goodenough where both types of vanadium displacements were regarded as independent and the zigzag-type motion considered as being essential for the metal-insulator transition [107, 108]. Still there remains an important aspect to be noticed: Despite the strong coupling of both types of metal atoms displacements revealed by the previous symmetry considerations the zigzag-like in-plane displacement of the metal atoms still has to be distinguished from the (anti)ferroelectric distortion discussed previously in the context of metal-oxygen bonding. This is due to the fact that the oxygen octahedron surrounding the central metal atom still is free to follow displacement of the latter: If the oxygen atoms experience a shift similar to that of the central atom metal-oxygen bonding will be mainly unaffected. In contrast, only if the oxygen cage remains in its original position the metal atoms shift induces an (anti)ferroelectric mode. We will come back to these arguments in the chapter 8 where we discuss the displacements in more detail. ii) An aspect, which seemingly has not been considered before but which has important implications for the discussion of the M_2 phase, arises from the fact, that metal-metal pairing along the rutile c axis, in addition to furthen the bonding-antibonding splitting of the $d_{x^2-y^2}$ bands, likewise causes an increased metal-oxygen overlap and thus, if not compensated by a corresponding displacement of the oxygen octahedron, likewise brings in an (anti)ferroelectric-like component. iii) As has been pointed out by Goodenough, metal-metal pairing is not the only source of an efficient splitting of the $d_{\parallel}$ band but the same effect could be achieved by exchange splitting coming with antiferromagnetic order [107, 108].

Finally, the local distortions away from the rutile structure induce a lowering of the lattice symmetry. Obviously, the metal-metal pairing along the tetragonal c axis causes a doubling of the unit cell along this axis. Moreover, as becomes clear from the previous symmetry considerations, the zigzag-like displacement leads to unit cell doubling both parallel to the c and a axis. However, from this information alone we are not able to derive the long range order of the metal atoms displacements and, hence, can not fully specify the wave vector describing the modulation of the tetragonal lattice. Instead, we recall the x-ray diffuse scattering measurements performed just above the metal-insulator transition by Terauchi and Cohen [241], which point to a lattice instability at the tetragonal R point with wave vector parallel to Γ-R and a polarization vector parallel to the c axis. These findings conform with theoretical work by Gervais and Kress who, using a shell model to calculate the phonon dispersion of several rutile-type compounds, found for VO_2 a phonon softening at the tetragonal R point [94]. Furthermore, analysis of the eigenvectors of the R point soft mode resulted in a metal atom displacement pattern equivalent to that of the monoclinic M_2 phase [94].

Combining our results on the local deformations with the previous information about the R point instability we arrive at the situation already sketched in Fig. 5.14. There is a doubling of the periodicity length both along the c and a axes which can be achieved by a simple monoclinic lattice with the primitive translations

$$\mathbf{a}_1 = \begin{pmatrix} 0 \\ 0 \\ -2c \end{pmatrix}, \quad \mathbf{a}_2 = \begin{pmatrix} -a \\ 0 \\ 0 \end{pmatrix}, \quad \mathbf{a}_3 = \begin{pmatrix} 0 \\ a \\ c \end{pmatrix}. \tag{7.4.1}$$

We have adopted the usual notation for the representation of the monoclinic transition metal dioxides. All these conclusions are in full accordance with the observed low-temperature M_1 and M_2 crystal structures of (doped) VO_2, which will be discussed in the following chapters.

7.5 Conclusion

In the present chapter first-principles ASW calculations were used to describe metallic rutile VO_2. The electronic properties are dominated by strong hybridization of O $2p$ and crystal field split V $3d$ states. The $p-d$ hybridization, besides leading to chemical stability, causes formation of O $2p$ dominated σ and π bonding bands. In contrast, σ^*, which result mainly from the V $3d$ e_g orbitals are found above the Fermi energy while the details of the electronic structure near the Fermi energy are due almost exclusively to the V $3d$ t_{2g}-derived π^* orbitals. Our results for the rutile structure serve as a reference for the subsequent investigation of the monoclinic M_1 and M_2 structures appearing below the metal-insulator transition temperature.

Furthermore, we discussed mechanisms which might lead to a destabilization of the rutile structure and possibly drive the phase transition. Investigation of the Fermi surface, however, did not reveal any reason for an instability. Instead, using a detailed analysis of the band characters and proposing the bond order optimization model (BOOM) we discussed the structural instability of the rutile phase in terms of down- and upshift of bonding and antibonding states and the resulting increase of bond order. In this model $p-d$ hybridization drives an antiferroelectric-type mode of the vanadium atoms, which causes upshift of two of the three t_{2g}-derived π^* bands, while the remaining $d_{x^2-y^2}$ band experiences splitting due to pairing of the vanadium atoms along the rutile c axis. The resulting separation of bonding and antibonding states increases chemical stability and, hence, lowers the total energy. The bond order optimization model thus provides a clue for all the early transtion metal dioxides. Fianlly, for the electron count of VO_2 bond order optimization could separate bonding and antibonding states completely, which fact opens the insulating gap.

Chapter 8

VO_2: II. The monoclinic M_1 phase

8.1 Motivation

At ambient pressure, stoichiometric VO_2 undergoes a first order metal-insulator transition at 340 K from the high-temperature rutile to the low-temperature monoclinic M_1 phase [45, 187]. Since the origin of this phase transition is as yet not fully resolved it has attracted long-standing interest in VO_2 and motivated a lot of experimental and theoretical work. Most investigations centered about the question whether the transition is driven mainly by a lattice instability, electron-phonon interaction, electron-electron correlations, or a combination of all these [45].

First evidence for the important role of the lattice degrees of freedom was given by the structural changes at the phase transition. They are characterized by an anisotropic change of the lattice constants but only a small discontinuous volume change of -0.044% [151]: While the rutile c axis increases by $\approx$ 1% the a axis decreases by $\approx$ 0.6% [182, 151]. At the same time, the thermal expansion coefficient drops by a factor of three [133]. The crystal structure changes are so strong that they could even break the crystals at the transition [209, 45]. Additional indications came from x-ray measurements, which revealed large thermal displacements in the rutile phase of both stoichiometric and Cr-doped VO_2, exceeding the values measured in the respective low-temperature phases as well as in the neighbouring rutile compounds TiO_2 and CrO_2 considerably [169, 179]. Finally, x-ray diffuse scattering measurements performed just above T_c pointed to a lattice instability at the tetragonal R point [241].

According to photoemission studies on metallic VO_2 the O 2p bands are located in the energy range from 8.5 to 2.5 eV below the Fermi energy while crystal field split V 3d bands extend from $\approx$ -1.5 to 1.7 eV and from 2.2 to 5.2 eV relative to E_F [32, 226, 1, 29, 103, 191]. Changes at the metal-insulator transition affect mainly the V 3d states: Whereas the occupied d bands experience a downshift and sharpening [226, 29, 103], bands right above E_F show a pronounced splitting [1, 191]. Most of these findings could be interpreted in terms of the molecular-orbital picture proposed by Goodenough [107, 108]. In this scheme, the t_{2g} states near the Fermi energy are split into a $d_{\parallel}$ band, which is directed along the rutile c axis, and the remaining π^* bands. In the monoclinic phase metal-metal pairing along the rutile c axis causes splitting of the $d_{\parallel}$ band into occupied bonding and empty antibonding states. In contrast, the π^* bands move to higher energies due to the antiferroelectric zigzag-type displacement of the vanadium atoms [107, 108]. According to Shin *et al.* the $d_{\|}$ band splitting amounts to ≈ 2.5 eV, while the π^* bands raise by ≈ 0.5 eV [226]. Finally, the vanadium atom pairing is reflected by the magnetic susceptibility, which shows Curie-Weiss behaviour above T_c and a nearly constant van Vleck-like contribution below [146, 28].

Previous theoretical work on the monoclinic M_1 phase of VO_2 includes a semiempirical calculation by Caruthers *et al.* [55] and a recent variable cell shape molecular dynamics study by Wentzcovitch *et al.*, which allowed to optimize the lattice vectors as well as the atomic positions [259]. As a result, Wentzcovitch *et al.* obtained crystal structure parameters, which are very close to the experimental values. In addition, the calculated electronic structure qualified monoclinic VO_2 as a semimetal with a band overlap of 0.04 eV. Although this contrasts the experimental finding of an insulating band gap of 0.6-0.7 eV [247, 217, 32, 226] the situation is not unlike that in small band gap semiconductors as Ge, where use of the local density approximation likewise leads to a metallic ground state. Wentzcovitch *et al.* interpreted the calculated electronic structure and the "pseudogap" for monoclinic VO_2 as confirmation of the energy band scheme by Goodenough [107, 108]. In addition, they found their results to be consistent with the Fermi surface nesting reported by Gupta *et al.* [111]. Still, the accurate molecular-dynamics calculations by Wentzcovitch *et al.* have not yet been complemented with state-of-the-art electronic structure calculations for monoclinic VO_2, which used the experimental crystal structure.

Although the strong coupling of the electronic and structural properties as demonstrated by the phase transition led to expect that electron-phonon interaction plays a major role many workers attributed the transition mainly to electron-electron correlations [279, 215]. Yet, in contrast to what is expected from a Mott-Hubbard-type transition, antiferromagnetic order below the transition temperature could be ruled out from susceptibility, NMR, and Mößbauer-effect measurements [133, 243, 146]. Nevertheless, the controversal discussion regarding the role of electron correlations and electron-lattice interaction is still ongoing. For this reason we include calculations for the monoclinic M_1 in our present study on VO_2.

In the preceding chapter (hereafter denoted as I) we performed calculations for metallic VO_2 in the rutile structure. These calculations served the purpose of (i) establishing a reference to which the electronic structure of the low-temperature phases could be compared and (ii) identifying mechanisms which might destabilize the rutile phase. As a result, we observed a dominant influence of the V $3d$ t_{2g} states near the Fermi energy whereas O $2p$- and V $3d$ e_g-derived bands are located, respectively, well below and above these states. From an analysis of the partial densities of states as well as the band characters of the states near E_F we arrived at the expectation that two of the three t_{2g} bands will move up as a consequence of an antiferroelectic mode caused by strong metal-oxygen hybridization whereas the remaining local $d_{x^2-y^2}$ states will be split due to metal-metal bonding along the rutile c axis. The bond order optimization model (BOOM) proposed in this context accounts for i) the local distortions of the crystal structure, ii) the metal-insulator transition, and iii) the stabilization due to down- and upshift of bonding and antibonding states.

In the present and the following chapter we continue by investigating the low-temperature monoclinic M_1 and M_2 phases of VO_2. Comparing the results to those for the rutile phase and, in particular, separating those features of the electronic structure, which are common to all phases, from those, which are unique to the monoclinic structures, we should be able to isolate important mechanisms for the stability of the latter. Finally, this may allow to identify the driving force for the metal-insulator transition and to check the validity of our bond order optimization model.

The present chapter deals in particular with the monoclinic M_1 structure. It is organized as follows: Referring to the discussion of the rutile structure as given in the preceding chapter we describe the main characteristics of the monoclinic M_1 structure in Sec. 8.2. After shortly summarizing in Sec. 8.3 methodological details which are unique to the present calculations we present the results in Sec. 8.4. The conclusion, Sec. 8.5, sums up the most important findings.

8.2 Crystal structure

The M_1 structure of VO_2 is characterized by a simple monoclinic (sm) lattice with space group $P2_1/c$ (C^5_{2h}) [13, 161]. According to Andersson the lattice constants and the monoclinic angle amount to $a_{M_1} = 5.743$Å, $b_{M_1} = 4.517$Å, $c_{M_1} = 5.375$Å, and $\beta_{M_1} = 122.61°$, respectively [13]. Lateron, Longo and Kierkegaard reported the values $a_{M_1} = 5.7517$Å, $b_{M_1} = 4.5378$Å, $c_{M_1} = 5.3825$Å, and $\beta_{M_1} = 122.646°$, respectively [161], which will be used in the subsequent calculations. The crystal structure is displayed in Fig. 8.1. The unit cell comprises four formula units and the metal atoms as well as the two different types of oxygen atoms occupy the general Wyckoff position (4e): $\pm(x, y, z)$, $\pm(x, \frac{1}{2} - y, \frac{1}{2} + z)$. The parameters given by Andersson as well as by Longo and Kierkegaard are listed in Tables 8.1 and 8.2.

Atom	Wyckoff positions	parameters		
		x	y	z
V	(4e)	0.242	0.975	0.025
O_1	(4e)	0.10	0.21	0.20
O_2	(4e)	0.39	0.69	0.29

Table 8.1: Crystal structure parameters as given by Andersson (from Ref. [13]).

We have adopted the usual notation

$$\mathbf{a}_{M_1,1} = \begin{pmatrix} 0 \\ 0 \\ -a_{M_1} \end{pmatrix}, \quad \mathbf{a}_{M_1,2} = \begin{pmatrix} -b_{M_1} \\ 0 \\ 0 \end{pmatrix},$$

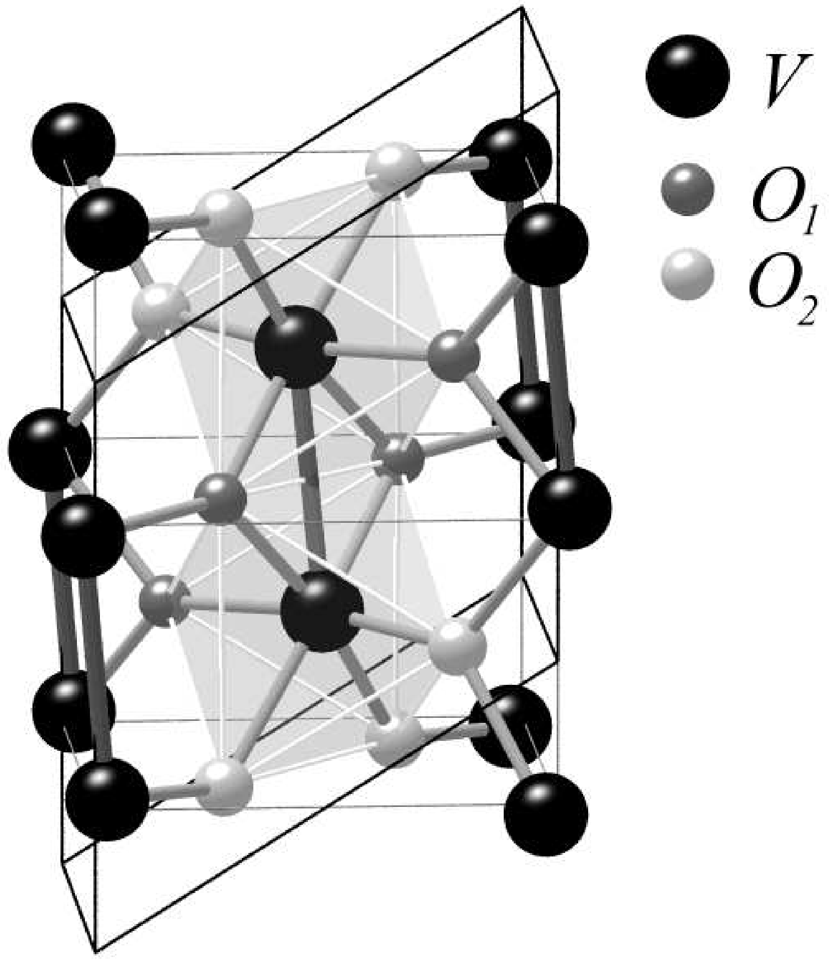

Figure 8.1: Crystal structure of monoclinic VO_2. Vanadium atoms are printed in black whereas oxygen atoms O_1 and O_2 are shaded dark and medium gray, respectively.

Atom	Wyckoff positions	parameters		
		x	y	z
V	(4e)	0.23947	0.97894	0.02646
O_1	(4e)	0.10616	0.21185	0.20859
O_2	(4e)	0.40051	0.70258	0.29884

Table 8.2: Crystal structure parameters as given by Longo and Kierkegaard (from Ref. [161]).

$$\mathbf{a}_{M_1,3} = \begin{pmatrix} 0 \\ c_{M_1} \sin \beta_{M_1} \\ -c_{M_1} \cos \beta_{M_1} \end{pmatrix} \tag{8.2.1}$$

for the primitive translations. Note, that the atomic positions have been shifted by half of the rutile c axis as compared to the high-temperature data.

Just for comparison and as a preparation for the later discussion we add the structural data, which arose from the variable cell shape molecular dynamics calculation by Wentzcovitch *et al.* [259]. These authors arrived at lattice constants a_{M_1} = 5.629Å, b_{M_1} = 4.657Å, c_{M_1} = 5.375Å, and a monoclinic angle β_{M_1} = 122.56°, respectively [259]. The calculated atomic parameters are listed in Table 8.3. Worth

Atom	Wyckoff positions	parameters		
		x	y	z
V	(4e)	0.233	0.976	0.021
O_1	(4e)	0.118	0.212	0.228
O_2	(4e)	0.399	0.685	0.293

Table 8.3: Crystal structure parameters as given by Wentzcovitch *et al.* (from Ref. [259]).

mentioning is the very good agreement with the measured lattice parameters and atomic positions. With only few small exceptions all calculated numbers are within the range spanned by the two sets of experimental data, which by themselves show some variation.

The close relationship of the monoclinic M_1 structure to the high-temperature rutile structure becomes visible from a comparison of Fig. 8.1 to Fig. 7.1. However, as for MoO_2 there exist three distinct differences: (i) We observe the metal-metal pairing along the rutile c axis in Fig. 8.1. As a consequence, two different metal-metal distances of 2.619 and 3.164Å arise, which contrast the average value of 2.851Å assumed in the rutile structure. (ii) We witness the zigzag-like in-plane displacements of the V atoms which are parallel to the local z axis, hence, parallel to the diagonal of the rutile basal plane (see I for a description of the local coordinate systems). These shifts likewise alternate along both the tetragonal a and c axis. As a consequence of the zigzag distortion two different apical vanadium oxygen bond lengths of 1.77 and 2.01Å arise. In contrast, the metal atom pairing leads to two short and two long equatorial V – O bond lengths of 1.86, 1.89, 2.03, and 2.06Å. (iii) There is a lattice strain which causes deviations of the ratios

$$\frac{c_{M_1} \sin \beta_{M_1}}{b_{M_1}} = 0.9988 , \qquad \frac{-2c_{M_1} \cos \beta_{M_1}}{a_{M_1}} = 1.0096$$

from unity and prohibits representation of the primitive translations (8.2.1) in the form given by equation (7.4.1).

Despite the many similarities of the monoclinic structures of MoO_2 and VO_2 a more detailed analysis of the crystal structure data reveals a striking difference between both compounds regarding the zigzag-like in-plane displacements of the metal atoms and the distortions of the surrounding oxygen octahedra: In MoO_2 the metal atoms experience, in addition to the metal-metal pairing, an in-plane shift, which makes an angle of 18° with the local z axis. The oxygen atoms follow the lateral displacements of the molybdenum atoms to a large degree while they hardly move parallel to the rutile c axis.

The situation is different in VO_2. As becomes obvious from the top view, Fig. 8.2, the vanadium atoms, in addition to dimerizing along the rutile c axis, experience

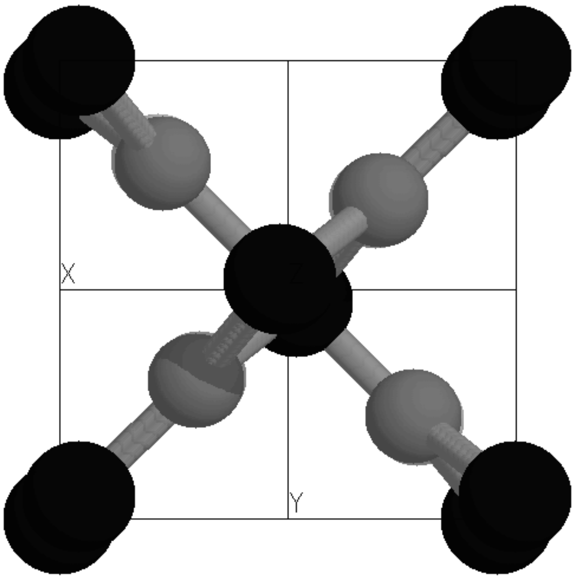

Figure 8.2: Crystal structure of monoclinic VO_2, top view. The shading of the atoms is the same as in Fig. 8.1.

in-plane shifts which are parallel to the local z axis, hence, the $\langle 110 \rangle$ direction. Even more striking is the response of the oxygen lattice to the displacements of the metal atoms at the phase transition: In contrast to MoO_2 they do not follow the metal atom shifts and stay almost at their original positions. As a consequence, the lateral displacement of the vanadium atoms causes a shift relative to the rather fixed oxygen octahedra such that there is indeed an antiferroelectric mode whereas in MoO_2 the molybdenum atom displacements are compensated to a large degree by the simultaneous motion of the surrounding oxygen atoms.

These differences for the two oxides have been already mentioned at the end of chapter 7. There we pointed out that the zigzag-type in-plane displacement of the metal atoms, which, according to symmetry considerations, is coupled to the vertical metal-metal pairing, does not automatically lead to an (anti)ferroelectric distortion of the whole VO_6 octahedra since the in-plane metal atom displacement may still be compensated by a corresponding displacement of the surrounding oxygen cage. This situation is realized in MoO_2, whereas in VO_2 the antiferroelectric mode is active insofar as it causes a vanadium atom shift *relative* to the surrounding oxygen atoms and thus changes the metal-oxygen bonding. Of course, such detailed analyses of the crystal structures are a necessary prerequisite for a correct interpretation of the electronic properties in terms of the proposed bond order optimization model.

8.3 Details of the calculation

Applying the sphere geometry optimization (SGO) algorithm to the open crystal structure of monoclinic VO_2 we were able, by inserting 14 empty spheres into the simple monoclinic unit cell, to keep the linear overlap of any pair of physical spheres below 22%, and the overlap of any pair of physical and empty spheres below 27%. The positions of the empty spheres, the atomic sphere radii for all spheres as proposed by the SGO algorithm as well as the basis set orbitals are listed in Tables 8.4 and 8.5. States given in parentheses were included as tails of the other orbitals. Finally, the Brillouin zone sampling was done using an increasing number of **k** points, which range from 54, 128, 432, 1024, 2000 to 6750 points within the irreducible wedge.

Atom	Wyckoff positions	parameters		
		x	y	z
E_1	(2d)	0.5	0.5	0.0
E_2	(4e)	0.1346	-0.0037	0.4998
E_3	(4e)	0.4026	0.1483	-0.2102
E_4	(4e)	0.0833	-0.2432	0.1602

Table 8.4: Empty sphere positions.

Atom	Radius/a_B	Orbitals			
V	2.215	$4s$	$4p$	$3d$	$(4f)$
O_1	1.892	$2s$	$2p$	$(3d)$	
O_2	1.787	$2s$	$2p$	$(3d)$	
E_1	2.000	$1s$	$2p$	$3d$	$(4f)$
E_2	1.857	$1s$	$2p$	$(3d)$	
E_3	1.844	$1s$	$2p$	$3d$	$(4f)$
E_4	1.903	$1s$	$2p$	$3d$	$(4f)$

Table 8.5: Atomic sphere radii and basis set orbitals.

8.4 Results and Discussion

8.4.1 Electronic structure and partial DOS

We display in Fig. 8.3 the electronic states along selected high symmetry lines within the simple monoclinic Brillouin zone, Fig. 8.4. The corresponding total as well as dominant partial density of states (DOS) are given in Fig. 8.5. We concentrate on

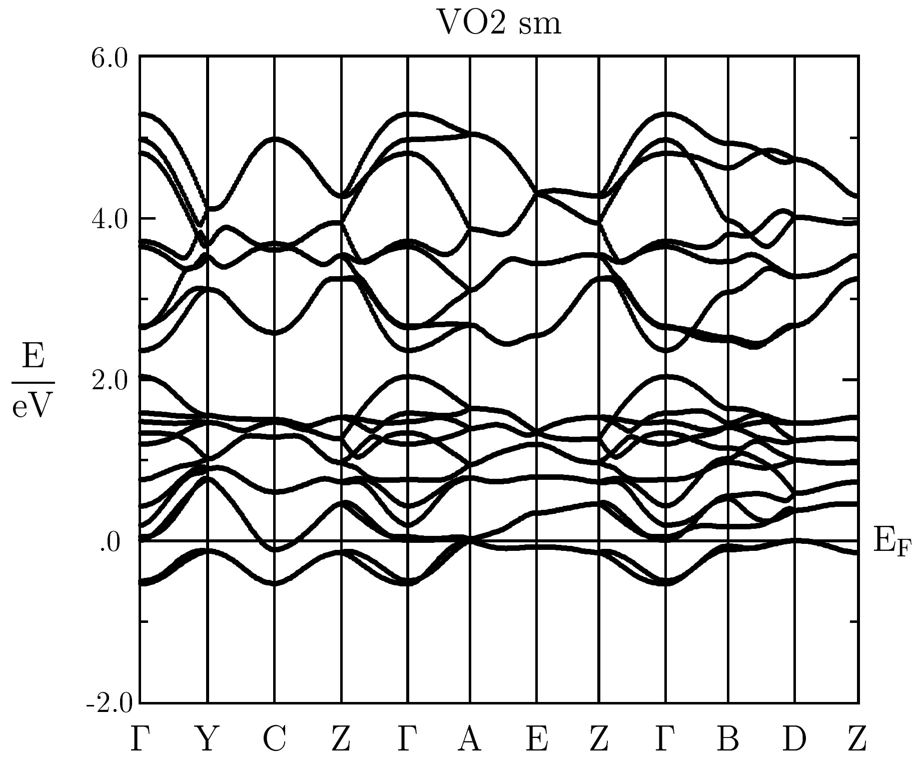

Figure 8.3: Electronic bands of monoclinic VO_2 along selected symmetry lines within the simple monoclinic Brillouin zone, Fig. 8.4.

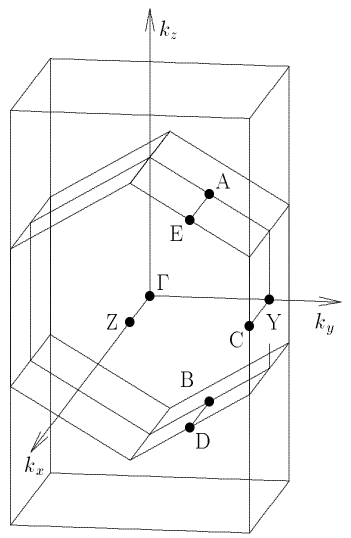

Figure 8.4: First Brillouin zone of the simple monoclinic lattice. The outer box marks the first Brillouin zone of the simple tetragonal lattice, see Fig. 7.3.

the same energy interval as in I and do not include e.g. low lying oxygen $2s$ states.

The similarities of the present results with those for rutile VO_2 are easily stated: As in I, we identify in Figs. 8.3 and 8.5 the three groups of bands which comprise 24 oxygen $2p$ dominated bands well below the Fermi level and two groups of 12 and 8 bands, respectively, below and above E_F. These latter two groups trace back mainly

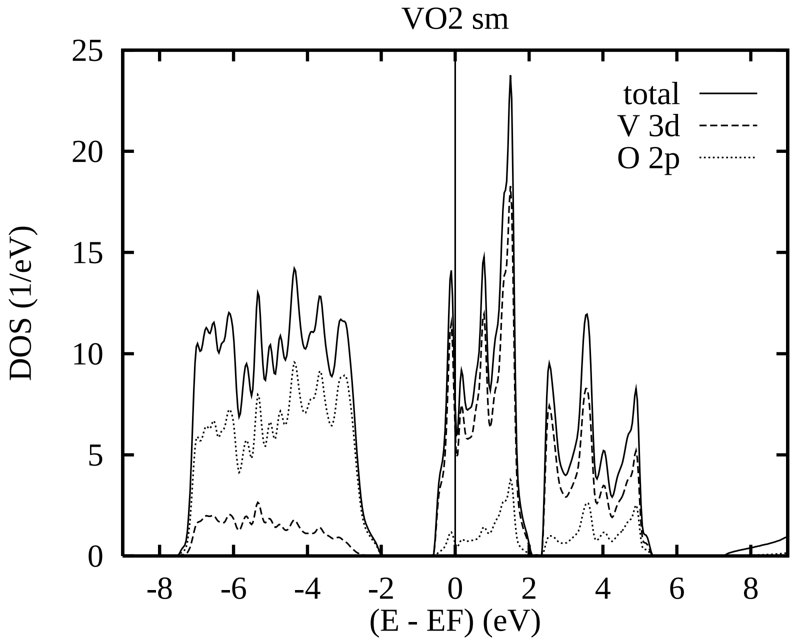

Figure 8.5: Total and partial densities of states (DOS) of monoclinic VO_2 per unit cell.

to V $3d$ states. Finally, $p-d$ hybridization leads to V $3d$ and O $2p$ contributions of the order of about 10% in the energy regions where the respective other partner dominates. The energetical separation between these two groups of bands turns out to be slightly smaller than in the rutile phase in agreement with the XPS results by Blaauw *et al.* [32]. In passing we recall the interpretation of the electronic states in terms of a molecular-orbital picture as given in chapter 7, where the lower and higher O $2p$-dominated bands are regarded as σ and π states, respectively, while the π^* and σ^* states are found in the bands originating mainly from V $3d$ states.

Fig. 8.6 displays the V $3d$ partial DOS due to the single vanadium atom at the corner of the underlying rutile cell. It is separated into its symmetry components, which are given relative to the local rotated reference frame defined in I. Again, we recognize the almost perfect energetical separation of the $3d$ t_{2g} and e_g groups of bands, which results from the octahedral crystal field splitting. We mention, in particular, the single peak of the d_{xz} partial DOS at 1 eV and the double peak structure in the d_{yz} curve. However, both bands have experienced a considerable energetical upshift.

In contrast, there is a striking difference to the rutile result for the V $3d_{x^2-y^2}$ bands. Comparing Fig. 7.5 to Fig. 8.6 of the present chapter, we observe the prominent splitting of the corresponding partial DOS into two peaks which are located just below E_F and at ≈ 1.3 eV. From the discussion at the end of chapter 7 we attribute this effect to the pairing of the vanadium atoms along the rutile c axis, which causes strong bonding-antibonding splitting of the $d_{x^2-y^2}$ dominated bands. Our results thus conform with the molecular-orbital picture sketched by Goodenough where the $d_{\|}$ or, as we call it, the $d_{x^2-y^2}$ band experiences a strong bonding-antibonding splitting due to the metal-metal bonding [107]. The situation becomes clearer from a comparison to the band structure of rutile VO_2, which we show in Fig. 8.7 after

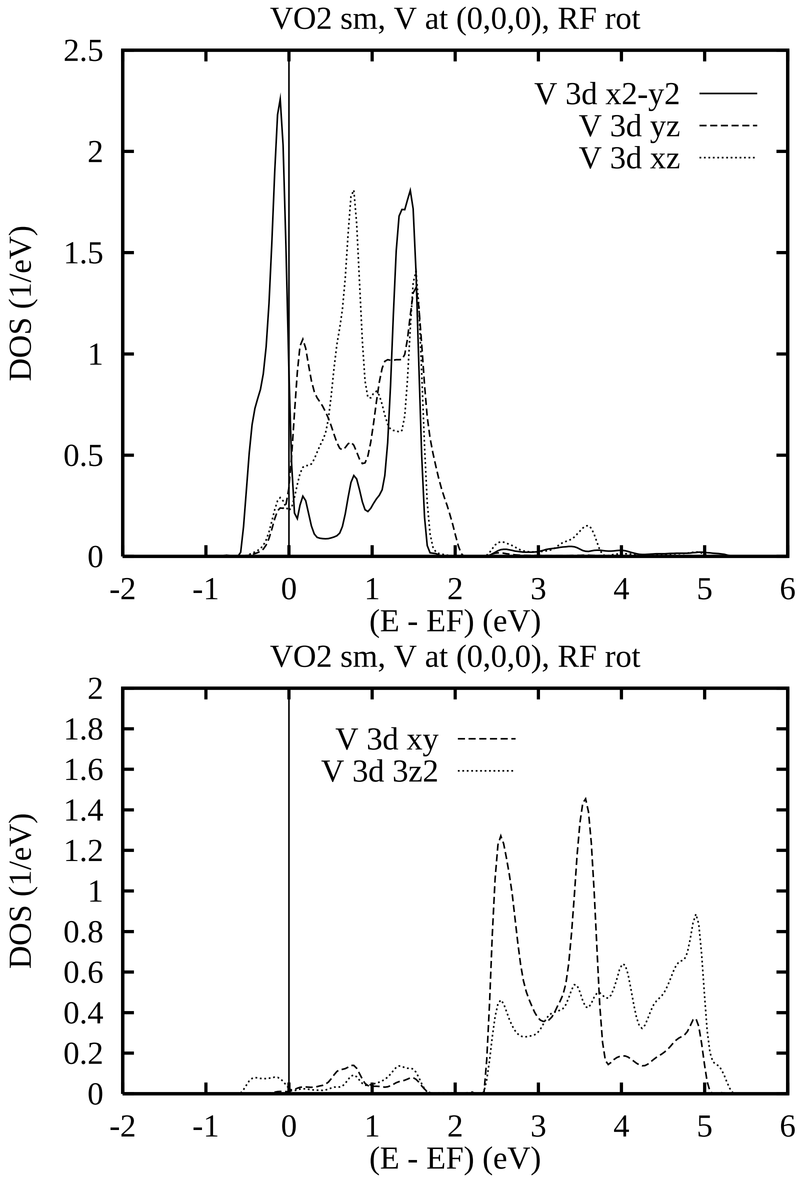

Figure 8.6: Partial V $3d$ t_{2g} and e_g densities of states (DOS) of monoclinic VO_2. Selection of orbitals is relative to the local rotated reference frame.

backfolding the bands to the first Brillouin zone of the simple monoclinic lattice, Fig. 8.4. Just in the same manner as for MoO_2, those two bands in Fig. 8.7, which give rise to the lowest states within the t_{2g}-derived group of bands at the Γ point, bend upwards along the line Γ-A and cross the higher lying bands. In monoclinic VO_2 these two bands are separated from the other states and form a split-off doublet, which, however, is still touching the higher lying bands at the A point. For this reason, we end up with a finite density of states at the Fermi energy, which spoils an insulating ground states. Instead, from the touching bands at the A point and the occupied band width of the conduction band at the C point of about 0.1 eV we would rather regard monoclinic VO_2 as a semimetal, in agreement with the results by Wentzcovitch *et al.* [259]. Like these authors we attribute the failure of density functional based calculations to reproduce the optical band gap to the shortcomings

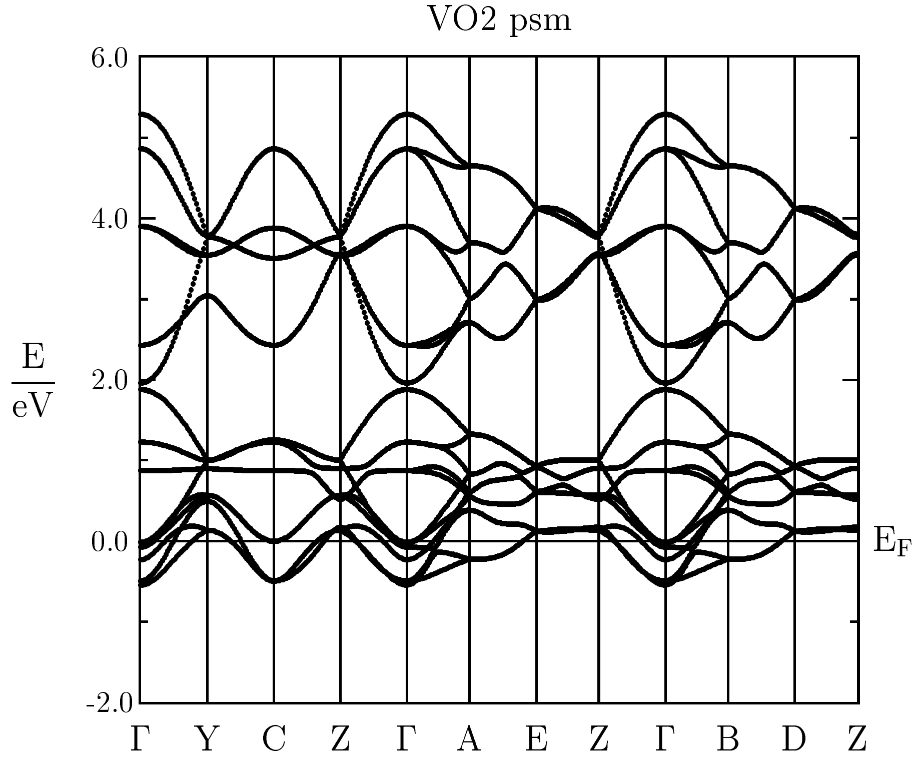

Figure 8.7: Electronic bands of rutile VO_2 along selected symmetry lines within the simple monoclinic Brillouin zone, Fig. 8.4.

of the local density approximation, which underestimates the band gap usually by about 50% and, in some small gap semiconductors like Ge, misses the gap at all. This seems to be also the case for monoclinic VO_2. Like in the zincblende-type semiconductors the optical band gap originates to a large part from bonding-antibonding splitting of hybridized bands which obviously is not well accounted for by the LDA. Our point of view is well supported by the previous findings for monoclinic MoO_2. From a comparison of the calculated DOS with both angle-resolved UPS and XAS data, we obtained perfect agreement with experiment except for the bonding and antibonding Mo $4d_{x^2-y^2}$ bands: Their splitting was underestimated by about 1 eV. For VO_2 the calculations yield a separation of ≈ 1.7 eV between the bonding and antibonding $d_{x^2-y^2}$ bands while a value of 2.0 to 2.5 eV has been extracted from UPS and XAS measurements [226, 1].

8.4.2 Chemical bonding

In order to address the chemical bonding we complement the band structure and the densities of states with the total and partial crystal orbital overlap populations (COOP). The result is shown in Fig. 8.8. Whereas the total COOP as well as the O $2p$ – O $2p$ partial COOP agree fairly well with the respective curves for rutile VO_2 as shown in Fig. 7.6, differences arise from the bonding and antibonding V $3d_{x^2-y^2}$ peaks, which lead to a significant positive contribution to the V – V curve between -0.6 eV and E_F and contrast the negative partial COOP in this energy range for rutile VO_2. As for monoclinic MoO_2 this signals the increased metal-metal bonding due

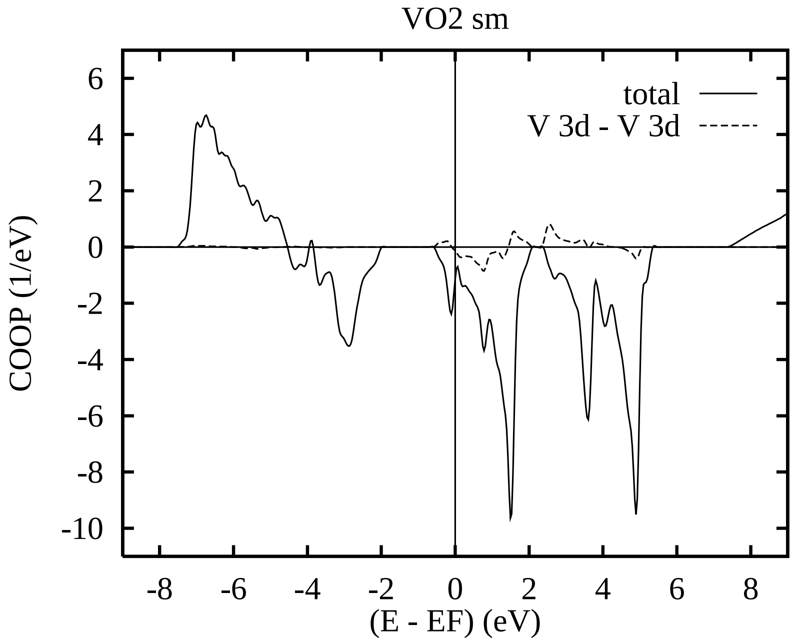

Figure 8.8: Total and partial crystal orbital overlap populations (COOP) of monoclinic VO_2.

to the pairing of the atoms in the monoclinic structure. Furthermore, the formation of bonding and antibonding V $3d_{x^2-y^2}$ states below and above the Fermi energy, respectively, increases the value of the total integrated COOP at the Fermi level (see Ref. [79] for details). It thus strengthens the V – V bond order and, hence, the overall chemical stability. Finally, the antibonding contributions to the V $3d$ – O $2p$ bonds experience a considerable upshift in energy. We have not included this partial COOP in Fig. 8.8 for clarity reasons but the effect is still visible in the total COOP curve.

8.4.3 Comparison to experiment

As for metallic VO_2 we display in Figs. 8.9 and 8.10 total and partial V $3d$ and O $2p$ densities of states folded with a Gaussian of 0.25 and 0.5 eV width, respectively, for the occupied and unoccupied part of the spectrum. Good agreement with the XPS and UPS spectra by Blaauw *et al.*, Shin *et al.*, Bermudez *et al.*, and Goering *et al.* is found [32, 226, 29, 98, 103]. Data by the latter group were added in Fig. 8.9. According to these experiments the UPS spectra taken in the metallic and the insulating phase are very similar with respect to the oxygen dominated bands but show distinct differences in the low binding region which arise from a sharpening and slight downshift of the V $3d$-derived peak [32, 226, 98, 103]. As a comparison of Fig. 8.9 with Fig. 7.7 reveals this experimental result is well accounted for by our calculations except for the fact that the V $3d$ downshift is underestimated as mentioned above.

More striking differences between metallic and insulating VO_2 are observed in the soft-x-ray absorption spectra (XAS) as measured by Müller *et al.* [190, 191], which we display in Fig. 8.10. The experimental data were shifted by 529.5 eV. As

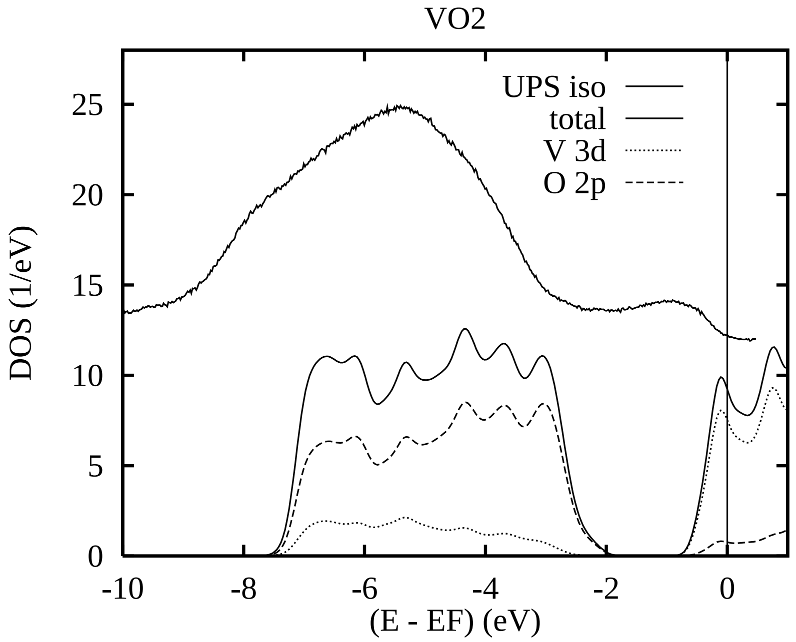

Figure 8.9: Total and partial densities of states (DOS) of monoclinic VO_2 folded with a 0.25 eV wide Gaussian (lower set of curves) and UPS spectra (upper curve; from Ref. [98, 103]).

already described in I the XAS spectra allowed to probe the angular dependence by varying the orientation of the polarization vector **E** from parallel ($\phi = 90°$) to perpendicular ($\phi = 0°$) to the rutile c axis. Dipole selection rules then allow for transitions from O $1s$ to either the O $2p_z$ or the O $2p_x$ and $2p_y$ states. This is reflected by the calculated partial DOS of the corresponding final states. However, note that the curve marked O $2p_x, p_y$ actually comprises only the mean average of these orbitals since the component perpendicular to **E** is not seen in experiment. For the same reason, the curve marked O $2p$ actually contains the contribution from $\frac{1}{2}(p_x + p_y) + p_z$.

According to the experiments by Müller *et al.* as well as by Abbate *et al.* major differences between the XAS spectra of metallic and insulating VO_2 originate from the appearance of an additional peak in the low-temperature phase [190, 191, 1]. In the spectra by Abbate *et al.* this new peak is located at 530.9 eV and seems to have split off from the peak at 529.9 eV, which, like the one at 532.5 eV, exists also in the metallic phase [1]. Abbate *et al.* interpreted the additional peak as arising from an upshift of the antibonding $d_{\parallel}$ band by about 1 eV while the other two t_{2g} bands, namely the π^* bands, stay at their original position. The XAS curves taken by Müller *et al.* are almost identical to the results of Abbate *et al.*. However, in a more detailed fit Müller assigned the spectra to five different peaks at 529.9, 530.4, 531.2, 532.7, and 533.9 eV [190].

Again, there is an overall good agreement between experiment and theory with respect to positions, intensities, and angular dependencies of the peaks. As a comparison with Fig. 7.8 reveals, the calculated curves reflect the upshift of the O $2p_z$ peak from 0.7 eV to 1.3 eV, which is the position of the upper $d_{x^2-y^2}$ peak in Fig. 8.7, while all other peaks hardly move. Nevertheless, this peak actually does not

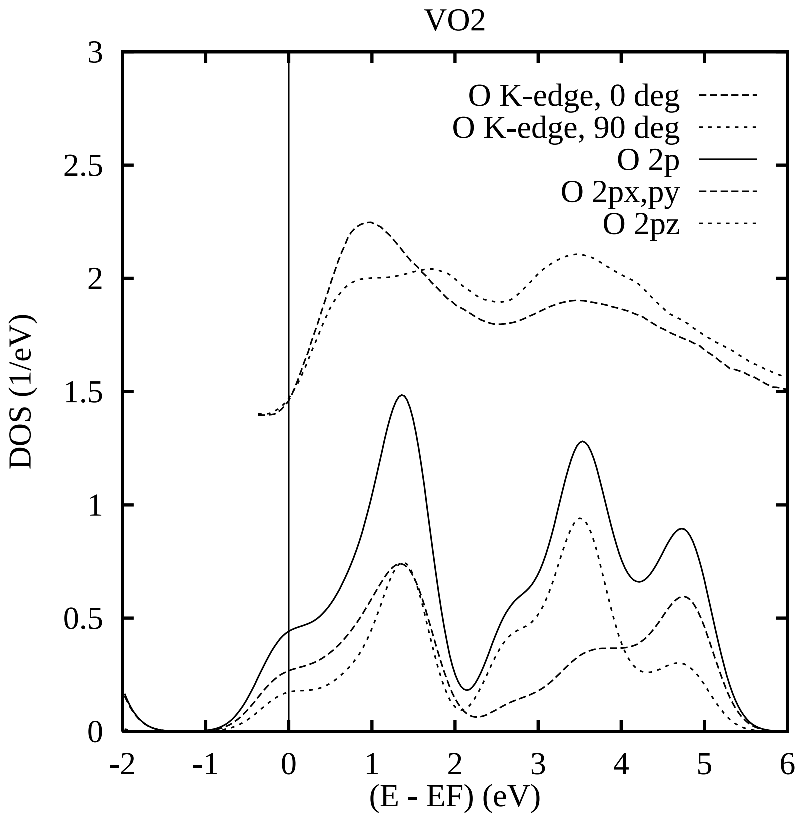

Figure 8.10: Partial O $2p$ densities of states (DOS) of monoclinic VO_2 folded with a 0.5 eV wide Gaussian (lower set of curves) and XAS O K edge spectra (upper set of curves; from Ref. [190, 191], data shifted by 529.5 eV).

separate from the maximum of the O $2p_x, p_y$ curve at 1.3 eV in contrast to the XAS results. Although matrix element effect might contribute to this difference we get the impression that the upshift is underestimated by the calculation in the same manner as in our previous work on MoO_2. Finally, as in chapter 7 on rutile VO_2 the calculated high-energy peak at $\approx$ 4.8 eV gives rise to only a very slight shoulder in the experimental curve. Yet, it can be fully resolved by the forementioned five peak analysis by Müller [190].

8.4.4 Bond order optimization scenario

Although the upshift of the V $3d_{xz}$ and d_{yz} bands as well as the bonding-antibonding splitting of the $d_{x^2-y^2}$ band as observed in the partial DOS already signaled the general validity of the bond order optimization model proposed in the previous chapter we still aim at obtaining more direct support for these ideas from the electronic structure. In order to prepare for the discussion we display in Figs. 8.11, 8.12, and 8.13 the weighted band structures of rutile VO_2, which result from those shown in Figs. 7.12 to 7.14 by backfolding to the monoclinic Brillouin zone, Fig. 8.4. We used the same special representation as before where the lengths of the bars given with each band at each $\mathbf{k}$ point is a measure of the contribution from a specified orbital.

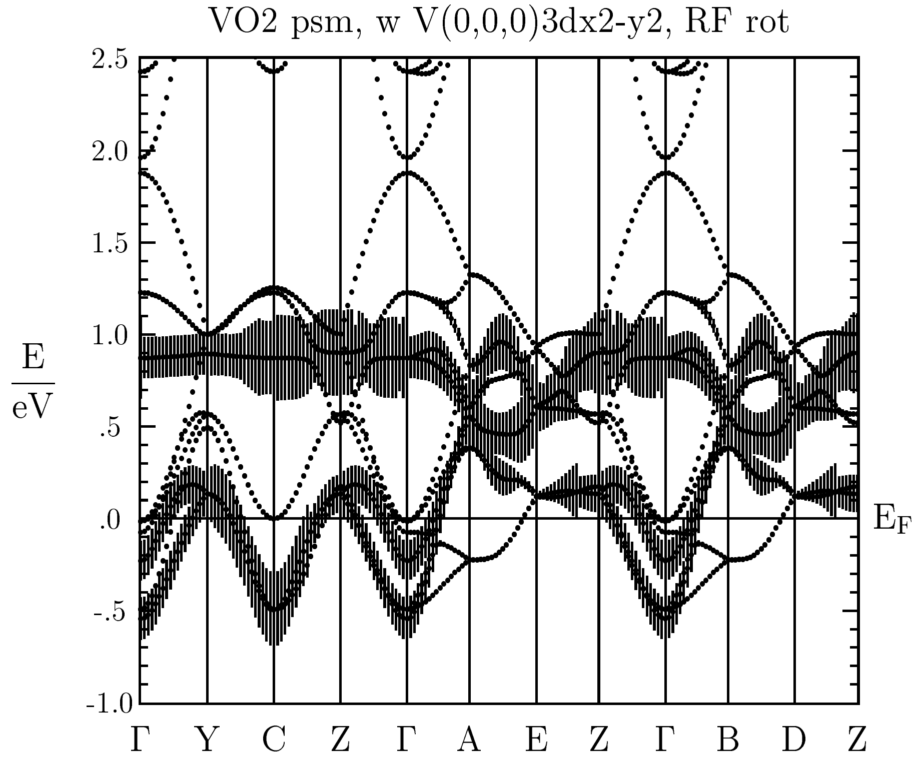

Figure 8.11: Weighted electronic bands of rutile VO_2. The width of the bars given for each band indicates the contribution due to the $3d_{x^2-y^2}$ orbital of the V atom at the corner of the rutile cell relative to the local rotated reference frame.

Note that again we refer to the local reference frame.

In Fig. 8.11 we observe a separation of the $d_{x^2-y^2}$ bands in two parts below and above 0.4 eV, respectively. They are connected by the dispersing bands especially along the lines Γ-A and Γ-B, which have components perpendicular to the rutile basal plane and correspond to half the line Γ-R of the tetragonal Brillouin zone. In contrast, the dispersion parallel to the rutile basal plane is suppressed to a large degree with the bands staying at energies either well below or above 0.4 eV, even if there is some dispersion in the lower group. Finally, $d_{x^2-y^2}$ bands along the lines A-E and B-D, while likewise displaying a reduced dispersion, stay at an intermediate energy in the middle between the two subgroups. Note that these lines lie completely within the planes at height $\frac{\pi}{2c}$. The general characteristics of these bands are thus very similar to those of the $4d_{x^2-y^2}$ bands of hypothetical rutile MoO_2 where the dispersionless bands along A-E and B-D were responsible for the flat portions of the Fermi surface and thus were interpreted as driving the Peierls-type instability of this structure.

In contrast, the V $3d_{xz}$ and d_{yz} bands as shown in Figs. 8.12 and 8.13 lack any subdivision in energetically lower and upper bands but display a rather strong dispersion along all the included symmetry lines.

Weighted band structures for monoclinic VO_2 which correspond to Figs. 8.11 to 8.13 are shown in Figs. 8.14, 8.15, and 8.16. The differences between both sets of figures are striking. On going from rutile to monoclinic VO_2 we clearly observe

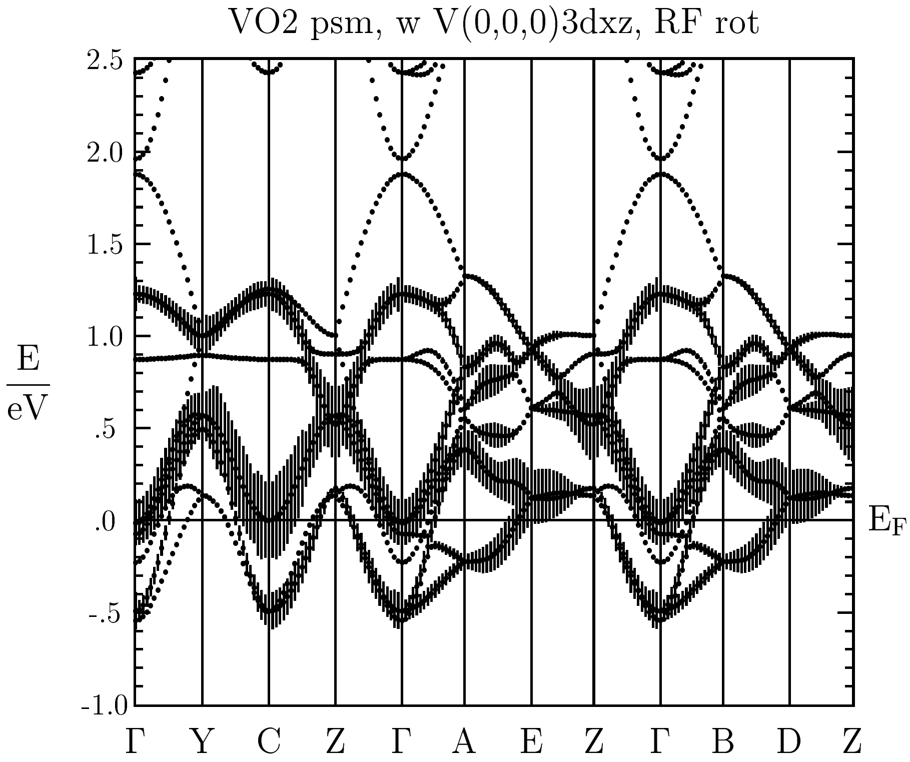

Figure 8.12: Weighted electronic bands of rutile VO_2. The width of the bars given for each band indicates the contribution due to the $3d_{xz}$ orbital of the V atom at the corner of the rutile cell relative to the local rotated reference frame.

a bonding-antibonding splitting of the V $3d_{x^2-y^2}$ bands, which places the rather narrow subbands at the lower and upper edge of the t_{2g} group of bands while suppressing the dispersion in between. As compared to Fig. 8.11 the $d_{x^2-y^2}$ bands along the lines Γ-A-E-Z and Γ-B-D-Z have moved downward and upward by as much as half an electronvolt in Fig. 8.14. As a consequence of these bandshifts, so far unoccupied portions of these bands between E_F and ≈ 0.4 eV are almost fully occupied and the Fermi surface due to the $d_{x^2-y^2}$ states has almost vanished. In contrast, the V $3d_{xz}$ and d_{yz} bands experience a considerable upshift by as much as half an electronvolt, which is in full agreement with the data by Shin *et al.* [226]. With only minor exceptions, this shift of the π^* bands leaves the general topology of these bands intact and causes their almost complete depopulation. Finally, our results agree with arguments given by Goodenough, who concluded from the isotropic conductivity that the π^* states should be located at the lower edge of the conduction band well below the antibonding $d_{\|}$ band [108]. Furthermore, Goodenough deduced from the measured low Hall mobility a narrowing of the π^* bands [108]. Indeed, our calculations result in a band width of about 2 eV of the π^* bands which is considerably lower than the 2.5 eV found in the rutile phase.

In passing we note that within our investigation of the monoclinic M_1 structure we are not able to uniquely attribute the upshift of the π^* bands to a specific atomic displacement. As already mentioned above the zigzag-type in-plane displacement of the vanadium atoms introduces an antiferroelectric mode which changes metal-

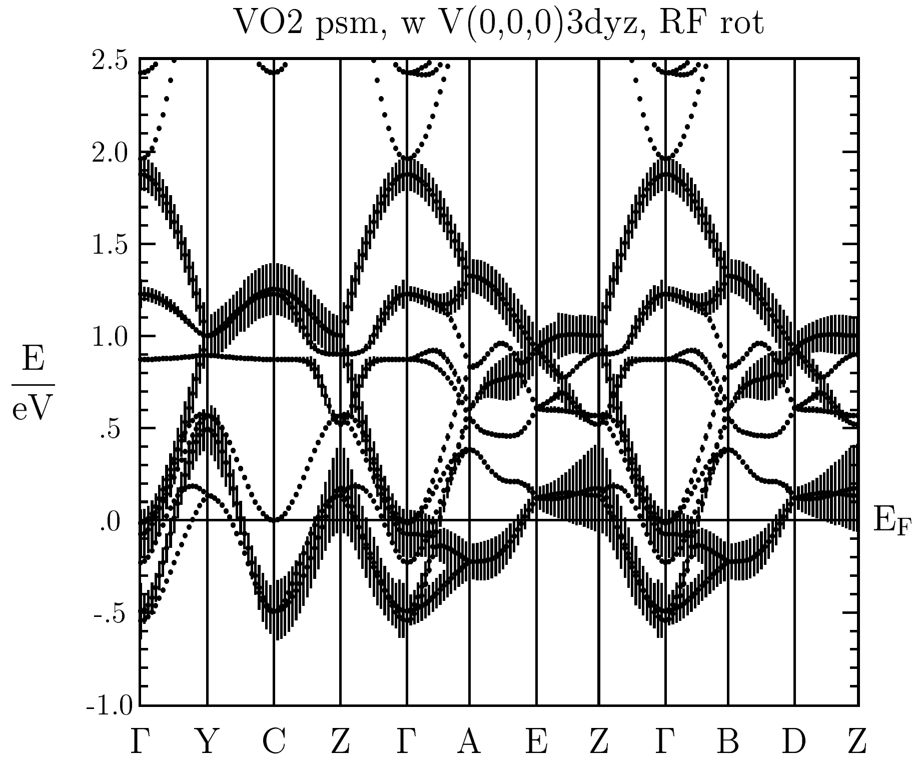

Figure 8.13: Weighted electronic bands of rutile VO_2. The width of the bars given for each band indicates the contribution due to the $3d_{yz}$ orbital of the V atom at the corner of the rutile cell relative to the local rotated reference frame.

oxygen bonding. However, the latter is likewise affected by the metal-metal pairing, which also shifts the vanadium atoms *relative* to the surrounding oxygen octahedra. The effect of these two components of the crystal structure changes cannot be distinguished since in the M_1 phase all metal chains experience the same dimerization and zigzag-type displacement. The issue can only be resolved in our subsequent study on the monoclinic M_2 phase, which displays a disproportionation of the vanadium chains.

To summarize the results for the M_1 phase, the calculated changes of the electronic structure indeed lead to a complete separation of states, which are bonding and antibonding, respectively, with respect to either metal-metal or metal-oxygen bonding, thus confirming the bond order optimization model as proposed in chapter 7. Nevertheless, as already discussed in Sec. 8.4.1 this band separation does not fully account for the insulating gap but leads to a semimetal with a band overlap of about 0.1 eV in the same manner as in the work by Wentzcovitch [259]. Since the band characters of the hole and electron bands are different we may still ask whether the structural changes which caused the forementioned changes of the electronic structure can in principle open a gap. Of course, answering of this question would shed some more light on the relative importance of electron-lattice interaction and electron-electron correlations.

In order to check the general validity of the bond order optimization model we thus append the previous calculations with an additional set, where the displace-

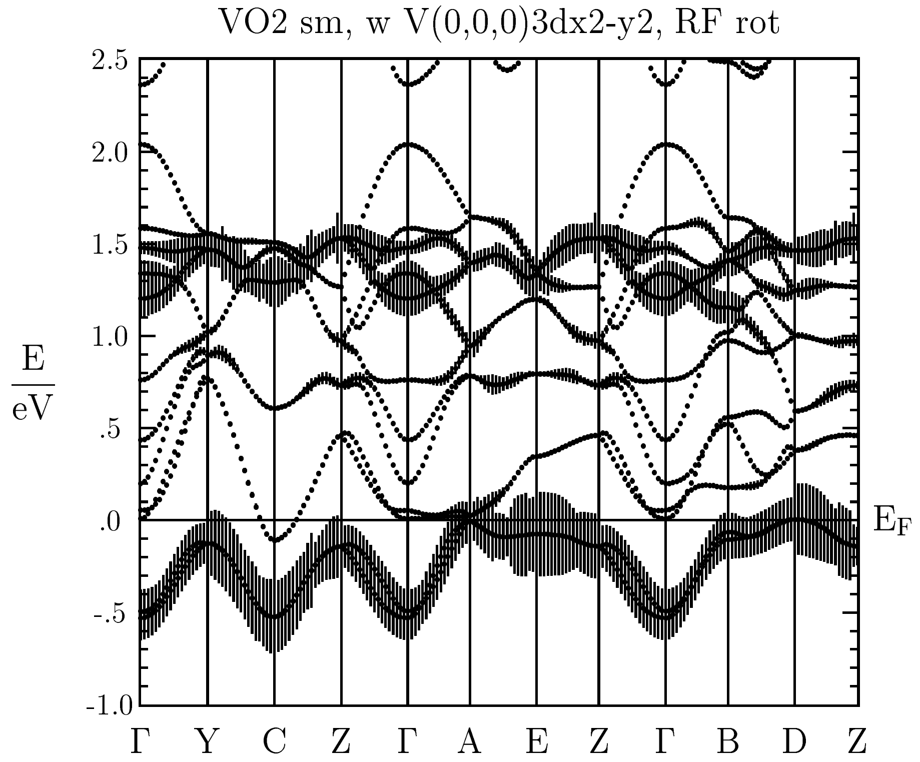

Figure 8.14: Weighted electronic bands of monoclinic VO_2. The width of the bars given for each band indicates the contribution due to the $3d_{x^2-y^2}$ orbital of the V atom at the corner of the rutile cell relative to the local rotated reference frame.

ments of the vanadium atoms in the monoclinic structure as compared to their "ideal" rutile positions are artificially exaggerated while the space group symmetry is conserved. These additional shifts apply to both the metal-metal pairing and the zigzag-like in-plane displacements. As a result, the vanadium positional parameters change from the values listed in Table 8.1 to $x = 0.23315$, $y = 0.96630$, and $z = 0.04234$. The metal-metal distances within the octahedral chains assume the values 2.487 and 3.350 Å, which should be compared to those given in Sec. 8.2 as well as to the corresponding distances of 2.524 and 3.138 Å arising from the variable cell shape molecular dynamics calculation by Wentzcovitch *et al.* [259].

We display in Figs. 8.17 and 8.18 the weighted electronic structure corresponding to the V $3d_{x^2-y^2}$ bands and the partial DOS of the t_{2g} manifold using again the local rotated reference frame. Obviously, the artificial exaggeration of the vanadium shifts causes a considerable increase of the bonding-antibonding splitting of the $d_{x^2-y^2}$ band as well as upshift of the d_{xz} and d_{yz} bands and opens an optical band gap of about 0.4 eV width. The reduced occupied band width of ≈ 0.35 eV as compared to 0.5 eV in Fig.8.15 results from the increased metal-metal pairing, which suppresses hopping between the pairs.

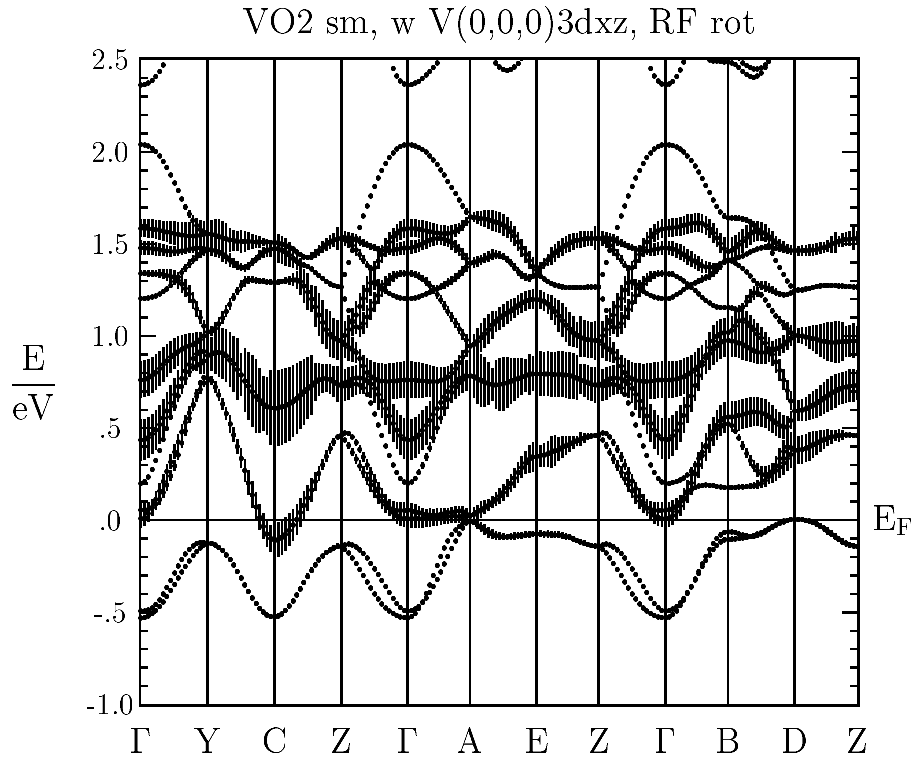

Figure 8.15: Weighted electronic bands of monoclinic VO_2. The width of the bars given for each band indicates the contribution due to the $3d_{xz}$ orbital of the V atom at the corner of the rutile cell relative to the local rotated reference frame.

8.5 Conclusion

In the present chapter first-principles ASW calculations were used to describe the electronic properties of monoclinic VO_2. As in the previous study on the rutile phase vanadium $3d$ t_{2g} states resulting from octahedral crystal field splitting are found near the Fermi energy while strongly hybridized O $2p$ and V $3d$ e_g states are located well below and above, respectively.

Deviations from the results for the rutile phase conform with the previously proposed bond order optimization model (BOOM) and arise mainly from metal-metal pairing along the rutile c axis, which causes complete separation of the bonding and antibonding $d_{x^2-y^2}$ bands and down- and upshift, respectively, of these states to below and above the Fermi energy. In contrast, the antiferroelectric zigzag-like in-plane displacement of the vanadium atoms increases the V $3d$ – O $2p$ overlap of the socalled π^* orbitals, which are antibonding with respect to metal-oxygen bonding, and drives their energetical upshift. Taken together, all modes lead to an efficient separation of bonding and antibonding states and thus cause an overall increase of the bond order. As a consequence, chemical stability is increased. Finally, due to the electron count of VO_2, bonding and antibonding states are separated and monoclinic VO_2 is found at the verge to being an insulator. The general validity of the bond order optimization model to describe the metal-insulator transition is more emphasized in a hypothetical calculation, where the displacive mode of the

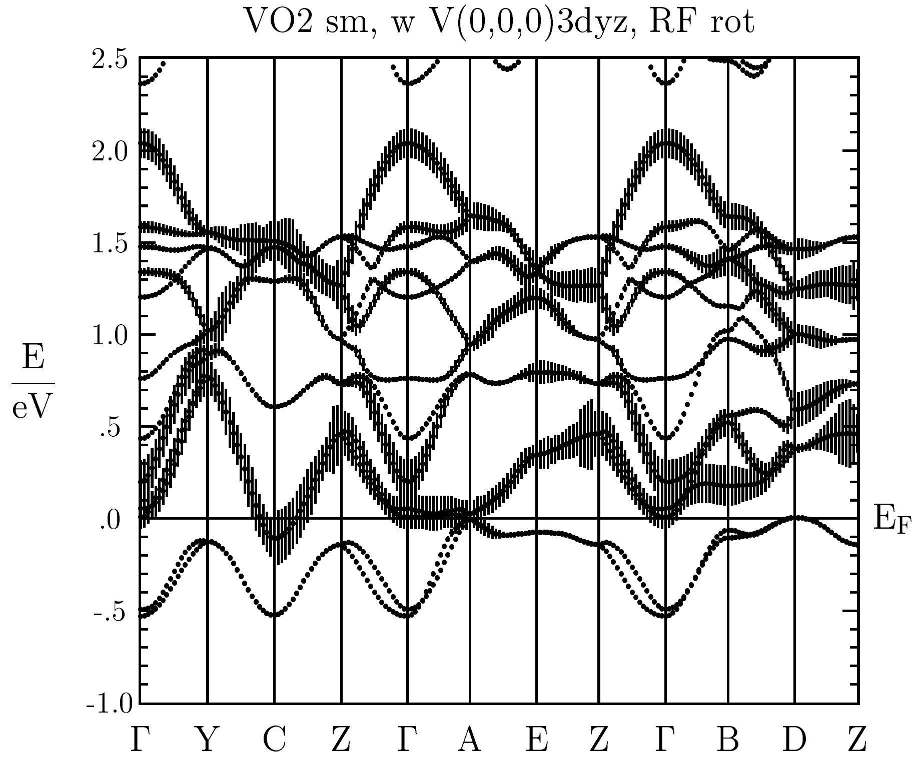

Figure 8.16: Weighted electronic bands of monoclinic VO_2. The width of the bars given for each band indicates the contribution due to the $3d_{yz}$ orbital of the V atom at the corner of the rutile cell relative to the local rotated reference frame.

vanadium atoms is exaggerated and which opens a gap of about 0.4 eV.

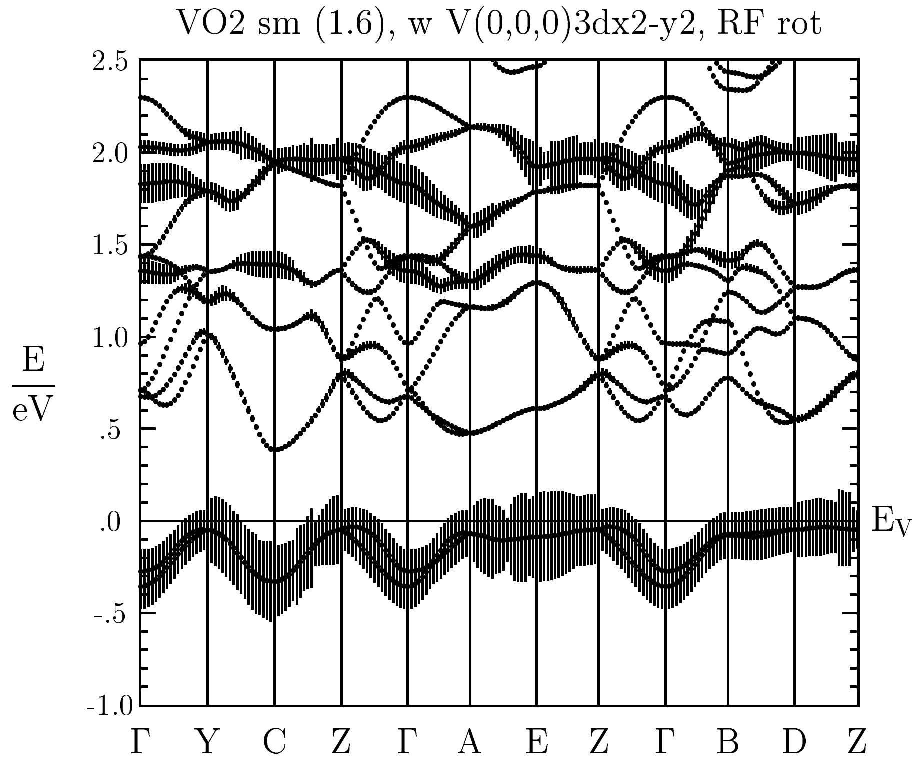

Figure 8.17: Weighted electronic bands of monoclinic VO_2 with exaggerated vanadium atom distortions. The width of the bars given for each band indicates the contribution due to the $3d_{x^2-y^2}$ orbital of the V atom at the corner of the rutile cell relative to the local rotated reference frame.

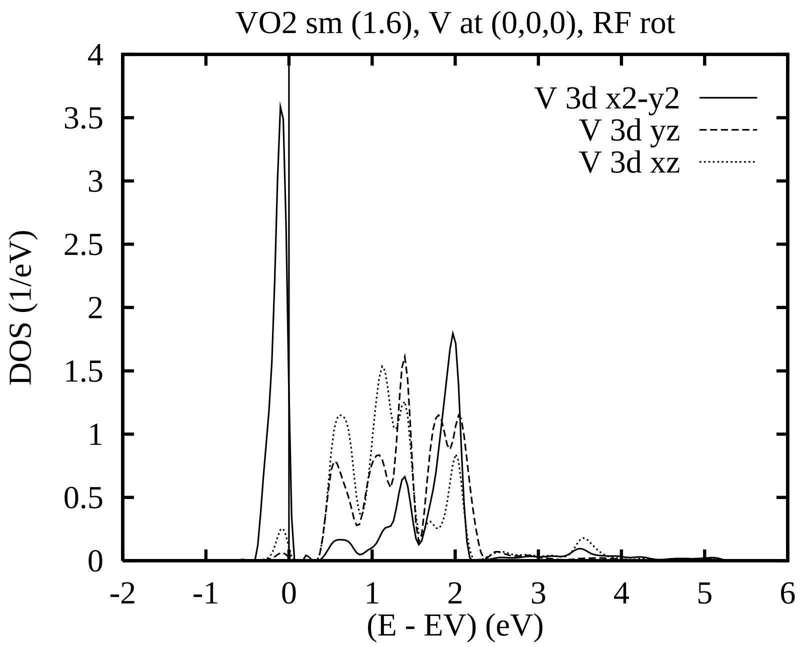

Figure 8.18: Partial V $3d$ t_{2g} densities of states (DOS) of monoclinic VO_2 with exaggerated vanadium atom distortions. Selection of orbitals is relative to the local rotated reference frame.

Chapter 9

VO_2: III. The monoclinic M_2 phase

9.1 Motivation

In the previous two chapter (hereafter referred to as I and II), we have investigated in detail both the metallic rutile and the insulating monoclinic (M_1) phase of VO_2 and, while emphasizing the role of bond order optimization, proposed a possible explanation for the origin of the metal-insulator transition. Our conclusions confirmed the previous findings of Wentzcovitch *et al.* who, using a molecular dynamics type approach, arrived at very similar results [259]. Still, the discussion by these authors was criticised by Rice *et al.* who focused attention on the monoclinic M_2 phase of VO_2, which so far has not been considered by electronic structure calculations [215]. Rice *et al.* called in question applicability of a single particle picture to the M_2 phase and, hence, to the physics of vanadium dioxide in general. From this they derived their criticism on the calculations for the M_1 phase.

As already mentioned in chapter 7 two additional insulating phases of VO_2 appear on application of uniaxial stress or on doping of VO_2 with small amounts of Cr, Fe, Al, or Ga of the order of few percent [169, 205, 45]. The phase diagram of Cr doped VO_2 as given by Pouget and Launois [205] is shown in Fig. 9.1. This phase diagram differs slightly from that given by other authors which fact has been attributed to differences in sample preparation and stoichiometry [169, 207]. Lateron, a similar phase diagram was reported for $V_{1-x}Al_xO_2$ by Ghedira *et al.* [95, 97]. According to Fig. 9.1, Cr-doped VO_2 enters, on cooling, the monoclinic M_2 phase. This metal-insulator transition is of first order [207]. On further lowering of the temperature, transition to the triclinic T phase occurs, which, for chromium concentrations smaller than 0.015, is followed by a first order transition to the monoclinic M_1 phase [169]. According to x-ray measurements by Marezio *et al.* each of the three low-temperature phases shows a particular distortion pattern of the atomic arrangement [169]. Whereas, as already explained in chapter 8, in the M_1 phase both the metal-metal pairing and the zigzag-type lateral displacement are observed on each chain, in the M_2 phase only half of the chains dimerize whereas the zigzag-type deviations are reserved to the other half of the chains. Finally, the T phase is intermediate, as those chains, which in the M_2 phase dimerize, gradually start

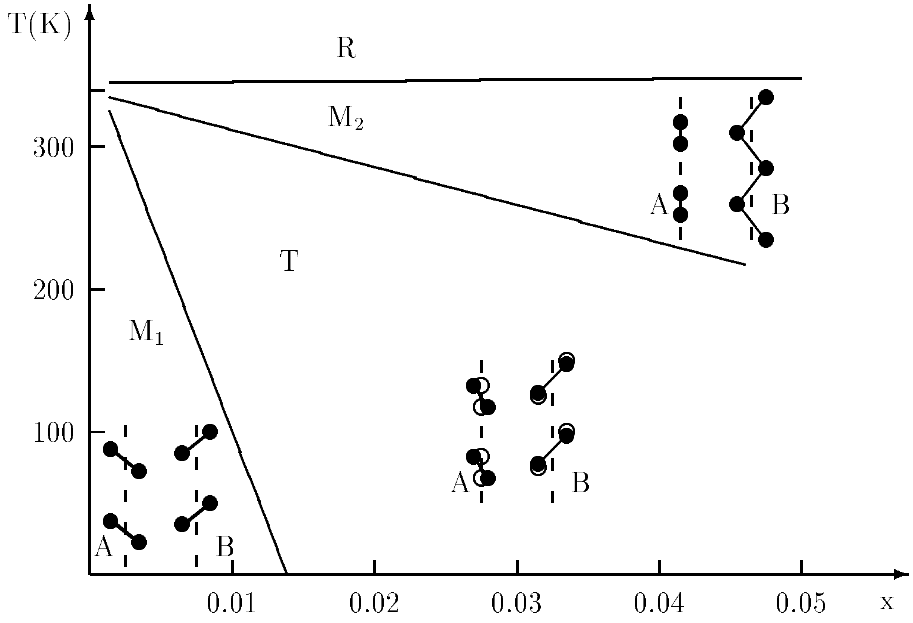

Figure 9.1: Phase diagram of $V_{1-x}Cr_xO_2$ according to Pouget and Launois [205]. The distortion patterns of the metallic chains are given in the insets (open circles in the T phase refer to the positions of the M_2 phase.

to tilt, whereas the zigzag chains start to dimerize until distortions in both chains are identical and eventually the M_1 is reached. Hence, the T and M_1 phases can be regarded as superpositions of two M_2-type displacements with unequal and equal weights, respectively. The role of the latter displacement pattern as the "fundamental" one may be understood from the symmetry considerations put forward by Pouget *et al.* as well as by Paquet and Leroux-Hugon, which we already mentioned in chapter 7 [207, 199, 215]. According to these considerations the pairing on one chain is intimately connected with the zigzag-type displacement on the neighbouring chains: If the vanadium atoms pair on one chain, the atoms on the neighbouring chains, which from the outset are vertically displaced by half the rutile c axis, move off the chain axis towards the apical oxygen atom whose V neighbours of the first sublattice have pulled apart. For this reason, the zigzag-like displacement may be viewed as being induced by the metal-metal pairing along the rutile c axis.

V^{51}-NMR measurements by Pouget *et al.* confirmed the x-ray experiments performed by Marezio *et al.* in that they revealed a positive Knight shift for the M_1 phase of $V_{1-x}Cr_xO_2$, which is similar to that of pure VO_2, while both a positive and a negative Knight shift were observed in the M_2 phase indicative of two different types of vanadium atoms [207]. Whereas the positive Knight shift again points to paired V sites the negative Knight shift gives evidence for V^{4+} atoms with localized $3d$ electrons. Finally, as D'Haenens *et al.* found from ESR data, the chromium atoms enter as substitutional Cr^{3+} ions on the zigzag-type chains [66, 67].

Magnetic susceptibility curves taken by Pouget *et al.* for $V_{1-x}Cr_xO_2$, which bear a striking similarity to corresponding data for Fe-doped VO_2 as measured by Kosuge [146], could be decomposed into a van Vleck contribution for the paired vanadium chains, a Curie-Weiss term representing the Cr^{3+} spins and an almost constant residual term. Using a model by Bonner and Fisher [37] Pouget *et al.* were able to attribute the latter contribution to noninteracting spin-$\frac{1}{2}$ linear Heisenberg chains, formed by the equispaced vanadium atoms, with an exchange constant of the order of room temperature [207]. The M_2 to T transition was thus viewed as a bonding or dimerization transition of a Heisenberg chain. This interpretation was confirmed by the observed decrease of the magnetic susceptibility [97]. In addition, the electrical conductivity increases by a factor of two [97]. From the existence of well localized $3d$ electrons at the V^{4+} sites, Pouget *et al.* concluded that the results should be interpreted in terms of a Mott-Hubbard-type picture and attributed the insulating gap to electronic correlations [207].

Lateron, Pouget *et al.* demonstrated that both the M_2 and T phase could be likewise stabilized by applying uniaxial stress along either the [110] or the $[1\bar{1}0]$ direction in stoichiometric VO_2 samples [206]. As can be easily visualized such uniaxial stress suppresses the zigzag-type displacements on those chains which have their tilting along the direction of the applied stress while the respective other chains are not affected. However, from the above symmetry considerations it follows that, as a consequence of the reduced tilt on one half of the chains, the pairing on the other chains will be also reduced. Additional NMR and EPR data revealed that the local symmetries as well as the magnetic properties of the two vanadium sites are identical in pure VO_2 under uniaxial stress and in $V_{1-x}Cr_xO_2$ [206].

As Pouget *et al.* pointed out, the critical uniaxial stress for appearance of the M_2 phase is so small that the free energies of the M_1 and M_2 phases in pure VO_2 must be extremely close at temperatures just below the metal-insulator transition [206]. The same conclusion was drawn for doped VO_2 by Pouget *et al.* from the fact that, although the M_2 and T phases involve substantial changes in the vanadium atom positions, they could be stabilized by impurity concentrations as low as 0.2% [207]. According to Pouget *et al.* the M_2 and the T phase must thus be interpreted as alternative phases of pure VO_2 whose free energies are only slightly higher than that of the M_1 phase of the pure material [207]. As a consequence, the M_2 phase was regarded as a metastable modification of the M_1 phase while the T phase is a transitional state, which displays characteristics of both monoclinic phases.

From these considerations both the dopants and the unixaxial stress appear as only small perturbations of pure VO_2 under ambient pressure, which, however, are able to enforce transition from the rutile to the M_2 rather than the M_1 phase. This point of view is supported by the fact that the rutile crystal structures of stoichiometric and doped VO_2 are identical as mentioned in I. As a consequence, we expect that the crystal structure parameters of the M_2 phase are essentially independent of the way this phase is enforced, hence, the type of dopant, the amount of doping or the strength of the uniaxial stress. Our expectation is supported by the fact that the crystal structure data given by Marezio *et al.* for $V_{0.976}Cr_{0.024}O_2$ and by Ghedira *et al.* for $V_{0.985}Cr_{0.015}O_2$ are almost identical [169, 97]. For this reason, it is justified to use these crystal structure data also as input for an investigation of the M_2 phase of pure VO_2.

The arguments given by Rice *et al.* as mentioned at the beginning aimed at the previous attempts to explain the metal-insulator transition purely in terms of the dimerization in the monoclinic M_1 phase [215]. If this were the only or the dominating driving force there would be no reason why VO_2 in the M_2 phase would be insulating, since only half of the chains dimerize. Instead, from the localized nature of the $3d$ electron on the vanadium atoms belonging to the linear Heisenberg chains, Rice *et al.* concluded that electron-electron correlations should play a major role in the M_2 and, consequently, also in the M_1 phase [215]. A different point of view was taken by Goodenough and Hong, who explained the insulating M_2 phase of VO_2 in terms of a splitting of *both* the $d_{\|}$ and the π^* bands, which lower part each comprises one quarter of the original rutile bands [110]. However, Goodenough and Hong did not take the antiferromagnetic order on the zigzag chains into account.

Still, the strong arguments by Rice *et al.* have not been met with state-of-the-art electronic structure calculations, which could make a point in one or the other direction. However, since an explanation of the origin of the metal-insulator transition of VO_2 has reached a level where consideration of the M_2 phase is crucial to further progress we have included an investigation of this phase in the present study. A discussion of the M_2 phase furthermore allows for a deeper understanding of the mechanisms active in the M_1 phase, since each chain shows only one of type of octahedral deformation. The present chapter will thus allow to distinguish the different types of vanadium atom displacements with respect to their coupling to the electronic states. Among other things this will also enable to identify the implications of the two different types of antiferroelectric modes arising from the zigzag-type and pairing displacements which could not be resolved in our investigation of the M_1 phase in chapter 8.

The chapter is organized as follows: Referring to the discussions of the rutile as well as the monoclinic M_1 structure as given in the preceding chapters we describe the main characteristics of the monoclinic M_2 structure in Sec. 9.2. After shortly summarizing in Sec. 9.3 methodological details which are unique to the present calculations we present the results in Sec. 9.4. The conclusion, Sec. 9.5, sums up the most important findings.

9.2 Crystal structure

In the M_2 phase VO_2 crystallizes in a centered monoclinic (cm) lattice with space group $C2/m$ (C_{2h}^3) [169, 97]. However, in contrast to the monoclinic M_1 structure, this time the monoclinic angle distorts the basal plane of the original rutile cell and, hence, the setup of the new primitive translations is different from that of the M_1 phase. Usually, the crystal structure of the M_2 phase is specified in terms of the underlying *simple* monoclinic lattice as defined by the primitive translations [169]

$$\mathbf{a}_{M_2,1} = \begin{pmatrix} a_{M_2} \\ 0 \\ 0 \end{pmatrix} , \quad \mathbf{a}_{M_2,2} = \begin{pmatrix} 0 \\ 0 \\ b_{M_2} \end{pmatrix} ,$$

$$\mathbf{a}_{M_2,3} = \begin{pmatrix} c_{M_2} \cos \beta_{M_2} \\ -c_{M_2} \sin \beta_{M_2} \\ 0 \end{pmatrix} \quad . \tag{9.2.1}$$

The lattice constants and monoclinic angle as resulting from the single crystal measurements on $V_{0.976}Cr_{0.024}O_2$ by Marezio *et al.* are $a_{M_2} = 9.0664$Å, $b_{M_2} = 5.7970$Å, $c_{M_2} = 4.5255$Å, and $\beta_{M_2} = 91.88°$, respectively [169]. There exist two different types of metal atoms and three types of oxygens, which occupy subsets of the general Wyckoff position (8j): $\pm(x, y, z)$, $\pm(x, -y, z)$, $(\frac{1}{2}, \frac{1}{2}, 0) \pm (x, y, z)$, and $(\frac{1}{2}, \frac{1}{2}, 0) \pm (x, -y, z)$. The parameters given by Marezio *et al.* are listed in Table 9.1. Ghedira *et al.* performed single crystal measurements on VO_2 doped with 1.5% of

Atom	Wyckoff positions	parameters		
		x	y	z
V_1	(4g)	0.0	0.7189	0.0
V_2	(4i)	0.2314	0.0	0.5312
O_1	(8j)	0.1482	0.2475	0.2942
O_2	(4i)	0.3969	0.0	0.2089
O_3	(4i)	0.1000	0.0	0.7987

Table 9.1: Crystal structure parameters of $V_{0.976}Cr_{0.024}O_2$ as given by Marezio *et al.* [169].

aluminum [95, 97]. They likewise found a simple monoclinic lattice with lattice constants $a_{M_2} = 9.060$Å, $b_{M_2} = 5.800$Å, $c_{M_2} = 4.5217$Å, monoclinic angle $\beta_{M_2} = 91.85°$, and the atomic positions as listed in Table 9.2. The striking close agreement of both

Atom	Wyckoff positions	parameters		
		x	y	z
V_1	(4g)	0.0	0.7189	0.0
V_2	(4i)	0.2312	0.0	0.5311
O_1	(8j)	0.1460	0.2474	0.2865
O_2	(4i)	0.3975	0.0	0.2284
O_3	(4i)	0.0980	0.0	0.7862

Table 9.2: Crystal structure parameters of $V_{0.985}Al_{0.015}O_2$ as given by Ghedira *et al.* [97].

data sets supports the interpretation of the M_2 phase as a metastable modification of the M_1 phase, which hardly depends on the dopant and the amount of doping. As already mentioned the M_2 phase can be likewise stabilized by the application of uniaxial pressure along the [110] direction [206]. Unfortunetely, no crystal structure data exist for this situation. As mentioned above, we will thus use the data of Cr-doped VO_2 for the present study of pure VO_2.

For the purpose of the present chapter we prefer using the centered monoclinic lattice, which comprises four instead of eight formula units. An alternative representation originates from a redefinition of the first lattice vector as

$$\mathbf{a}_{M_2,1} = \frac{1}{2} \begin{pmatrix} a_{M_2} \\ 0 \\ b_{M_2} \end{pmatrix} \tag{9.2.2}$$

while $\mathbf{a}_{M_2,2}$ and $\mathbf{a}_{M_2,3}$ are the same as in Eq. (9.2.1). Using this definition and comparing the lattice constants of the rutile and the M_2 phases we note the following approximate relation for the primitive translations [169]

$$\mathbf{a}_{M_2,1} \approx \begin{pmatrix} a_R \\ 0 \\ c_R \end{pmatrix} , \quad \mathbf{a}_{M_2,2} \approx \begin{pmatrix} 0 \\ 0 \\ 2c_R \end{pmatrix} ,$$

$$\mathbf{a}_{M_2,3} \approx \begin{pmatrix} 0 \\ -a_R \\ 0 \end{pmatrix} , \tag{9.2.3}$$

which emphasises the close relationship to the primitive translations proposed in Eq. (7.4.1) for the monoclinic M_1 phase. Indeed, were it not for the lattice strain present in both low-temperature structures, which hinders writing the primitive translations as linear combinations of the rutile lattice vectors, the primitive translations of the M_1 and M_2 structure were identical (except for a rotation by 90° about the Cartesian z axis). This is a consequence of the fact that both monoclinic phases result from the same R point instability of the rutile phase as has been pointed out by Brews [43] and by Blount (as mentioned by McWhan *et al.* [179]). In passing we note that this will allow to use the same setup of Brillouin zones for both monoclinic lattices which fact lateron facilitates discussion of the band structures. The close relationship between the two monoclinic phases becomes also obvious from Fig. 9.2 where we display the crystal structure of the M_2 phase using the unit cell spanned by the lattice vectors (9.2.1) and (9.2.2). We identify the vanadium atoms V_1 and V_2 at the corners and centers, respectively, of the underlying stacked rutile cells. Oxygen atoms of type O_1 are located at the apices of the octahedra centered about vanadium atoms V_1 and, hence, span the equatorial planes of the octahedra centered about vanadium atoms V_2. In contrast, oxygen atoms of types O_2 and O_3 are equatorial atoms for V_1 and apical atoms relative to V_2. Since the latter are shifted along the axis $O_2 - V_2 - O_3$ (see below) the identity of these two oxygen atoms is lost and two different apical $V_2 - O$ bond lengths evolve.

As for the M_1 structure, differences between the R and M_2 phases arise from the distinct local deformations of the VO_6 octahedra. Again, basic entities are i) the metal-metal pairing along the rutile c axis and ii) the zigzag-like in-plane displacements of the vanadium atoms parallel to the local z axis, hence, parallel to the

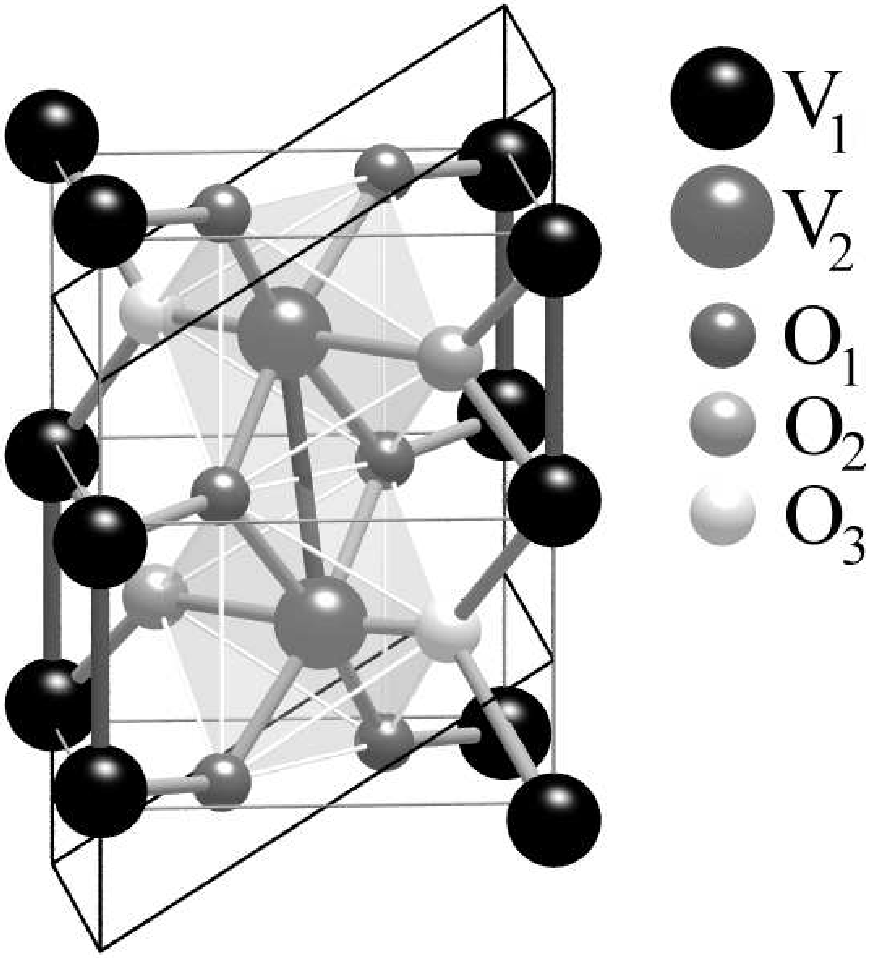

Figure 9.2: Crystal structure of monoclinic M_2 VO_2. Vanadium atoms V_1 and V_2 are printed in black and dark gray whereas oxygen atoms O_1, O_2, and O_3 are shaded dark, medium, and light gray, respectively.

diagonal of the rutile basal plane (see I for a description of the local coordinate systems). As in the M_1 structure these shifts alternate along both the tetragonal a and c axis. Furthermore, as is visible in the top view, Fig. 9.3, the oxygen atoms hardly move such that the antiferroelectric mode causes a displacement of the vanadium atoms *relative* to the surrounding oxygen octahedron and is not suppressed as in MoO_2.

Yet, in contrast to the M_1 phase, the forementioned basic distortion patterns are not equally displayed by both chains. As becomes clearer from Figs. 9.2 and 9.3 only half of the chains dimerize (V_1 chains) while the other half (V_2 chains) experiences the zigzag-like displacement without showing any pairing. As a consequence, two different $V_1 - V_1$ bond lengths of 2.538 and 3.259 Å appear while there is only one $V_2 - V_2$ bond length of 2.933 Å. Within the octahedra centered about V_1 the two apical $V_1 - O_1$ distances are 1.868 Å. Due to the vanadium-vanadium dimerization within these chains two short $V_1 - O_2$ distances of 1.852 Å and two long $V_1 - O_3$ distances of 2.089 Å arise. In contrast, in the octahedra centered about the tilted vanadium atoms the four equatorial $V_2 - O_1$ bond lengths of 1.931 and 1.974 Å are

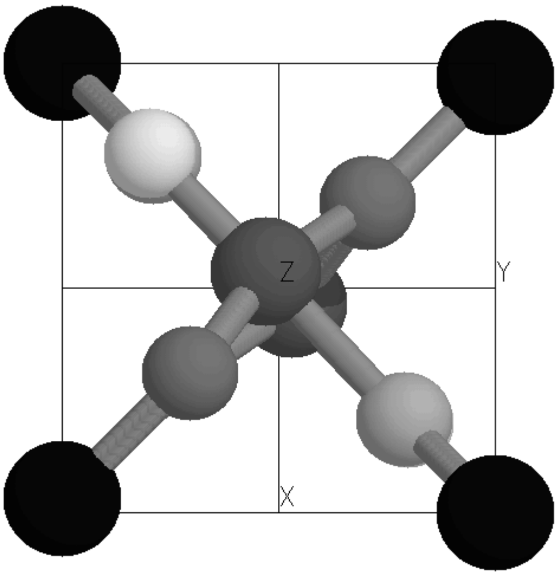

Figure 9.3: Crystal structure of monoclinic M_2 VO_2, top view. The shading of the atoms is the same as in Fig. 9.2.

very similar while the distances between the central V_2 atom and the apcial O_2 and O_3 disproportionate and assume the values 2.127 and 1.726 Å.

Finally, we mention the lattice strain, which, in addition to the strains present in the M_1 lattice, distorts the rutile basal plane. The resulting parallelogram would be likewise expected to result from uniaxial pressure along the [110] direction. It suppresses the zigzag-like displacement on those chains, which have their local z axes parallel to the shorter diagonal of the parallelogram. Since, according to the above mentioned symmetry arguments, the zigzag mode is connected to the dimerization of metal atoms on the neighbouring chains, suppression of the in-plane displacement on half of the chains may well lead to a suppression of the metal-metal pairing on the other half.

9.3 Method of calculation

In order to meet the requirements of the atomic sphere approximation (ASA) [8] to insert socalled empty spheres into the open crystal structure, we applied the sphere geometry optimization (SGO) algorithm [78]. We were able, by inserting 19 empty spheres into the monoclinic unit cell, to keep the linear overlap of any pair of physical spheres below 22%, and the overlap of any pair of physical and empty spheres below 27%. The positions of the empty spheres are listed in Table 9.3. The atomic sphere radii for all spheres as proposed by the SGO algorithm as well as the basis set orbitals are listed in Table 9.4, where states given in parentheses were included as tails of the other orbitals. Finally, the Brillouin zone sampling was done using an increasing number of **k** points, which range from 63, 144, 468 to 1088 points

Atom	Wyckoff positions	parameters		
		x	y	z
E_1	(8j)	0.2491	0.1251	-0.0019
E_2	(2c)	0.0	0.0	0.5
E_3	(4h)	0.0	0.3149	0.5
E_4	(4i)	0.0765	0.0	0.1518
E_5	(8j)	0.1597	0.2525	-0.3270
E_6	(4i)	0.3736	0.0	-0.1461
E_7	(8j)	0.0075	0.1525	-0.2867

Table 9.3: Empty sphere positions.

Atom	Radius/a_B	Orbitals				
V_1	2.290	$4s$	$4p$	$3d$	$(4f)$	
V_2	2.180	$4s$	$4p$	$3d$	$(4f)$	
O_1	1.906	$2s$	$2p$	$(3d)$		
O_2	1.957	$2s$	$2p$	$(3d)$		
O_3	1.658	$2s$	$2p$	$(3d)$		
E_1	1.767	$1s$	$2p$	$(3d)$		
E_2	1.329	$1s$	$(2p)$			
E_3	1.897	$1s$	$2p$	$(3d)$		
E_4	2.121	$1s$	$2p$	$3d$	$4f$	$(5g)$
E_5	1.757	$1s$	$2p$	$(3d)$		
E_6	1.872	$1s$	$2p$	$3d$	$(4f)$	
E_7	0.909	$1s$	$(2p)$			

Table 9.4: Atomic sphere radii and basis set orbitals.

within the irreducible wedge.

9.4 Results and Discussion

9.4.1 Non-spinpolarized calculations

We display in Fig. 9.4 the electronic states along selected high symmetry lines within the centered monoclinic Brillouin zone, which except for the small, basal plane distorting lattice strain, is identical to the simple monoclinic Brillouin zone of the M_1 phase given by Fig. 8.4. The total and partial densities of states (DOS) are given in Fig. 9.5. As for the M_1 phase of VO_2 we observe many similarities with the rutile

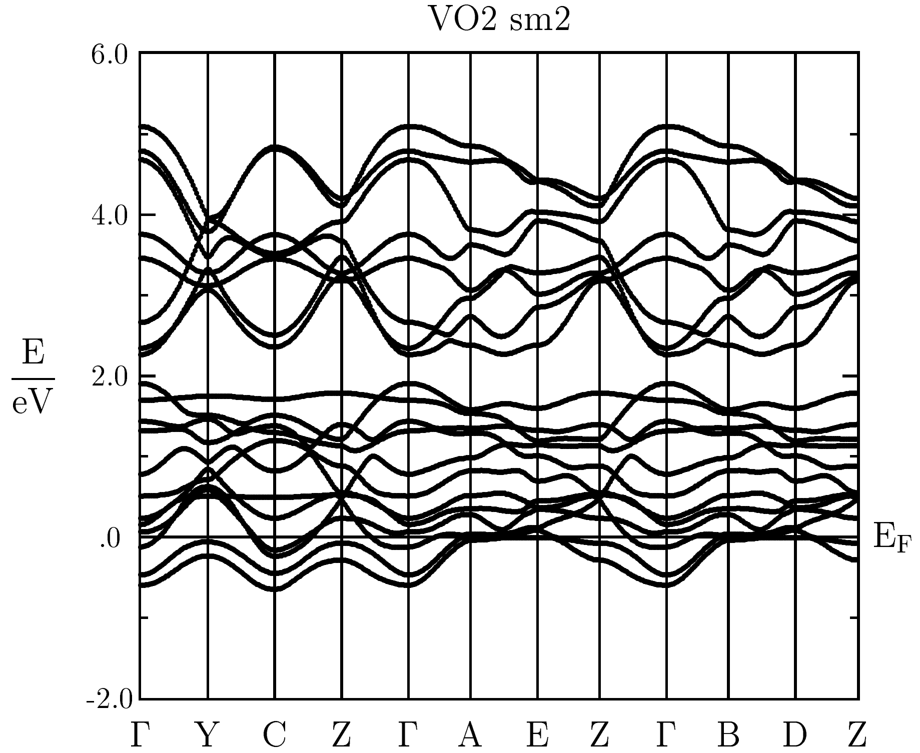

Figure 9.4: Electronic bands of monoclinic M_2 VO_2 along selected symmetry lines within the simple monoclinic Brillouin zone, Fig. 8.4.

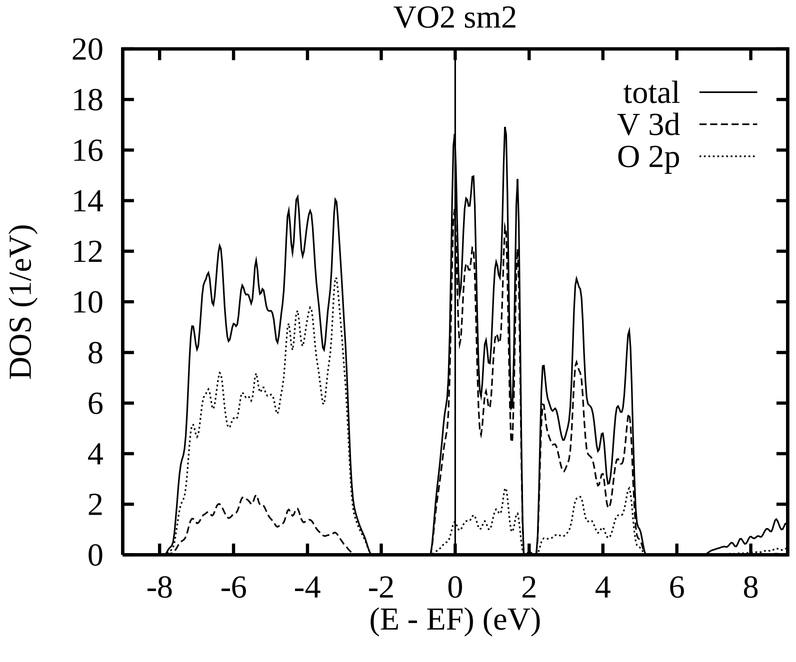

Figure 9.5: Total and partial densities of states (DOS) of monoclinic M_2 VO_2 per unit cell.

results as concerns the ordering, widths and separations of the bands. Still, we find the O $2p$-, V $3d$ t_{2g}- and e_g-dominated groups of bands below, at and above the Fermi energy, respectively as well as a hybridization of these states of about 10%.

Differences between the results for the low-temperature phases show up in a closer inspection of the V $3d$ partial DOS. Due to the presence of two different chains in the M_2 phase we have to distinguish between the two types of vanadium atoms. The partial DOS corresponding to V_1 and V_2 atoms, which belong to the dimerizing and zigzag-like chains, respectively, are displayed in Figs. 9.6 and 9.7.

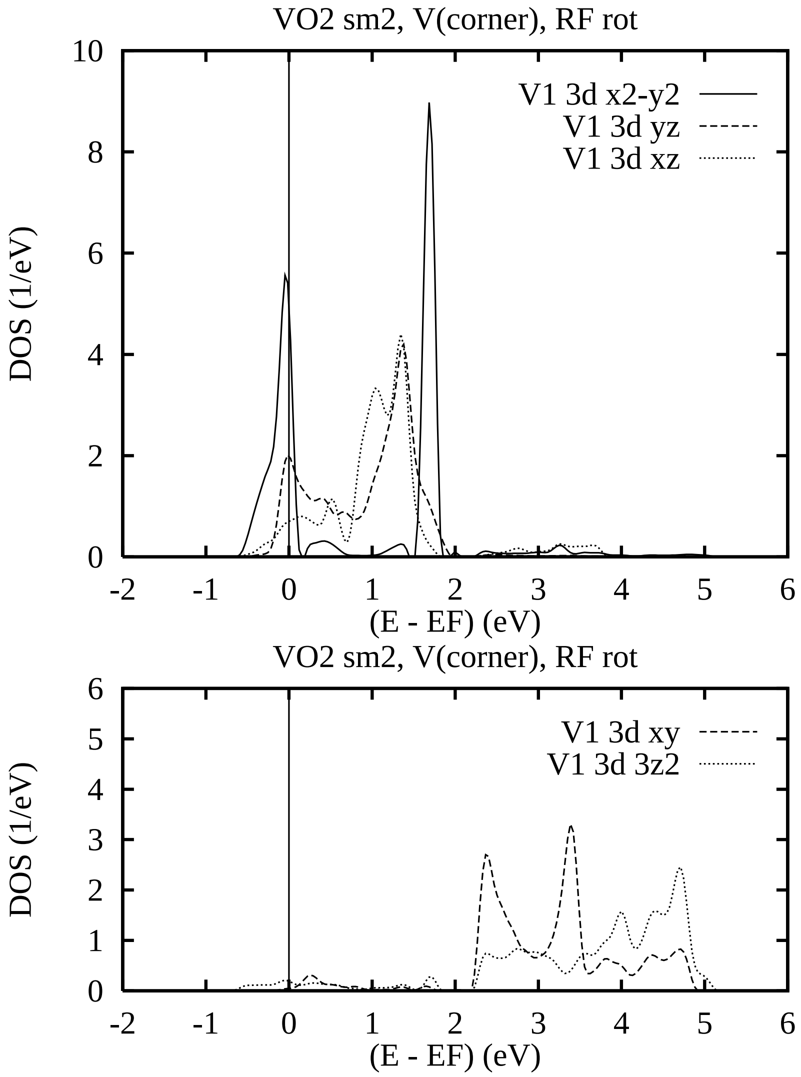

Figure 9.6: Partial V_1 $3d$ t_{2g} and e_g densities of states (DOS) of monoclinic M_2 VO_2. Selection of orbitals is relative to the local rotated reference frame.

Again, we have resolved the $3d$ states into their symmetry components relative to the respective local reference frame of each chain (see chapter 5 for the definition of the local coordinate systems). As for the rutile and the M_1 phase we observe for both types of vanadium atoms the energetical separation of the $3d$ t_{2g} and e_g groups of bands resulting from the crystal field splitting. Yet, V_1 and V_2 display distinct differences: The t_{2g} partial DOS of the paired V_1 atoms as shown in Fig. 9.6 closely resemble the t_{2g} partial DOS of the M_1 phase as given by Fig. 8.6, which are characterized by the strong bonding-antibonding splitting of the $d_{x^2-y^2}$ bands.

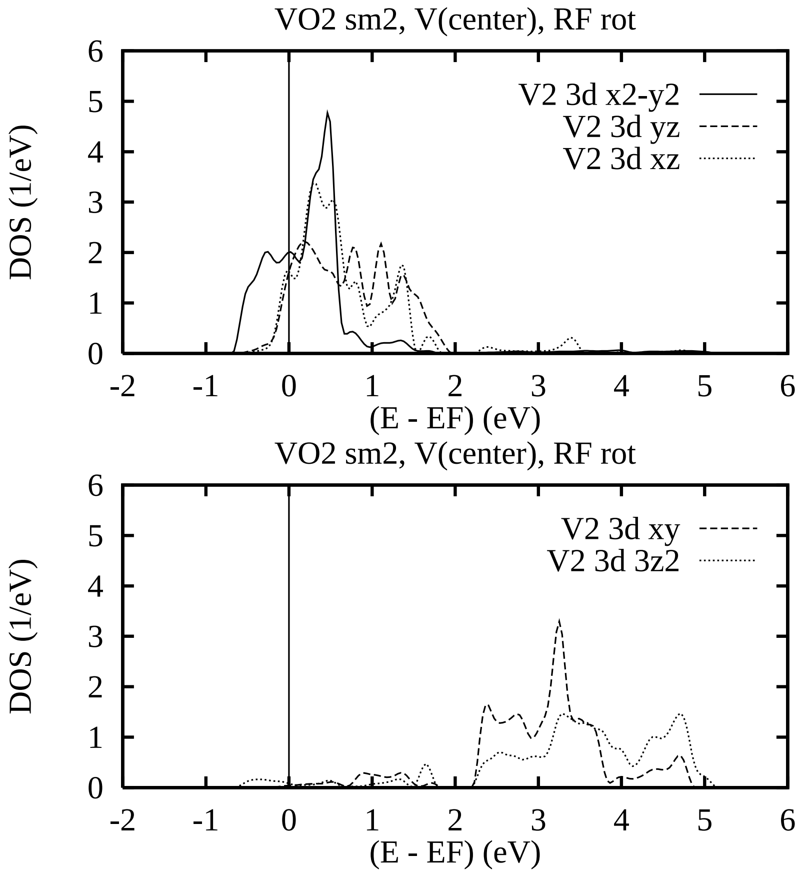

Figure 9.7: Partial V_2 $3d$ t_{2g} and e_g densities of states (DOS) of monoclinic M_2 VO_2. Selection of orbitals is relative to the local rotated reference frame.

This result fully agrees with the NMR data, which revealed the strong similarity of the Knight shift due to the dimerized vanadium atoms to that measured in the M_1 phase [207]. In contrast, we observe a completely different behaviour for the V_2 atoms belonging to the zigzag chains. The $d_{x^2-y^2}$ states located at these atoms do not experience any bonding-antibonding splitting at all. Instead the $d_{x^2-y^2}$ partial DOS displays a prominent peak at about 0.5 eV and a broad shoulder below E_F, while there are only minor contributions above $\approx$ 0.7 eV. It thus bears a strong similarity to the corresponding DOS of the rutile phase, Fig. 7.5, rather than to that of the monoclinic M_1 phase.

Interestingly, the behaviour of the d_{xz} and d_{yz} bands does not meet our expectations. Both bands experience a considerable upshift in energy similar to that stated for the M_1 phase, irrespective of the type of chain they belong to. From the discussion started in the previous two chapters, where we attributed the upshift of these bands to the antiferroelectric mode of the vanadium atoms coming with the zigzag-like in-plane displacements, we would have expected a raise in energy only for the d_{xz} and d_{yz} states of the V_2 atoms but not for those vanadium atoms which belong to the dimerizing chains. However, a closer look at the partial DOS in Fig. 9.6 and 9.7 reveals that actually the energetical upshift of the socalled π^* bands is higher on the dimerizing chains. This holds especially for the d_{xz} bands. At the same time the V_2 $3d_{yz}$ states display a rather small partial DOS without any significant maxima while the V_1 $3d_{yz}$ partial DOS bears a strong similarity to that of the M_1 phase. These differences may be traced back to the zigzag-like displacement of the V_2 atoms, which undermines the in-plane overlap of the d_{yz} orbitals and, hence, reduces their bonding-antibonding splitting.

While the changes due to the d_{yz} states on going from one phase to another are rather well understood the situation becomes more complicated for the d_{xz} states. From the previously discussed antiferroelectric mode we would have expected a strong upshift of these bands especially on the zigzag chains while the d_{xz} states originating from the dimerizing chains should stay at lower energies. Yet, the opposite is found. An explanation can be found from an analysis of the possible metal-oxygen overlaps using Table 9.5 where we combine those particular V $3d$ t_{2g}

	O_1	O_2	O_3
V_1 $3d_{x^2-y^2}$		$2p_x, 2p_y$	$2p_x, 2p_y$
V_1 $3d_{xz}$	$2p_x$	$2p_z$	$2p_z$
V_1 $3d_{yz}$	$2p_y$	$2p_z$	$2p_z$
V_2 $3d_{x^2-y^2}$	$2p_x, 2p_y$		
V_2 $3d_{xz}$		$2p_x$	$2p_x$
V_2 $3d_{yz}$		$2p_y$	$2p_y$

Table 9.5: V $3d$ – O $2p$ orbital overlaps.

and O $2p$ orbitals which, within a molecular-orbital picture, are expected to overlap. We complement the Table with the partial O $2p$ partial DOS in Fig. 9.8 where we have again used the local rotated frame of reference for the labeling of the orbitals. Note that we opted for the local reference frame corresponding to the dimerizing V_1 chains. As outlined at the beginning of chapter 7 interpretation in terms of the reference frame of the zigzag-like V_2 chains simply requires to exchange the y and z components. For the following discussion we recall that the O_1 atoms are the apical oxygen atoms of the dimerizing V_1 chains and occupy the equatorial positions of the zigzag-like V_2 chains. For oxygen atoms O_2 and O_3 things are reversed, with the latter having the shorter distance to the central V_2 atom. In addition, due to the dimerization, O_2 have a very short bond with the vanadium atoms of type V_1.

The forementioned geometry is reflected by the partial DOS. In Fig. 9.8 we observe a striking similarity of the partial DOS corresponding to atom O_2 to the V_1 $3d$ partial DOS as shown in Fig. 9.6. In general, all contributions in Figs. 9.6 to 9.8 can be well understood using the orbital overlaps listed in Table 9.5. In particular, we observe the hybridization of the V_2 $3d_{xz}$ peak at ≈ 0.4 eV with the O_3 $2p_x$ contribution. Onset of the zigzag-like mode increases this overlap and shifts these states to higher energies. In contrast the V_1 $3d_{xz}$ states, which are mainly found above 0.8 eV, overlap with the $2p_z$ states of their equatorial O_2 and O_3 partners. This overlap increases with increasing dimerization on these chains

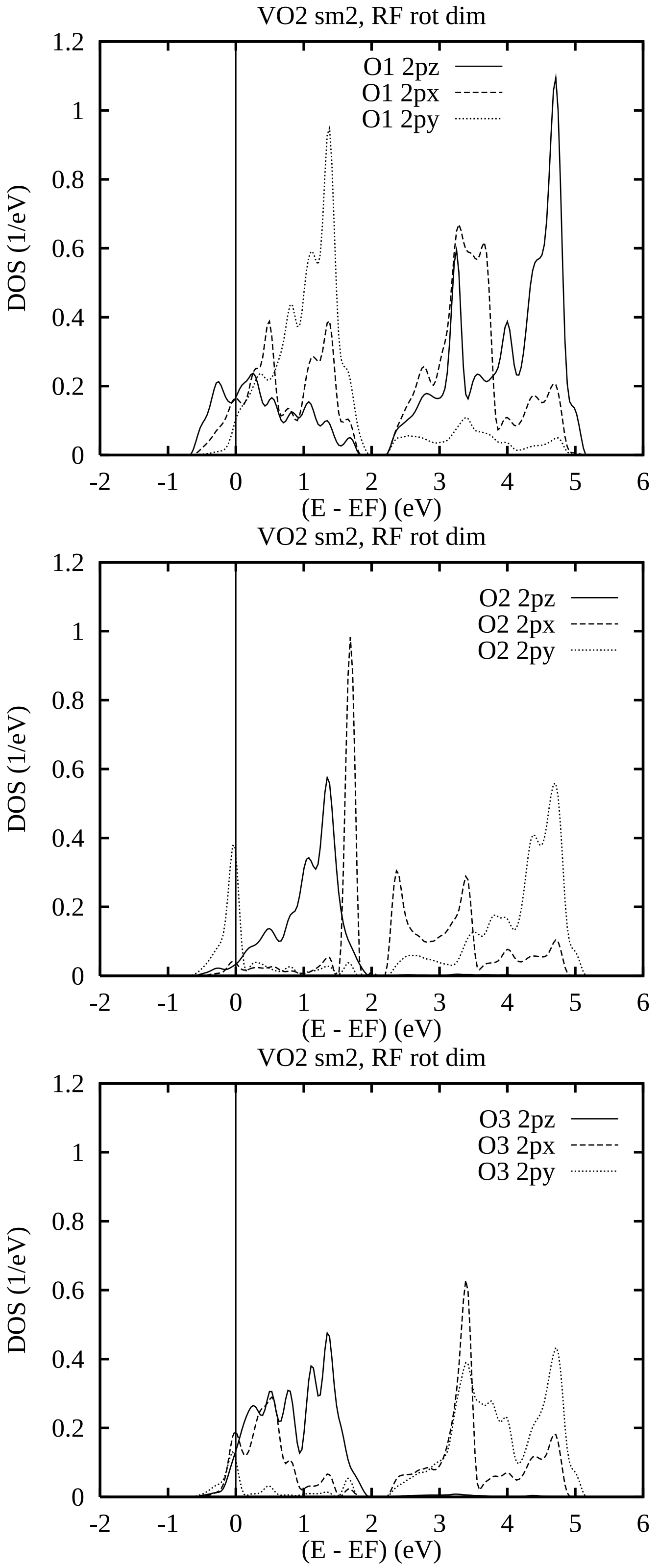

Figure 9.8: Partial O $2p$ densities of states (DOS) of monoclinic M_2 VO_2. Selection of orbitals is relative to the local rotated reference frame of atom V_1.

and thus likewise causes an upshift in energy. Hence, we witness a considerable antiferroelectric component of the metal-metal pairing which drives upshift of the π^* states on the corresponding chains and which we already proposed at the end of chapter 7.

Finally, the weighted band structure as displayed in Figs. 9.9 and 9.10 confirm

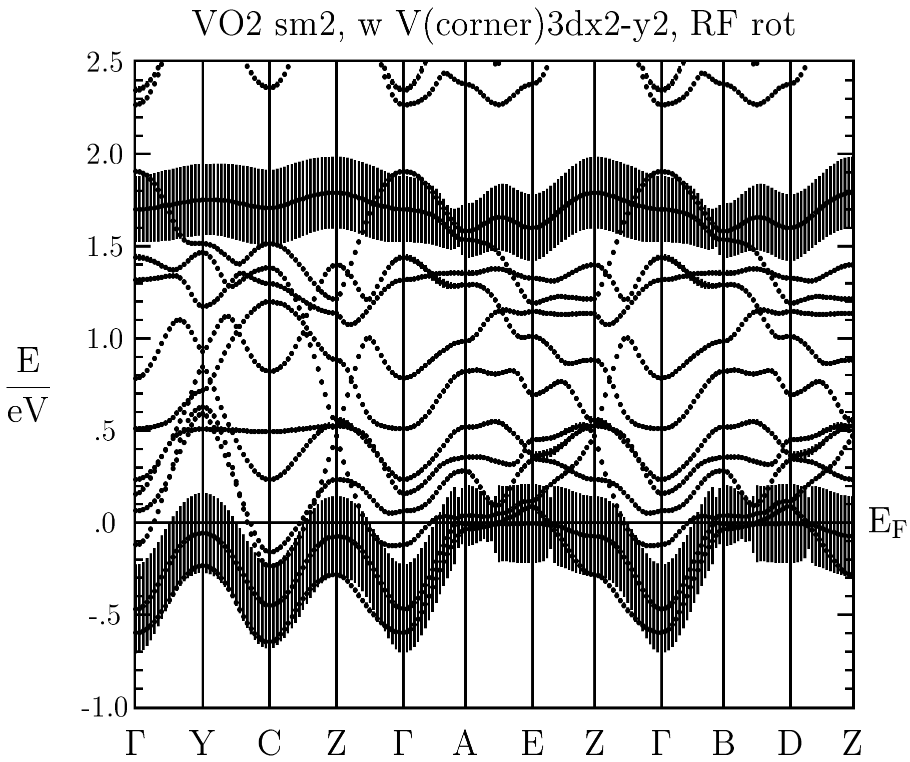

Figure 9.9: Weighted electronic bands of monoclinic M_2 VO_2. The width of the bars given for each band indicates the contribution due to the $3d_{x^2-y^2}$ orbital of atom V_1, which belongs to a dimerizing chain, relative to the local rotated reference frame.

the interpretation based on the partial densities of states. In complete analogy with the M_1 phase the $d_{x^2-y^2}$ bands of the V_1 atoms show the strong bonding-antibonding splitting, which results from the metal-metal pairing on the V_1 chains. In contrast, the $d_{x^2-y^2}$ bands of the V_2 atoms, which have equal metal-metal distances, resemble the dispersion of these bands in the rutile structure. Yet, we observe a reduction of the band width by ≈ 0.3 eV, which reflects the increased $V_2 - V_2$ distance in the zigzag chains. Finally, the d_{xz} and d_{yz} bands experience a global energetical upshift which is almost independent of the chain on which these orbitals are located.

9.4.2 Spinpolarized calculations

Whereas so far degeneracy of both spin channels was enforced we now turn to the spinpolarized calculations as suggested by the experimental finding of antiferromagnetic Heisenberg chains in the M_2 phase of VO_2. As a result we obtain a stable antiferromagnetic solution with a total energy which is by 0.5 mRyd per unit cell lower than that of the non-spinpolarized calculation. Magnetic moments of $0.49\mu_B$

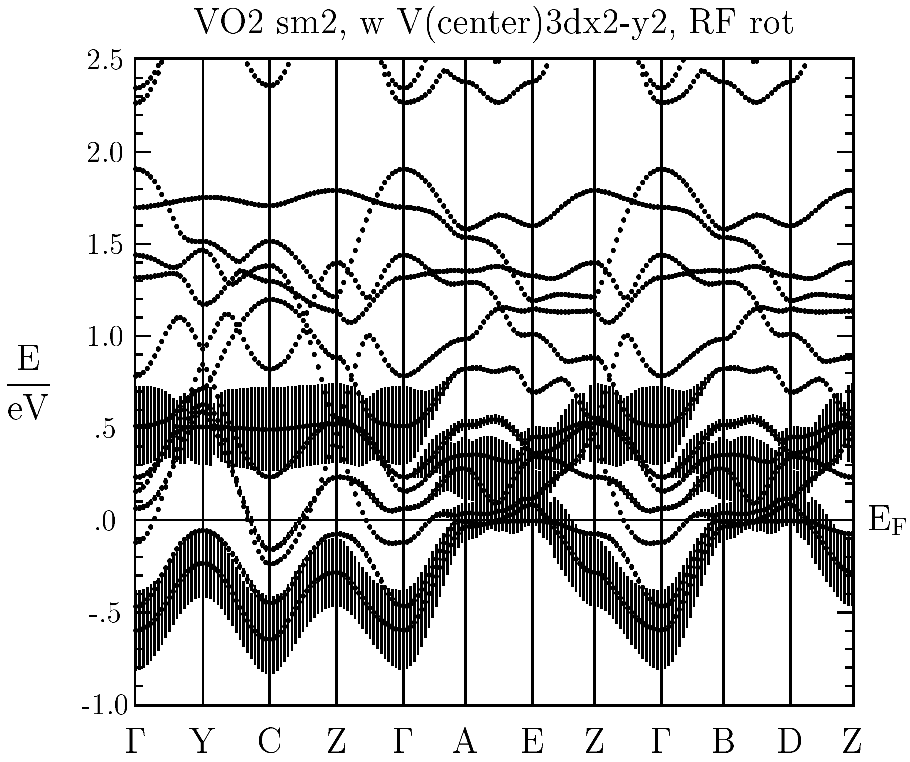

Figure 9.10: Weighted electronic bands of monoclinic M_2 VO_2. The width of the bars given for each band indicates the contribution due to the $3d_{x^2-y^2}$ orbital of atom V_2, which belongs to a zigzag chain, relative to the local rotated reference frame.

are carried by the $3d$ states of the V_2 atoms while the moments of all other atoms are either negligibly small or exactly zero as in case of the V_1 the latter fact being due to symmetry. We display the band structure along the same symmetry lines as in Fig. 9.4 as well as the partial DOS in Figs. 9.11 and 9.12. Note that *all* curves in Fig. 9.12 comprise contributions from one of the magnetic sublattices only. On comparing Figs. 9.11 and 9.12 with Figs. 9.4 and 9.5 for the non-spinpolarized case we recognize the main changes arising from spinpolarization in the small energy interval from -1 to 1 eV about the Fermi energy. Whereas the spin up DOS displays a rather high peak at E_F the spectral weight of the spin down DOS is distributed over to smaller peaks at E_F and 0.8 eV.

The changes originating from antiferromagnetic order are reflected by an analysis of the V $3d$ partial DOS, which we display in Figs. 9.13 and 9.14. The identical spin up and spin down densities of states of the V_1 atoms reflect the vanishing magnetic moments of these atoms. In contrast, we observe spin-dependent shifts of the V_2 partial DOS in the energy interval $[-1 : +1]$ and, to a lesser degree, between 2 and 4 eV. While spin-splitting of the d_{xz} and d_{yz} states is rather small the magnetic moment originates mainly from the local $d_{x^2-y^2}$ states. Recalling their non-spinpolarized partial DOS as shown in Fig. 9.7 with its prominent peak at $\approx$ 0.5 eV and the broad should below E_F we can now attribute the peak at 0.5 eV mainly to the spin down states while the broad shoulder comprises almost exclusively the spin up states. The situation is thus quite similar to that in our

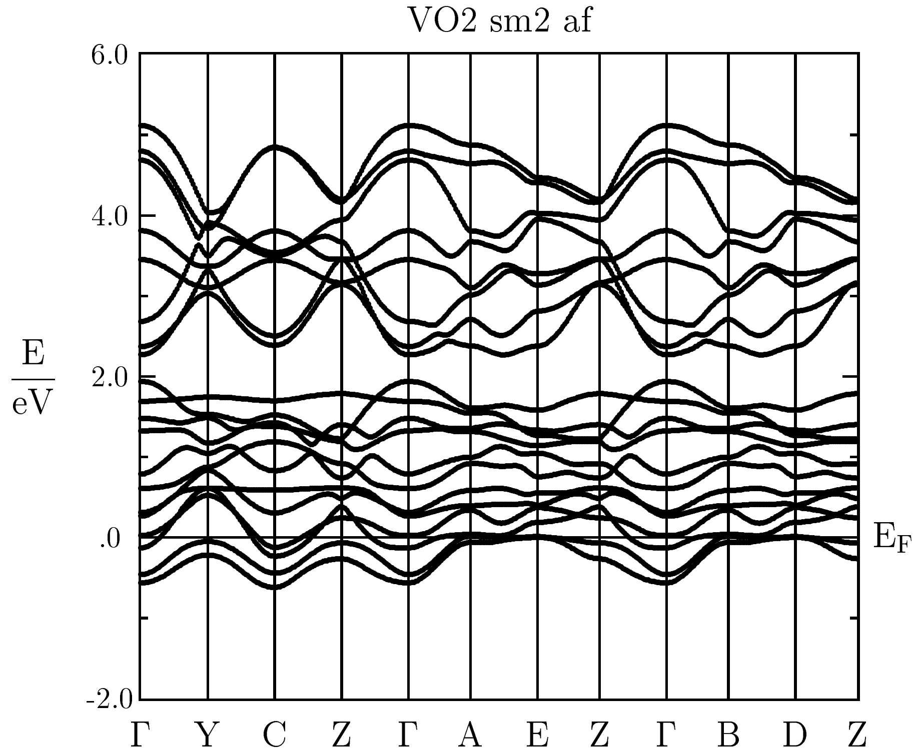

Figure 9.11: Electronic bands of antiferromagnetic monoclinic M_2 VO_2 along selected symmetry lines within the simple monoclinic Brillouin zone, Fig. 8.4.

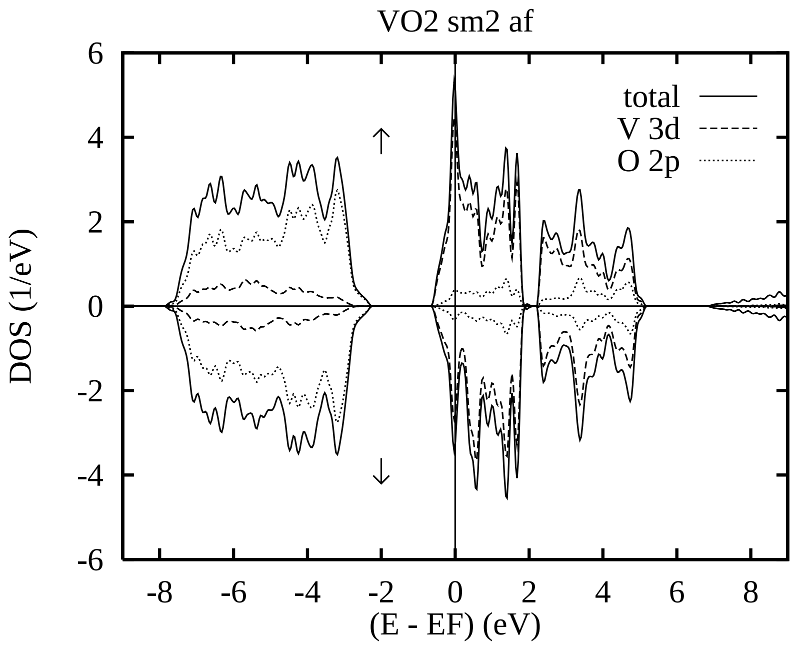

Figure 9.12: Total and partial densities of states (DOS) of antiferromagnetic monoclinic M_2 VO_2 per unit cell.

previous study on the molecule-based magnets $CsMn[Cr(CN)_6]$ and $CsNi[Cr(CN)_6]$. In the former compound those transition metal 3*d* orbitals, which carry the localized

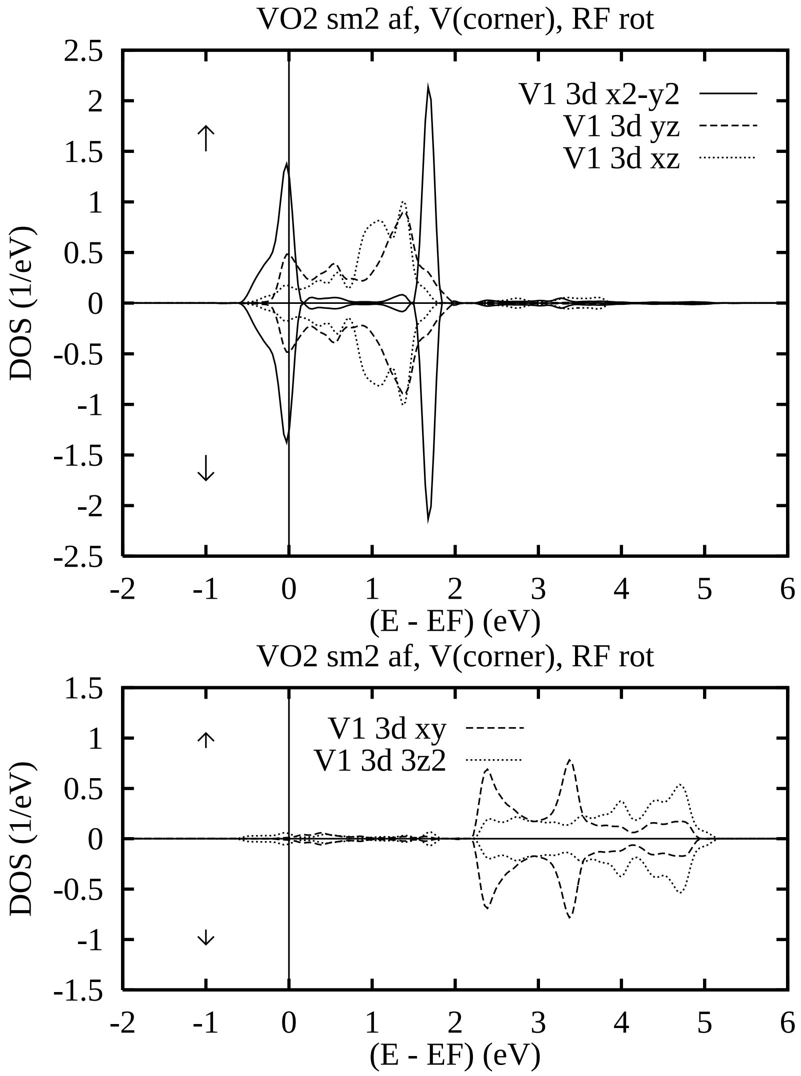

Figure 9.13: Partial V_1 $3d$ t_{2g} and e_g densities of states (DOS) of antiferromagnetic monoclinic M_2 VO_2. Selection of orbitals is relative to the local rotated reference frame.

magnetic moments, overlap and thus cause a splitting of these bands into bonding and antibonding states. In the spinpolarized case these two take over the role of the spin splitted states. The bonding orbital then comprises two electrons and eventually causes the antiferromagnetic alignment [87].

The situation becomes clearer from the weighted electronic structures as given by Figs. 9.15 and 9.16, which highlight the spin up and down V_2 $3d_{x^2-y^2}$ bands relative to the local reference frame of the single atom belonging to the spin up sublattice.

Still, the band structures and densities of states shown for the monoclinic M_2 phase of VO_2 lack the observed optical band gap. The situation is thus similar to that in the previous chapter on the M_1 phase. However, our main interest was not to end up with a finite gap but rather to demonstrate the applicability of the bond order optimization model which causes in general down- and upshift of bonding and antibonding orbitals. Nevertheless, we would also like to show that this scenario

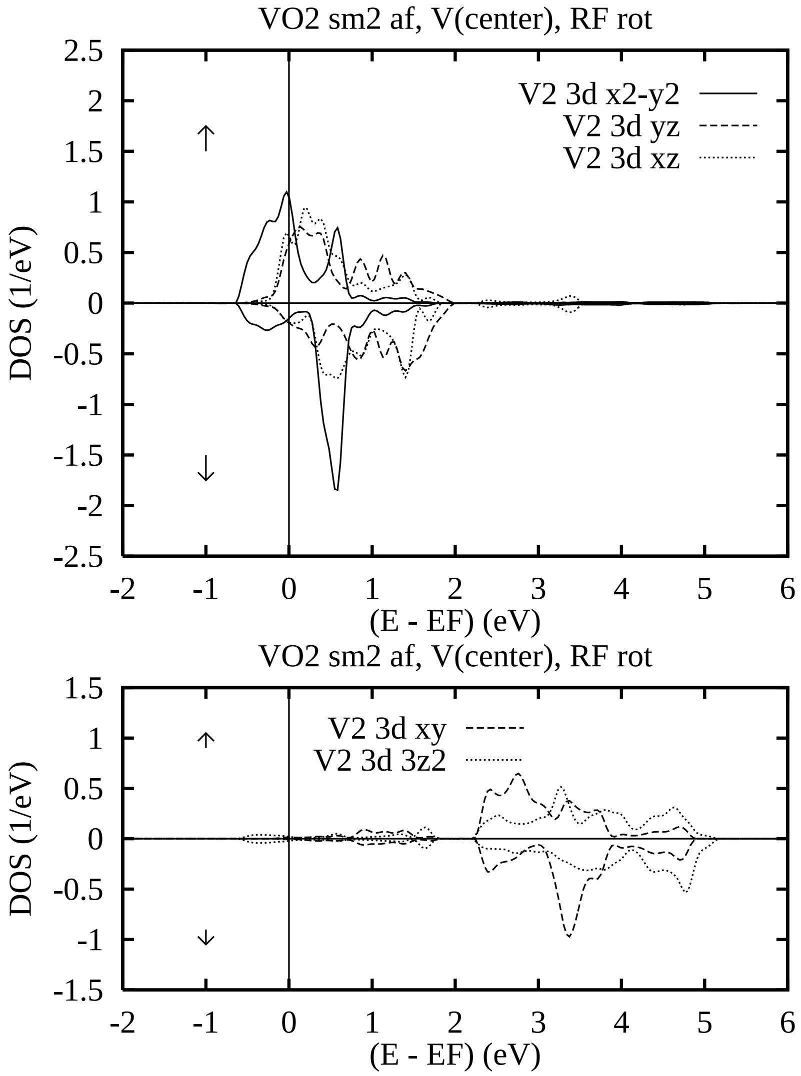

Figure 9.14: Partial V_2 $3d$ t_{2g} and e_g densities of states (DOS) of antiferromagnetic monoclinic M_2 VO_2. Selection of orbitals is relative to the local rotated reference frame.

may, in principle, be able to drive the metal-insulator transition. In order to check this possibility, we complement the previous investigation with calculations, where we exaggerated the dislacements of the vanadium atoms on going from the rutile to the monoclinic M_2 structure in the same manner as in chapter 8 on the M_1 phase. The resulting weighted band structure and partial densities of states, which correspond to Figs. 9.13 to 9.16, are given in Figs. 9.17 9.18, 9.19, and 9.20. They clearly reveal an insulating ground state and thus confirm the applicability of the bond order optimization model to the metal-insulator transition.

9.5 Conclusion

First-principles ASW calculations were used to study the electronic properties of the monoclinic M_2 phase of VO_2, which is accessible both by doping with Cr or Al

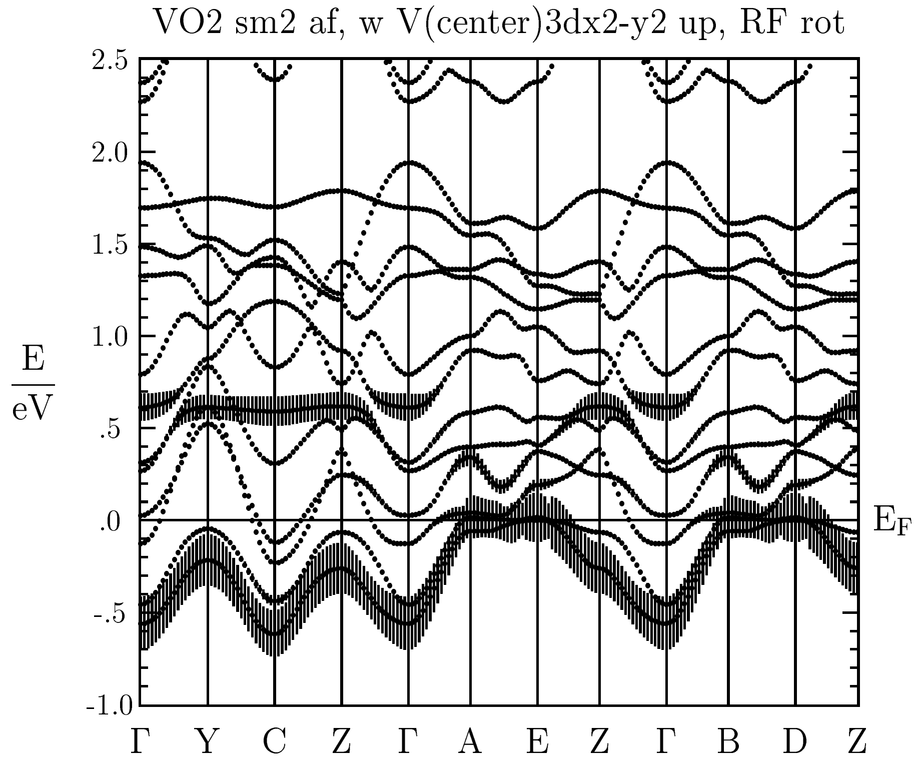

Figure 9.15: Weighted electronic bands of antiferromagnetic monoclinic M_2 VO_2. The width of the bars given for each band indicates the contribution due to the spin up $3d_{x^2-y^2}$ state of atom V_2, which belongs to a zigzag chain, relative to the local rotated reference frame.

and by applying uniaxial pressure and is thus regarded as a metastable modification of the M_1 phase. While the gross features of the electronic structure as discussed in connection with the rutile and the monoclinic M_1 phase as the dominant influence of O $2p$ as well crystal field split V $3d$ t_{2g} and e_g states and their considerable hybridization are still visible differences originate from the small but distinct deviations of the crystal structures. Metal-metal pairing on one half of the vertical chains causes complete bonding-antibonding splitting of the $d_{x^2-y^2}$ states located on these chains and, at the same time, upshift of the d_{xz} and d_{yz} bands. In contrast, on those chains, where the vanadium atoms undergo the zigzag-like displacement, this antiferroelectric mode causes upshift of the d_{xz} and d_{yz} states but no splitting of the $d_{x^2-y^2}$ bands. As a consequence, their bonding and antibonding subbands are still connected across the Fermi energy.

The situation changes in an antiferromagnetic calculation, which leads to a stable magnetic solution and polarizes mainly the local V_2 $d_{x^2-y^2}$ bands. Local magnetic moments of 0.5 μ_B arise while V_1 moments vanish for symmetry reasons. At the V_2 sites spin up and down states take over the role of bonding and antibonding $d_{x^2-y^2}$ states, which are now separated and allow for opening the insulating gap. The latter fact becomes more obvious in a final hypothetical calculation where again the vanadium atom displacements are exaggerated thus causing a band gap of ≈ 0.1 eV. As in the preceding two chapters our investigation of the monoclinic M_2 phase of

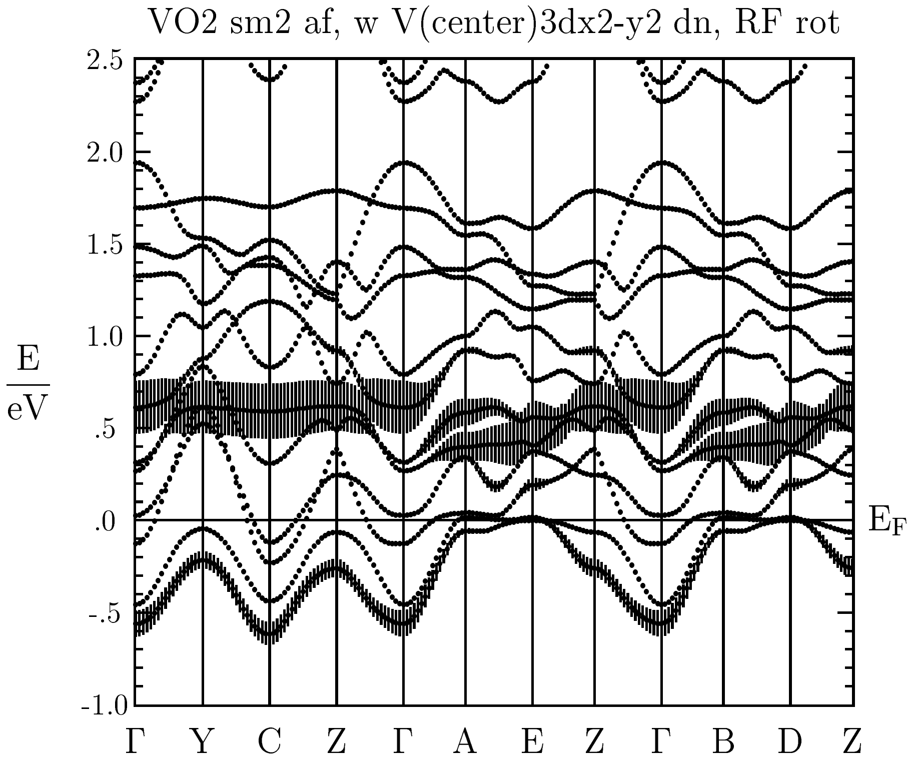

Figure 9.16: Weighted electronic bands of antiferromagnetic monoclinic M_2 VO_2. The width of the bars given for each band indicates the contribution due to the spin down $3d_{x^2-y^2}$ state of atom V_2, which belongs to a zigzag chain, relative to the local rotated reference frame.

VO_2 confirms the previously proposed bond order optimization model.

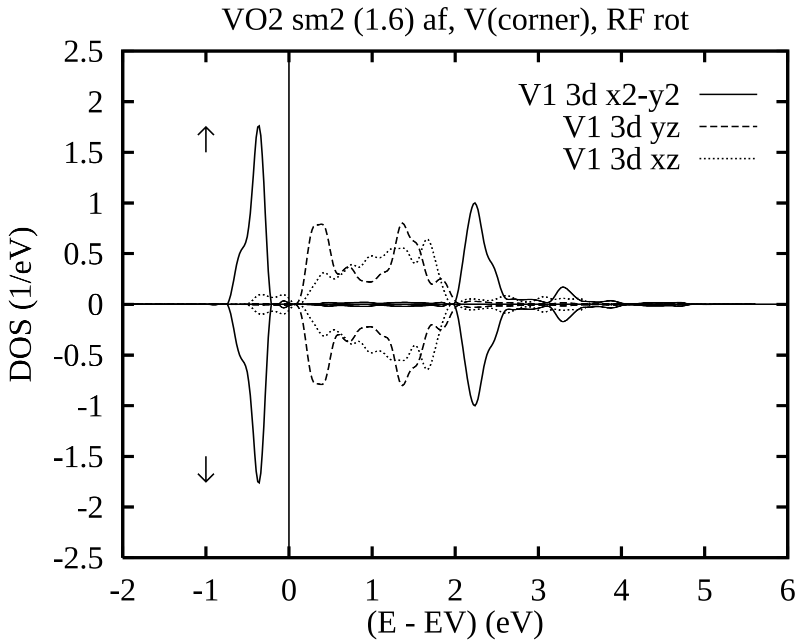

Figure 9.17: Partial V_1 $3d$ t_{2g} densities of states (DOS) of antiferromagnetic monoclinic M_2 VO_2 with the vanadium atom distortions exaggerated. Selection of orbitals is relative to the local rotated reference frame.

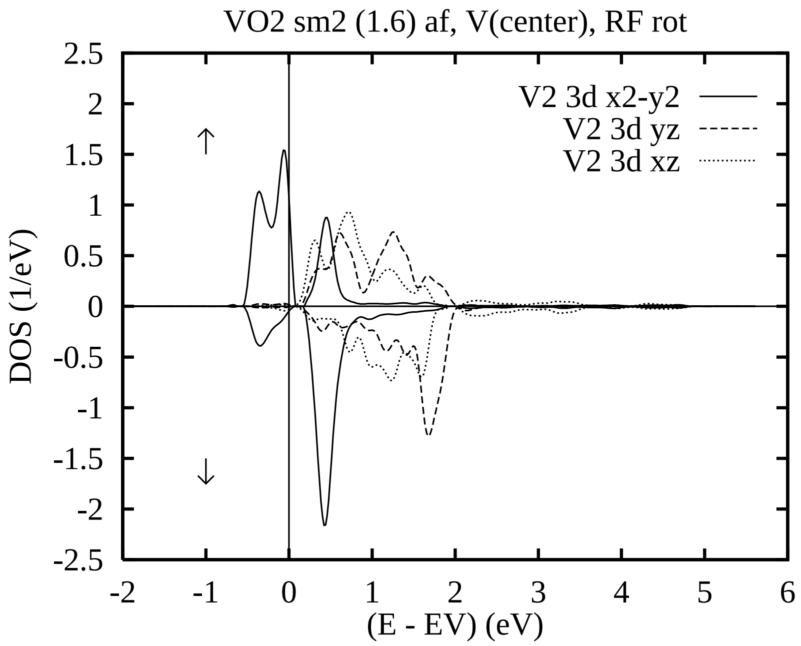

Figure 9.18: Partial V_2 $3d$ t_{2g} densities of states (DOS) of antiferromagnetic monoclinic M_2 VO_2 with the vanadium atom distortions exaggerated. Selection of orbitals is relative to the local rotated reference frame.

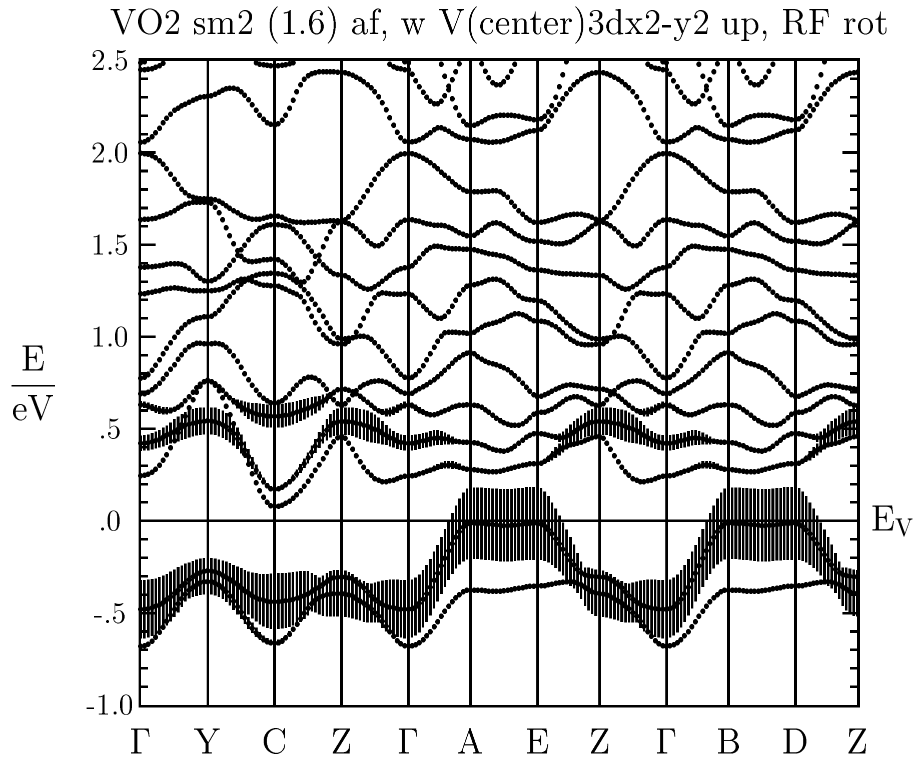

Figure 9.19: Weighted electronic bands of antiferromagnetic monoclinic M_2 VO_2 with the vanadium atom distortions exaggerated. The width of the bars given for each band indicates the contribution due to the spin up $3d_{x^2-y^2}$ state of atom V_2, which belongs to a zigzag chain, relative to the local rotated reference frame.

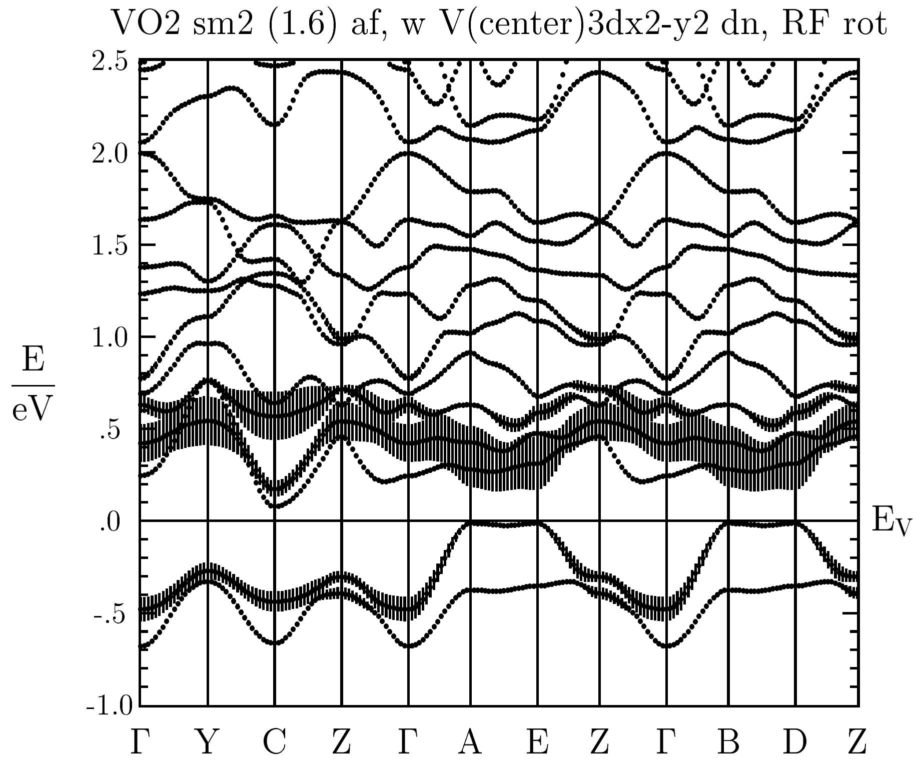

Figure 9.20: Weighted electronic bands of antiferromagnetic monoclinic M_2 VO_2 with the vanadium atom distortions exaggerated. The width of the bars given for each band indicates the contribution due to the spin down $3d_{x^2-y^2}$ state of atom V_2, which belongs to a zigzag chain, relative to the local rotated reference frame.

Chapter 10

Summary

In the present work we have used all-electron first principles calculations to study the electronic and structural properties as well as their mutual interaction in various, in some aspects prototypical, compounds. In particular, it was a major goal to establish a link between local geometries, chemical bonds, and the electronic structure. We aimed at combining schemes, which are guided by chemical and physical intuition, with quantitative state-of-the-art calculations.

In all the compounds studied the electronic structure was dominated by the strong hybridization of chalcogen (oxygen or sulfur) p and transition metal d states. Being subject to the crystal electric field formed by the surrounding chalcogen atoms, which built deformed octahedra, the d states split into lower t_{2g} and upper e_g states. These rather general features constituted the first step in the formation of the electronic structure in as they led to the formation of bonding and antibonding σ and π states.

The second step was influenced rather by the details of the respective compounds, which left enough room for variation and, in particular, allowed to study the impact of various deviations from the ideal octahedral geometry on the electronic structure. The differences between the compounds considered here affected mainly exact energetical position and ordering of the particular bands, which eventually were responsible for the electronic properties. In order to allow for a better understanding we proposed a discussion in terms of the bond order optimization model (BOOM). Using this approach, we were able to discuss in very detail the deviations from octahedral symmetry especially in V_2O_5, MoO_2, and VO_2 and gave a clue to the metal-insulator transition of the latter compound.

Octahedral deformations were observed to play an important role in semiconducting iron pyrite, FeS_2, where the upper part of the valence band is formed mainly from Fe $3d$ t_{2g}-derived states while the conduction band comprises the e_g-derived levels. Yet, the conduction band minimum is exclusively due to S $3p$ states this fact explaining the observed high optical absorption. In addition, the presence of sulfur $3p$ states, which result from strong binding sulfur-atom pairs, at the conduction band minimum lays ground for the high sensitivity of the optical bands gap on the bond lengths of the sulfur pairs. We demonstrated that only small deviations in the sulfur pair bond lengths involve rather drastic changes of the near-gap electronic states which might even turn the indirect bandgap into a direct one.

The electronic properties of semiconducting V_2O_5 are governed by three different types of oxygen atoms which are responsible for five different bonds within the strongly deformed VO_6. The strong deviations of the VO_6 octahedra from cubic coordination give rise to the narrow split-off conduction band as a characteristic feature of V_2O_5. Furthermore, by calculating the electronic structure for V_2O_5 using various hypothetically idealized crystal structures we could demonstrate that distortions of the octahedra along the crystallographic c axis drastically increase the bonding-antibonding splitting of the V $3d_{xz}/3d_{yz}$-derived bands whereas distortions perpendicular to the c axis reduce the bandwidth of the split-off V $3d_{xy}$ bands. Both effects were shown contribute to the stability of V_2O_5 and enhance the optical band gap.

Molybdenum dioxide crystallizes in a monoclinic structure which deviates only slightly from the rutile structure and is characteristic of several other dioxides. In order to lay ground for the discussion of mechanisms favouring the monoclinic structure we started from a hypothetical rutile reference phase for this compound. Near the Fermi energy we found almost exclusively Mo $4d$ t_{2g} orbitals. Local $d_{x^2-y^2}$ states pointing along the rutile c axis exhibit considerable but still incomplete bonding-antibonding splitting indicative of metal-metal bonding parallel to this axis. At the same time, these orbitals cause nesting on large portions of the Fermi surface. The resulting Peierls-type instability points to the monoclinic cell which allows for a pairing of the metal atoms.

The electronic properties of monoclinic MoO_2 exhibit characteristic deviations from those of the previously studied hypothetical rutile reference phase. While strongly hybridized O $2p$ and Mo $4d$ e_g states were still found well below and above the Fermi energy, metal-metal pairing along the rutile c axis causes a considerably increased bonding-antibonding splitting of the Mo $4d_{x^2-y^2}$-derived bands near the Fermi energy. As a consequence, these bands shift away from E_F thus confirming the previously proposed Peierls-like scenario. In contrast, metallic conductivity derives exclusively from the Mo $4d_{yz}$ and $4d_{xz}$ bands which are both partially occupied.

As for hypothetical rutile MoO_2 the electronic properties of rutile VO_2 are dominated by strong hybridization of O $2p$ and crystal field split V $3d$ states. While O $2p$ and V $3d$ e_g states are located well below and above the Fermi energy, respectively, states near E_F originate almost exclusively from V $3d$ t_{2g} orbitals. In contrast to MoO_2 the calculated Fermi surface sections for rutile VO_2 did not give any indications for a structural instability in the calculated Fermi surface sections. Analysis of the band characters revealed a predominantly one-dimensional dispersion of the local V $3d_{x^2-y^2}$ states, which mediate overlap along the vertical metal chains characteristic of the rutile structure. Splitting of these states due to metal-metal pairing and simultaneous upshift of the remaining two t_{2g} bands as a consequence of strong metal-oxygen hybridization may increase the overall bond order, hence, the chemical stability. While this general scenario holds for all early rutile-related transition metal dioxides it could lead to the observed insulating ground state in the low-temperature structure for the d^1 systems VO_2 and NbO_2.

The validity of the bond order optimization model was demonstrated by the calculations for the monoclinic low-temperature phases of vanadium dioxide. The electronic properties of VO_2 in the monoclinic M_1 phase exhibit characteristic deviations from those of the rutile phase. While strongly hybridized O $2p$ and V $3d$ e_g states remained at the positions assumed in the rutile phase well below and above the Fermi energy, a considerable bonding-antibonding splitting of the V $3d_{x^2-y^2}$-derived bands near the Fermi energy originates from the dimerization of the vanadium atoms along the rutile c axis. This effect showed up likewise in the crystal orbital overlap population. While these bands shift away from E_F, the V $3d_{yz}$ and $3d_{xz}$ bands experience a considerable upshift due to the antiferroelectric in-plane displacement of the vanadium atoms. The results were in full agreement with the previously proposed bond order optimization model. Although from the calculations we obtained a semimetallic ground state on the verge of an insulator, an additional set of calculations, where the vanadium displacments were exaggerated, resulted in an insulating ground state with a band gap of more than 0.4 eV. Our investigation thus confirmed the general ability of a single particle description for the metal-insulator transition.

Finally, we complemented our study by an investigation of the monoclinic M_2 phase of VO_2 which involves a disproportionation of the octahedral chains formed by the metal atoms in as far as only half of the chains dimerize and the other half exhibits a zigzag-like displacement of the vanadium atoms. For this reason, in contrast to the monoclinic M_1 phase the electronic structure in the M_2 phase and especially the insulating ground state can not be explained in terms of only one of these vanadium atom displacements. The electronic properties of monoclinic M_2 VO_2 exhibit characteristic deviations from those of both the rutile reference and the monoclinic M_1 phase. Increased bonding-antibonding splitting of the $d_{x^2-y^2}$ bands was found only for the states originating from the dimerized vanadium atoms. In contrast, no splitting was observed for $d_{x^2-y^2}$ bands arising from vanadium atoms of the zigzag-type chains. We were able to identify antiferroelectric distortions in both types of chains as the main responsible for the upshift of antibonding metal-oxygen bond π^* bands. On releasing the constraint of spin-degeneracy in a subsequent spinpolarized calculation we obtained exchange splitting of these latter bands of 0.8 eV coming along with antiferromagnetically ordered magnetic moments of about 0.5 μ_B and a lowering of the total energy. In the spinpolarized calculation the role of the missing metal-metal pairing is taken over by antiferromagnetic ordering, which, eventually, separates the spin up and down bonding and antibonding bands. As for the M_1 structure the valence and conduction band still displayed a small overlap of 0.2 eV, which, however, turned into a finite gap of 0.1 eV width when the vanadium displacements were exaggerated.

Bibliography

[1] M. Abbate, F. M. F. de Groot, J. C. Fuggle, Y. J. Ma, C. T. Chen, F. Sette, A. Fujimori, Y. Ueda, and K. Kosuge, Phys. Rev. **B43**, 7263 (1991).

[2] K. Adachi, K. Sato, K., Yamanchi, and M. Ohashi, J. Phys. Soc. Japan **32**, 573 (1972).

[3] D. Adler and H. Brooks, Phys. Rev. **155**, 826 (1967).

[4] D. Adler, J. Feinleib, H. Brooks, and W. Paul, Phys. Rev. **155**, 851 (1967).

[5] P. B. Allen, R. M. Wentzcovitch, W. W. Schulz, and P. C. Canfield, Phys. Rev. **B48**, 4359 (1993).

[6] T. Allersma, R. Hakim, T. N. Kennedy, and J. D. Mackenzie, J. Chem. Phys. **46**, 154 (1967).

[7] O. K. Andersen, Solid State Comm. **13**, 133 (1973)

[8] O. K. Andersen, Phys. Rev. **B12**, 3060 (1975).

[9] O. K. Andersen, *Linear Methods in Band Theory*, in: *The Electronic Structure of Complex Systems*, edited by P. Phariseau, W. Temmerman, Plenum Press, New York, 1984, pp. 11-66

[10] O. K. Andersen, O. Jepsen, and D. Glötzel, *Canonical Description of the Band Structures of Metals*, in: *Highlights of Condensed-Matter Theory*, Proceedings of the International School of Physics "Enrico Fermi", Course LXXXIX, edited by F. Bassani, F. Fumi, and M. P. Tosi, North-Holland, Amsterdam 1985, pp. 59-176.

[11] O. K. Andersen, O. Jepsen, and M. Sob, *Linearized Band Structure Methods*, in: *Electronic Band Structure and its Applications*, edited by M. Yussouff, Springer, Berlin, 1986, pp. 1-57.

[12] O. K. Andersen, A. P. Postnikov, and S. Yu. Savrasov, *The Muffin-Tin Orbital Point of View*, in: *Applications of Multiple Scattering Theory to Materials Science*, edited by W. H. Butler, P. H. Dederichs, A. Gonis, R. L. Weaver, MRS Symposia Proceedings No. 253 (Materials Research Society, Pittsburgh, 1992), p. 37.

[13] G. Andersson, Acta Chim. Scand. **10**, 623 (1956).

[14] E. Antoncik, J. Phys. Chem. Solids **10**, 314 (1959).

[15] N. W. Ashcroft and N. D. Mermin, *Solid State Physics*, Holt-Saunders, Philadelphia, 1976.

[16] B. J. Austin, V. Heine, and L. J. Sham, Phys. Rev. **127**, 276 (1962).

[17] G. B. Bachelet, D. R. Hamann, and M. Schlüter, Phys. Rev. **B26**, 4199 (1982).

[18] H. G. Bachmann, F. R. Ahmed, and W. H. Barnes, Z. Krist. **115**, 110 (1961).

[19] H. G. Bachmann and W. H. Barnes, Z. Krist. **115**, 215 (1961).

[20] A. Baldereschi, Phys. Rev. **B7**, 5212 (1973).

[21] U. von Barth, in: *The Electronic Structure of Complex Systems*, edited by P. Phariseau and W. M. Temmerman, Plenum Press, New York, 1984, pp. 67-140.

[22] U. von Barth, in: *Many-Body Phenomena at Surfaces*, edited by D. Langreth and H. Suhl, Academic Press, Orlando, 1984, pp. 3-50.

[23] U. von Barth, in: *Methods of Electronic Structure Calculations*, edited by V. Kumar, O. K. Andersen, and A. Mookerjee, World Scientific, Singapore, 1994, pp. 21-62.

[24] U. von Barth, L. Hedin, J. Phys. **C5**, 1629 (1972).

[25] N. Beatham and A. F. Orchard, J. El. Spec. Rel. Phen. **16**, 77 (1979).

[26] A. D. Becke, Phys. Rev. **A38**, 3098 (1988).

[27] A. D. Becke, K. E. Edgecombe, J. Chem. Phys. **92**, 5397 (1990).

[28] C. N. Berglund and H. J. Guggenheim, Phys. Rev. **185**, 1022 (1969).

[29] V. M. Bermudez, R. T. Williams, J. P. Long, R. K. Reed, and P. H. Klein, Phys. Rev. **B45**, 9266 (1992).

[30] M. Birkholz, S. Fiechter, A. Hartmann, and H. Tributsch, Phys. Rev. **B43**, 11926 (1991).

[31] T. A. Bither, R. J. Bouchard, W. H. Cloud, P. C. Donohue, and W. J. Siemons, Inorg. Chem. **7**, 2208 (1968).

[32] C. Blaauw, F. Leenhouts, F. van der Woude, and G. A. Sawatzky, J. Phys. **C8**, 459 (1975).

[33] F. Bloch, Z. Phys. **52**, 555 (1929).

[34] P. E. Blöchl, O. Jepsen, and O. K. Andersen, Phys. Rev. **B49**, 16223 (1994).

[35] A. A. Bolzan, C. Fong, B. J. Kennedy, and C. J. Howard, Acta Cryst. **B53**, 373 (1997).

[36] P. F. Bongers, Solid State Commun. **3**, 275 (1965).

[37] J. C. Bonner, M. E. Fischer, Phys. Rev. **135**, A640 (1964).

[38] M. Born, R. Oppenheimer, Ann. Phys. (Leipzig) **84**, 457 (1927).

[39] J. Boros, Z. Phys. **126**, 721 (1949).

[40] L. P. Bouckaert, R. Smoluchowski, and E. P. Wigner, Phys. Rev. **50**, 58 (1936).

[41] C. J. Bradley and A. P. Cracknell, *The Mathematical Theory of Symmetry in Solids*, Clarendon Press, Oxford, 1972.

[42] B. G. Brandt and A. C. Skapski, Acta Chim. Scand. **21**, 661 (1967).

[43] J. R. Brews, Phys. Rev. **B1**, 2557 (1970).

[44] P. J. Brown, and K. R. A. Ziebeck, J. Phys. **C11**, 2791 (1978).

[45] W. Brückner, H. Oppermann, W. Reichelt, J. I. Terukow, F. A. Tschudnowski, and E. Wolf, *Vanadiumoxide*, Akademie-Verlag, Berlin, 1983.

[46] K. Büker, S. Fiechter, V. Eyert, and H. Tributsch, submitted to J. Electrochem. Soc.

[47] D. W. Bullett, J. Phys. **C13**, L595 (1980).

[48] D. W. Bullett, J. Phys. **C15**, 6163 (1982).

[49] J. K. Burdett, Inorg. Chem. **24**, 2244 (1985).

[50] A. Bystrom, K. A. Wilhelmi, and O. Brotzen, Acta Chem. Scand. **4**, 1119 (1950).

[51] J. Callaway, *Energy Band Theory*, Academic Press, New York, 1964.

[52] J. Callaway, *Quantum Theory of the Solid State*, Academic Press, New York, 1974.

[53] R. Car and M. Parrinello, Phys. Rev. Lett. **55**, 2471 (1985).

[54] P. A. Carpy and J. Galy, Acta Cryst. **B31**, 1481 (1975).

[55] E. Caruthers, L. Kleinman, and H. I. Zhang, Phys. Rev. **B7**, 3753 (1973).

[56] E. Caruthers and L. Kleinman, Phys. Rev. **B7**, 3760 (1973).

[57] D. M. Ceperley and B. J. Alder, Phys. Rev. Lett. **45**, 566 (1980).

[58] D. J. Chadi and M. L. Cohen, Phys. Rev. **B8**, 5747 (1973).

[59] L. L. Chase, Phys. Rev. **B10**, 2226 (1974).

[60] A. K. Cheetham and C. N. R. Rao, Acta Cryst. **B32**, 1579 (1976).

[61] V. M. Cherkashenko, V. E. Dolgikh, and V. L. Volkov, Sov. Phys. Solid State **30**, 220 (1988).

[62] M. L. Cohen, Phys. Rep. **110**, 293 (1984).

[63] M. L. Cohen and V. Heine, in: *Solid State Physics*, Vol. 24, edited by H. Ehrenreich, F. Seitz and D. Turnbull, Academic Press, Orlando, 1970, pp. 37-248.

[64] P. A. Cox, *Transition Metal Oxides*, Clarendon Press, Oxford, 1992.

[65] F. M. F. de Groot, M. Grioni, J. C. Fuggle, J. Ghijsen, G. A. Sawatzky, and H. Petersen, Phys. Rev. **B40**, 5715 (1989).

[66] J. P. D'Haenens, D. Kaplan, and J. Tuchendler, Solid State Commun. **15**, 635 (1974).

[67] J. P. D'Haenens, D. Kaplan, and P. Merenda, J. Phys. **C8**, 2267 (1975).

[68] M. A. K. L. Dissanayake and L. L. Chase, Phys. Rev. **B18**, 6872 (1978).

[69] R. M. Dreizler and E. K. U. Gross, *Density Functional Theory*, Springer, Berlin Heidelberg, 1990.

[70] R. M. Dreizler and J. de Providência, *Density Functional Methods in Physics*, Plenum Press, New York, 1983.

[71] R. Enjalbert and J. Galy, Acta Cryst. **C42**, 1467 (1986).

[72] A. Ennaoui, S. Fiechter, W. Jaegermann, and H. Tributsch, J. Electrochem. Soc. **133**, 97 (1986).

[73] A. Ennaoui, S. Fiechter, Ch. Pettenkofer, N. Alonso-Vante, K. Büker, M. Bronold, Ch. Höpfner, and H. Tributsch, Sol. Energy Mat. Sol. Cells **29**, 289 (1993).

[74] H. Eschrig, *Optimized LCAO Method and the Electronic Structure of Extended Systems*, Springer, Berlin, 1989.

[75] H. Eschrig, *The Fundamentals of Density Functional Theory*, Teubner, Stuttgart, 1996.

[76] V. Eyert, PhD-Thesis, Technische Hochschule Darmstadt, 1991.

[77] V. Eyert, J. Comp. Phys. **124**, 271 (1996).

[78] V. Eyert, Hahn-Meitner-Institute Report B548, Berlin 1997

[79] V. Eyert, *Electronic structure calculations for crystalline materials*, in: *Density Functional Methods: Applications in Chemistry and Materials Science*, edited by M. Springborg, Wiley, Chichester, 1997, pp. 233-304.

[80] V. Eyert, *The ASW method: A comprehensive treatment*, (unpublished).

[81] V. Eyert and K.-H. Höck, Phys. Rev. **B57**, 12727-12737 (1998).

[82] V. Eyert and K.-H. Höck, (unpublished).

[83] V. Eyert, K.-H. Höck, S. Fiechter, and H. Tributsch, Phys. Rev. **B57**, 6350-6359 (1998).

[84] V. Eyert, R. Horny, K.-H. Höck, and S. Horn, submitted to Phys. Rev. **B**

[85] V. Eyert, R. Horny, K.-H. Höck, and S. Horn, submitted to Phys. Rev. **B**

[86] V. Eyert and S. F. Matar, (unpublished).

[87] V. Eyert, B. Siberchicot, and M. Verdaguer, Phys. Rev. **B56**, 8959-8969 (1997).

[88] I. J. Ferrer, D. M. Nevskaia, C. de las Heras, and C. Sánchez, Solid State Commun. **74**, 913 (1990).

[89] L. Fiermans, R. Hoogewijs, and J. Vennik, Surf. Sci. **47**, 1 (1975).

[90] S. L. Finklea III, L. Cathey, and E. L. Amma, Acta Cryst. **A32**, 529 (1976).

[91] W. Folkerts, G. A. Sawatzky, C. Haas, R. A. de Groot, and F. U. Hillebrecht, J. Phys. **C20**, 4135 (1987).

[92] Y. Fujii, H. Nakao, T. Yosihama, M. Nishi, K. Nakajima, K. Kakurai, M. Isobe, Y. Ueda, and H. Sawa, J. Phys. Soc. Japan **66**, 326 (1997).

[93] C. D. Gelatt, Jr., H. Ehrenreich, and R. E. Watson, Phys. Rev. **B15**, 1613 (1977).

[94] F. Gervais and W. Kress, Phys. Rev. **B31**, 4809 (1985).

[95] M. Ghedira, J. Chenavas, and M. Marezio, J. Phys. **C10**, L309 (1977).

[96] M. Ghedira, C. Do-Dinh, M. Marezio, and J. Mercier, J. Solid State Chem. **59**, 159 (1985).

[97] M. Ghedira, H. Vincent, M. Marezio, and J. C. Launay, J. Solid State Chem. **22**, 423 (1977).

[98] E. Goering, PhD-Thesis, Universität Augsburg, 1996.

[99] E. Goering, O. Müller, M. L. denBoer, and S. Horn, Physica **B194-196**, 1217 (1994).

[100] E. Goering, O. Müller, M. Klemm, J. P. Urbach, H. Petersen, C. Jung, M. L. denBoer, and S. Horn, Physica **B208&209**, 300 (1995).

[101] E. Goering, O. Müller, M. Klemm, M. L. denBoer, and S. Horn, Phil. Mag. **B75**, 229 (1997).

[102] E. Goering, M. Schramme, O. Müller, H. Paulin, M. Klemm, M. L. denBoer, and S. Horn, Physica **B230-232**, 996 (1997).

[103] E. Goering, M. Schramme, O. Müller, R. Barth, H. Paulin, M. Klemm, M. L. denBoer, and S. Horn, Phys. Rev. **B55**, 4225 (1997).

[104] D. E. Goldberg, *Genetic Algorithms in Search, Optimization, and Machine Learning*, Addison-Wesley, Reading 1989.

[105] H. Gollisch and L. Fritsche, phys. stat. sol. (b) **86**, 145 (1978).

[106] J. B. Goodenough, Phys. Rev. **117**, 1442 (1960).

[107] J. B. Goodenough, J. Solid State Chem. **3**, 26 (1971).

[108] J. B. Goodenough, *Metallic Oxides*, in: *Progress in Solid State Chemistry*, edited by H. Reiss, Pergamon Press, Oxford, 1971, pp. 145-399.

[109] J. B. Goodenough, J. Solid State Chem. **5**, 144 (1972).

[110] J. B. Goodenough and H. Y.-P. Hong, Phys. Rev. **B8**, 1323 (1973).

[111] M. Gupta, A. J. Freeman, and D. E. Ellis, Phys. Rev. **B16**, 3338 (1977).

[112] D. R. Hamann, Phys. Rev. Lett. **42**, 662 (1979).

[113] D. R. Hamann, Phys. Rev. **B40**, 2980 (1989).

[114] J. M. Hastings and L. M. Corliss, IBM J. Res. Dev. **14**, 227 (1970).

[115] A. Haug, *Theoretical Solid State Physics*, Pergamon Press, New York, 1972.

[116] C. J. Hearn, J. Phys. **C5**, 1317 (1972).

[117] L. Hedin and B. I. Lundquist, J. Phys. **C4**, 2064 (1971).

[118] V. Heine, in: *Solid State Physics*, Vol. 24, edited by H. Ehrenreich, F. Seitz and D. Turnbull, Academic Press, Orlando, 1970, pp. 1-36.

[119] C. Herring, Phys. Rev. **57**, 1169 (1940).

[120] L. Hodges, R. E. Watson, and H. Ehrenreich, Phys. Rev. **B5**, 3953 (1972).

[121] R. Hoffmann, *Solids and Surfaces: A Chemist's View of Bonding in Extended Structures*, VCH, New York, 1988.

[122] P. Hohenberg and W. Kohn, Phys. Rev. **136**, B864 (1964).

[123] R. Horny, Diploma-Thesis, Universität Augsburg, 1997.

[124] R. Horny, V. Eyert, K.-H. Höck, and S. Horn, Verhandl. DPG (VI) **33**, TT21.31 (1998).

[125] S. Hüfner, *Photoelectron Spectroscopy*, Springer, Berlin, 1995.

[126] V. A. Ioffe and I. B. Patrina, phys. stat. sol. **40**, 389 (1970).

[127] M. Isobe and Y. Ueda, J. Phys. Soc. Japan **65**, 1178 (1996).

[128] H. S. Jarrett, W. H. Cloud, R. J. Bouchard, S. R. Butler, C. G. Frederick, and J. L. Gillson, Phys. Rev. Lett. **21**, 617 (1968).

[129] R. J. Jelitto, J. Phys. Chem. **30**, 609 (1969).

[130] O. Jepsen and O. K. Andersen, Z. Phys. **B97**, 35 (1995).

[131] W. Jones and N. H. March, *Theoretical Solid State Physics*, Wiley, London, 1973.

[132] T. Kawakubo, J. Phys. Soc. Jap. **20**, 516 (1965).

[133] T. Kawakubo and T. Nakagawa, J. Phys. Soc. Jap. **19**, 517 (1964).

[134] J. Keller, J. Phys. **C4**, L85 (1971).

[135] N. Kenny, C. R. Kannewurf, and D. H. Whitmore, J. Phys. Chem. Solids **27**, 1237 (1966).

[136] M. A. Khan, J. Phys. **C9**, 81 (1976).

[137] K. Kikuchi, T. Miyadai, H. Itoh, and T. Fukui, J. Phys. Soc. Japan **45**, 444 (1978).

[138] C. Kittel, *Introduction to Solid State Physics*, Wiley, New York, 1986.

[139] S. Klimm, PhD-Thesis, Universität Augsburg, 1997.

[140] D. D. Koelling and B. N. Harmon, J. Phys. **C10**, 3107 (1977).

[141] W. Kohn and N. Rostoker, Phys. Rev. **94**, 1111 (1954).

[142] W. Kohn and L. J. Sham, Phys. Rev. **140**, A1133 (1965).

[143] W. Kohn and P. Vashishta, *General Density Functional Theory*, in: *Theory of the Inhomogeneous Electron Gas*, edited by S. Lundquist and N. H. March, Plenum Press, New York, 1983, pp. 79-147.

[144] J. Korringa, Physica **13**, 392 (1947).

[145] G. F. Koster, in: *Solid State Physics*, Vol. 5, edited by F. Seitz and D. Turnbull, Academic Press, Orlando, 1970, pp. 173-256.

[146] K. Kosuge, J. Phys. Soc. Jap. **22**, 551 (1967).

[147] W. W. Kou and M. S. Seehra, Phys. Rev. **B18**, 7062 (1978).

[148] O. V. Kovalev, *Irreducible Representations of Space Groups*, Gordon and Breach, New York, 1965.

[149] E. S. Kryachko and E. V. Ludeña, *Energy Density Functional Theory of Many-Electron Systems*, Kluwer Academic Publishers, Dordrecht Boston London, 1990.

[150] J. Kübler and V. Eyert, *Electronic structure calculations*, in: *Electronic and Magnetic Properties of Metals and Ceramics*, edited by K. H. J. Buschow, VCH Verlagsgesellschaft, Weinheim 1992, pp. 1-145. Volume 3A of the series: *Materials Science and Technology*, edited by R. W. Cahn, P. Haasen, and E. J. Kramer, VCH Verlagsgesellschaft, Weinheim 1991-1996.

[151] D. Kucharczyk and T. Niklewski, J. Appl. Cryst. **12**, 370 (1979).

[152] E. V. Kuz'min and S. G. Ovchinnikov, Sov. Phys. Solid State **19**, 1752 (1977).

[153] W. Lambrecht, B. Djafari-Rouhani, M. Lannoo, and J. Vennik, J. Phys. **C13**, 2485 (1980).

[154] W. Lambrecht, B. Djafari-Rouhani, M. Lannoo, P. Clauws, L. Fiermans, and J. Vennik, J. Phys. **C13**, 2503 (1980).

[155] W. Lambrecht, B. Djafari-Rouhani, and J. Vennik, J. Phys. **C14**, 4785 (1981).

[156] S. Lauer, A. X. Trautwein, and F. E. Harris, Phys. Rev. **B29**, 6774 (1984).

[157] M. Levy, Proc. Natl. Acad. Sci. (USA) **76**, 6062 (1979).

[158] M. Levy, Phys. Rev. **A26**, 1200 (1982).

[159] E. K. Li, K. H. Johnson, D. E. Eastman, and J. L. Freeouf, Phys. Rev. Lett. **32**, 470 (1974).

[160] M. Lohmann, A. Loidl, M. Klemm, G. Obermeier, and S. Horn, Solid State Comm. **104**, 649 (1997)

[161] J. M. Longo and P. Kierkegaard, Acta Chim. Scand. **24**, 420 (1970).

[162] T. Loucks, *Augmented Plane Wave Method*, Benjamin, New York, 1967.

[163] W. Ludwig and C. Falter, *Symmetries in Physics*, Springer, Berlin, 1996.

[164] H.-D. Lutz, G. Kliche, and H. Haeuseler, Z. Naturforsch. **36a**, 184 (1981).

[165] H.-D. Lutz, G. Schneider, and G. Kliche, J. Phys. Chem. Solids **46**, 437 (1985).

[166] H.-D. Lutz, P. Willich, and H. Haeuseler, Z. Naturforsch. **31a**, 847 (1976).

[167] A. H. MacDonald and S. H. Vosko, J. Phys. **C12**, 2977 (1979).

[168] A. Magnéli and G. Andersson, Acta Chim. Scand. **9**, 1378 (1955).

[169] M. Marezio, D. B. McWhan, J. P. Remeika, and P. D. Dernier, Phys. Rev. **B5**, 2541 (1972).

[170] B.-O. Marinder, Arkiv Kemi **19**, 435 (1962).

[171] S. Matar, G. Demazeau, J. Sticht, V. Eyert, and J. Kübler, J. Phys. I France **2**, 315-328 (1992); J. Phys. I France **4**, 1259 (1994).

[172] S. F. Matar, V. Eyert, J. Magn. Magn. Mat. **166**, 321-328 (1997)

[173] S. F. Matar, V. Eyert, B. Chevalier, and J. Etourneau, Int. J. Quantum Chem. **61**, 705-709 (1997)

[174] S. F. Matar, V. Eyert, A. Mavromaras, S. Najm, B. Chevalier, and J. Etourneau, J. Magn. Magn. Mat. **174**, 219-235 (1997)

[175] S. F. Matar, V. Eyert, S. Najm, B. Chevalier, and J. Etourneau, J. Mat. Chem. **8**, 1303-1310 (1998)

[176] S. Matar, V. Eyert, J. Sticht, J. Kübler, and G. Demazeau, J. Phys. I France **4**, 1199-1215 (1994).

[177] L. F. Mattheiss, Phys. Rev. **133**, A1399 (1964).

[178] L. F. Mattheiss, Phys. Rev. **B13**, 2433 (1976).

[179] D. B. McWhan, M. Marezio, J. P. Remeika, and P. D. Dernier, Phys. Rev. **B10**, 490 (1974).

[180] M. S. Methfessel and A. T. Paxton, Phys. Rev. **B40**, 3616 (1989).

[181] A. Michalak, M. Witko, and K. Hermann, Surf. Science **375**, 385 (1997).

[182] S. Minomura and H. Nagasaki, J. Phys. Soc. Jap. **19**, 131 (1964).

[183] T. Miyadai, K. Kikuchi, and Y. Ito, Physica **86-88B**, 901 (1977).

[184] S. Miyahara and T. Teranishi, J. Appl. Phys. **39**, 896 (1968).

[185] V. G. Mokerov, V. L. Makarov, V. B. Tulvinskii, and A. R. Begishev, Opt. Spectrosc. **40**, 58 (1976).

[186] H. J. Monkhorst and J. D. Pack, Phys. Rev. **B13**, 5188 (1976).

[187] F. J. Morin, Phys. Rev. Lett. **3**, 34 (1959).

[188] V. L. Moruzzi, J. F. Janak and A. R. Williams, *Calculated Electronic Properties of Metals*, Pergamon Press, New York, 1978.

[189] N. F. Mott, Phil. Mag. **6**, 287 (1961).

[190] O. Müller, PhD-Thesis, Universität Augsburg, 1996.

[191] O. Müller, E. Goering, J. P. Urbach, T. Weber, H. Paulin, M. Klemm, M. L. denBoer, and S. Horn, J. Phys. IV France **7**, Colloque C2, 533 (1997).

[192] W. Müller, H. H. Bertschat, K. Biedermann, R. Kowallik, E. Lahmer-Naim, H.-E. Mahnke, S. Seeger, W.-D. Zeitz, S. Fiechter, and H. Tributsch, Phys. Rev. **B41**, 8624 (1990).

[193] R. A. Munson, W. DeSorbo, and J. S. Kouvel, J. Chem. Phys. **47**, 1769 (1967).

[194] A. V. Nikolaev, Y. N. Kostrubov, and B. V. Andreev, Sov. Phys. Solid State **34**, 1514 (1992).

[195] S. Ogawa, J. Appl. Phys. **50**, 2308 (1979).

[196] S. Ogawa, S. Waki, and T. Teranishi, Int. J. Magn. **5**, 349 (1974).

[197] T. Ohama, M. Isobe, H. Yasuoka, and Y. Ueda, J. Phys. Soc. Japan **66**, 545 (1997).

[198] A. Ohsawa, H. Yamamoto, and H. Watanabe, J. Phys. Soc. Japan **37**, 568 (1974).

[199] D. Paquet and P. Leroux-Hugon, Phys. Rev. **B22**, 5284 (1980).

[200] M. C. Payne, M. P. Teter, D. C. Allan, T. A. Arias, and J. D. Joannopoulos, Rev. Mod. Phys. **64**, 1045 (1992).

[201] J. P. Perdew, J. A. Chevary, S. H. Vosko, K. A. Jackson, M. r. Pederson, D. J. Singh, and C. Fiolhais, Phys. Rev. **B46**, 6671 (1992).

[202] D. G. Pettifor, *Bonding and Structure of Molecules and Solids*, (Clarendon Press, Oxford, 1995).

[203] J. C. Phillips, Phys. Rev. **112**, 685 (1958).

[204] J. C. Phillips and L. Kleinman, Phys. Rev. **116**, 287 (1959).

[205] J. P. Pouget and H. Launois, J. Phys. (France) **C4-37**, 49 (1976).

[206] J. P. Pouget, H. Launois, J. P. D'Haenens, P. Merenda, and T. M. Rice, Phys. Rev. Lett. **35**, 873 (1975).

[207] J. P. Pouget, H. Launois, T. M. Rice, P. Dernier, A. Gossard, G. Villeneuve, and P. Hagenmuller, Phys. Rev. **B10**, 1801 (1974).

[208] R. J. Powell, C. N. Berglund, and W. E. Spicer, Phys. Rev. **178**, 1410 (1969).

[209] J. Y. Prieur, P. Seznec, S. Ziolkiewicz, J. Phys. Lett. **38**, L25 (1977).

[210] R. Pynn, J. D. Axe, and R. Thomas, Phys. Rev. **B13**, 2965 (1976).

[211] A. K. Rajagopal, Adv. Chem. Phys. **41**, 59 (1980).

[212] A. K. Rajagopal and J. Callaway, Phys. Rev. **B7**, 1912 (1973).

[213] M. V. Ramana and A. K. Rajagopal, Adv. Chem. Phys. **54**, 231 (1983).

[214] K. V. K. Rao, S. V. N. Naidu, and L. Iyengar, J. Phys. Soc. Jap. **23**, 1380 (1967).

[215] T. M. Rice, H. Launois, and J. P. Pouget, Phys. Rev. Lett. **73**, 3042 (1994).

[216] D. B. Rogers, R. D. Shannon, A. W. Sleight, and J. L. Gillson, Inorg. Chem. **8**, 841 (1969).

[217] W. H. Rosevear and W. Paul, Phys. Rev. **B7**, 2109 (1973).

[218] T. A. Sasaki and K. Kiuchi, Chem. Phys. Lett. **84**, 356 (1981).

[219] T. A. Sasaki, T. Soga, and H. Adachi, phys. stat. sol. (b) **113**, 647 (1982).

[220] A. Schlegel and P. Wachter, J. Phys. **C9**, 3363 (1976).

[221] M. Schramme, R. Barth, V. Eyert, E. Goering, O. Müller, and S. Horn, Verhandl. DPG (VI) **32**, O18.7 (1997).

[222] M. Schramme, R. Barth, V. Eyert, E. Goering, O. Müller, S. Horn, and M. L. denBoer, Bull. Am. Phys. Soc. **42**, 138 (1997).

[223] M. Schramme, R. Barth, V. Eyert, E. Goering, O. Müller, K.-H. Höck, S. Horn, and M. L. denBoer, (unpublished).

[224] B. Segall and F. S. Ham, in: *Methods in Computational Physics*, edited by B. Alder, S. Fernbach, and M. Rotenberg, Academic Press, New York, 1968, pp. 251-293.

[225] S. M. Shapiro, J. D. Axe, G. Shirane, and P. M. Raccah, Solid State Commun. **15**, 377 (1974).

[226] S. Shin, S. Suga, M. Taniguchi, M. Fujisawa, H. Kanzaki, A. Fujimori, H. Daimon, Y. Ueda, K. Kosuge, and S. Kachi, Phys. Rev. **B41**, 4993 (1990).

[227] D. J. Singh, *Planewaves, Pseudopotentials and the LAPW Method*, Kluwer Academic Publishers, Boston Dordrecht London, 1994.

[228] H. L. Skriver, *The LMTO Method*, Springer, Berlin New York, 1984.

[229] J. C. Slater, Phys. Rev. **51**, 846 (1937).

[230] J. C. Slater, *Quantum Theory of Molecules and Solids*, Vol. 2, McGraw-Hill, New York, 1965.

[231] P. I. Sorantin and K. Schwarz, Inorg. Chem. **31**, 567 (1992).

[232] C. Sourisseau, R. Cavagnat, and M. Fouassier, J. Phys. Chem. Solids **52**, 537 (1991).

[233] E. D. Stevens, M. L. DeLucia, and P. Coppens, Inorg. Chem. **19**, 813 (1980).

[234] J. Sticht, K.-H. Höck, and J. Kübler, J. Phys. Cond. Matt. **1**, 8155 (1989)

[235] S. Suga, M. Taniguchi, S. Shin, M. Seki, S. Shibuya, K. Sato, and T. Yamaguchi, Physica **117B&118B**, 353 (1983).

[236] C. Sugiura, J. Chem. Phys. **74**, 215 (1981).

[237] C. Sugiura, I. Suzuki, J. Kashiwakura, and Y. Gohshi, J. Phys. Soc. Japan **40**, 1720 (1976).

[238] W. M. Temmerman, P. J. Durham, and D. J. Vaughan, Phys. Chem. Miner. **20**, 248 (1993).

[239] V. M. Teplinskiǐ, Sov. Phys. JETP **51**, 995 (1980).

[240] K. Terakura, in: *Computational Physics as a New Frontier in Condensed Matter Research*, edited by H. Takayama, M. Tsukuda, H. Shiba, F. Yonezawa, M. Imada, and Y. Okabe, The Physical Society of Japan, Tokyo, 1995.

[241] H. Terauchi and J. B. Cohen, Phys. Rev. **B17**, 2494 (1978).

[242] E. I. Terukov, W. Reichelt, M. Wolf, H. Hemschik, and H. Oppermann, phys. stat. sol. (a) **48**, 377 (1978).

[243] J. Umeda, H. Kusumoto, K. Narita, and E. Yamada, J. Chem. Phys. **42**, 1458 (1965).

[244] D. Vanderbilt, Phys. Rev. **B41**, 7892 (1990).

[245] H. van der Heide, R. Hemmel, C. F. van Bruggen, and C. Haas, J. Solid State Chem. **33**, 17 (1980).

[246] A. N. Vasil'ev, A. I. Smirnov, M. Isobe, and Y. Ueda, Phys. Rev. **B56**, 5065 (1997)

[247] H. W. Verleur, A. S. Barker, Jr., and C. N. Berglund, Phys. Rev. **172**, 788 (1968).

[248] G. Vignale and M. Rasolt, Phys. Rev. Lett. **59**, 2360 (1987).

[249] G. Vignale and M. Rasolt, Phys. Rev. **B37**, 10685 (1988).

[250] H. Vincent and M. Marezio, *On Strucutral Aspects of Molybdenum Bronzes and Molybdenum Oxides in Relation to Their Low-Dimensional Transport Properties*, in: *Low-Dimensional Electronic Properties of Molybdenum Bronzes and Oxides*, edited by C. Schlenker, Kluwer Academic Publishers, Dordrecht 1989, pp. 49-86.

[251] H. Vogt, T. Chattopadhyay, and H. J. Stolz, J. Phys. Chem. Solids **44**, 869 (1983).

[252] E. P. Vol'skiĭ, A. G. Gapotchenko, E. S. Itskevich, and V. M. Teplinskiĭ, Sov. Phys. JETP **49**, 848 (1979).

[253] E. P. Vol'skiĭ and V. M. Teplinskiĭ, Sov. Phys. JETP **36**, 550 (1973).

[254] E. P. Vol'skiĭ and V. M. Teplinskiĭ, Sov. Phys. JETP **42**, 373 (1975).

[255] S. H. Vosko, L. Wilk, and M. Nusair, Can. J. Phys. **58**, 1200 (1980).

[256] C. S. Wang, J. Callaway, Comput. Phys. Commun. **14**, 327 (1978).

[257] R. E. Watson, H. Ehrenreich, and L. Hodges, Phys. Rev. Lett. **15**, 829 (1970).

[258] M. Weiden, R. Hauptmann, C. Geibel, F. Steglich, M. Fischer, P. Lemmens, and G. Güntherodt, Z. Phys. **B103**, 1 (1997).

[259] R. M. Wentzcovitch, W. W. Schulz, and P. B. Allen, Phys. Rev. Lett. **72**, 3389 (1994).

[260] R. M. Wentzcovitch, W. W. Schulz, and P. B. Allen, Phys. Rev. Lett. **73**, 3043 (1994).

[261] F. Werfel and E. Minni, J. Phys. **C16**, 6091 (1983).

[262] S. Westman, Acta Chim. Scand. **15**, 217 (1961).

[263] G. Wiech and E. Zöpf, J. Phys. (Paris) **C4**, 200 (1971).

[264] A. R. Williams, Phys. Rev. **B1**, 3417 (1970).

[265] A. R. Williams and U. von Barth, in: *Theory of the Inhomogeneous Electron Gas*, edited by S. Lundquist and N. H. March, Plenum Press, New York, 1983, pp. 189-307.

[266] A. R. Williams, J. Kübler, and C. D. Gelatt, Jr., Phys. Rev. **B19**, 6094 (1979).

[267] A. R. Williams and J. van W. Morgan, J. Phys. **C7**, 37 (1974).

[268] J. A. Wilson, Adv. Phys. **21**, 143 (1972).

[269] J. A. Wilson and G. D. Pitt, Philos. Mag. **23**, 1297 (1971).

[270] J. A. Wilson and A. D. Yoffe, Adv. Phys. **18**, 193 (1969).

[271] X. Yao, Y.-K. Kuo, D. K. Powell, J. W. Brill, and J. M. Honig, Phys. Rev. **B56**, 7129 (1997).

[272] J. J. Yeh and I. Lindau, At. Data Nucl. Data Tables **32**, 1 (1985).

[273] H. Yoshino, K. Shimikoshi, and E. Miyazaki, J. El. Spec. Rel. Phen. **36**, 269 (1985).

[274] T. Yosihama, M. Nishi, K. Nakajima, K. Kakurai, and Y. Fujii, M. Isobe, Y. Ueda, Physica **B234-236**, 539 (1997)

[275] Z. Zhang and V. E. Henrich, Surf. Science **321**, 133 (1994).

[276] G. L. Zhao, J. Callaway, and M. Hayashibara, Phys. Rev. **B48**, 15781 (1993).

[277] J. M. Ziman, *Principles of the Theory of Solids*, Cambridge University Press, Cambridge, 1965.

[278] R. Zimmermann, R. Claessen, F. Reinert, P. Steiner, and S. Hüfner, J. Phys.: Cond. Mat. **10**, (June 1998).

[279] A. Zylbersztejn and N. F. Mott, Phys. Rev. **B11**, 4383 (1975).

Acknowledgement

It is a great pleasure for me to thank K.-H. Höck for the longstanding friendship and cooperation. His continuous support and the numerous valuable discussions without doubt had a large impact on my scientific work during the last years.

I would like to express my gratitude to U. Eckern and S. Horn for strongly supporting my cooperation with the Forschergruppe in Augsburg, which only laid ground for this thesis. I acknowledge very gratefully the many important discussions we had as well as their continuous support and interest.

I am likewise indebted to all other members of the Forschergruppe in Augsburg for numerous discussions, in particular to D. Maurer, V. Müller, G. Schütz, and A. Muramatsu.

I would like to thank R. Horny, S. Klimm, E. Goering, O. Müller, and W.-D. Yang for the very good cooperation, many helpful discussions, a lot of technical help and, last not least, for the experimental data.

I am very grateful to my friend S. F. Matar for the longstanding cooperation on many projects ranging from our early work on CrO_2 to the recent implementation of the COOP.

I am likewise very grateful to O. K. Andersen and O. Gunnarsson for their support as well as the very good cooperation during the last years.

It is a pleasure for me to thank R. Claessen and S. Hüfner for a lot of valuable discussions, which helped me to extend my knowledge about photoemission, as well as for the very fruitful cooperation over the last years.

I am indebted to H. Tributsch and S. Fiechter for the very good cooperation on iron pyrite.

I would like to express my gratitude to E. Holub-Krappe and W.-D. Zeitz for the interesting and very fruitful cooperation on various projects as well as for their support during the last years.

Last but not least, my greatest thanks go to Anja, Florian and Carolin to whom I dedicate this thesis. Without their neverending patience and support this work would, of course, never have been possible.